DESIGN AND FABRICATION OF A LONG-LIFE STIRLING CYCLE COOLER FOR SPACE APPLICATION

Phase III - Prototype Model

C. Keung, P. J. Patt, M. Starr, R. C. Sweet, L. A. Bourdillon,
R. Figueroa, M. Hartmann, R. McFarlane

PHILIPS LABORATORIES
North American Philips Corporation
Briarcliff Manor, New York 10510

November 1990
Final Report for Period September 1981 - September 1990

Prepared for

NASA
GODDARD SPACE FLIGHT CENTER
Greenbelt, Maryland 20771

DESIGN AND FABRICATION OF A LONG-LIFE STIRLING CYCLE COOLER FOR SPACE APPLICATION

Phase III - Prototype Model

C. Keung, P. J. Patt, M. Starr, R. C. Sweet, L. A. Bourdillon,
R. Figueroa, M. Hartmann, R. McFarlane

PHILIPS LABORATORIES
North American Philips Corporation
Briarcliff Manor, New York 10510

November 1990
Final Report for Period September 1981 - September 1990

Prepared for

NASA
GODDARD SPACE FLIGHT CENTER
Greenbelt, Maryland 20771

1. Report No.	2. Government Accession No.	3. Recipient's Catalog No.
4. Title and Subtitle DESIGN AND FABRICATION OF A LONG-LIFE STIRLING CYCLE COOLER FOR SPACE APPLICATION Phase III - Prototype Model		5. Report Date November 1990 6. Performing Organization Code
7. Author(s) C. Keung, P.J. Patt, M. Starr, R.C. Sweet, L.A. Bourdillon, R. Figueroa, M. Hartmann, R. McFarlane		8. Performing Organization Report No. PL-11-CR90-1116
9. Performing Organization Name and Address PHILIPS LABORATORIES North American Philips Corp. Briarcliff Manor, New York 10510		10. Work Unit No. 11. Contract or Grant No. NAS5-26688
12. Sponsoring Agency Name and Address NASA GODDARD SPACE FLIGHT CENTER Greenbelt, Maryland 20771		13. Type of Report and Period Covered Final Report Sept. 1981 - Sept. 1990 14. Sponsoring Agency Code
15. Supplementary Notes		

16. Abstract

A second-generation, Stirling-cycle cryocooler (cryogenic refrigerator) for space applications, with a cooling capacity of 5 watts at 65°K, was recently completed. The refrigerator, call the Prototype Model, was designed with a goal of 5-year life with no degradation in cooling performance. The free displacer and free piston of the refrigerator are driven directly by moving-magnet linear motors with the moving elements supported by active magnetic bearings. The use of clearance seals and the absence of outgassing material in the working volume of the refrigerator enable long-life operation with no deterioration in performance. Fiber-optic sensors detect the radial position of the shafts and provide a control signal for the magnetic bearings. The frequency, phase, stroke and offset of the compressor and expander are controlled by signals from precision linear position sensors (LVDTs). The vibration generated by the compressor and expander is cancelled by an active counterbalance which also uses a moving-magnet linear motor and magnetic bearings. The driving signal for the counterbalance is derived from the compressor and expander position sensors which have wide bandwidth for suppression of harmonic vibrations. The efficiency of the three active members, which operate in a resonant mode, is enhanced by a magnetic spring in the expander and by gas springs in the compressor and counterbalance. The cooling was achieved with a total motor input power of 139 watts. The magnetic-bearing stiffness was significantly increased from the first-generation cooler to accommodate shuttle launch vibrations.

17. Key Words (Selected by Author(s))	18. Distribution Statement
Stirling Cycle, Cryogenic Refrigerator, Magnetic Bearings, Optical Position Sensor, Cryocooler, Clearance Seals, Linear Motor, Linear Position Sensor, Thermodynamic Cycle, Engineering Model, Prototype Model, Magnetic Spring, Gas Springs	

19. Security Classif. (of this report)	20. Security Classif. (of this page)	21. No. of Pages	22. Price*
		189	

PREFACE

This program was the third phase in the development of a long-life cryogenic refrigerator for spaceborne missions. Traditional mechanical systems have been only marginally suitable for long life because of wear, fatigue and friction associated with bearings, seals and linkages. In the first two phases, Philips Laboratories designed and constructed a laboratory-model refrigerator (Engineering Model), based on the Stirling Cycle, to demonstrate feasibility of long-life operation. The system used linear stationary coil motors for reciprocating the moving members of the compressor and expander. Frictionless operation was achieved by suspending the moving parts via active magnetic bearings which provide clearance seals between the compressor and expander. In a subsequent life test the refrigerator, designed to provide 5 watts of cooling at 65°K, operated for 5 years with over 500 start/stop cycles.

The second-generation refrigerator, called the Prototype Model and described in this report, improved on the original design in several key areas to enhance reliability, power efficiency and weight reduction, and to enable the system to withstand launch loads and operate in any orientation. In addition, the goal was to preserve the five-year system lifetime demonstrated by the Engineering Model. A new electronic rack was designed and constructed to provide: drive signals to the active elements, monitoring of several operating parameters, a system of interlocks for graceful shutdown in the event of failure, and remote operation by external computer. The refrigerator has two operating modes - Standby and Operate.

The system performance results of the Prototype Model refrigerator were excellent. The overall weight of the machine was lower than the design requirement, as was the input power required to produce the specified cooling. The time needed to achieve cryogenic temperatures, starting from ambient, was much shorter than maximum design specification. Still to be verified are the ability of the refrigerator to withstand launch loads and the five-year lifetime. These attributes will be verified by testing at NASA.

The design of the refrigerator is well documented in drawings and specifications, so that replication is possible by any qualified fabricator. The electronic support system was constructed from commercial-grade components and therefore is not qualified for flight. A program to design flight qualified electronics would be a logical next step in the evolution of the refrigerator for satellite service.

ACKNOWLEDGMENTS

The authors wish to express their deep appreciation to Dr. S. Castles and M. Gasser of NASA Goddard Space Flight Center for their support and their confidence in the ability of the Philips Laboratories team to successfully complete the Prototype Model Refrigerator. Our acknowledgement of M. Gasser recognizes his ongoing support from the conception of the program in 1978 through the development of the first model and the Prototype Model.

The authors also thank A. Daniels for his continuing support which began with the early stages of the Philips Laboratories' cryogenics program in the 1960's and continued to completion, even after he was not officially involved, and Dr. G. Blom for his guidance and leadership in bringing this program to a successful conclusion. We thank A. Shaik for his contribution in the design and development of fiber-optic radial position sensors and stress analysis, and R. Eggleston and E. Lindale for their engineering contributions in pressure transducers, magnetic materials, heat treatment and joining of dissimilar materials. Our thanks go to L. Casey for his valuable assistance in bearing driver technology.

For the excellent drawings which facilitated construction of the Prototype Model and made it possible for the refrigerator to be reproduced, we thank R. Carminucci, the late J. Hejduk, M. Mohammed, J. Sanchez and R. Wilhelm under the direction of G. Culhane.

We extend special thanks to those responsible for the mechanical fabrication of the refrigerator, primarly the late E. Harkins who served as leader of the Philips NASA shop team for the first half of the program, and also G. Grotkopp, J. Muccini, A. Morrison, A. Valinoti, R. Shoreland and H. Zwiefel. We also thank W. Schroeder for fabrication of the electronic subassemblies.

The authors wish to thank L. Miller for his able administration of the contract and extend special thanks to J. Lebid whose contract administration services, report management, editing, and attention to detail resulted in the accurate and timely monthly and final reports and other technical documentation of the program.

Finally, we thank those whose efforts resulted in the lucid and attractive documentation of the research and development effort: J. Provenzano, J. Hessler, A. Santiago and M. Jones of the Business Systems and Documentation Department; D. McCoach, J. Rouchard, V. Diehl and M. Salamack of the Graphics Department; and F. Molinaro for his photographic coverage.

TABLE OF CONTENTS

Section			Page
BIBLIOGRAPHIC DATA SHEET			i
PREFACE			iii
ACKNOWLEDGMENTS.			iv
LIST OF ILLUSTRATIONS			x
LIST OF TABLES			xiii
1.	INTRODUCTION		1-1
	1.1	Background	1-1
	1.2	System Design Requirements	1-1
2.	DESCRIPTION OF REFRIGERATION SYSTEM		2-1
	2.1	Background	2-1
	2.2	Major Design Concepts	2-3
		2.2.1 Stirling Cycle	2-3
		2.2.2 All Metal/Ceramic Surfaces.	2-3
		2.2.3 Rectilinear Drive and Linear Motors	2-4
		2.2.4 Magnetic and Gas Springs.	2-6
		2.2.5 Actively Controlled Magnetic Bearings and Optical Sensors	2-7
		2.2.6 Clearance Seals	2-8
		2.2.7 Actively Controlled Counterbalance	2-9
	2.3	Prototype Model Cooler	2-10
		2.3.1 General.	2-10
		2.3.2 Expander Subassembly	2-10
		2.3.3 Compressor Subassembly	2-13
		2.3.4 Counterbalance Subassembly	2-16
3.	THERMODYNAMIC AND DYNAMIC DESIGN		3-1
	3.1	Introduction	3-1
	3.2	Thermodynamics and Dynamics of a Free-Displacer, Free-Piston, Stirling-Cycle Refrigerator..	3-2
		3.2.1 Pressure Variation in a Stirling Refrigerator	3-2
		3.2.2 Cold Production and Input Power	3-3
		3.2.3 Coupling of Thermodynamics and Dynamics	3-4
		3.2.4 Displacer Dynamics and Motor Input Power	3-4
		3.2.5 Gas-Pressure-Driven Displacer	3-5
		3.2.6 Piston Dynamics and Input Power	3-6

TABLE OF CONTENTS (Cont'd.)

Section			Page
	3.3	Design Optimization of a Stirling-Cycle Refrigerator	3-7
4.		DESIGN OF PHILIPS LINEAR MOTORS	4-1
	4.1	Working Principles	4-1
	4.2	Soft and Hard Magnetic Materials	4-3
		4.2.1 Hard Materials for Permanent Magnets	4-3
		4.2.2 Magnet Uniformity	4-4
		4.2.3 Soft Magnetic Materials	4-5
		4.2.4 Motor	4-5
		4.2.5 Test Results	4-6
	4.3	Magnetic Circuits	4-7
	4.4	Optimization of Linear Motors	4-8
	4.5	Motor Coil	4-9
	4.6	Displacer Spring/Motor	4-10
		4.6.1 Spring/Motor Design	4-10
		4.6.2 Dynamic Test Results	4-12
5.		ACTIVE COUNTERBALANCE	5-1
	5.1	Design Description	5-1
	5.2	Gas Spring Design	5-2
	5.3	Gas Spring Performance	5-4
6.		MAGNETIC BEARING SYSTEM	6-1
	6.1	System Description	6-1
	6.2	Design Requirements	6-3
		6.2.1 Launch Vibrations	6-3
		6.2.2 Non-Launch Associated Loads: Internal or Self Generated Side Loads	6-4
	6.3	Bearing System Analysis and Results	6-7
		6.3.1 Analysis	6-7
		6.3.2 System Dynamics	6-16
		6.3.3 System Predictions and Measurements	6-20
	6.4	Optical Radial Position Sensors	6-24
		6.4.1 Introduction	6-24
		6.4.2 Principle of Operation	6-26
		6.4.3 Model of Optical Sensor Response	6-27
		6.4.4 Magnetic Bearing Sensor Design	6-30

TABLE OF CONTENTS (Cont'd.)

Section			Page
	6.5	Radial Control System	6-34
		6.5.1 Bearing Current Driver	6-34
		6.5.2 Bearing Test Fixture	6-35
	6.6	References	6-41
7.		AXIAL POSITION CONTROL SYSTEMS	7-1
	7.1	General	7-1
	7.2	Motor Drivers	7-2
		7.2.1 Piston Loop Optimization	7-2
	7.3	Axial Position Sensors	7-5
		7.3.1 Basic Operation of LVDT	7-5
		7.3.2 Use in Refrigerator	7-7
		7.3.3 Special Considerations	7-8
		7.3.4 Electronics Signal Conditioning Circuit	7-10
	7.4	Reference Waveform Generator	7-12
	7.5	Counterbalancing	7-13
8.		SYSTEM CONTROL AND INSTRUMENTATION	8-1
	8.1	System Controller	8-1
		8.1.1 Hardware Description	8-2
		8.1.2 Software Description	8-3
	8.2	Power Supplies	8-10
		8.2.1 DC Supplies	8-10
		8.2.2 Logic Interface	8-12
	8.3	Instrumentation	8-13
		8.3.1 Cold Finger Temperature	8-13
		8.3.2 Housing Temperature	8-13
		8.3.3 Housing Pressure	8-13
	8.4	Heat Load	8-14
	8.5	Interlocks	8-15
		8.5.1 Power Supplies	8-15
		8.5.2 Axial Drivers	8-15
		8.5.3 Watchdog Timer	8-17
		8.5.4 Analog Parameters	8-17
		8.5.5 Bearing Interlock	8-17
		8.5.6 Remote Operation	8-20
		8.5.7 Ancillary Interlocks	8-20

TABLE OF CONTENTS (Cont'd.)

Section			Page
9.	MECHANICAL FABRICATION		9-1
	9.1	General	9-1
	9.2	Displacer and Regenerator	9-1
	9.3	Electrical Coils	9-2
		9.3.1 General	9-2
		9.3.2 Requirements	9-3
		9.3.3 Preparation of Varnish	9-5
		9.3.4 Procedure for Impregnating Coils	9-5
		9.3.5 Procedure Notes	9-6
	9.4	Heat Exchangers	9-8
		9.4.1 General	9-8
		9.4.2 Aluminum-Titanium Heat Exchanger	9-8
		9.4.3 Titanium-Titanium Heat Exchanger	9-10
	9.5	Fiber-Optic Radial Position Sensors	9-11
		9.5.1 General	9-11
		9.5.2 Procedure: Fiber Optic Sensor, Bulkhead Fitting	9-11
	9.6	LVDT	9-12
		9.6.1 Bobbin Description and Assembly	9-12
	9.7	Mechanical Fabrication - Manufacture of Clearance Seals	9-12
		9.7.1 General	9-12
		9.7.2 Procedure	9-14
	9.8	Magnetic Bearing Pole Pieces	9-16
		9.8.1 General	9-16
		9.8.2 Procedure	9-16
10.	ASSEMBLY PROCEDURES		10-1
	10.1	General	10-1
	10.2	Counterbalance Assembly	10-1
	10.3	Compressor Assembly	10-4
	10.4	Expander Assembly	10-10
		10.4.1 Subassembly LVDT Unit	10-10
		10.4.2 Subassembly of Dewar Housing	10-10
		10.4.3 Assembly of Cold Side (Expander) Section	10-10
	10.5	Purge and Fill Procedure	10-13
		10.5.1 General	10-13
		10.5.2 Requirements	10-14
		10.5.3 Procedure	10-14

TABLE OF CONTENTS (Cont'd.)

Section		Page
11.	REFRIGERATOR PERFORMANCE TESTS	11-1
	11.1 Performance Measurements	11-1
	11.2 Search for Optimal Operating Conditions	11-7
	11.3 Cool Down Characteristics	11-9
	11.4 Vibration Measurements	11-9
	11.5 Parametric Testing	11-10
	11.6 Instrumentation for Performance Tests	11-16

LIST OF ILLUSTRATIONS

Figure		Page
2-1	Schematic representation of a conventional Stirling Refrigerator	2-1
2-2	Contaminated displacer/regenerator	2-3
2-3	Cross-sectional view of contaminated displacer/regenerator	2-3
2-4	Illustration of wear associated with dry seals	2-3
2-5	Cross-sectional view of displacer and piston motors	2-4
2-6	Cross-sectional view of piston motor	2-5
2-7	Cross-sectional view of displacer motor/magnetic spring	2-6
2-8	Method of magnetically suspending shafts	2-7
2-9	Typical cross section of magnetic bearing	2-8
2-10	Schematic of conventional piston seal configuration	2-8
2-11	Schematic of clearance seal configuration	2-9
2-12	Photograph of Prototype Model Cooler	2-11
2-13	Cross-sectional view of Prototype Model Cooler	2-12
2-14	Cross section of expander subassembly	2-13
2-15	Cross section of compressor subassembly	2-14
2-16	Cross section of counterbalance subassembly	2-15
3-1	a) Pressure and volume variation in ideal Stirling cycle (p-V diagram). b) Position of piston P and displacer D, with integrated regenerator, in working space at the points 1-4 in (a)	3-1
4-1	Schematic of linear motor for piston	4-1
4-2	Flux plot of linear motor for piston	4-2
4-3	Schematic of linear motor for displacer	4-2
4-4	Linear motor for counterbalance	4-3
4-5	Two dimensional magnetic circuit	4-7
4-6	Schematic of integral displacer magnetic spring/linear motor	4-11
4-7	Static test of single magnetic pair vs. analysis	4-13
4-8	Dynamic test results	4-15
4-9	Motor test results - displacement spectrum	4-16
5-1	Active counterbalance	5-1
5-2	Gas spring	5-4
5-3	Schematic of test setup	5-5
5-4	Photograph of test setup	5-5
5-5	Pressure and piston motion of gas spring	5-6
5-6	Harmonics of pressure wave in gas spring	5-7
5-7	Harmonics of piston motion	5-7
5-8	P-V diagram of gas spring	5-8

LIST OF ILLUSTRATIONS (Cont'd)

Figure		Page
6-1	Geometry of magnetic bearing	6-2
6-2	Radial force generation in magnetic bearing plane	6-2
6-3	Block diagram of bearing control system	6-3
6-4	Detail of single bearing actuator geometry in bearing plane	6-8
6-5	Squeeze-film damping factor correction, γ, for journal bearings of finite length	6-13
6-6	ANSYS simulation of piston and displacer shaft radial displacement as a function of frequency for different damping factors	6-15
6-7	Frequency dependence of K, L, R. of piston bearing	6-18
6-8	Open-loop transfer function (OLTF) measurements of the displacer, piston and counterbalance bearings	6-21
6-9	Effective displacer bearing stiffness as a function of frequency for two values of damping coefficient, B	6-22
6-10	Comparison of phase of open-loop transfer function (OLTF) of piston bearing without compensation for two values of daming coefficient, B	6-23
6-11	Measured and predicted behavior of the open-loop transfer function (OLTF) of displacer bearing in the cooler for two different values of the gas damping factor, B	6-24
6-12	Comparison between measured and predicted behavior of displacer stiffness in bearing test fixture	6-25
6-13	Fiber pair response	6-26
6-14	Some fiber bundles and their responses	6-28
6-15	Relative radiant flux density of OP260 IR LED	6-29
6-16	Calculation of fiber pair response	6-29
6-17	Fiber pair responses for several inter-fiber distances	6-31
6-18	Comparison of model and experiment	6-32
6-19	Fiber optic sensor for magnetic bearings	6-33
6-20	Output of magnetic bearing sensor and phototransistors A & B	6-34
6-21	Displacer bearing test fixture	6-36
6-22	Fixture in test stand	6-37
6-23	Technique for measuring open-loop frequency response	6-39
6-24	Static load characteristics. Bearing load vs. radial displacement	6-39
6-25	Bearing stiffness vs. frequency - 7g acceleration	6-40
6-26	Bearing stiffness vs. frequency - 2g acceleration	6-40
7-1	Block diagram of axial control system	7-1
7-2	Block diagram of motor driver	7-2
7-3	Piston open-loop transfer function	7-3
7-4	Compensated displacer OLTF	7-4
7-5	Compensated counterbalance OLTF	7-4

Figure		Page
7-6	Sectional-view of a three-coil LVDT	7-6
7-7	Simplified model of a broadband transformer	7-7
7-8	Broadband model expanded (a) to represent more closely transmission line characteristics of actual transformer	7-8
7-9	Multi-section multi-winding LVDT as used in final design	7-9
7-10	Block diagram showing LVDT and associated signal-conditioning electronics	7-10
7-11	Block diagram of Axial Reference Generator	7-13
7-12	Block diagram of counterbalance command circuit	7-14
8-1	Block diagram of cooler electronic system	8-1
8-2	Block diagram of cooler system controller	8-2
8-3	Flowchart of fundamental software execution	8-3
8-4	RESET flowchart	8-5
8-5	STANDBY flowchart	8-6
8-6	RUN flowchart	8-7
8-7	CHANGE flowchart	8-7
8-8	REPORT SYSTEM STATUS flowchart	8-8
8-9	REPORT RADIAL STATUS flowchart	8-8
8-10	REPORT ANALOG PARAMETERS flowchart	8-9
8-11	Block diagram of power supply system	8-11
8-12	Block diagram of heater controller	8-14
8-13	Block diagram of bearing monitor	8-18
8-14	Bearing interlock sevice flowchart	8-19
9-1	Vacuum pressure impregnation chamber	9-4
9-2	LVDT impregnation fixture	9-8
9-3	Pictorial illustrating direction of wind for each coil	9-13
9-4	Displacer LVDT bobbin shown prior to installation within field shield	9-13
10-1	Compressor motor stator assembly plate	10-5
10-2	Core removal tool	10-14
10-3	Fill-purge setup	10-15
11-1	Spectral behavior of piston	11-2
11-2	Spectral behavior of displacer	11-3
11-3	Bearing displacement errors	11-5
11-4	Cooldown curve - no heat load	11-9
11-5	Displacement and acceleration at cold end	11-11
11-6	Radial acceleration spectrum at piston housing	11-13
11-7	Radial acceleration spectrum at counterbalance end	11-13
11-8	Cooler performance for varied heat load (constant motion parameters)	11-14
11-9	Piston motor power required to produce cooling to 65°K	11-15

LIST OF TABLES

Table		Page
3-1	Summary of Thermodynamic and Dynamic Design Parameters	3-8
4-1	Assessment of Permanent Magnet Materials	4-3
4-2	Magnet Properties - After Stabilization	4-4
4-3	Frequency Dependence of Motor Impedance	4-6
4-4	Design Parameters of Linear Motors	4-10
4-5	Power Comparison: Integral Spring/Motor vs. Linear Motor	4-11
4-6	Static Side Load Test Results	4-12
5-1	Design Parameters of Gas Spring	5-4
6-1	Quasi-Static Launch Vibrations	6-4
6-2	Resultant Radial Force from Fringing	6-5
6-3	Bearing Force Characteristics	6-10
6-4	Effective Bearing Mass	6-11
6-5	Damping Factors	6-14
6-6	Effective Time Constants for Each Bearing Type	6-19
6-7	System Resonances and Bounds on the OLTF	6-20
6-8	Measured Open-Loop Transfer Function at Specific Frequencies and Calculated Bearing Stiffness	6-23
7-1	Axial Reference Generator Performance	7-13
8-1	Power Supply Specifications	8-12
8-2	Valid Interlock Status Codes	8-16
11-1	Heater Controller Performance	11-1
11-2	Electrical Power - System at STANDBY Mode	11-6
11-3	Electrical Power - System at RUN Mode (65°K 5 W)	11-7
11-4	Refrigerator Design and Optimized Operating Parameters	11-8

1. INTRODUCTION

1.1 Background

In 1982, Philips Laboratories completed the design and fabrication of a laboratory-grade, Stirling-cycle refrigerator (cooler) for NASA to prove the feasibility of long-life, frictionless operation producing 5 watts of cooling at 65°K in a 20°C ambient. The refrigerator, called the Engineering Model, extended the relatively short maintenance-free life of mechanical refrigeration systems by essentially eliminating wear. This was accomplished by electromagnetically suspending the moving parts of the refrigerator, thereby eliminating contact and the associated wear, and permitting the use of clearance seals rather than contact seals. The Engineering Model also improved flexibility of operation by using direct electronically controlled linear drives for the moving elements, thereby allowing adjustment of amplitude and frequency.

A life test of the Engineering Model was completed in 1989. The system operated for 5 years with no refrigerator failure over 500 start/stop cycles, and the electromagnetic suspension (magnetic bearings) operated successfully for 7 years. Feasibility and life were thus demonstrated. This report describes the succeeding phase of development (phase III) in which a flight-worthy prototype cooler was designed and constructed to provide 5 watts of cooling at 65°K and, in addition, to withstand launch and operate in a zero G environment.

1.2 System Design Requirements

The Prototype Model is similar in design concept to the Engineering Model. Linear moving-magnet motors drive a compressor and an expander, suspended by frictionless magnetic bearings. However, much of the design and the components are different in order that the system meet the requirements of launch survival and long unattended life.

The system is designed for remote as well as local operation, using a two-command sequence. In the standby mode the active elements are suspended but motionless. In the operate mode, the active elements are reciprocated and cold is produced. The major design requirements were:

• Cooling Capacity	5 watts @ 65°K initially with a 20°C rejection temperature, and 5°K degradation over system lifetime.
• Life	3 years minimum, 5 year goal with 1,000 on/off cycles
• Ambient Temperature	20 ± 15°C
• Launch Load	3g at dc, 5.4 g at 7 Hz
• Cold End Stability	Less than 10^{-5} inch lateral motion, less than 10^{-3} inch axial motion
• Power Consumption	250 watts operating, 50 watts standby
• Weight	200 lbs, excluding electronic module.

In addition, the refrigerator must reach stable operation in less than 5 hours after start-up, and the short-term temperature change of the cold end under stable operating conditions must be within 0.1°K over a 24 hour period. The system must also be operable in any orientation in an Earth environment, in zero G, and on any type of spacecraft without deterioration of performance.

2. DESCRIPTION OF REFRIGERATION SYSTEM

This section describes the major characteristics of the refrigeration system, with emphasis on the rationale behind the selection of the system design concepts and critical components of the refrigerator.

2.1 Background

The most significant life-limiting mechanisms in a typical cryogenic refrigerator are degradation of its cooling performance by contamination of the working fluid and wear of its bearing and seal surfaces. The contamination and wear mechanisms are interrelated. The nature of that relationship is illustrated with the aid of Figure 2-1, a schematic representation of a conventional Stirling machine.

For long, reliable operation, bearings and seals are normally oil-lubricated. In Stirling machines, however, the seal separating the "thermodynamic" working spaces from the crankcase which contains the drive mechanism, and consequently the bearings, is not perfect, or truly hermetic. Consequently, the lubricant migrates past the seal and contaminates the working space.

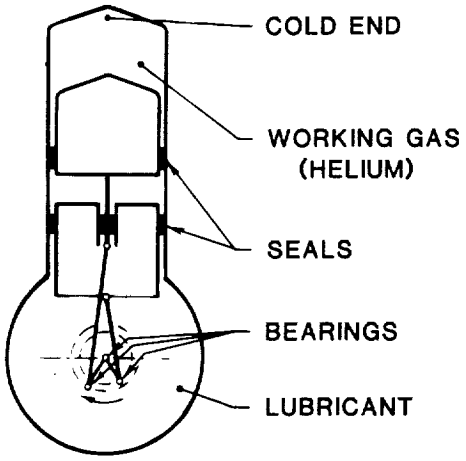

Figure 2-1. Schematic representation of a conventional Stirling Refrigerator.

It should be noted that substances other than lubricants if present in the refrigerator also contribute to contamination of the working space. The most common contaminants are: air, small traces of which are difficult to remove from the refrigerator during purging; hydrogen, adsorbed during brazing and heat treatment of refrigerator components; CO and CO_2, which are outgassing products of many organic materials; and water, which is adsorbed on all refrigerator surfaces during assembly.

Figure 2-2 shows tangible evidence of the contamination process just described. The crankcase of a small cryogenic refrigerator was intentionally contaminated with very small quantities of water, air, and CO_2, and operated for several hours. At the end of that period, the cold head of the refrigerator was removed in a dry helium chamber, and the displacer was thus exposed for viewing and photographing. The contaminants, which leaked past the piston and displacer seals (see Fig. 2-3), then froze out on the surface of the displacer/regenerator subassembly. The resulting "ice" layer increased the thermal losses which normally occur in the annular gap between the cold finger and displacer; the increased losses resulted in the degradation of the refrigerator performance.

ORIGINAL PAGE
BLACK AND WHITE PHOTOGRAPH

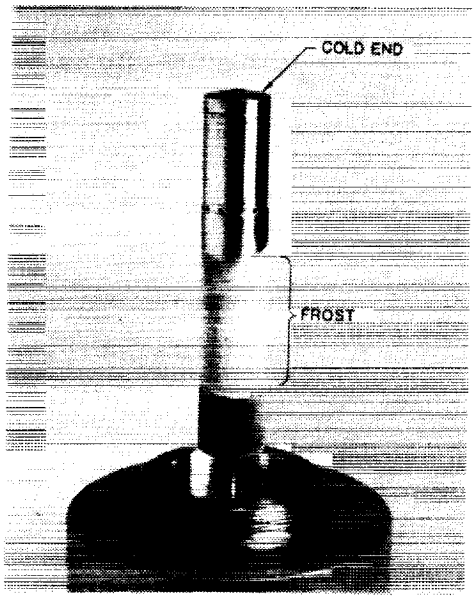

Figure 2-2. Contaminated displacer/regenerator.

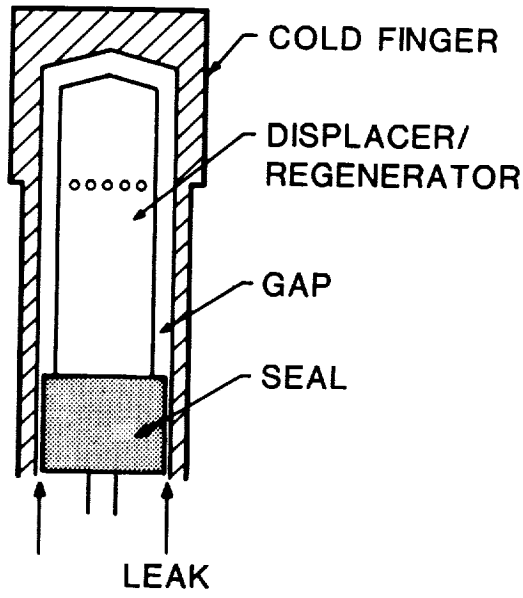

Figure 2-3. Cross-sectional view of contaminated displacer/regenerator.

An obvious solution to the degradation problem is to eliminate the sources of contamination. This suggests either dry or boundary-lubricated seals and bearings. Indeed, many cryogenic refrigerator designs rely on reinforced Teflon seals reciprocating against hardened metal surfaces, and on essentially dry bearings. The problem this approach creates, however, is illustrated in Figure 2-4,

Figure 2-4. Illustration of wear associated with dry seals.

a photograph of a reinforced Teflon seal and the adjoining surfaces after several hundred hours of refrigerator operation. As the photograph indicates, seal wear has taken place. This wear mechanism not only increases the leakage past the seal, but also generates solid particles which clog critical passages in the refrigerator, a condition which also contributes to performance deterioration. Indeed, during the few hundred hours of operation, the temperature of the refrigerator degraded by several degrees.

The problems discussed and illustrated above suggest that if "years" of life are to be attained, methods have to be found to either eliminate or minimize seal and bearing wear, and to prevent contaminants from reaching the working spaces of the refrigerator.

2.2 Major Design Concepts

All design concepts are also selected to meet the design requirements of long life, low-power consumption and low system weight. To eliminate the life-limiting problems of wear and contamination, we selected non-contacting magnetic suspension for all moving parts, clearance seals and all-metal/ceramic pressure walls for the working volumes. To implement these concepts in a manufacturable refrigerator design, the number of moving parts must be kept to a minimum. A direct rectilinear drive system powered by linear motors will result in a refrigerator with minimum number of moving parts. The Stirling cycle will provide high thermodynamic efficiency for the refrigerator with the desired cooling capacity. All reciprocating masses are resonating with gas springs or magnetic springs to achieve minimum power requirements. All these major features of the refrigerator are discussed in the following sections.

2.2.1 Stirling Cycle

In selecting the type of cryogenic refrigerator system for a given application, the primary factors are cooling temperature, cooling capacity, operating life, system power and weight. Various systems can satisfy different cooling requirements and each offers different combinations of life, weight and power. In general, there are stored cryogens, mechanical refrigerators, thermoelectric coolers and passive radiators.

The present cooling requirements of 5 W at 65°K together with the low weight requirements can only be attained by mechanical refrigerators. Stored cryogen systems for a 3 to 5-year mission became excessively bulky and heavy for space applications. Thermoelectric coolers are inefficient and cannot reach the required temperature. Passive radiators would require impractically large radiating surfaces to achieve the required cooling.

Of the various thermodynamic cycles in which mechanical coolers operate, the Stirling cycle has proved to be more efficient for the required cooling performance than the Vuilleumier, reverse Brayton and Gifford-McMahon cycles. In addition, the Stirling cycle requires no valves and only two moving elements - the piston and the displacer. The dynamic seals in a Stirling cooler see low pressure differences. All these features enable the practical implementation of non-contacting magnetic suspension of all moving parts and clearance seals, which allow Stirling coolers to achieve long maintenance-free operating life.

2.2.2 All-Metal/Ceramic Surfaces

The presence of impurities in the working gas of a cryogenic refrigerator is detrimental to its thermal stability. Specifically, impurities tend to migrate to the low-temperature regions of the refrigerator's working volume and freeze out on critical surfaces and in vital passages. The formation of such frozen impurity layers reduces the effectiveness of the regenerators and increases flow losses. These phenomena lead to a decrease in the cooling performance of the refrigerator.

Impurities can either be introduced into the refrigerator with the working gas during the initial filling procedure, or be generated during operation. Past experience has shown that the initial introduction can be prevented by filling the refrigerator through cryogenically cooled gas lines. The generation

of impurities during refrigerator operation, however, is a complex phenomenon which until now has eluded an effective solution.

All materials used in the working volume of a typical cryogenic refrigerator contain impurities. Some, like the metals used in the structure, regenerator matrix, piston, etc., can be outgassed (or baked) at relatively high temperatures; others, organic materials like reinforced Teflon seals and bushings for instance, cannot be outgassed and will continue to generate impurities while in intimate contact with the pure helium working gas. Some organic materials have outgassing rates which permit their integration into refrigerators when long, maintenance-free operation is not critical. This is clearly not the case in spaceborne applications.

To eliminate the possibility of working gas contamination and to prevent the associated temperature degradation, the Prototype Model refrigerator was designed to have no organic materials in contact with the helium working gas. This was accomplished by encapsulating all organic materials in titanium envelopes and by using ceramic materials for parts which would normally be made of plastics, such as electrical insulators.

2.2.3 Rectilinear Drive and Linear Motors

The Stirling cycle requires the interphased reciprocating motion of its two major elements, the piston and the displacer. Traditionally, this motion was generated by conventional linkage mechanisms such as crank-types or rhombic drives. In both instances, the rotary motion supplied by an electric motor had to be translated into the required rectilinear motion.

In the present design, a direct rectilinear drive actuated by a linear motor is used to reciprocate the displacer or piston. To reduce power dissipation, the displacer was designed to resonant with magnetic springs at the normal operating frequency. The piston mass was also designed to resonate with the gas spring of the working volume. A cross section of the drive for the Prototype Model is shown schematically in Figure 2-5. The displacer contains the regenerator and the armature (moving

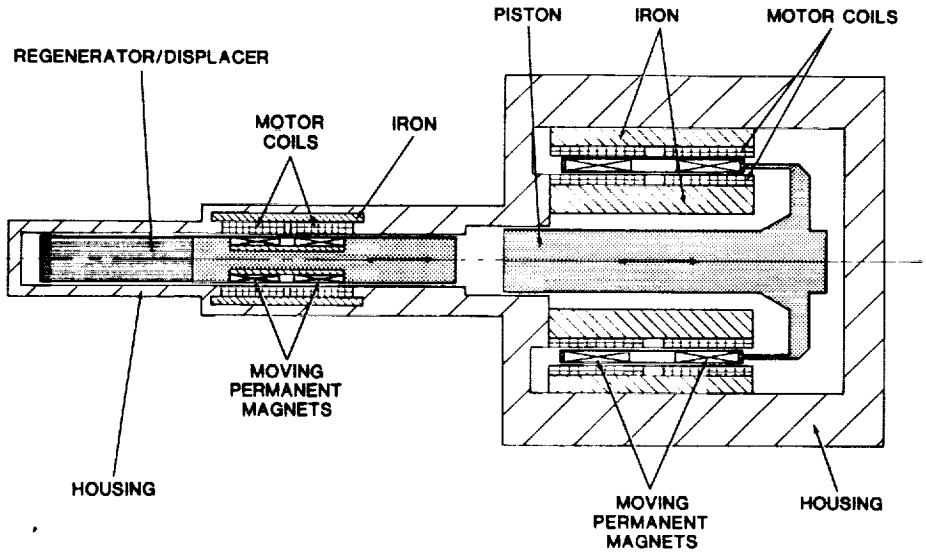

Figure 2-5. Cross-sectional view of displacer and piston motors.

magnets) of the linear motor and magnetic springs. In a similar fashion, the piston is directly coupled to the armature, or moving-magnet assembly, of its linear motor. The direct rectilinear system which reduces the number of bearings required to a minimum is a key feature that enables the practical implementation of magnetic suspension in a mechanical refrigerator.

The linear motors operate on the principle of the Lorenz force law ($F = i \times B$). When a current flows in the motor coils, it interacts with a dc magnetic flux, and a proportional force is imparted to the load. When the polarity of the current is reversed, the direction of force is reversed; hence, the reciprocating motion. Such a dc flux field can be obtained either from an additional dc winding or from permanent magnets. The motor designs in the Prototype Model use permanent magnets, for two major reasons. A dc coil would require power to sustain the field, while permanent magnets supply the field with no power requirement. Furthermore, the availability of samarium cobalt permanent-magnet materials having comparatively high energy products results in compact, highly-efficient, motor designs.

The linear motors in the Prototype Model use stationary coils and moving magnets. This design approach offers a significant advantage where long life and high reliability are critical: there are no flexing power-carrying leads (i.e., wires). One drawback is that magnetic attraction forces due to small asymmetries of construction and inhomogeneities in the properties of the permanent magnets result in radial magnetic loads which must be supported by the bearings.

The major features of the moving-magnet motor that drives the piston are illustrated in the cross-sectional view of Figure 2-6. Samarium cobalt permanent magnets are affixed to a hollow arbor (armature) which, in turn, is fastened to the reciprocating member - in this case, the piston rod. The motor coil is circumferentially wound around the permanent magnet structure. The coil is enveloped by ferromagnetic material designed to provide the required magnetic flux paths.

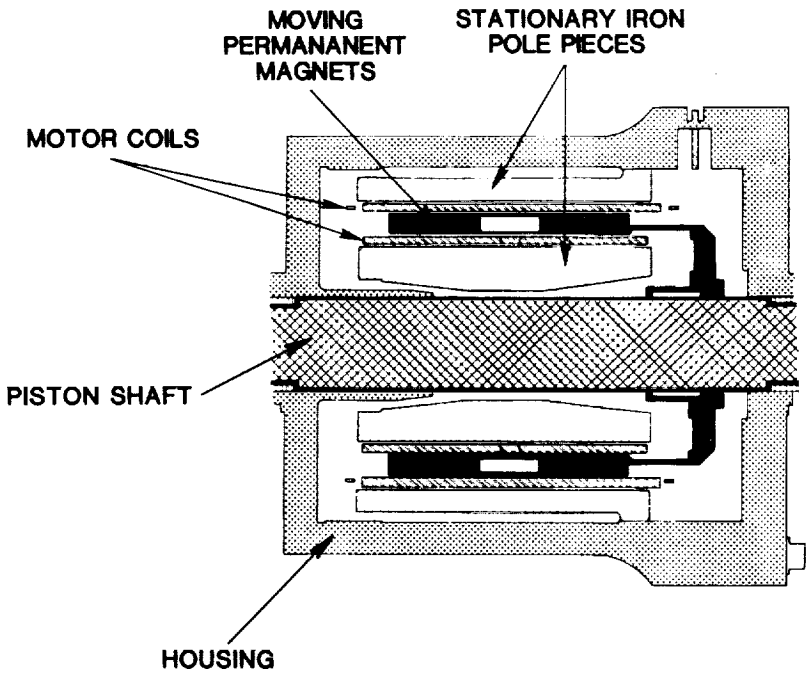

Figure 2-6. Cross-sectional view of piston motor.

The displacer is driven by a motor basically similar to that used for the piston, but with a somewhat different geometry, as illustrated in Figure 2-7. As shown, the inner-iron return path is an integral part of the displacer armature, resulting in a more compact structure.

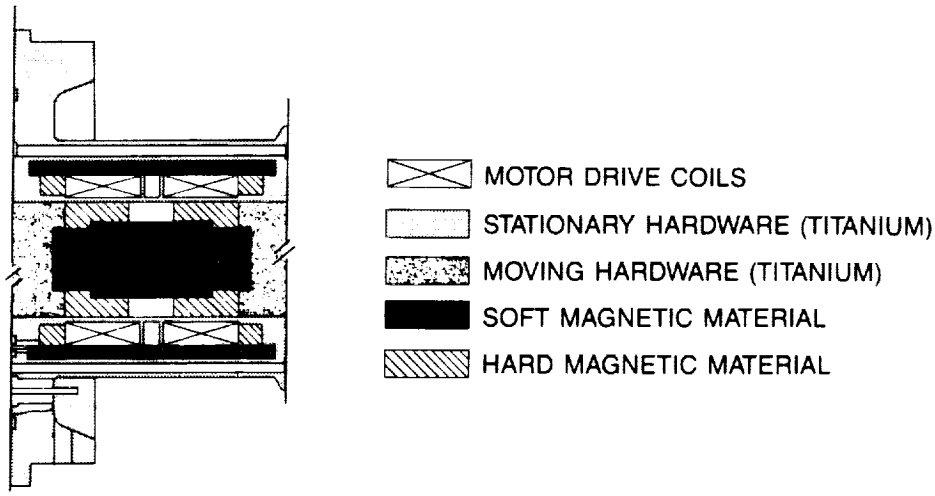

Figure 2-7. Cross-sectional view of displacer motor/magnetic spring.

The use of direct drives results in a free-piston and free-displacer system in which the piston and displacer motion can be varied and independently controlled by close-loop feedback systems. The position signals are provided by linear variable differential transformers.

2.2.4 Magnetic and Gas Springs

To ensure low power operation of the refrigerator, the motion of the displacer, the piston and the countermass are provided by resonant spring-mass systems. Mechanical resonant systems usually employ mechanical springs as a mean of energy storage. However, mechanical springs are life limited because of cyclic stress fatigue failures. To meet the long-life requirement of the Prototype, permanent magnet springs and gas springs with magnetically suspended spring pistons are used.

The compressor piston resonates with the gas spring of the working gas volume. The mass of the moving piston is designed to resonate with the charge helium pressure of the refrigerator at the operating frequency. The use of the working volume as the gas spring for the piston is a convenient choice because it is a necessary component required to execute the Stirling cycle anyway. Except for the loss due to seal leakage, it does not dissipate additional power over the input power to the Stirling cycle.

The displacer has a set of magnetic springs consisting of concentric rings of permanent magnets (Fig. 2-7). Both the outer and inner rings are radially magnetized but in the opposite direction. The magnetic springs offer very low losses, and their designs are independent of the thermodynamics. A gas spring is undesirable for the displacer because its design is restricted by the thermodynamic parameter of the Stirling cycle. Unlike the piston, the action of a gas spring for the displacer is not part of Stirling cycle--its power dissipation is a total waste since it does not contribute to the cooling process.

The counterbalance needs a tunable spring-mass system to better adapt to any design change in the operating speed. The gas spring is the clear choice for this purpose because the resonating frequency can be tuned by simply changing the gas pressure. The narrow annular clearance between the

stationary housing and the moving countermass created by the magnetic bearing serves conveniently as the clearance seal for the spring volume. Nitrogen, which is a more efficient gas-spring fluid than helium, can be used since the counterbalance is physically separated from the refrigerator working volume.

2.2.5 Actively Controlled Magnetic Bearings and Optical Sensors

To eliminate the possibility of wear, the displacer and piston are supported and guided by magnetic bearings. Although, in most applications contactless relative motion between machine elements has been attained in the past through the use of rotary magnetic bearings, the current linear magnetic bearings operate on essentially the same principle. Therefore, the design and control of these bearings are based on proven technology.

The method used to achieve the magnetically suspended linear motion is illustrated in Figure 2-8. Electromagnetic coils positioned on orthogonal circumferential positions provide the attractive forces designed to float the reciprocating ferromagnetic shaft. Radial displacements of the shaft induced by either design of stray loads are detected with the aid of optical position sensors which provide a signal proportional to shaft position. An electronic control system compares this signal with the center-position reference and creates a correction signal which produces a change in the current to the electromagnets and a corresponding restorative force which reduces the error in the radial position of the shaft.

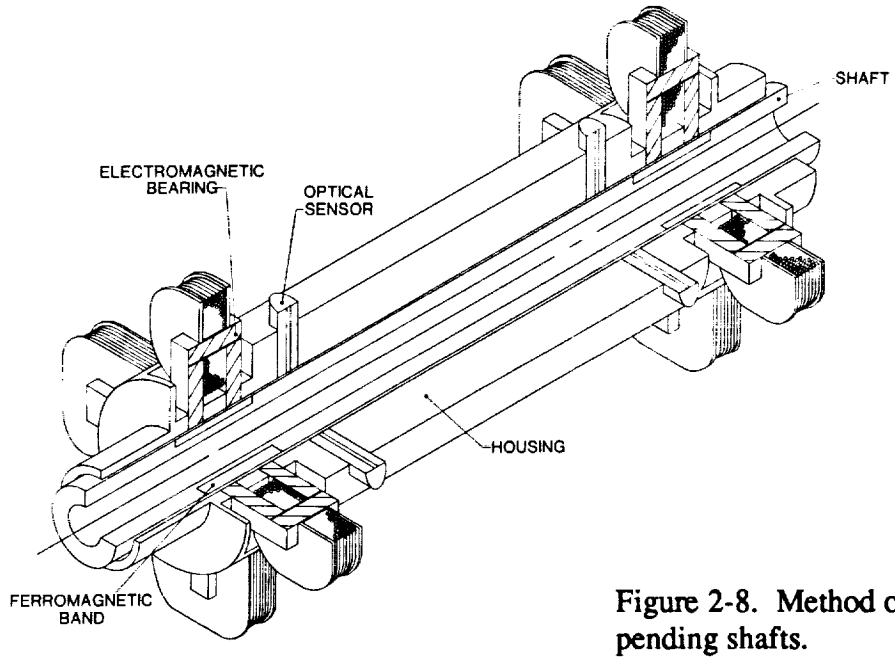

Figure 2-8. Method of magnetically suspending shafts.

A more detailed view of the suspension method, without the associated sensor, is shown in Figure 2-9. The gap which is established between the reciprocating shaft and the adjoining housing is shown (out of proportion for clarity) on both sides of the view. It should be noted that the gap, which acts as the clearance seal between the working volumes of the Stirling cycle, is made possible by the magnetic suspension and the accuracy with which the position of the suspended shaft can be controlled.

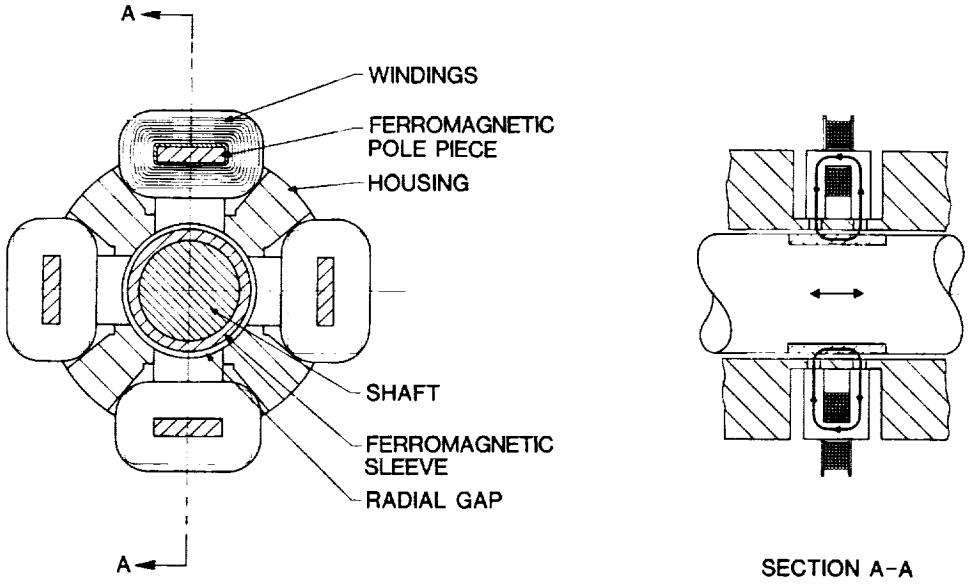

Figure 2-9. Typical cross section of magnetic bearing.

2.2.6 Clearance Seals

The sealing method most widely used in Stirling refrigerators has reinforced-Teflon piston seal rings and wear rings riding in intimate contact against hardened metal cylindrical surfaces, as illustrated schematically in Figure 2-10.

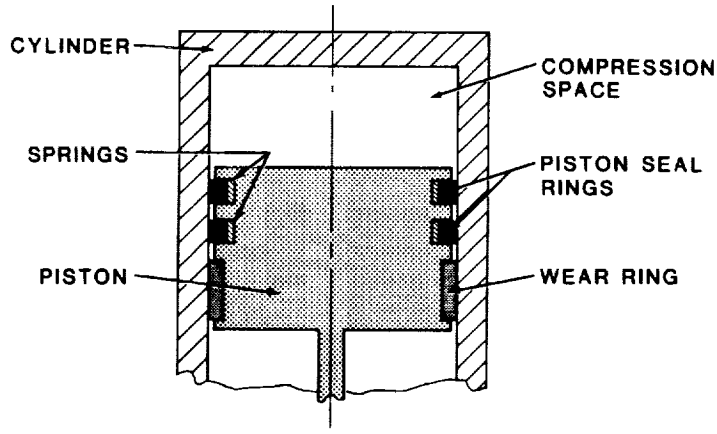

Figure 2-10. Schematic of conventional piston seal configuration.

The sealing approach is an important consideration in Stirling refrigerator designs; the seal has to be "close to" hermetic, have acceptable endurance life, and be free of contaminants. The sealing configuration shown in Figure 2-10 meets these criteria to some degree. The leakage associated with it appears to be acceptable in most applications; its useful life is reported to range from a "few hundred" to a "few thousand" hours; and although it is not contamination-free, the amount of impurities it generates is less than that produced by alternate sealing approaches.

However, for applications which require "years" of reliable refrigerator operation, the sealing method of Figure 2-10 is inadequate. Although its lack of hermeticity is acceptable, the life-limiting wear associated with a tight, and therefore relatively leak-free, ring-to-mating surface contact is not.

It is interesting to note that wear not only increases leakage, but also generates contaminants: the friction between the reinforced Teflon and the mating surface is associated with localized high-temperature spots which generate combustion products detrimental to the thermal stability of the refrigerator. To avoid the problems just discussed, Philips Laboratories incorporated clearance seals in the design of the Prototype Model.

In general terms, a clearance seal is a long, narrow, annular gap established between the outside surface of a reciprocating cylindrical element and the internal surface of a mating cylinder. Sealing is attained by the flow restriction provided by the long narrow gap. Further, since the pressure gradient imposed on the seal is oscillatory from the reciprocating motion of the moving member, the net volume of gas which traverses the seal is extremely small. The manner in which clearance seals were incorporated into the overall refrigerator design is shown in Figure 2-11. The piston clearance seal prevents gas from leaking in and out of the working volume during the pressure cycle. Clearance seals in the displacer section serve to prevent working gas from bypassing the heat exchangers and regenerators.

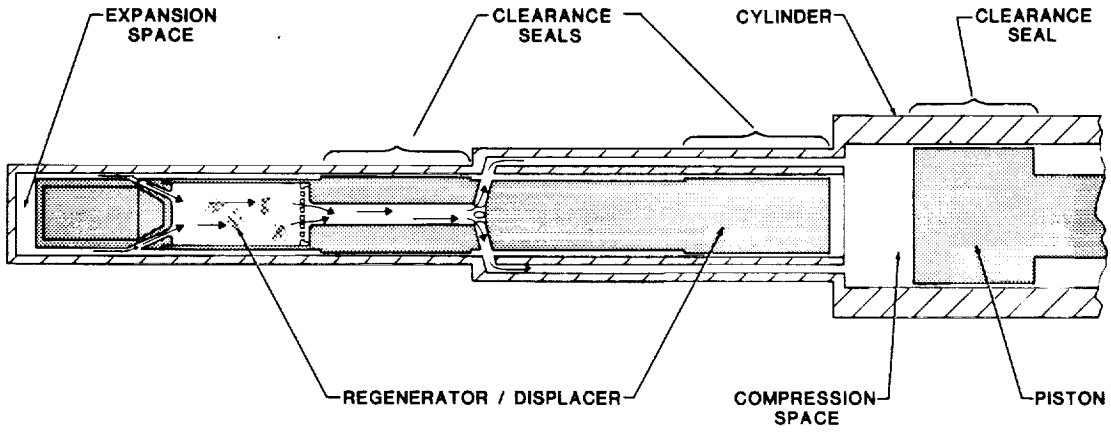

Figure 2-11. Schematic of clearance seal configuration.

2.2.7 Actively Controlled Counterbalance

In order to minimize the imbalance force introduced by the reciprocation of the piston and displacer, an actively controlled counterbalance is used. A counterbalance removes imbalances by providing an opposing force with equal magnitude to the combined force imposed by the piston and the displacer. In the past, a passive counterbalance was used to remove only the majority of the imbalance force at the fundamental frequency. In this passive system, a spring-mass system is tuned to the fundamental frequency so that it counter-reacts against the disturbing force when excited. The passive system removes a significant portion of the imbalance at the fundamental frequency, but does nothing about the forces at the higher harmonics. Thus, the residual vibration may be unacceptable to the overall system requirement.

An actively controlled counterbalance with closed-loop control is capable of attenuating the imbalance at higher harmonic frequencies as well as the fundamental. Position signals from the piston and the displacer are fed into the counterbalance position control loop. The countermass is then commanded to move in opposition to the vector sum of these motions.

All the design features for long operating life found in the refrigerator are carried over in the counterbalance. The counterbalance consists of a spring-mass system and a linear motor. Gas springs are selected for their long-life and tuning capability. The countermass is magnetically suspended with the spring volumes sealed by clearance seals. Double-acting nitrogen gas springs are chosen for their high efficiency and compactness.

2.3 Prototype Model Cooler

2.3.1 General

The Prototype Model Cooler, shown in Figure 2-12, was designed to produce 5 W of cooling power at an operating temperature of 65°K with high-efficiency and to maintain that cold production for a period of 5 years or longer. To attain the desired high-efficiency and compactness, the refrigerator is based on the Stirling cycle. To achieve the required, maintenance-free life, the design contains six major features previously discussed: a rectilinear drive, linear electric motors, magnetic bearings, magnetic and gas springs, clearance seals, and all-metal/ceramic working-volume surfaces.

The refrigerator, shown in cross section in Figure 2-13, is composed of three major subassemblies. In the expander section, gas is cyclically shuttled between the cold expansion end and the rear compression chamber which is held at ambient temperature with an external liquid-cooled heat exchanger. In the compressor section, the gas is expanded and compressed by the action of a piston. Finally, in the third section a spring-mass active counterbalance minimizes axial vibrations when tuned to the refrigerator operating frequency. All moving elements are supported on magnetic bearings. It is important to note that the refrigerator is symmetric about its center-line, and the linear motions of the piston, displacer, and counterbalance are directed along the same axis.

2.3.2 Expander Subassembly

The expander section is shown in detail in Figure 2-14. Helium gas, the working fluid, is free to flow from the expansion space at the 65°K flange through the heat exchanger which is maintained at 293°K with a water jacket. The regenerator is an integral part of the displacer. Annular areas under the magnetic bearing form the two clearance seals, forcing the helium to flow through the regenerator and through the heat exchanger. The magnetic bearing consists of four pole pieces at right angles together with four radial position sensors. The displacer is driven axially with a moving-magnet linear motor, and its motion is measured with a linear variable differential transformer (LVDT). A gas transport manifold surrounding the LVDT forms the gas passage to the compression space. All electrical power connections are hermetically made using nickel and ceramic feedthroughs. A vacuum Dewar thermally insulates the cold finger.

Two sets of concentric magnetic-rings are mounted on each axial end of the motor. Each set consists of two concentric rings of magnet which are magnetized radially in the opposite direction. The larger diameter rings are mounted in the stationary expander housing; the two smaller rings are mounted in the moving displacer. These magnet rings constitute the magnetic spring of the displacer.

The expander subassembly is instrumented (not shown) with: a strain-gauge pressure transducer to measure the compression pressure, thin film detectors (TFD's) to measure the temperature at various points along the housing, and two calibrated silicon-diode sensors to measure the cold-finger temperature. A resistive heater applies a heat load to the 65°K cold end.

ORIGINAL PAGE
BLACK AND WHITE PHOTOGRAPH

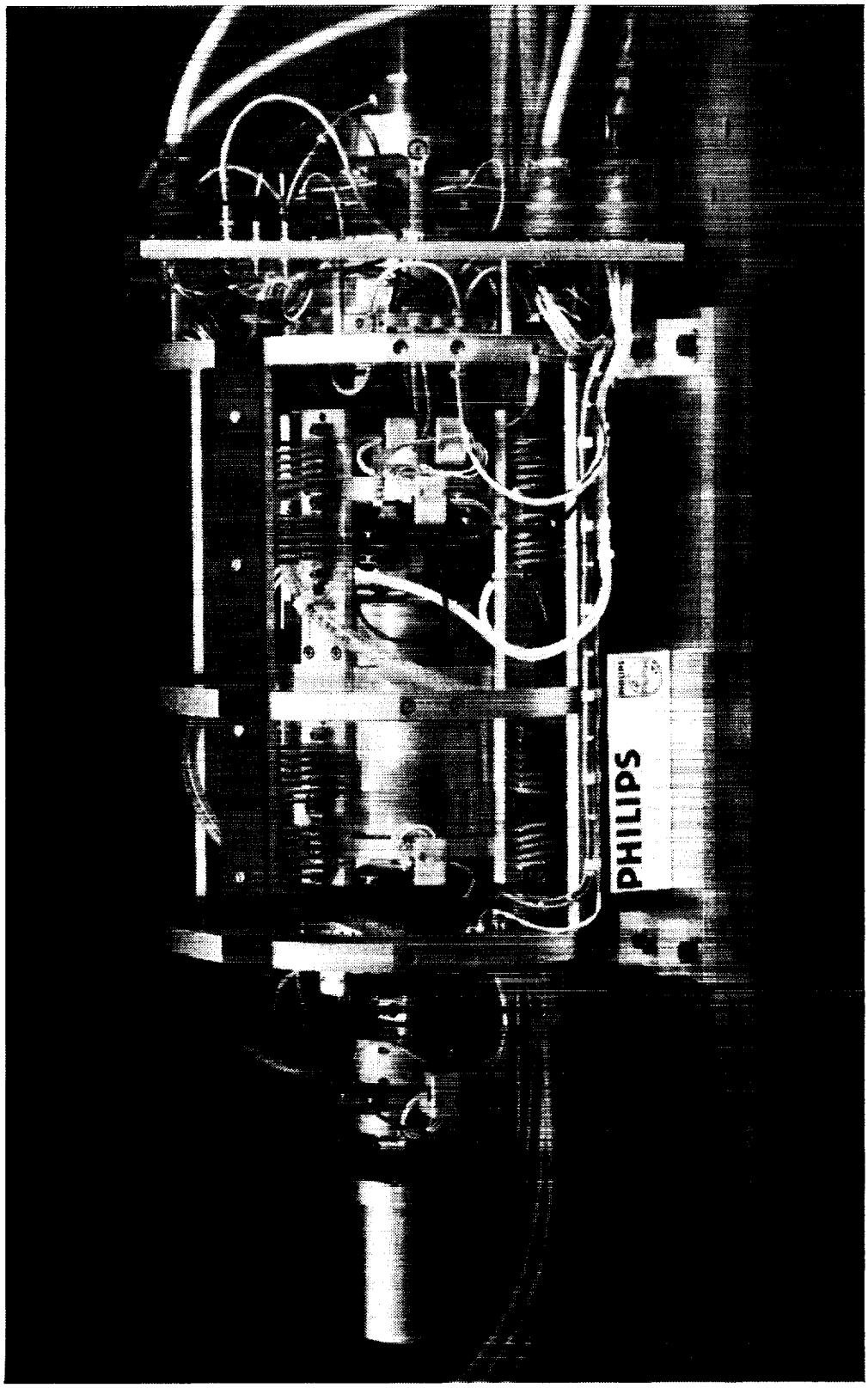

Figure 2-12. Photograph of Prototype Model Cooler.

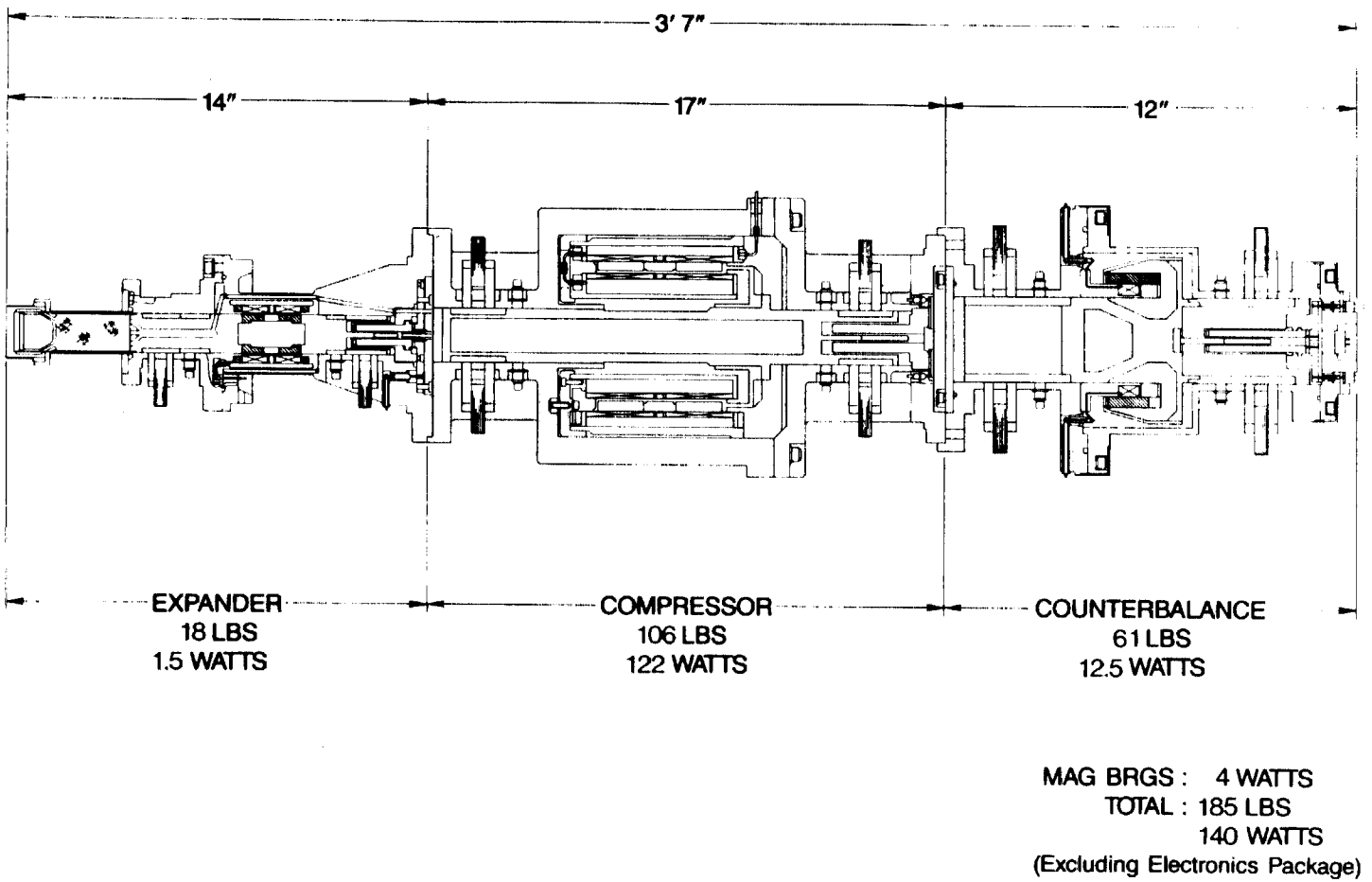

Figure 2-13. Cross-sectional view of Prototype Model Cooler.

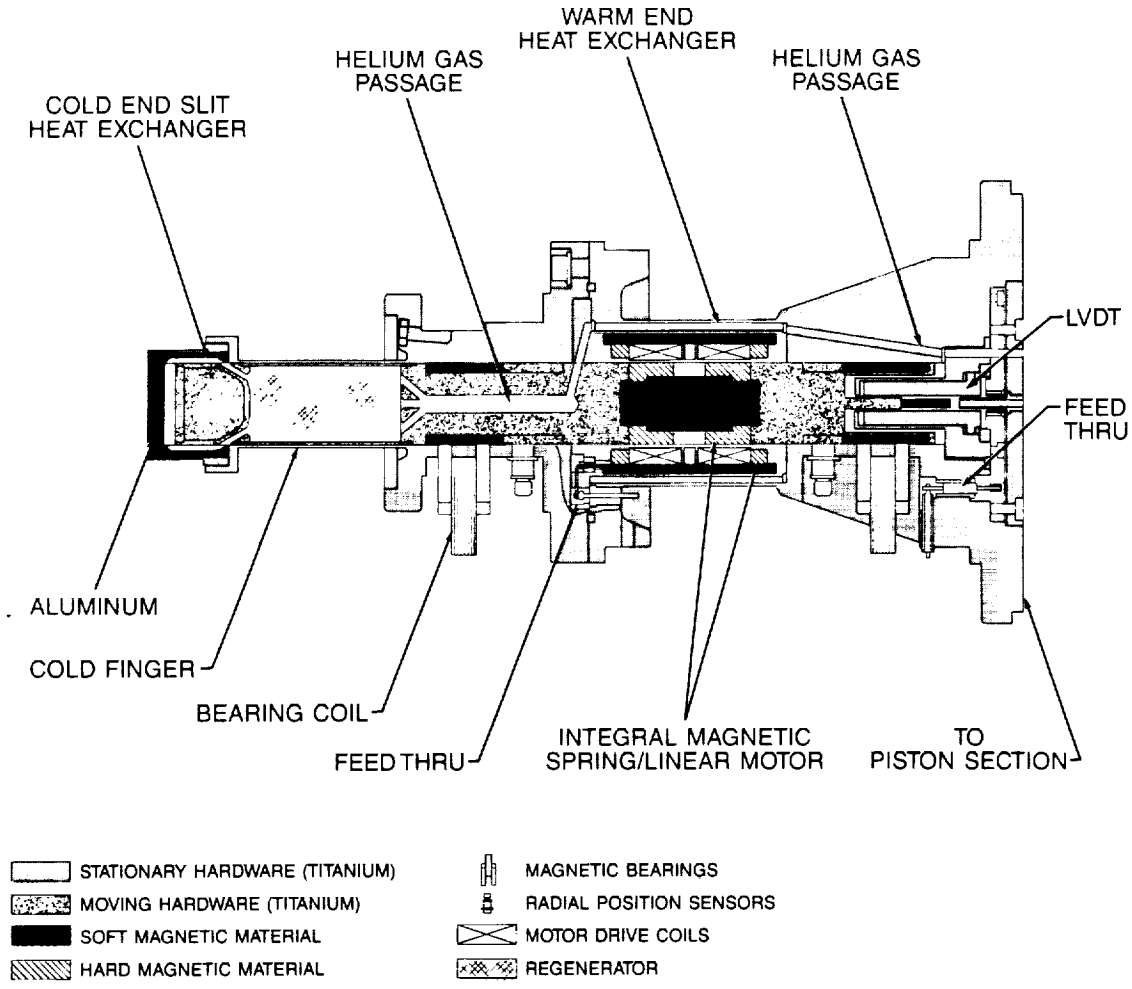

Figure 2-14. Cross section of expander subassembly.

2.3.3 Compressor Subassembly

The compressor section is shown in detail in Figure 2-15. Annular areas under the magnetic bearing on the left form the piston clearance seal, maintaining the cyclic pressure in the compression space. The additional magnetic bearing at the rear of the piston supports the shaft but does not form a seal. As in the expander section, each magnetic bearing is formed of four pole pieces and four radial position sensors. The hollow vented piston shaft and the large volume in the center of this section constitute a buffer space for the helium gas. As in the displacer, the control of the axial motion entails the use of a moving-magnet linear motor and an LVDT.

The compressor subassembly is instrumented (not shown) with a pressure transducer to measure the mean buffer pressure and TFD's to measure the temperature at various points along the housing. A water-cooled heat exchanger maintains the temperature of the housing in the area of the motor.

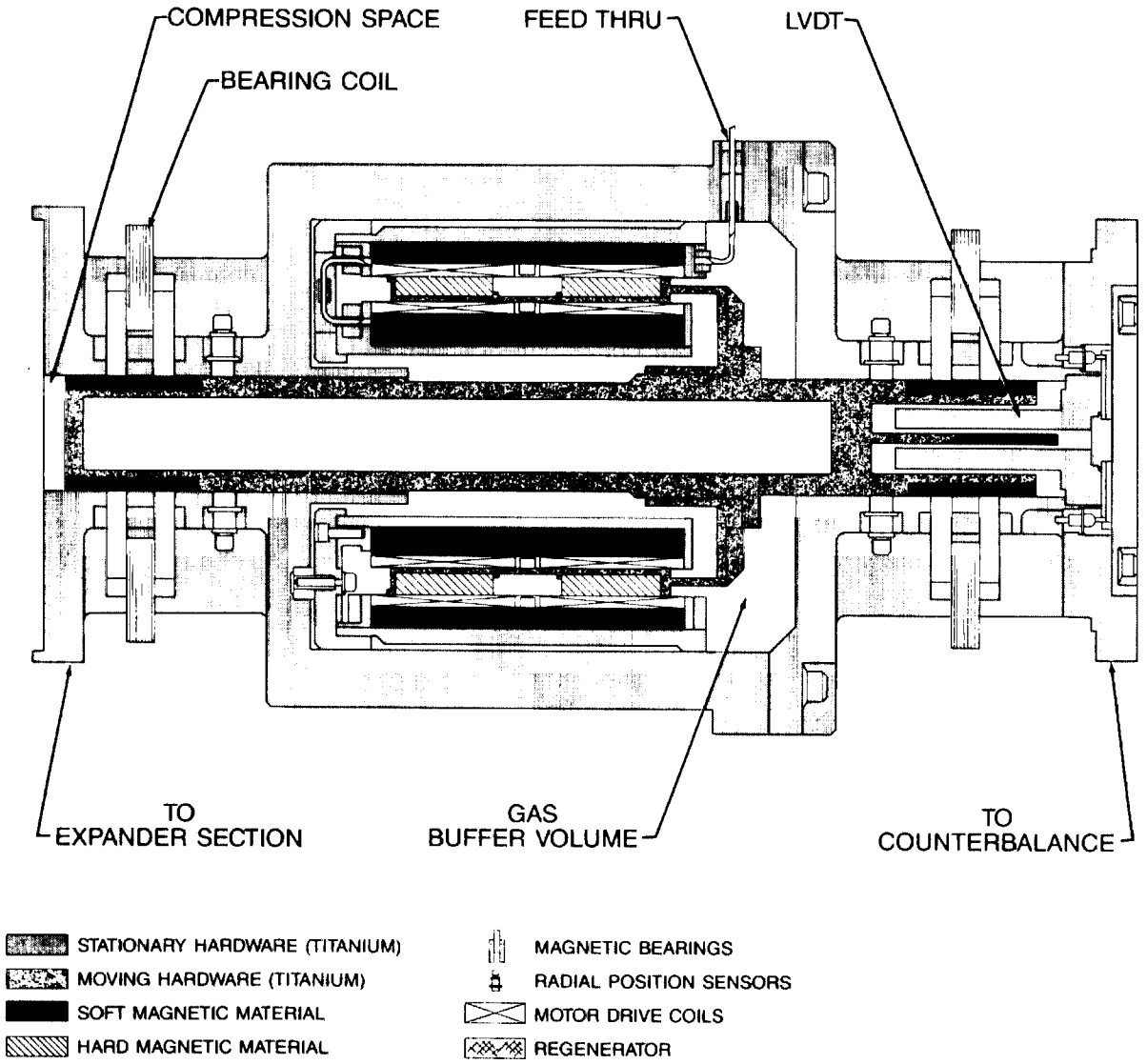

Figure 2-15. Cross section of compressor subassembly.

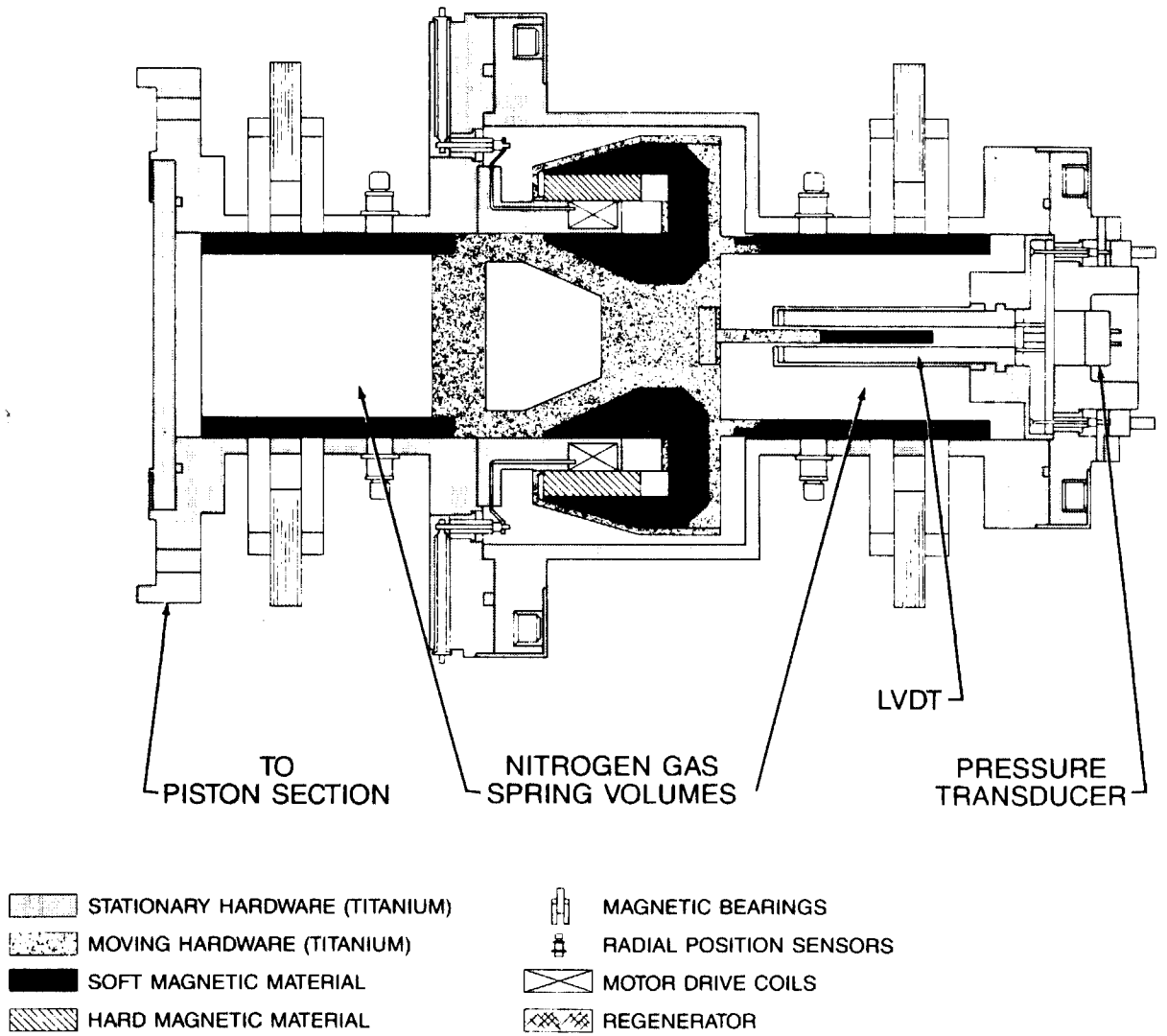

Figure 2-16. Cross section of counterbalance subassembly.

2.3.4 Counterbalance Subassembly

The counterbalance is shown in cross section in Figure 2-16. It reciprocates in opposition to the combined piston and displacer motion with the gas spring-mass system tuned to the refrigerator operating frequency. Annular areas under magnetic bearings form the two clearance seals of the gas springs. To minimize weight, the motor iron is also the moving countermass.

The counterbalance is physically separated from the refrigerator and is filled with nitrogen which is a less dissipative fluid for the gas springs than helium. The counterbalance is instrumented with a pressure transducer to measure the charge pressure and an LVDT to measure the axial position. The outer housing surface is water cooled to remove the heat dissipated by the motor and gas spring.

3. THERMODYNAMIC AND DYNAMIC DESIGN

3.1 Introduction

In a Stirling refrigerator, a piston and a displacer reciprocate in a space filled with a working gas, usually helium. To understand how the piston and displacer have to move with respect to each other, we will first describe the basic operating principles of the Stirling refrigeration cycle. In this process, a quantity of helium in the working space of the machine goes through a thermodynamic cycle with four distinct stages, see Figure 3-1a: compression at room temperature (I), cooling to operating (cold) temperature (II), expansion at operating temperature (III) and, finally, reheating to room temperature (IV). The desired refrigeration occurs during the expansion of the working gas in stage III.

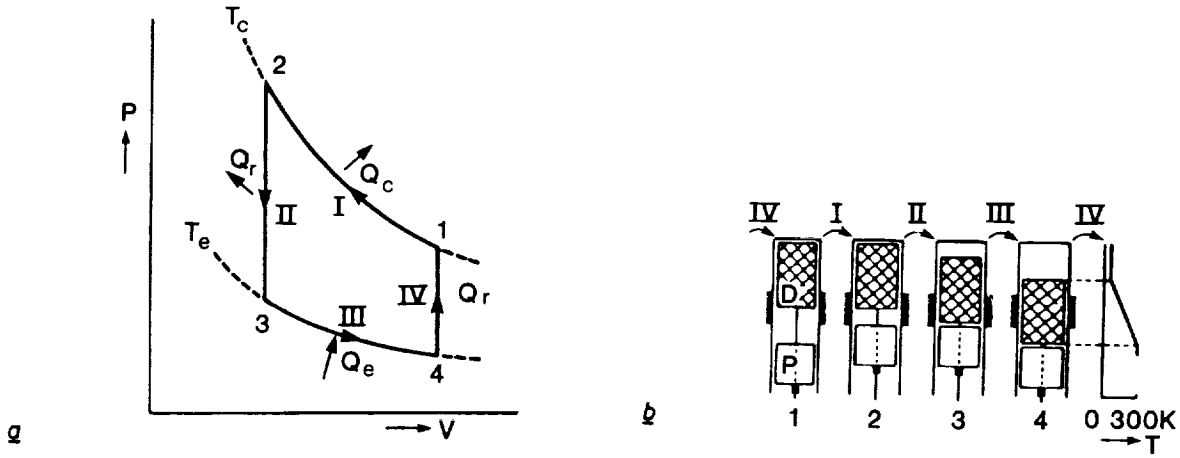

Figure 3-1. a) Pressure and volume variation in ideal Stirling cycle (p-V diagram). b) Position of piston P and displacer D, with integrated regenerator, in working space at points 1-4 in (a).

The working gas is forced to go through this cycle by the reciprocating movements of the piston P and the displacer D, as indicated in Figure 3-1b. The piston first compresses the gas and then allows it to expand. The displacer transfers the gas from the compression space -- i.e., the room-temperature volume between the piston and the displacer -- to the expansion space -- the (cold) operating-temperature volume above the displacer. Twice in a cycle the gas is forced through the regenerator, which, in the refrigerator described in this article, is part of the displacer. The regenerator consists of porous materials (copper gauze, for example) possessing a high heat capacity and a large heat-transferring surface. When flowing through the regenerator, the gas is alternately cooled and reheated by giving off and absorbing the quantity of heat Q_r. The work performed on the gas in the nearly isothermal compression is dissipated to the environment as heat Q_c, in a cooler or heat exchanger. The work performed by the gas during the nearly isothermal expansion is drawn from the environment as heat Q_e. As a result, the temperature of the upper wall of the working space -- referred to as the cold head or the cold finger -- is lowered significantly. The temperature curve over the longitudinal direction of the working space is shown schematically on the right-hand side of Figure 3-1b.

The motion of the piston and displacer, illustrated in Figure 3-1b, is carried out by simple harmonic motion in the refrigerator. As can be seen, the motion of the displacer must be approximately a quarter period ahead of the motion of the piston (corresponding to a phase difference of approximately $\pi/2$).

The expansion side of the refrigerator includes the displacer which contains the thermal regenerator. The moving armature of the displacer motor is an integral part of the displacer; the stator is part of the housing. The compression side contains the piston which is directly coupled to the moving magnets of its linear motor. In both motors, the magnets, reacting to current in the stationary coils, impart linear reciprocating motion to the displacer or piston.

Since the displacer and piston each have a linear motor and displacement transducer, each is "free", in that the motions are not mechanically imposed. The phase angle and reciprocating amplitudes are regulated by an electronic axial-control system. It should be noted that there is a significant difference between a mechanical drive and a "free" linear drive. In the former, the dynamics of the system are set by the parameters of the mechanical drive; therefore, the optimization of such a system deals with thermodynamic parameters only. For high mechanical efficiency in the "free" linear approach, the dynamic parameters, such as the moving masses, have to be closely matched to the thermodynamics; therefore, optimization of the refrigerator involves a coupled thermodynamic process which is more difficult to analyze.

In addition to the force exerted by the displacer motor, the displacer is also driven by the pressure differential established by the flow friction of the helium working gas, as it flows back and forth through the regenerator matrix. Knowledge of this pneumatic force is required to describe the mechanical dynamics of the displacer.

3.2 Thermodynamics and Dynamics of a Free-Displacer, Free-Piston, Stirling-Cycle Refrigerator

A first harmonic analysis of the cycle dynamics was carried out to model the coupling of the thermodynamics and the dynamics of a free-displacer and free-piston Stirling refrigerator. This model, though simplified, provides the necessary design criteria governing the dynamics and the performance characteristics of the Stirling machine.

3.2.1 Pressure Variation in a Stirling Refrigerator

In the first harmonic model, both the displacer and the piston positions are assumed to vary sinusoidally. The pressure variation is approximated by a linear function of positions and velocities of the displacer and the piston. Specifically, the pressure variation in the working volume is induced by:

- The position of the piston, y, which determines the total gas volume at any given time in the work space,
- The position of the displacer, x, which determines the distribution of the working gas, at a given time, between the compression and expansion spaces, and
- Flow losses due to motion of the displacer, which gives rise to a pressure difference in the compression and expansion spaces.

These result in the following expression for the pressure in the compression space (P_c) and in the expansion space (P_e):

$$P_c = P_m + k_1 y + k_2 x \tag{1}$$

$$P_e = P_m + k_1 y + k_2 x + b_1 \dot{y} + b_2 \dot{x} \tag{2}$$

where P_m is the mean charge pressure; k_1, k_2, b_1 and b_2 are constant coefficients.

If the displacer is leading the piston by a phase angle ϕ, the displacer and the piston positions are given by

$$x = X \cos \omega t \tag{3}$$

$$y = Y \cos(\omega t - \phi) \tag{4}$$

where ω = angular frequency of the Stirling cycle and t = time.

3.2.2 Cold Production and Input Power

The cold production, Q_e is given by

$$Q_e = \frac{\omega}{2\pi} \oint P_e \, S_d \, dx$$

when S_d is the cross section area of the displacer. Using Eqs. (2), (3) and (4)

$$Q_e = -\frac{1}{2} \omega S_d \, (XY k_1 \sin\phi - b_1 \omega XY \cos\phi - b_2 \omega X^2) \tag{5}$$

Under ideal conditions, there are no flow losses (i.e., $b_1 = b_2 = 0$), and the cold production becomes

$$Q_{e,\,ideal} = -\frac{1}{2} \omega S_d XY k_1 \sin\phi \quad .$$

The mechanical input power (shaft power) $\dot{W}$ to the Stirling cycle is given as

$$\dot{W} = \frac{\omega}{2\pi} \oint P_c \, S_p \, dy$$

where S_p is the cross section area of the piston head.

Substituting (1), (3) and (4) in the above expression for $\dot{W}$,

$$\dot{W} = \frac{1}{2}\,\omega\, k_2\, S_p\, XY\sin\phi \tag{6}$$

3.2.3 Coupling of the Thermodynamics and Dynamics

The equations of motion for the displacer and the piston are given by balancing the inertia force, pressure force and motor force on the displacer or the piston. They are

$$m_d\ddot{x} - (p_c - p_e)S_d + k_dX - f_di_d = 0 \tag{7}$$

$$m_p\ddot{y} - (p_m - p_c)S_p - f_di_p = 0 \tag{8}$$

where
- m = mass
- f = motor force constant (N/A)
- i = motor current
- k_d = displacer spring constant,

and subscripts d and p refer to displacer and piston, respectively.

Also, the voltages in the motor circuits are given by

$$L_d\,\frac{di_d}{dt} + R_di_d + f_d\dot{x} - E_d = 0 \tag{9}$$

$$L_p\,\frac{di_p}{dt} + R_pi_p + f_p\dot{y} - E_p = 0 \tag{10}$$

where L, R and E are the inductance, resistance and applied voltage of the motor coil.

In the design of a Stirling refrigerator with a required cooling performance, the displacer and piston amplitudes and their phase angle are determined by the thermodynamic analysis of the cycle. Also, in the same analysis, the pressure coefficients, k_1, k_2, b_1 and b_2 are obtained. With these known, the driving current and voltage of the linear motors required to deliver the displacer and the piston motions can be calculated from Eqs. (1) to (4) and (7) to (10).

3.2.4 Displacer Dynamics and Motor Input Power

From Eq. (7), the displacer motor current can be calculated as

$$i_d = I_c\cos\omega t + I_s\sin\omega t$$

with

$$I_c = (-m_d\omega^2X + b_1S_d\omega Y\sin\phi + k_dX)/f_d \tag{11}$$

$$I_s = -(b_1S_d\omega Y\cos\phi + b_2S_d\omega X)/f_d \tag{12}$$

From Eq. (9), with above expression for i_d ,

$$E_d = (L_d\omega I_s + R_d I_c)\ \cos\omega t + (R_d I_s - L_d I_c\omega - f_d\omega X)\ \sin\omega t.$$

The displacer motor input power, P_d , can then be calculated as,

$$P_d = \frac{\omega}{2\pi}\oint i_d\ E_d dt$$

$$= \frac{1}{2}\left[R_d\left(I_c^2 + I_s^2\right) - \omega X f_d I_s\right]$$

The first term is the ohmic loss of the motor coil, and the second term is the rate of work done on the gas by the displacer motor.

3.2.5 Gas-Pressure-Driven Displacer

An important special case in the study of displacer dynamics is the reciprocation of the displacer by the gas pressure wave only (no motor force), created by the piston motion. In this case, the motor current is zero, and it is an ideal high-efficiency operation. The Prototype is designed to operate at these conditions. The presence of the displacer motor allows fine tuning of the operating parameters, if necessary.

With zero motor current, $I_c = I_s = 0$, and Eqs. (11) and (12) give

$$X = -\frac{b_1}{b_2} Y\ \cos\phi \tag{13}$$

and

$$\tan\phi = \frac{k_d - m_d\omega^2}{b_2 S_d \omega} \tag{14}$$

With a given piston amplitude, Eqs. (13) and (14) determine the resulting displacer amplitude and phase angle, and the resulting cold production is given by substituting Eq. (13) into Eq. (5), which yields

$$Q_e = -\frac{1}{2}\ \omega S_d\ Y^2\ \frac{b_1}{b_2}\ \ (b_1\ \omega\cos^2\phi - k_1\ \sin\phi\cos\phi)$$

and the maximum Q_e is obtained when

$$\tan 2\phi = \frac{-k_1}{b_1\omega} \tag{15}$$

If $b_1 << k_1/\omega$, that is, the flow losses are small, it can be seen from Eq. (15) that the maximum cold production occurs when $\phi = 45°$, and the resulting cold production is

$$Q_{e,max} = -\frac{1}{4}\,\omega\, S_d\, Y^2 \frac{b_1}{b_2}\, k_1 \quad .$$

3.2.6 Piston Dynamics and Input Power

From Eq. (8), the piston motor current required to produce the desired X, Y and ϕ is given by

$$i_p = J_c \cos\omega t + J_s \sin\omega t \tag{16}$$

with

$$J_c = (BY\cos\phi + S_p k_2 X)/f_p,$$

$$J_s = BY\sin\phi,$$

and

$$B = -m_p\omega^2 + S_p k_1 \quad .$$

The corresponding motor voltage is given by Eq. (10) as

$$E_p = \left(L_p\omega J_s + R_p J_c + f_p\omega Y\sin\phi\right)\cos\omega t$$

$$+ (-L_p\omega J_c + R_p J_s - f_p\omega Y\cos\phi)\,\sin\omega t$$

The piston motor input power P_p can be calculated as

$$P_p = \frac{\omega}{2\pi}\oint i_p\, E_p dt$$

$$= \frac{1}{2}\,[R_p(J_c^2 + J_s^2) + \omega XYk_2S_p\,\sin\phi]$$

The first term in the expression for P_p is the ohmic loss and the second term can be recognized from Eq. (6) as the mechanical input power to the Stirling cycle.

To insure efficient power operation, the piston motor should be designed to operate with minimum ohmic loss. The ohmic loss becomes a minimum when

$$m_p = S_p(k_2\,\frac{X}{Y}\,\cos\phi + k_1)/\omega^2 \quad . \tag{17}$$

Substituting Eq. (17) into Eq. (16),

$$i_p = S_p k_2\, X\,\sin\phi\,\cos(\omega t - \phi + \frac{\pi}{2}\,)$$

Thus, if the piston motor is designed to operate with minimum ohmic loss, Eq. (17) has to be satisfied and the motor current leads the piston motion by 90°.

3.3 Design Optimization of a Stirling-Cycle Refrigerator

The Philips Stirling Computer Program was used to design the refrigerator for minimum input power. The computer results included physical dimensions of the expansion and compression spaces, operating parameters such as charge pressure and speed, and regenerator size and material. Practical considerations of weight, reliability, and complexity of fabrication were then applied to perturb the theoretically optimized design. Throughout the design process, practical considerations and thermodynamic performance were iterated to achieve the optimal, physically-realizable refrigerator. The thermodynamic parameters are summarized in Table 3-1.

The cold production and thermodynamic input power were calculated by the Philips Stirling Computer Program. The analysis included: the effects of regenerator losses, flow losses, heat leakage through the regenerator matrix and walls, imperfect heat transfer between the gas and the heat exchanger wall, annulus losses, losses due to shuttle heat transfer and seal leakage. All these effects are considered in characterization of the thermodynamic parameters. The result of the optimization is a design in which the sum of these losses is minimized.

To produce 5 Watts at 65°K, the thermodynamic design requires that the piston sweep a certain volume to create the required pressure wave. For optimal system efficiency with a free piston and a linear motor, the diameter of the piston and the mass of the piston assembly is selected (Eq. 17) so that the assembly resonates with the gas-spring force of compression at the refrigerator operating frequency. Leakage past the piston is restricted by a clearance seal with a 19μm (0.00075 in.) gap and a 13 cm length. Effects of piston leakage are included in the thermodynamic computations.

TABLE 3-1. Summary of Thermodynamic and Dynamic Design Parameters.

No. of expansion stages	1
Working gas	helium
Displacer diameter	3.155 cm
Piston diameter	4.445 cm
Max. displacer amplitude	0.33 cm
Max. piston amplitude	0.9 cm
Regenerator	
Type wire	mesh
Material	phosphor bronze
Wire diameter	53 μm
Fill factor	0.36
Cross-sectional area	7.31 cm^2
Length	6.0 cm
Cold-end Heat Exchanger:	
Type	slit
No. of slits	40
Slit width	0.0305 cm
Slit depth	0.2 cm
Slit length	2.0 cm
Ambient Heat Exchanger:	
Type	slit
No. of slits	20
Slit width	0.07 cm
Slit depth	0.22 cm
Slit length	7.0 cm
Clearance Seals:	19 μm (0.00075 in) gap
Operating Parameters:	
Heat sink temperature	293°K
Expansion temperature	65°K
Mean pressure	1.81 MPa (17.9 atm)
Operating frequency	18.3 Hz (1100 cpm)
Displacer amplitude	0.23 cm
Piston amplitude	0.74 cm
Displacer-piston phase angle	60°
Max. pressure	2.14 MPa
Min. pressure	1.52 MPa
Cooling power	5 W
Thermodynamic input power	100 W

4. DESIGN OF PHILIPS LINEAR MOTORS

4.1 Working Principles

A significant aspect of the refrigerator design is the application of direct-drive linear motion for the compression/expansion and displacement of gas in the Stirling cycle. This departure from the traditional conversion of rotary to linear motion eliminates a large number of life limiting bearings, a crankshaft, connecting rods, and the resulting mechanical inefficiency. By using linear motors and axial control electronics, only two linear bearings per shaft are needed, and the stroke amplitudes and piston/displacer phase angle can be adjusted during operation. Thus, the drive offers high reliability, efficiency, and versatility.

The principle of operation of the linear motor used in this refrigerator (see Fig. 4-1) is similar to that of the actuators used in most loudspeakers. Permanent magnets, rather than a field coil, establish

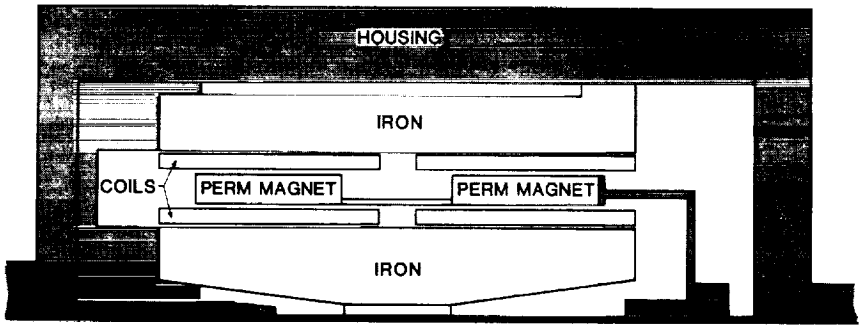

Figure 4-1. Schematic of linear motor for piston.

a steady magnetic flux field (see Fig. 4-2). The current through the coil interacts with the flux to produce a force between the coil and the permanent magnet. Since the flux is oriented radially and the coil is wound circumferentially, the force is directed along the axis of the motor, thereby producing linear motion.

The structure of the piston motor shown in Figure 4-1 is essentially two motors connected back-to-back. The figure also shows an inner and an outer coil section for each of the two "motor sections". The presence of substantial non-magnetic gaps (the coils) on each side of the magnet rings reduces the radial force generated between the moving-magnet armature and the stationary iron stator rings. These side forces represent a significant load for the magnetic bearings. The effect of radially moving the magnet ring is reduced with this geometry.

An additional feature of this motor design is the ability to hermetically isolate the helium working fluid from all possible sources of organic contamination. As discussed previously, contamination results in long-term degradation of refrigerator performance, an obvious detriment. The hermetic seal is made by welding thin-walled titanium cans over the magnets and the coils. If the cans are

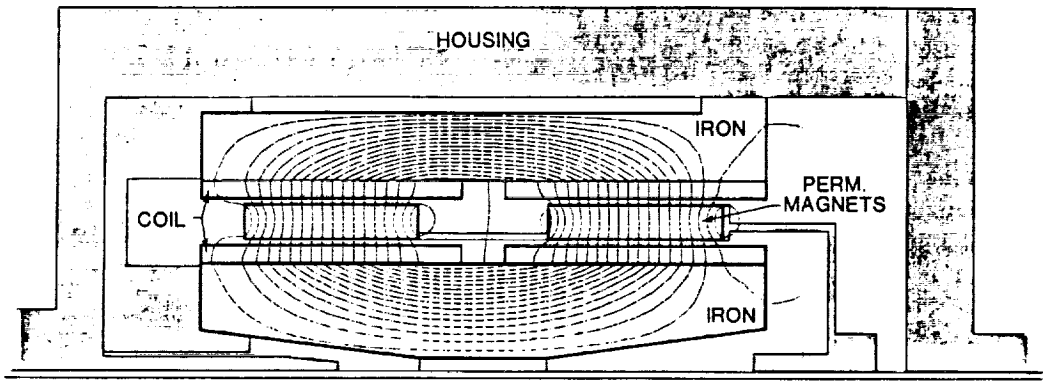

Figure 4-2. Flux plot of linear motor for piston.

thin enough (0.3 mm), the reduction in the motor efficiency will be small. Electrical connection to the motors is made with nickel/ceramic feedthroughs.

The displacer motor shown schematically in Figure 4-3 operates the same as the piston motor (see also Fig. 2-7). The geometry is somewhat different in that there is only one coil section for each magnet section, and the inner iron is part of the armature. The small size of this motor, governed by the diameter of the displacer, dictates these changes.

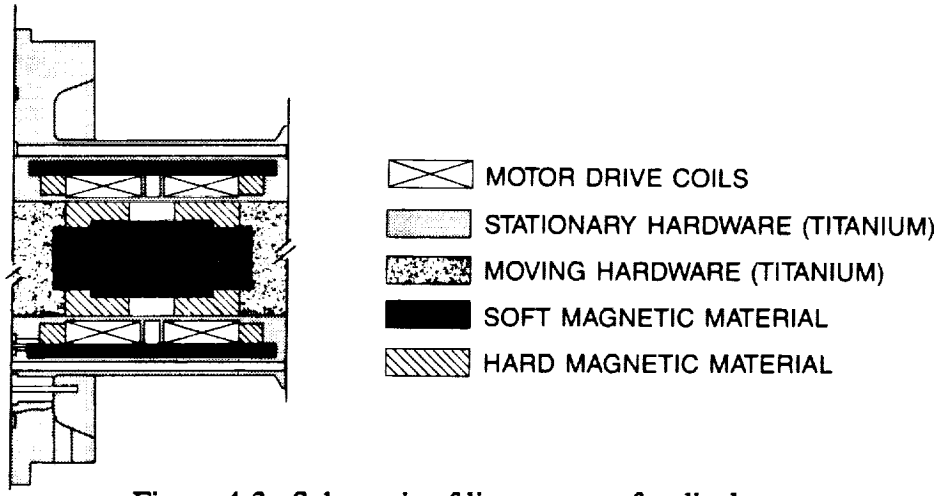

Figure 4-3. Schematic of linear motor for displacer.

The counterbalance motor is essentially one-half of the displacer motor configuration with one coil and one radial magnet ring. The flux path is completed by adding a soft-iron (Corovac) shunt piece (Fig. 4-4). To effectively use the weight of the motor, the flux carrying iron piece and the magnet ring also function as a major portion of the countermass. In this motor design the coil is fixed to the housing, and the rest of the magnetic circuit elements of the motor is attached to the moving gas-spring piston. The function of the motor is to provide power to compensate for the gas-spring losses as well as providing forces to counteract the imbalance of the refrigerator occurring at higher harmonics.

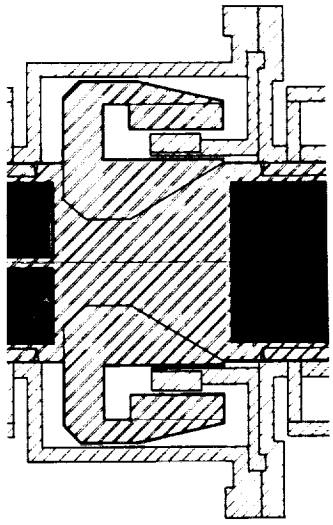

Figure 4-4. Linear motor for counterbalance.

4.2 Soft and Hard Magnetic Materials

4.2.1 Hard Materials for Permanent Magnets

A well-known design guideline for permanent magnet (PM) systems is that the magnet volume required to produce a field in an air gap is a minimum if the magnet operates at its "maximum energy product" point. The size of the magnet is minimized if the magnet is operated at its BH_{max} point; thus, the larger the BH_{max} product, the less magnet material required.

In addition to the energy product, additional considerations that are important in long-life cooler design are the material's thermal and aging stability. The overall design requirements are summarized in Table 4-1. Also listed is a competitive ranking of PM materials that was available in the early design phases (circa 1984-1985).

TABLE 4-1. Assessment of Permanent Magnet Materials.

	Performance Attribute		
PM Material	Initial Energy Product (MGOe)	Post Assembly * Energy Product (MGOe)	Long-Term Aging
SmCo1-5	22-24	21-22	Excellent
SmCoPr	27-29	25	Poor
Sm2Co17	25-29	22-27	Good
NeFeB	30-35	**	***

*After assembly temperature of 250°C for plating.
**Not recommended for use after exposure to that temperature.
***Unknown-data not available in 1984.

The energy product of the magnet is irreversibly reduced when exposed to high temperatures,and the magnet is completely demagnetized when the Curie point of the magnet is reached. Thus, the energy product of the magnet after exposure to the highest-temperature fabrication steps is needed to evaluate candidate magnet materials.

Three generic candidate PM materials considered were: Nd-Fe-B, $SmCo_5$, Sm_2Co_{17}. The first material was relatively new when the initial designs were being generated (circa 1984), and no long-term stability data was available. The temperature coefficient was very poor, and service of the magnets was limited to 150°C. In particular, the long-term stability is related to the intrinsic coercive strength - a parameter that was noticeably lower for the Nd-Fe-B magnets than for the SmCo-based magnets. A thermally curing 2-part epoxy (Scotch-Weld™ 2214) was the candidate glue for the magnet assembly and required cures of at least 110°C for high bond strength. A good epoxy bonding of the assembly was required to make sure the glued mosaic of magnets remained structurally sound and solid for a number of years. In addition, ion implantation or ion plating techniques were initially considered for the shafts and housing to act as emergency "wear resistant" contact surfaces in case of a complete bearing failure. The lowest plating temperature reported was about 250°C.

The magnet segments could have been shielded and actively cooled during plating. However, to be conservative, a minimum exposure of 200°C was initially planned for the displacer armature (later in the program the plating was not used), and the displacer and piston magnets were specified to be uniform and stable following exposures to this temperature.

NdFeB was not further considered as a candidate magnet material because of poor thermal and unknown long-term stability. $SmCo_5$ doped with Pr was rejected for stability reasons as well. The piston and displacer magnets use Sm_2Co_{17} recipe with the specifications summarized in Table 4-2. The counterbalance motor uses $SmCo_5$ because it had a lower power density requirement, i.e., a significant large moving mass was needed for counterbalancing, and there was no advantage to moving to a higher energy product magnet.

TABLE 4-2. Magnet Properties - After Stabilization.*

	Piston	Displacer
Maximum Energy Product (BH - MGOe)	27	25
Residual Induction (B_r - Tesla)	10.2	10.1
H_k (kOe)	14.0	>12. 0
H_c - Normal Coercive Force (kOe)	10.1	9.6
H_{ci} -Intrinsic Coercive Force (H_{ci})	>16.0	

4.2.2 Magnet Uniformity

The bearing side loads in the dc to operating frequency range are dominated by magnetic field uniformity as compared to geometric eccentricities. Thus, one key element to successful implementation of the linear motor/magnetic bearing cooler was to minimize the magnetic field nonuniformity. This was accomplished by careful quality control on every magnet (100% testing) used in the cooler. Each magnet was tested and mounted on the respective motor armatures in such as way as to minimize any radial imbalance forces from asymmetries in the radial magnetic field (see Sect. 6.2.2).

For the high coercivity Sm_2Co_{17} magnets, typical second and third quadrant demagnetization curves were provided for each magnet segment after thermal aging. This ensured the long-term magnet

stability and quality. Open or nearly closed-circuit magnet measurements could not indicate the intrinsic coercive force -- a parameter usually associated with long-term stability. Actual magnet traces were needed for each magnet segment. This is especially important in the displacer spring magnets where very large field gradients occur at the edge of the facing magnet segments. Magnet tracing of every segment required a 100% remagnetization and back-check against Helmholz readings following thermal treatments to ensure repeatability. Though tedious and expensive, this method guaranteed the initial condition and long-term behavior of these magnets. The $SmCo_5$ magnets were more reproducibly produced and only statistical lot testing of the demagnetization properties was needed.

Another useful technique to quick batch selection is to use a Helmholz coil (an integrated flux reading from a pick-up coil as the sample is displaced through a coil). For samples of constant geometry it is a good means of matching magnet segments if they operate at or near the open circuit "in air" condition. Such a technique was used to group the piston magnets into a mosaic and to verify/double check the magnetization curves for the magnet segments. For the piston magnets in the cooler, the Helmholz readings ranged from a maximum 152.0 to a minimum of 149.5 Maxwell Turns (MXT).

4.2.3 Soft Magnetic Materials

Soft magnetic materials typically have very high permeability with very low coercivity. The soft materials are used in the magnetic bearing pole pieces and armatures as well as in the linear motors. They are supposed to confine the magnetic flux to specific areas. Ideally these materials should have:

- high resistivity (to minimize eddy currents).
- high permeability and flux saturation (to minimize motor size).

The soft magnetic material of the bearing armature had additional requirements,

- thermal - mechanical stability (bearing surface).
- hermeticity - brazing compatibility.

For high performance, compact electromagnetic actuators, typically 3-4% SiFe or 2V-Permendur were used. Though SiFe would have been the preferred choice over Permendur because of its higher resistivity and hence lower eddy currents, it was dropped in favor of 2V-Permendur because of extreme difficulty in forming hermetic brazes to titanium.

4.2.4 Motor

The requirements for the motor were somewhat different than those for the bearing. Because significant power was being delivered by the motors (in particular the piston motor), we wanted these motors to be very efficient - or have very little eddy currents. For control reasons, it was also desirable to have an efficient motor to minimize the phase angle between force and current such that as wide a bandwidth axial control system could be realized based on a simple current driver (position feedback only). On the other hand, restrictions that were placed on the bearing actuator material - that it be compatible with a hermetic environment (no organics) - were removed because titanium sealing cans around the motors were planned.

In the Engineering Model, a solid Si-Fe material was slit to emulate a laminated structure in an attempt to minimize eddy currents. A newer material became available and was employed in all

the motors (excluding the displacer armature because of temperature limitations) of the Prototype Model. The material called Corovac (available through VAC) has high electrical resistivity (~ 1 ohm-cm), high saturation flux density (~ 1.9 T) and low core loss up to 10 kHz. The limitation of the material was that it had a relatively low relative permeability (~100), low maximum exposure temperature (150°C), and was partly composed of organic binder material.

The thermal limitations were not a problem except for the displacer armature, where conventional 2V-Permendur was used. The 150°C temperature was still compatible with epoxy cure cycles and the motor "iron" segments need not be plated. A significant advantage of the material was that it need not be laminated at all and could, if higher productions required, be directly cast to shape.

The effective permeability of the magnetic circuit for the large air-gap permanent magnet linear motors was quite low. Thus, relatively low permeability soft magnetic material had only a minor impact on leakage.

4.2.5 Test Results

A measure of the wide bandwidth capability and efficiency of these motors is the frequency dependency of the force constant and inductance. Direct measurements of the force constant of the displacer motor as a function of frequency indicated that the force constant was "flat" (equivalent to the dc value) to at least 200 Hz with only a 7° phase shift between current and force up to 500 Hz. As expected, the inductance also remained "flat" in this frequency range.

Inductance and effective resistance measurements were also performed on the counterbalance and piston motors. Table 4-3 summarizes the results. The motors indeed have wide bandwidth capabilities with minimal eddy currents (or motor to current phase shift) in the frequency range of the axial control loop (less than 100 Hz).

TABLE 4-3. Frequency Dependence of Motor Impedance.

Frequency	Piston		Counterbalance		Displacer	
(Hz)	L(mH)	R(ohms)	L(mH)	R(ohms)	L(mh)	R(ohms)
5	3.40	0.330	20.5	2.66	N/A	
10	3.34	0.330	20.1	2.67	5.61	2.13
20	3.30	0.339	19.7	2.74	5.64	2.14
40	3.28	0.358	19.3	2.89	5.64	2.14
60	3.26	0.390	19.1	3.08	5.63	2.15
80	3.25	0.425	19.0	3.35	N/A	
100	3.23	0.474	18.9	3.66	5.62	2.18

Thus, by using Corovac, simple-to-construct and wide bandwidth motors were realized. The excellent wide bandwidth inductance of these motors should be compared/contrasted to the poor frequency characteristics of the bearing actuators as described in Section 6. The radial bearings used an unlaminated, highly conductive structure with a small air gap (high permeability circuit) whereas the motors employed more resistive solid soft magnetic material with a relatively large air gap circuit or low effective system permeability.

4.3 Magnetic Circuits

The electromagnetic force generated by a current flowing through a coil in the linear motor is given by:

$$F = Bli$$

where F is the force, B is the magnetic flux density, l is the length of the wire-winding of the coil within the magnetic field, and i is the current. The magnetic flux is created by a magnetic circuit consisting of permanent magnets, soft magnetic irons, and air gaps. It is necessary to design a magnetic circuit to supply the required magnetic flux density in the air gap occupied by the motor coils.

To calculate the magnetic flux density, a reasonable approximation can be made using a simplified analytical technique. This method can be outlined by the simple two-dimensional example of Figure 4- 5. Applying Gauss' Law and Ampere's Law to the magnetic circuit in Figure 4-5, one obtains,

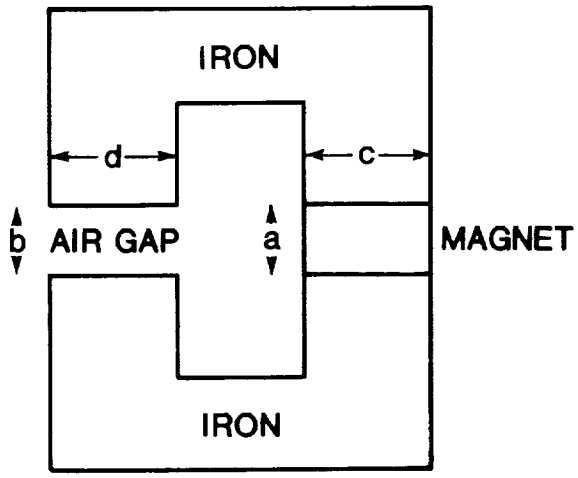

Figure 4-5. Two dimensional magnetic circuit.

$$B_m c = B_g d \sigma, \tag{4-1}$$

and

$$H_m a = H_g b r = \frac{B_g}{\mu_o} b r \tag{4-2}$$

where H and B are magnetic intensity and flux density, respectively, σ is the flux leakage factor, and r is the reluctance factor. Subscripts m and g refer to magnet and air gap, respectively. Expressions for leakage factor σ can be found in Electromagnetic Devices by Roters for various geometries.

The relationship between B_m and H_m is a property of the magnetic material. For samarium cobalt magnets used in the Prototype Model, a simple linear behavior exists that can be expressed as,

$$B_m = \frac{B_r}{H_c} H_m + B_r \qquad (4\text{-}3)$$

where B_r is the remanence and H_c is the coercive force of the magnets.

Equations (4-1) to (4-3) determine the magnetic flux density in the air gap given the dimensions of the magnetic circuit. The magnetic circuit of the linear motors can be analyzed in the same way. A substantially more accurate calculation can be made by using finite-element modelling. The Philips computational software 'MAGGY' is available for this purpose.

4.4 Optimization of Linear Motors

Motor efficiency (η) is defined as the ratio of the mechanical output power ($\dot{W}$) from the motor to the electrical input power (P_{in}), i.e.,

$$\eta = \dot{W}/P_{in}$$

Since the losses in the motor are nearly all ohmic in the coil windings,

$$P_{in} = \dot{W} + \frac{1}{2} I^2 R$$

where I is peak current amplitude, and R is the coil resistance.

The motor output power W is equal to the magnitude of the work done on the motor by the piston. One has,

$$\dot{W} = \frac{1}{2} I V_b \sin\theta$$

where V_b is the back emf of the motor coil, and θ is the phase between I and V_b. V_b is induced across the motor coil by the piston motion; thus,

$$V_b = \omega B l Y$$

where B is the magnetic flux density seen by the coil windings with a wire length l moving with a peak amplitude Y and an angular frequency ω.

Now the motor efficiency can be written as

$$\eta = \frac{1}{1 + \frac{2\dot{W}}{(\omega BY \sin\theta)^2} \frac{R}{l^2}}$$

The ratio R/l^2 can be rewritten as

$$\frac{R}{l^2} = \frac{\rho}{V_c}\left(\frac{l_o}{l}\right)^2$$

where ρ and V_c are the resistivity and the total conductor volume of the coil, respectively, with a total winding length l_o.

Finally,

$$\eta = \frac{1}{1 + \left[\frac{2\dot{W}}{(\omega Y \sin\theta)^2}\right] \cdot \left[\frac{\rho}{B^2 V_c}\left(\frac{l_o}{l}\right)^2\right]}$$

It can be seen from this equation that the motor efficiency depends on two groups of design parameters. The first group is related to the operating conditions. The efficiency is higher when (1) the output power is lower, (2) the frequency is higher, (3) the stroke is larger, and (4) the phase angle between the current and motion is closer to 90°. The second group is determined by motor size and materials. The magnetic flux density is a function of the magnet size and magnet material. The motor efficiency is higher when (1) the motor is larger so that both the magnet and coil sizes are larger and (2) the coil winding is more conductive.

In designing the Prototype Model, the moving-magnet mass, speed and stroke of the motor armature assembly are determined by the thermodynamics. Motor design optimization is essentially a trade-off between motor efficiency and motor weight. With the operating parameters constrained by the thermodynamics, one optimizes the motor design by searching for the minimum weight motor that can deliver the required efficiency. Motor optimization was carried out to satisfy this criterion.

4.5 Motor Coil

In the previous section, it can be seen that motor efficiency is independent of the number of turns and wire size of the motor coil. Thus, one can select these parameters to allow the motor to operate at the available drive voltage without affecting the efficiency.

The equations relating the number of turns and wire sizes to the required operating voltage (E) can be calculated from the motor voltage equation:

$$E = L\frac{di}{dt} + iR + Bl\,\dot{y}$$

where L is the coil inductance and $\dot{y}$ the relative velocity of the coil. For the case of sinusoidal operation, this can be reduced to algebraic equations.

To obtain higher efficiency and better heat dissipation, magnet wires with rectangular cross section were chosen for the coil.

The design parameters of the linear motors are summarized in Table 4-4. The displacer motor with its integral magnetic spring is described in more detail in the next section.

TABLE 4-4. Design Parameters of Linear Motors.

Design Parameters	Displacer Motor	Piston Motor	Counterbalance Motor
Frequency (Hz)	18.3	18.3	18.3
Max. Amplitude (mm)	3.3	9.0	9.0
Magnet Material	Sm_2Co_{17}	Sm_2Co_{17}	$SmCo_5$
Max. Energy Product (MGOe)	25	27	25
Coil Wire Size (mm x mm)	0.69 x 0.86	1.76 x 2.45	0.66 x 0.81
No. of Turns	480	176	240
Coil Resistance (Ohm)	2.3	0.34	2.6
Coil Inductance (mH)	5.6	2.6	28
Mechanical Output (W)	--	100	10
Electrical Input (W)	0-3	135	16.5

4.6 Displacer Spring/Motor

4.6.1 Spring/Motor Design

During operation, the displacer shuttles gas between the cold and warm ends, reciprocating at a specified frequency, stroke, and phase relative to the piston motion. The displacer construction includes the regenerator mesh, bearing armature and radial position 'target' material, structural walls, and linear motor. For designs of this type, the fluid damping forces acting on the displacer are small in comparison to inertial forces during operation. Ideally, for compact cooler design, the machine should operate at the highest frequency allowed by the regenerator heat capacity and fluid viscous losses. In addition to the size and weight reduction, the size of the linear compressor motor decreases with higher speeds, because the output force decreases. However, the displacer motor power loss is proportional to the fourth power of frequency while the cooling capacity is only linearly proportional to frequency. The significance of the displacer motor power had resulted in larger, lower frequency cooler designs in the Engineering Model.

Due to the large ratio of inertial to damping forces, a resonant displacer/spring system would greatly reduce the required motor power. In fact, 'free displacer' coolers have been made which have no displacer motors. These coolers use the operating pressure wave to drive a resonant displacer/mechanical spring system.

Long life mechanical springs can be designed provided the operating stress levels are sufficiently low. The damping forces for a well mounted mechanical spring are also quite low. However, experience with mechanical spring balancers has shown that small particles are generated during operation. Because these particles would be catastrophic to the clearance seals, mechanical springs could not be used in the design. Gas springs have no wear problems, but do have limited linearity, higher damping than mechanical springs, and require an additional clearance seal. In addition, the mean gas pressure of the spring and the cooler would have to be the same, thereby limiting design flexibility. For these reasons, the gas spring was not used in this design. Magnetic springs, on the other hand, do not need clearance seals and have no life-limiting properties. As a result of the advances made in permanent magnet material, new, high-strength magnets with minimal long term aging and good temperature stability are now available. These improvements have made magnetic springs feasible, and the Prototype Model incorporates one in the displacer design.

One advantage of the Engineering Model linear motor drive system is the freedom to adjust the displacer and piston strokes independently as well as the phase. In a free displacer design, control and flexibility is lost, though fewer components are needed. Thus, an adjustable spring or a spring and motor is desirable to maintain operating flexibility.

The Prototype Model incorporates such an integrated magnetic spring/motor. The motor provides control of the displacer motion. A schematic of the integral spring/motor with the displacer at full stroke is shown in Figure 4-6. The moving magnets act as springs and interact with the stationary coil to produce a force which is proportional to the current in the coils.

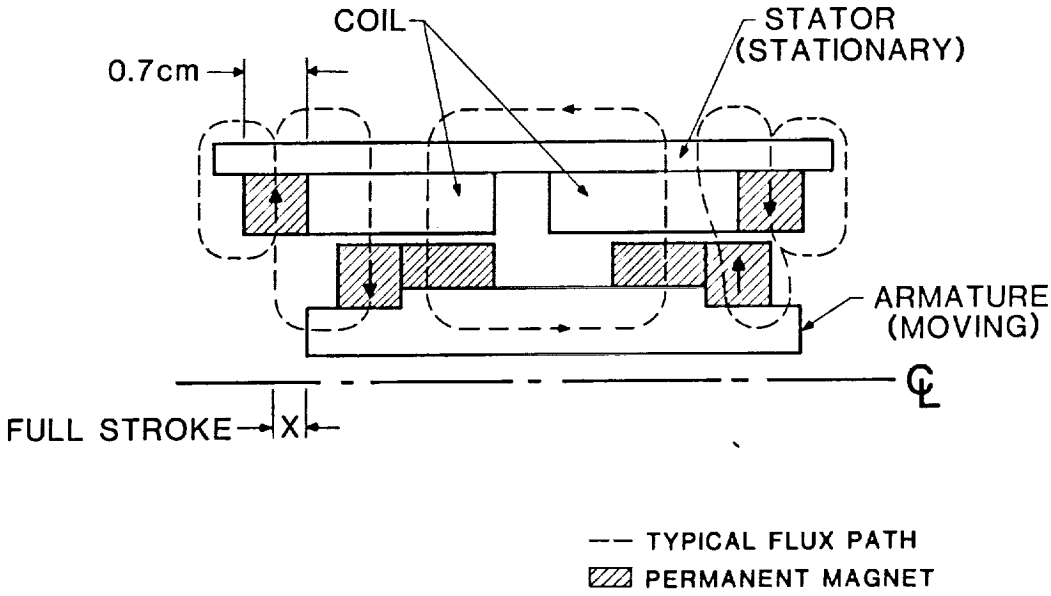

Figure 4-6. Schematic of integral displacer magnetic spring/linear motor.

The construction of the motor is similar to that of the displacer linear motor of the Engineering Model. Radially magnetized magnets are added to the stator at both ends of the coils to provide a self-centering magnetic spring. Good linearity is achieved over the design stroke by proper positioning of the concentric magnets. Another advantage of this design is the single diameter construction. No dead space or void volumes are introduced which would have existed with a conventional face-to-face repulsion magnet spring. The springs reduce the peak force requirements of the motor. Table 4-5 compares the power requirements of the integral spring/motor design and the linear motor design. In both cases $SmCo_5$ magnets are used because of their rigid magnetization and excellent thermal and long term aging stability.

TABLE 4-5. Power Comparison: Integral Spring/Motor vs. Linear Motor.

	Prototype Model Spring/Motor	Engineering Model Linear Motor
Peak inertial force (N)	35	25
Moving mass (kg)	1.0	0.345
Total electric power (W)	2	70

Eddy current damping generated in this magnetic spring is difficult to predict accurately. The eddy currents dissipate stored energy and lower the spring quality factor (Q). Another problem with a magnetic spring of this design is the radial instability and resulting side loads. The side loads occur not only from magnetic eccentricities resulting from mechanical construction, but also from magnet non-uniformity. The side loads have static as well as dynamic components. Because of the difficulty in estimating these effects, tests were performed with a dedicated test fixture.

Axial springs of this design have a radial stiffness instability which is less than or equal to -1/2 the axial stiffness. The sign is critical since a 10 N/m axial stiffness PM spring has a radial stiffness ranging from -5 N/m to negative infinity. For designs involving no soft magnetic material, the inequality qualifier can be removed.

The stiffness of a simple magnet pair (no soft magnetic material) was tested and compared to a finite element analysis of the same geometry (Fig. 4-7). The characteristic geometry of the magnet rings is very close to the spring/motor design. Side load tests were performed by displacing the inner ring toward the outer ring and measuring the radial force. The radial stiffness was measured to be -1/2 the axial stiffness. The side loads for zero mechanical eccentricity of various magnet pairs were measured to determine the magnet non-uniformity. Table 4-6 summarizes the test results which indicate that matched magnet segments must be used to produce acceptable performance.

TABLE 4-6. Static Side Load Test Results.

Radial instability of single magnetic spring pair

Axial stiffness at mid position	11,000 N/m
Radial instability stiffness:	
• Theoretical analysis	5,500 N/m
• Finite element analysis	5,500 N/m
• Measured	5,000 - 7,000 N/m

Magnet non-uniformity

Magnet pair number	1	2	3	4
Peak radial side force (N) (in concentric position)	2.0	1.1	2.6	0.25
Equivalent geometric eccentricity (cm)			0.047	0.005

4.6.2 Dynamic Test Results

Following these static tests, two sets of springs were mounted to an active radial magnetic-bearing test fixture which exhibited no friction and extremely low damping in the axial direction. Figure 4-8a is a schematic of the test fixture. The integral magnetic spring/motor was in effect split and placed at either end of the bearing test fixture. Figure 4-8b is a scope trace of the position of the moving mass vs. time resulting from an initial step displacement. The resulting Q of about 70 - 100 (an efficiency of 91-94%) indicates that there is very little eddy current damping in the magnets. The quality factor, Q, does get lower as additional magnets or magnetic material are placed near the spring, indicating that eddy current damping is not negligible.

The setup was further modified to test the integral motor/spring concept. An additional small magnet ring was attached to each inner magnet ring as in Figure 4-8c, and a coil was placed around

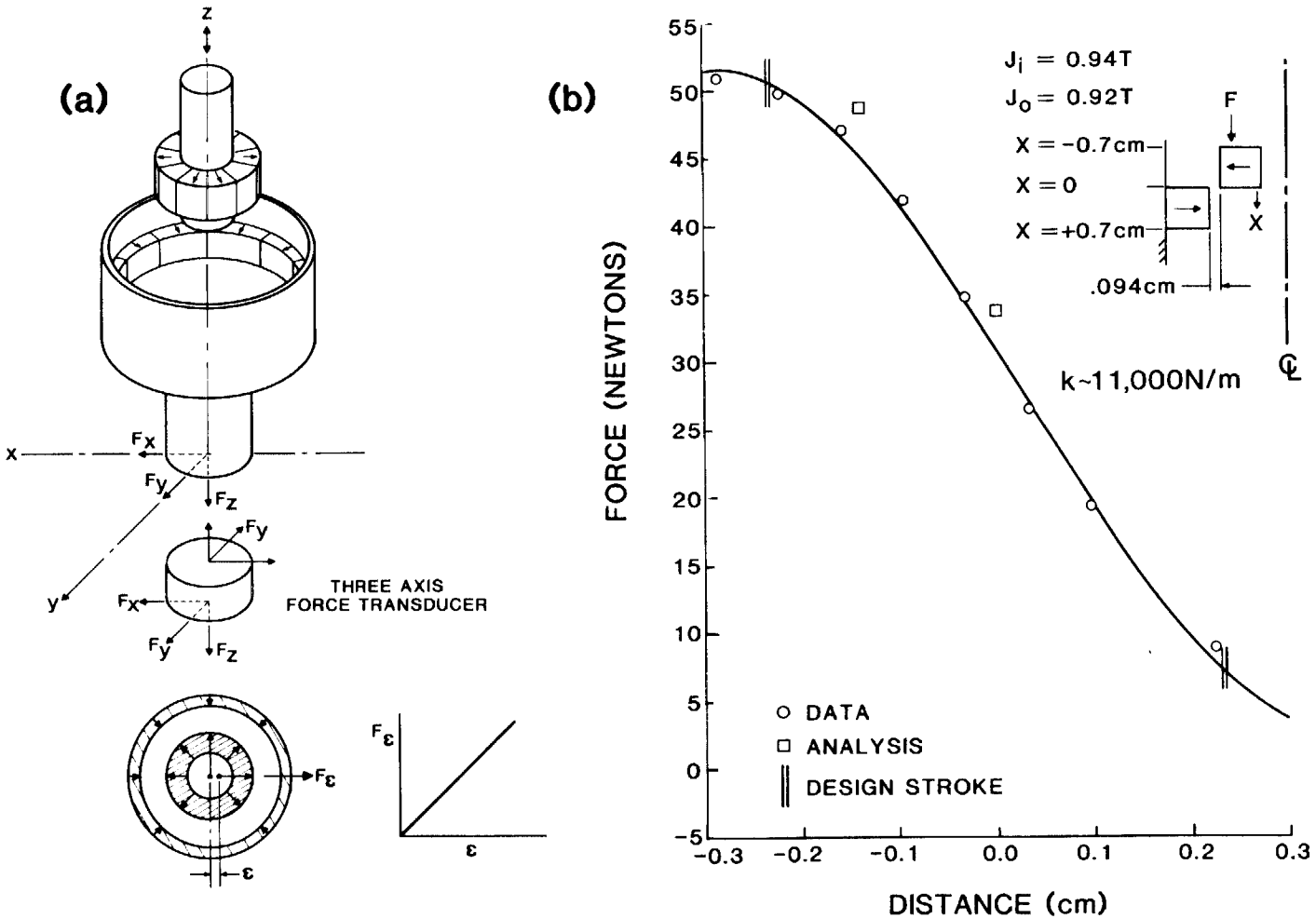

Figure 4-7. Static test of single magnet pair vs. analysis.
a) Test setup . b) Axial test results.

each inner magnet ring. This test was performed to verify the analytic procedure used to determine the force constant of the displacer motor. Both dc and ac tests were performed using the motor to excite the moving mass. The dc force constant of the motor agrees well with the predictions. The displacer was driven off-resonance (as it would be in operation) and open-loop, and the resulting frequency spectrum of the displacement was recorded. Figure 4-9a(1) is a force displacement curve of the spring for positive and negative displacements. At low amplitudes, the curves match well, indicating that there should not be any even harmonics in the displacement spectrum. At larger strokes the curves vary, indicating that even harmonics will be present. The resulting frequency spectrum measurement of the displacement is shown in Figure 4-9b(2). These harmonics produce insignificant adverse effects on the thermodynamics.

Through the introduction of bonded high energy product magnets, the damping can be further reduced because of their very high resistivity. In a free displacer design, the motor can be eliminated and axially magnetized springs can be used, thus simplifying the fabrication.

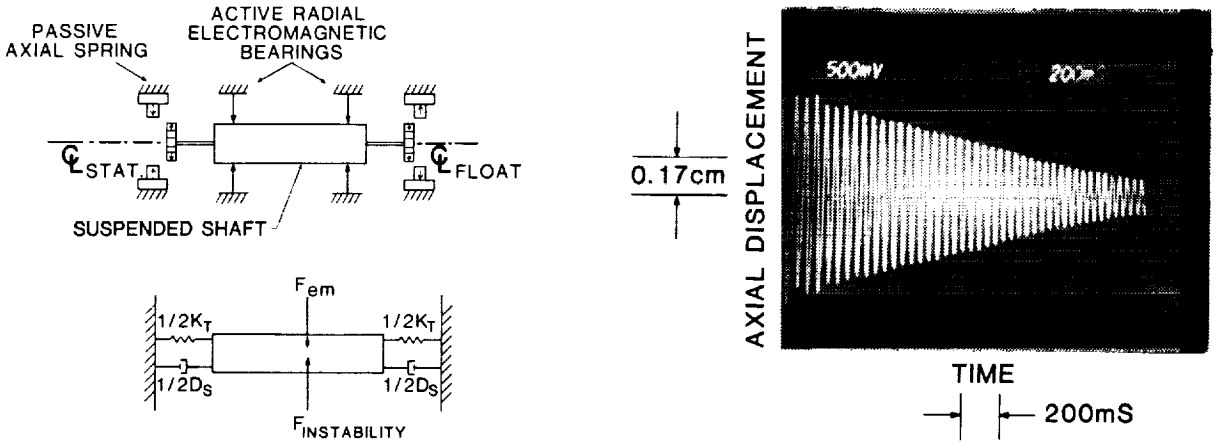

(a) Dynamic test schematic. (b) Damping with Permendur backing (Q = 70).

DYNAMIC SPRING TEST - ONE SIDE

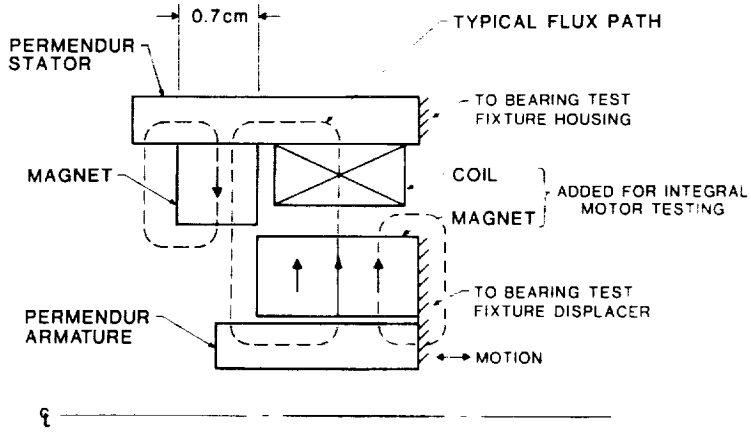

(c) Dynamic test fixtures with coil and additional magnets.

Figure 4-8. Dynamic test results.

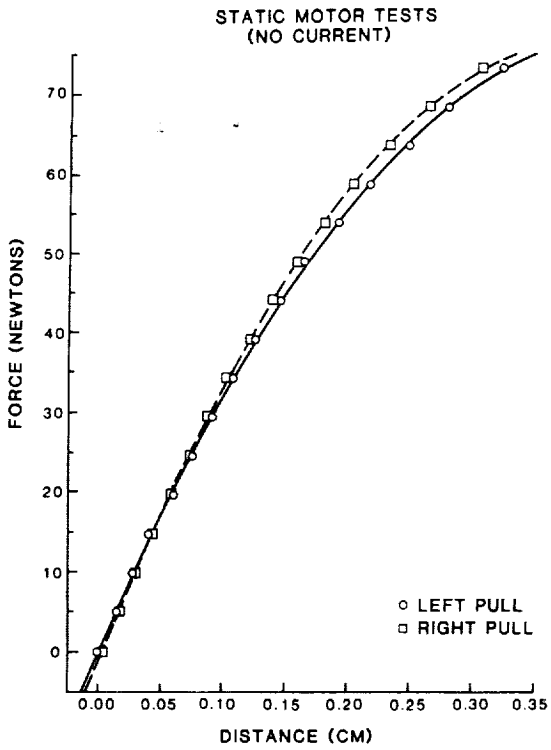

(a) pull to left and right.

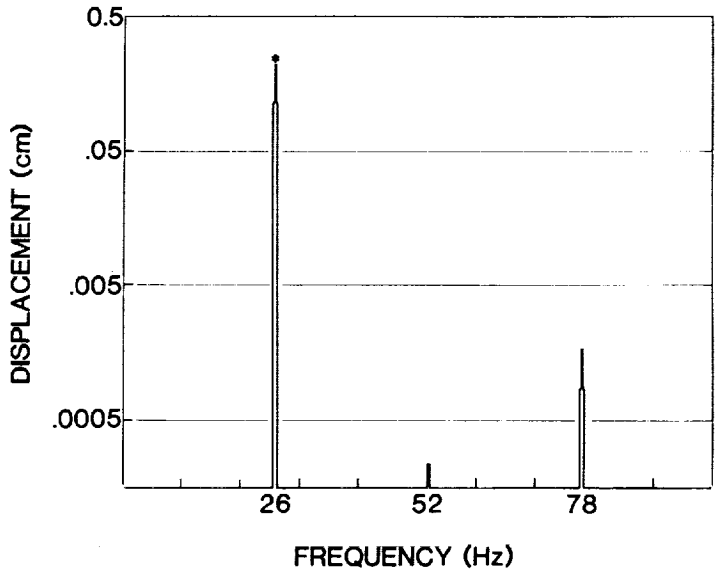

(b) large stroke.

Figure 4-9. Motor Test Results - Displacement Spectrum.

5. ACTIVE COUNTERBALANCE

The sum of the reciprocating motions of the displacer and piston results in an unbalanced force on the refrigerator and whatever it is mounted to. This unbalanced force is attenuated by a counterbalance system. In the Prototype Model, the counterbalance removes imbalances by providing an opposing force with equal magnitude to the combined force imposed by the piston and the displacer. This is done by a countermass moving in opposition to the sum of the displacer and piston motions.

5.1 Design Description

The counterbalance of the Engineering Model is a simple passive system consisting of a mass on a spring so that its natural resonance would keep it reciprocating 180° out-of-phase with the combined motion of the piston and displacer at the refrigerator's operating frequency. Due to aging and fatigue problems associated with a mechanical spring, it is difficult to achieve a five-year life with such a passive system. Also, a passive system can only remove a portion of the imbalance at the fundamental frequency and does nothing about the forces at higher harmonics.

The counterbalance of the Prototype Model has a linear motor and an active control system. This greatly improves performance by providing compensation to spring damping and balancing at higher harmonics. The Prototype counterbalance has a linear motor and a linear variable differential transformer (LVDT). These, together with the motor control electronics, provide the active position control of the countermass, which gives the necessary motion to balance the refrigerator. To save power, the countermass is resonating with a double-acting gas spring. The motor has multiple functions: it serves as the linear actuator, the countermass, and the gas-spring piston (see Fig. 5-1). The motor with the exception of the coil is mounted on a hollow shaft suspended by magnetic bearings. The narrow annular gaps (19 μm) between the housing and the shaft along the bearing sections function as the clearance seals for the gas spring volumes. The efficient use of mass and space results in a compact counterbalance design.

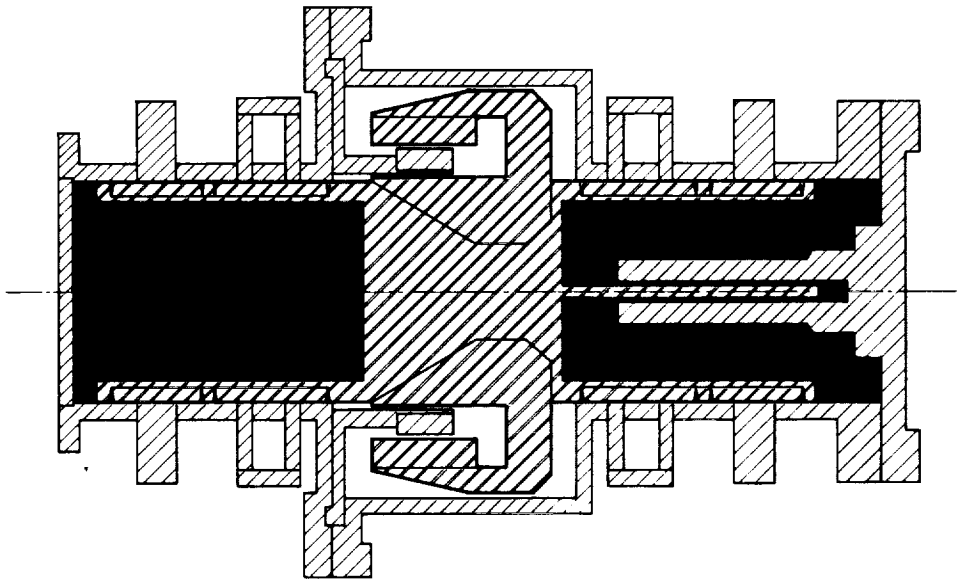

Figure 5-1. Active counterbalance.

The nominal inertial force generated by the combined motion of the piston and displacer is about 500-600 N. The countermass weighs 6.9 kg and requires a reciprocation amplitude of 6 mm to counteract 500 N. To resonate the countermass at 19 Hz, a gas-spring stiffness of 97,500 N/m is required. The counterbalance motor and its axial control system are described in Sections 4 and 7, respectively.

5.2 Gas Spring Design

Gas springs together with magnetic bearings and clearance seals provide the necessary high reliability and compactness for the Prototype Model. Its design is also flexible because the stiffness is tunable by adjusting the charge pressure. The primary disadvantage of a gas spring is the relatively higher losses due to heat-transfer effects and seal leakage. This is minimized in this design by using the more "adiabatic" nitrogen working gas and a low compression ratio.

To cancel the net imbalance from the refrigerator, various combinations of moving mass and stroke can be selected. Since the motor is part of the moving mass, the selection of the value for the moving mass determines the efficiency of the motor. On the other hand, the overall size and weight of the counterbalance are mainly affected by the stroke selected. Also, the selection of the mass or stroke determines the stiffness of the gas spring required.

Spring losses are caused mainly by imperfect heat transfer and seal leakage, and these two losses depend on the compression ratio (or pressure wave amplitude) of the gas spring. The higher the pressure amplitude, the higher the peak gas temperature in the spring volumes; thus, the higher the heat transfer losses. Also, higher pressure amplitude causes higher seal leakage. An ideal counterbalance will have a large enough moving mass to allow an efficient motor design and a small enough stroke to allow a compact gas spring design with low compression ratio. The low compression ratio will also produce lower unwanted higher harmonic forces in the gas spring. Higher harmonic forces generated by the compression and expansion of the gas spring will require additional motor power to compensate for them.

For an adiabatic gas spring, its stiffness k as a function of displacement x is:

$$k = \frac{nP_o S^2}{V_o} \left[\frac{1}{1 - \left(\frac{S}{V_o} \right) x} \right]^{n+1}$$

where, P_0 is the gas pressure at a reference displacement, V_0 is the corresponding volume of the contained gas, n is the ratio of specific heats of the gas, and S is the piston frontal area. If the change in volume is small relative to the initial volume V_0, ($S\ x << V_0$), the expression for stiffness reduces to:

$$k = \frac{nP_o S^2}{V_o}$$

The gas spring losses are due to irreversible thermal losses and leakage past the seal. The losses can be equated to the work done on the gas by the piston which is:

$$\dot{W} = N\ S \oint P dx \text{ (watts)} \qquad (3)$$

where N is the reciprocating frequency of the piston, and P is the gas pressure. If P and x vary sinusoidally with time t, Eq. (3) becomes:

$$\dot{W} = \pi N \hat{P} \hat{x} S \sin\phi \tag{4}$$

where $\hat{P}$ and $\hat{x}$ are pressure and displacement amplitudes, respectively, and ϕ is the phase angle between P and x.

The first harmonic equation of motion for the countermass is described by:

$$m\ddot{x} = \text{pressure force} + \text{motor force}$$

$$= -2\hat{p}\cos(\omega t - \phi) + f\ i \tag{5}$$

where f is the motor force constant (N/A), m is the mass of the countermass, and i is the motor current.

From Equation (5), the motor current can be written as

$$i = \frac{1}{f}[-m\omega^2 \hat{x}\cos\omega t + 2\hat{p}S\cos(\omega - \phi)] \tag{6}$$

For minimum power, the countermass and gas pressure are turned to satisfy

$$m\omega^2 = 2\hat{p}S\cos\phi \tag{7}$$

With Equation (7), the current becomes

$$i = \frac{2\hat{p}S\sin\phi}{f}\sin\omega t \tag{8}$$

The total input power P to the motor can then be written as

$$P = \dot{W} + N\oint i^2 R dt$$

or

$$P = \dot{W} + \frac{\hat{P}SR}{f^2}\sin^2\phi$$

Since the losses in gas spring involve complicated processes, they cannot be predicted with confidence. An experiment (see Sect. 5.3) was performed to measure the pressure amplitude (p) and the phase angle (ϕ) between the piston position and the pressure wave. The design parameters for the gas spring are summarized in Table 5-1.

TABLE 5-1. Design Parameters of Gas Spring.

Spring Configuration	Double-Acting Gas Spring
Working Fluid	Nitrogen
Frequency	18.9 Hz
Moving Mass	6.9 kg
Charge Pressure	78.4 psia.
Amplitude	6 mm
Piston Diameter	70 mm
Mean Gas Volume	230 cc each
Max. Vol./Min. Vol.	1.2
Spring Stiffness	97,300 N/m

5.3 Gas Spring Performance

The following instruments were used in the experiment:

- vibration exciter system (Bruel & Kjaer, 4818 & 4802T)
- power amplifier (Bruel & Kjaer)
- sine random generator (Bruel & Kjaer, 1027)
- LVDT (Schaevitz, 499 XS-C)
- LVDT signal conditioner (Schaevitz, CAS-100)
- pressure transducer (Kulite Semiconductor Products, xt-190-100)
- dynamic analyzer (Spectral Dynamics, SD375)

The geometry of the gas spring tested was one-half that of the double-acting gas spring in the counterbalance (see Fig. 5-2).

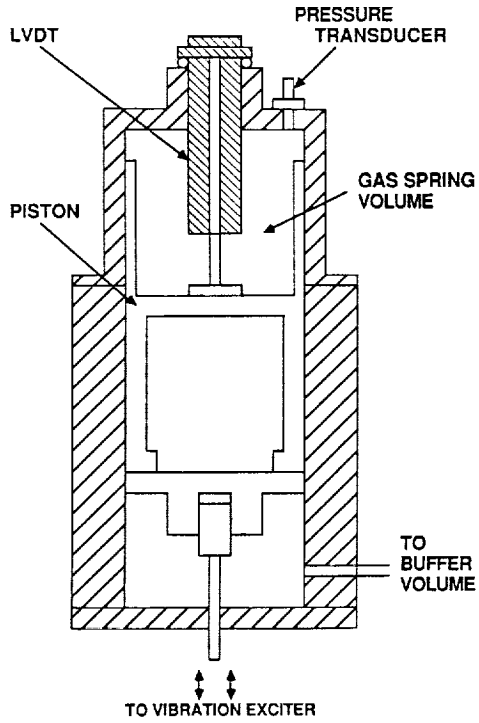

Figure 5-2. Gas spring.

Figure 5-3 is a schematic of the test setup. The gas-spring piston was connected to the vibration exciter which provided the reciprocating motion, and a sine random generator was used to control the sinusoidal motion of the piston. The motion of the piston was given by the output of an LVDT, and the pressure wave was measured with a pressure transducer. The outputs of the LVDT and the pressure transducer were read from the dynamic analyzer which also measured the harmonic contents of the pressure and the piston motion. Figure 5-4 is a photograph of the setup.

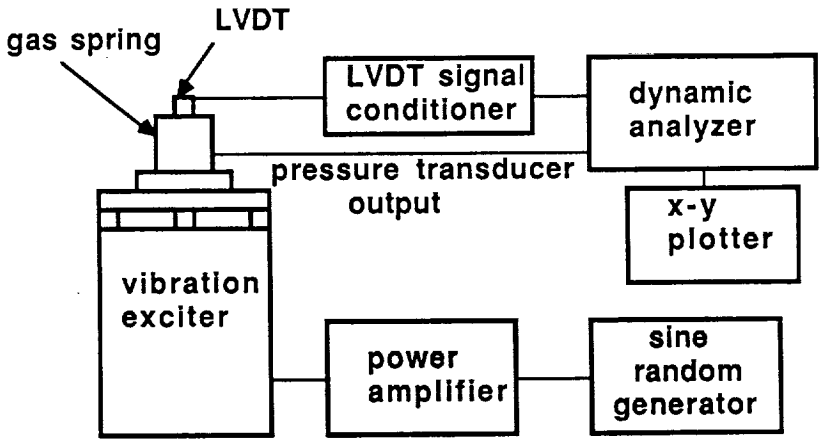

Figure 5-3. Schematic of test setup.

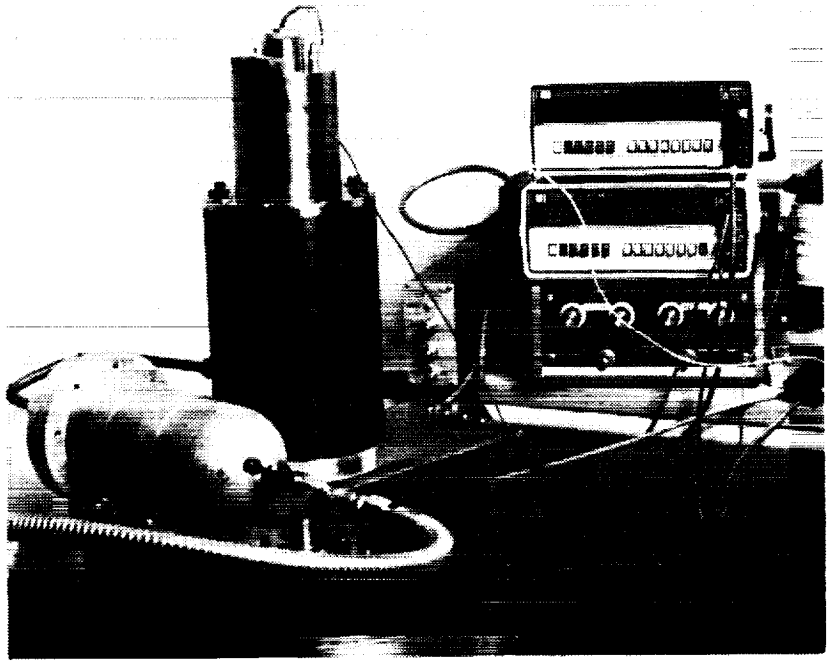

Figure 5-4. Photograph of test setup.

Figure 5-5 shows the pressure wave in the gas spring volume and the piston motion. Figure 5-6 and 5-7 are the harmonic contents of the pressure wave and the piston motion, respectively. Figure 5-8 is the P-V diagram of the gas spring; the area enclosed by the loop is the spring loss per cycle. The measured results and the results calculated under the adiabatic assumption are as follows:

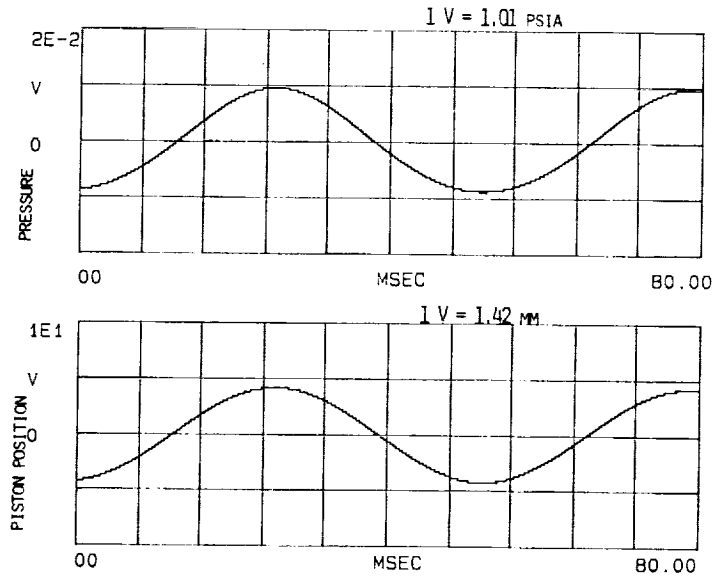

Figure 5-5. Pressure and piston motion of gas spring.

	Adiabatic (calculated)	Measured	Designed
Spring stiffness (N/m)	41,800	40,700	40,250
Max. pressure (MPa)	0.531	0.528	
Min. pressure (MPa)	0.400	0.400	
Phase (pressure/motion) (°)	-	-2.2°	
Spring loss (thermal) (W)	-	4	
Spring quality (Q)	-	22	

This experiment shows that the design of the gas spring of the counterbalance for the Prototype-Model achieved the necessary spring stiffness. The nitrogen gas spring was proven to have high spring quality (Q=22) with low losses. The double-acting gas spring in the counterbalance dissipates about 10 W. This experiment also shows that the nitrogen gas spring operates very close to the adiabatic condition.

With the piston moving sinusoidally, the second harmonic of the pressure wave is 5% of the fundamental, as expected from an adiabatic gas spring. The double-acting gas spring of the counterbalance will have lower second harmonics due to cancelling of the second harmonics from each of the gas springs.

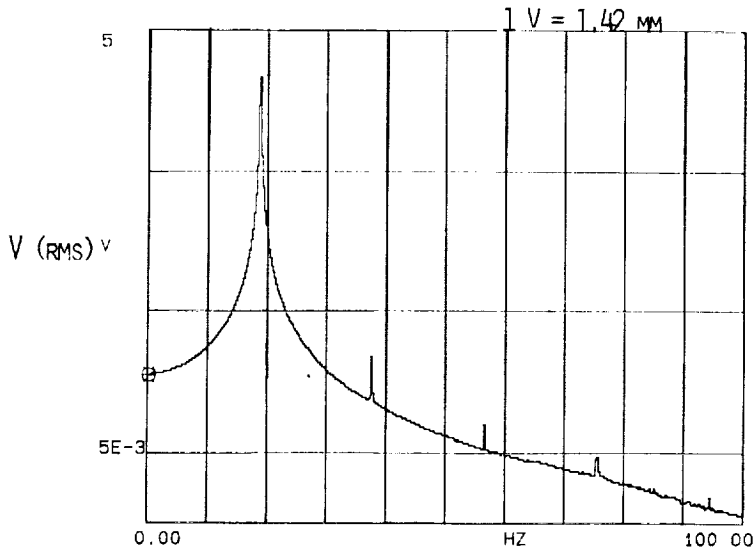

Figure 5-6. Harmonics of pressure wave in gas spring.

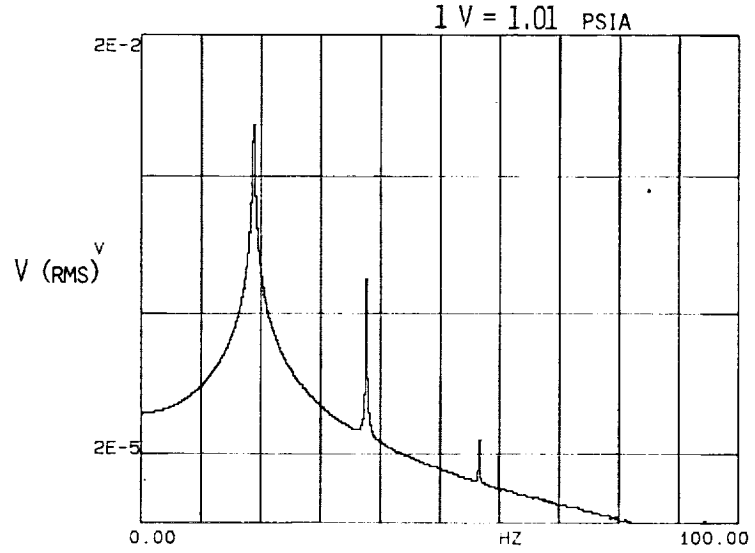

Figure 5-7. Harmonics of piston motion.

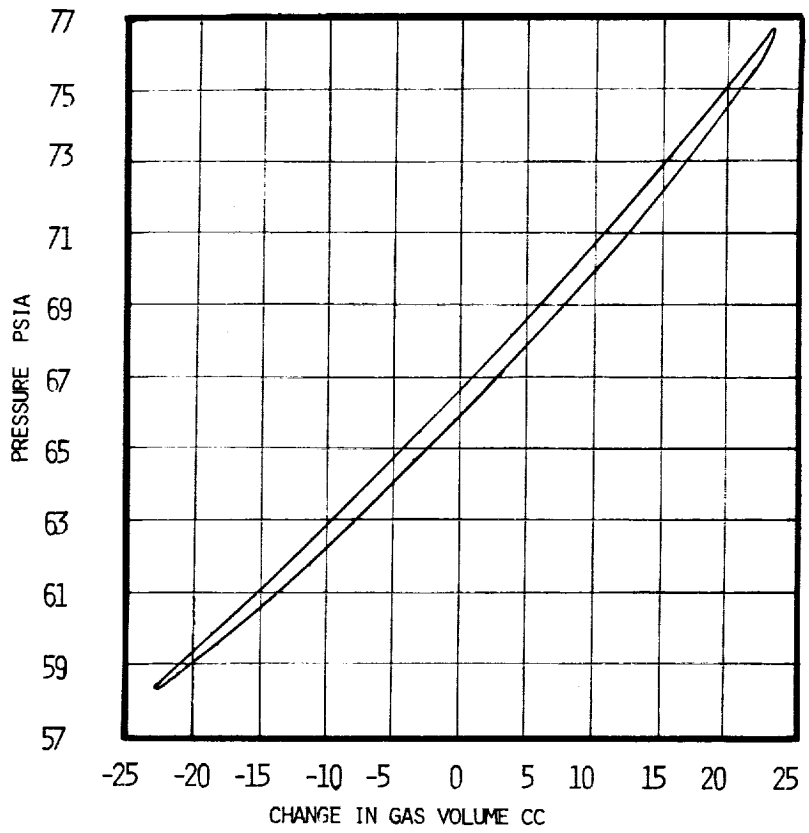

Figure 5-8. P-V diagram of gas spring.

6. MAGNETIC BEARING SYSTEM

6.1 System Description

The mechanical advantages of clearance seals, namely low friction and long mechanical life with an all-metal/ceramic (i.e., non-lubricated) construction were made possible through the use of magnetic bearings. Because the moving elements are electromagnetically suspended in their bores without contact, wear is eliminated and mechanical life is governed solely by electronic reliability. Contamination and thermodynamic degradation, classical problems of mechanical Stirling cycle refrigerators, are completely absent.

The linear magnetic bearings used in this Prototype Cooler are similar in concept to those used in the earlier Engineering Model. The general design of the linear magnetic bearing actuator is identical to the more popular, conventional active radial magnetic bearing [1,2]. There are, however, two areas of notable difference. First, significant development was needed to hermetically seal the bearings into the cooler housing. For the Prototype Cooler, this requirement led to the use of "solid" bearings and precluded the use of laminated actuator structures. This resulted in bearings that have eddy currents well within the bearing control loop. As a result, a careful understanding of the frequency dependent behavior of the bearings is essential to a proper modeling and design of the bearing system. The fabrication techniques are covered in Section 9.

The other significant difference in the behavior of linear magnetic bearings comes from mechanical system considerations. Because these bearings are also used as clearance seals, there is a very narrow gap between the housing and the shafts. Gas damping plays a significant role in shaft dynamics and hence magnetic bearing performance. The gas damping provided by the clearance seals plays a larger role than mass (inertia) in shaft dynamics in the launch and operating frequencies. This is the most important difference between these magnetic bearings and those readily available for conventional rotating systems.

The magnetic bearing consists of three major components: the ferromagnetic pole pieces (the actuators), the optical position sensors, and the electronic feedback system (the controller). The configuration of the actuators and sensors is shown diagrammatically in Figure 6-1. Each ferromagnetic pole piece exerts a radial attractive force on the reciprocating shaft when current is applied to its coil winding. By situating poles diametrically opposite, one end of the shaft may be controlled in one plane by regulating the current in each of these two poles (see Fig. 6-2). By positioning sets of poles at orthogonal planes at each end, the shaft may be suspended. The radial position of the shaft is transduced with optical position sensors (see Sect. 6.4).

A block diagram of the electronic controller is shown in Figure 6-3. The pole-piece magnetics are highly nonlinear: the force is proportional to the square of the current and inversely proportional to the square of the air gap. The electromagnetic field in the iron is influenced by the effects of eddy currents, hysteresis, and magnetic saturation. The shaft dynamics also includes a damping force caused by the gas squeeze film in the 19 μm air gap.

The action of the feedback loop can be explained as follows. A reference center position of zero volts is compared to the transduced position voltage from the optical position sensors. Any error between these two voltages regulates the differential current in a diametrically opposite pole piece pair so as to reduce this error. The compensator is designed to provide stability for the large restoring forces over a wide frequency band. To do this effectively, the control loop bandwidth must be large and insensitive to changes resulting from the nonlinear nature of the magnetics and dynamics. A

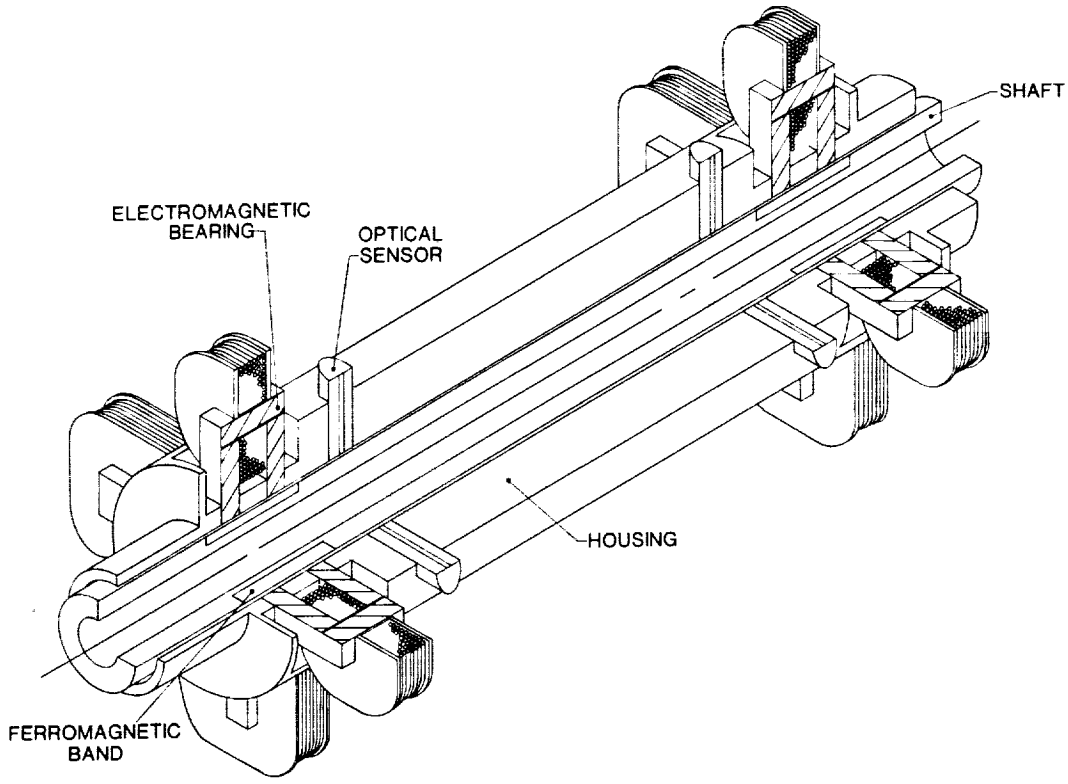

Figure 6-1. Geometry of magnetic bearing.

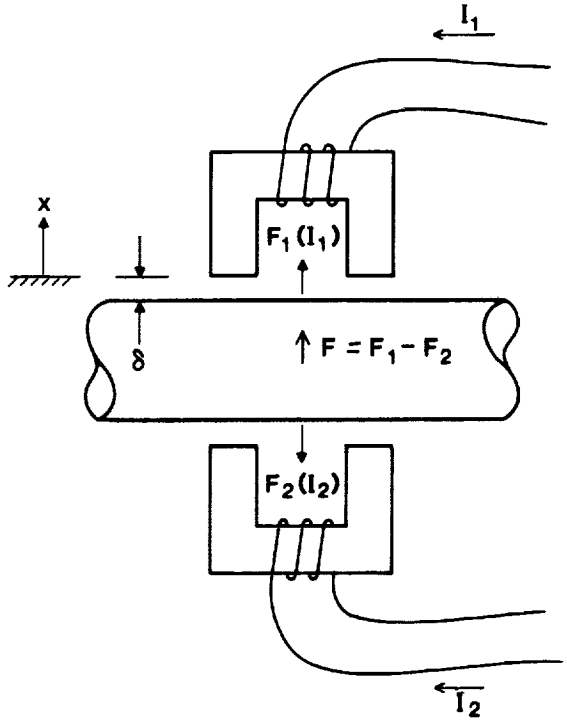

Figure 6-2. Radial force generation in magnetic bearing plane.

current amplifier reduces the destabilizing phase shifts caused by the coil inductance and actuator eddy currents.

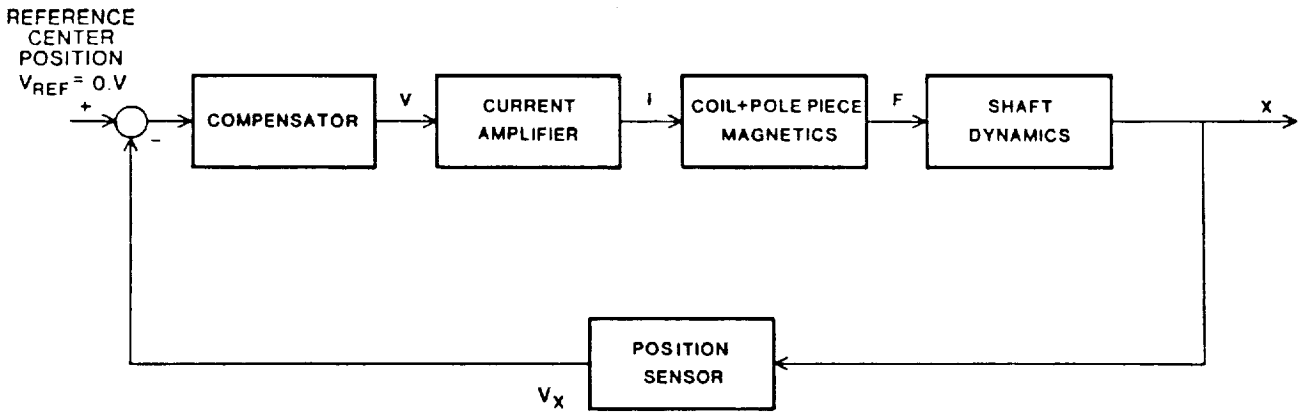

Figure 6-3. Block diagram of bearing control system.

In the following sections, the pole piece actuator and shaft dynamics are analyzed. Then, following an estimation of bearing loads and vibrational resonances and a discussion of the optical position sensors, the design and measurement of the magnetic bearing control system are presented.

6.2 Design Requirements

A prime goal in the design of the cooler was to stiffen the system such that the moving parts could withstand launch aboard a shuttle. The previous bearing system (Engineering Model) was designed to maintain clearance in a 1g field and support only the internally generated imbalance forces. This cooler, on the other hand, has to withstand a force level several times that of the gravity at "ac" conditions.

6.2.1 Launch Vibrations

The launch vibrations are described by three independent specifications; random, acoustic, and quasi-static. It has been shown [3] that the random vibrations and acoustic loads applied to the cooler are much less severe than the quasi-static loads. The accelerations of the cooler housing resulting from random launch vibrations were shown to be less than 0.020 g rms.

NASA uses a third specification to include the effects of shock loads, mount amplification, and launch uncertainty. This specification is termed "Quasi-Static Loading" and is by far the most severe of the three specifications on the refrigerator design. This data was compiled from previous flights and represents the maximum acceleration levels measured on devices with similar isolation mounts.

The specification describes the vibrations during the three launch phases: lift-off, transonic/maximum aerodynamic pressure, and ascent. Each phase has an ac and dc acceleration component which is applied to the refrigerator simultaneously in three orthogonal axes for specified duration.

The isolation mount frequency determines the ac acceleration specification of the design frequency of 7 Hz, yielding the specifications shown in Table 6-1.

TABLE 6-1. Quasi-Static Launch Vibrations.

Occurrence	dc Acceleration (g)	ac Acceleration at 7.0 Hz (g)	Vibration Duration (seconds)
Lift-off	1.5	5.4	20.
Transonic/Maximum Aerodynamic Pressure	3.0	2.7	10.
Ascent	3.2	0.	100.

Thus, these bearings must be significantly "stiffer" than those designed earlier, not only at "dc" but also at 7 Hz, the natural frequency of the isolation mount. The actuators must be stiff enough to withstand these accelerations. The relative motion between the shaft and the bore must be smaller than some fraction of the radial clearance gap. A maximum excursion of 50% of the radial gap is used as the design goal.

6.2.2 Non-Launch Associated Loads: Internal or Self Generated Side Loads.

The other internally generated forces resulting from the axial motion of the shaft and any asymmetries in the system (motors) are much smaller in magnitude than the launch loads given earlier. These loads are important, however, for vibration considerations in space - i.e., asymmetries and side loads must either be compensated for, or are in some degree, transmitted through the isolation mounts to the satellite. These transmitted residual forces may pose a problem for very sensitive sensors that require stable, almost "inertial", reference frames. The analysis presented in the earlier report [4] is sufficient to approximate the magnitude of the dc side forces in all cases. The ac forces resulting from the axial displacement of the center of gravity were shown to be quite small. However, the radial ac forces resulting from the motor asymmetry was not addressed and is estimated below.

(1) AC Radial Motor Forces - Fringing

Because of the extreme symmetry employed during design and fabrication of the motors, the dc forces resulting from system nonuniformity are insignificant in comparison to gravity forces. However, these second-order asymmetries are significant in terms of ac loads. As will be shown, the bearings are not "stiff" at the higher frequencies, and symmetry requirements primarily come from the need to minimize these ac loads.

When the field windings are off, there is still a dc centering force in each motor armature and as a result of energy conservation laws, there is an associated radial instability. Based on a calculated radial instability stiffness K_r, the axial stiffness, K_z can be approximated by:

$$K_z \sim 2\ K_r.$$

The proof of this is based on conservation principles and is good for motor structures with large air gaps (permanent magnet dc motors). The axial fields are considered to be "leakage" or "fringing" fields and have an asymmetry of about 5% (the test specifications, however, for the motor magnets is written in terms of the radial field component and not the leakage, axial fields). These fringing

fields will produce a side force when the motor windings are energized. An estimate of the magnitude of this effect follows.

The axial force from the radial instability stiffness is $K_z z$. An equivalent magnetic field in the axial direction is on the order of:

$$B_z \sim (2\mu_o F_{zr}/A)^{1/2}$$

where,

F_{zr} = reluctance force in the axial direction at a given displacement given by $2 K_r z$, and A = surface over which B_Z is integrated. Thus,

$$B_z \sim (4\mu_o K_r \frac{z}{A})^{1/2},$$

and the magnitude of the nonuniform field is

$$B_{ze} = B_z \varepsilon,$$

where, ε = relative magnitude of nonuniformity,
μ_o = permeability of free space = 1.25×10^{-6}.

The residual axial field interacts with the circumferential field windings to produce a net radial force given by:

$$F_r = J \times B_{ze} \qquad \text{or,}$$

$$F_r = B_{ze}(F_{xm}/B_r)$$

where,

F_{xm} = axial motor force
B_r = nominal radial field

Thus, an estimate of the radial ac force as a result of the asymmetric leakage fields can be made based on an assumed axial leakage nonuniformity. Table 6-2 presents the results of such an analysis based on an assumed 5% axial field nonuniformity.

TABLE 6-2. Resultant Radial Force from Fringing.

	Piston	Displacer
Effective Surface Area (m^2)	0.020	0.004
K_r (N/m)	140,000	14,000
Axial Displacement, z (m)	0.008	0.0025
Axial Field Nonuniformity, ε	0.05	0.05
Equivalent Axial Field Strength, B_{ze} (T)	0.5	0.25
Axial Motor Force, Fx_m (N)	220	10
Radial Field, B_r (T)	0.3	0.3
Radial Side Force (N)	19.0	0.7

(2) AC Side Loads from Radial Field Asymmetry

A second source of ac radial magnetic side forces emanate from asymmetries in the radial magnetic field created during changes in the magnetic circuit. As the magnets are displaced or as the external field from the coil is varied, the average dc working point of the magnet changes. This is also referred to as dynamic working or "recoiling". This recoiling can come from a change in system reluctance as wells an externally applied field.

The ac side forces resulting from axial field asymmetry are discussed above. An estimate is made here of the ac side forces resulting from non-uniformity of trajectory of the working point of the magnets along the "working point" curve (See Sect. 4.3).

To the first order, the net radial dc side force F_{rdc}, is

$$F_{rdc} \sim \frac{\varepsilon B_r^2 A}{2 \mu_o}$$

where,

ε = % field nonuniformity
A = effective area of integration of radial field.

During operation, the working point of the magnets changes as a result of applied field. We estimate the magnitude of the ac component to be:

$$F_{acr} \sim \frac{\varepsilon_{ac} B_r^2 A}{2 \mu_o}$$

$$\sim F_{rdc} \frac{\varepsilon_{ac}}{\varepsilon}$$

where,

$\varepsilon_{ac}/\varepsilon$ = normalized asymmetric change in field strength during operation.

Based on measured values of the selected piston and displacer magnets, we estimate that $\varepsilon_{ac}/\varepsilon$ is on the order of 1.0. The ac forces for the piston and displacer based on dc side forces given earlier [5] are about 10 N and 4 N for the piston and displacer, respectively.

In other words, the magnitude of the ac side force is about equal to the dc side force. This makes sense since the absolute value of field is directly proportional to the magnets "working point" which, in turn, is determined by the demagnetization slope and the field strength in the nominal centered position.

We have measured radial accelerations on the cooler housing of the Engineering Model to be on the order of 0.5m/sec^2. For a complete cooler housing mass of at least 100 lbs, or about 50 kg, the radial imbalance force is on the order of 25 N, which agrees in magnitude with the above analysis.

The above was calculated for pure sinusoidal axial motion. If any harmonics in motion are present, the appropriate amplitude at a specific frequency should be used. Note that these are the ac forces, produced as the shaft is held in the geometric center. Had a more sophisticated controller been used, these side forces could have been minimized by adjusting the radial and theta orientation.

In summary, these forces are less severe than the launch loads, but are, however, important for vibration considerations.

6.3 Bearing System Analysis and Results

As mentioned, the analysis and design of the magnetic bearings are hampered by the high nonlinearity of the magnetic/mechanical system. Techniques for handling nonlinear control systems directly are few; the most effective ones deal with linearization and the subsequent use of the powerful linear control theory. In the case of the bearing, linearization assumes that the radial displacement and current change little from the nominal value. Under this assumption, each of the nonlinearities is linearized for small perturbations. The feedback loop is modeled as a conventional linear regulator, and the bearing performance can be estimated using classical single input-single output techniques.

The analysis of the magnetic bearing is in several parts. This first part is concerned with the general analysis of the magnetic/mechanical system. Models of the force-current relationship, eddy-current effects in the pole pieces, and squeeze-film damping are discussed. The second part is concerned with the analysis specific to the refrigerator configurations. Finally, system predictions and measurements of bearing performance are presented.

6.3.1 Analysis

(1) Force Properties

Consider the magnetic bearing shown in Figure 6-4. This single-ended bearing will produce forces on the armature and attempt to reduce the co-energy stored in the system by reducing the total gap, g.

The normal (perpendicular) force on ferromagnetic material is determined by the magnetic pressure, B_p. This pressure (also known as the Maxwell stress) is:

$$B_p = \frac{B^2}{2\mu_o} \quad .$$

Thus, the force over a given surface area can be written in terms of the normal field directly as

$$F = \frac{A\,B^2}{2\mu_o} \quad .$$

The field, B, is related to the geometry of the system by

$$B = \frac{Ni\mu_o}{2g}$$

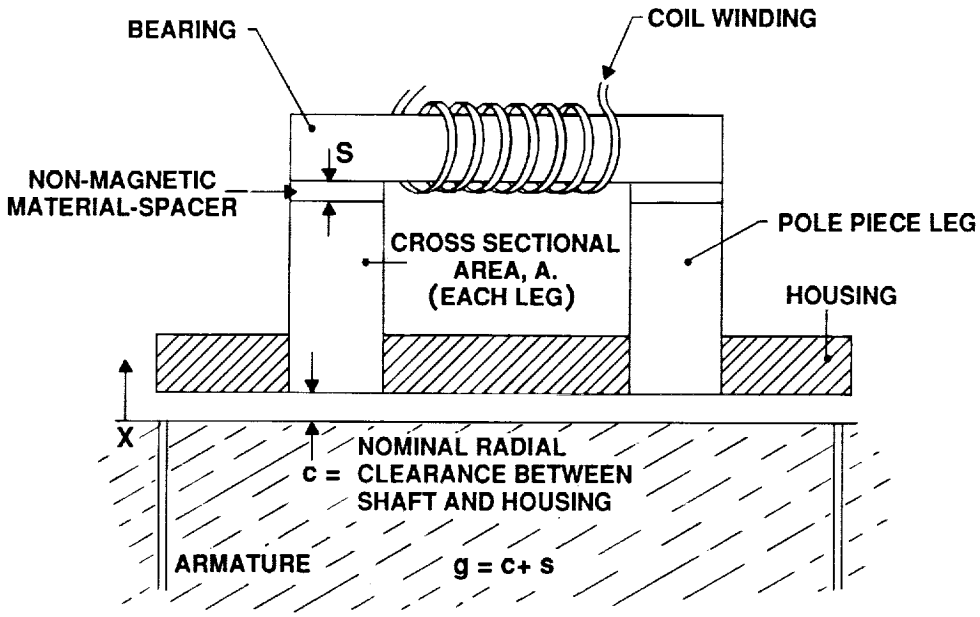

Figure 6-4. Detail of single bearing actuator geometry in bearing plane.

where,
g = nominal gap for each leg
= s + c

We have ignored fringing fields (leakage) and the coil energy stored in the magnetic core material (iron). Thus, for the case of a single bearing, and considering contributions from both legs, the total force is given by

$$F = \frac{\mu_o A (Ni)^2}{4 g^2} \quad ,$$

where "A" is the cross sectional area of each leg, and "N" is the number of turns of wire to produce the coil. The force is quadratic in both current and position gap. The magnetic bearings used in this cooler have "bias" or linearizing gaps "S" placed in the magnetic path. The above relationships apply to the total gap as depicted in Figure 6-4 and not only the displacement, or perturbation, of the gap, x.

For the magnetic bearings used in this cooler, two bearings are employed for each independent axes and are placed 180° apart; thus, the net magnetic force acting on the shaft is the resultant of these two bearings, or

$$F_{netmag} = F_{top} - F_{bottom}$$

For a generalized electromechanical actuator the magnetic coenergy is a function of current and position. Thus, it is conventional to consider the force (or energy) contribution from each independent "controlling" variable. That is, determine the net force on the shaft for small changes in current (keeping the position constant) and the net force resulting from small displacements (keeping the current constant). Hence, two types of force constants can be developed, one for current and another for position.

For the case of no displacements, and using the Taylor series expansion for $i = i_b + \delta i$, the force constant K_i for small changes in current is

$$K_i = \frac{-N^2 A \mu_o i_b}{g^2}$$

where, i_b = the bias or constant current.

By convention, it is assigned a negative magnitude, i.e., as the current increases, there is an increase in the net attractive force (as opposed to a repulsive force in a conventional mechanical spring).

It is useful to simplify this relationship by relating the force constant to the inductance of the bearing,

$$L = \frac{\mu_o N^2 A}{2g} \quad .$$

Thus, the current force constant in terms of "dc" inductance, L_{dc}, is,

$$K_i = \frac{2 L_{dc} i_b}{g} \quad .$$

The above relationship is found to be extremely useful in understanding bearing behavior. A very accurate indication of the current force constant, K_i, can be made without having to perform any force-type measurements directly. The control loop in the Prototype Cooler uses a "clipping" circuit to ensure that there are no zero or negative currents; thus, for the case near equilibrium about the bias current level, only positive current excursions are allowed, and the actual force constant about the dc condition is actually only one-half that given above, or

$$K_{ic} = \frac{- L_{dc} i_b}{g} \quad ,$$

which is also the result for a single-sided magnetic bearing. The subscript "c" is used to distinguish it from the case where no clipper circuit is employed. It should be noted that this is the correct force-to-current relationship and that the relationship presented in the previous report [6] was incorrect.

The magnetic bearing has some bias current to linearize the bearing circuits and stiffness. This bias current produces an instability force, viz., as the shaft is displaced toward the bearing, the attraction force grows.

The instability position stiffness, K_u, is related to the previous stiffness by

$$K_u = \frac{K_i \, i_b}{g} \quad ,$$

where the negative sign is included in the K_i term above.

In the above analysis the conventional Taylor series expansion was used and second-order terms are dropped. Thus, for each bearing, the complete dc force constant parameters, can be simply summarized in terms of inductance, gap size and bias current. Table 6-5 summarizes these values for each of the bearing types in the Prototype Cooler.

TABLE 6-3. Bearing Force Characteristics.

	PISTON	DISPLACER	COUNTERBALANCE
DC bearing inductance:			
L_{dc} (h)	0.7	0.31	0.5
G	69×10^{-6}	273×10^{-6}	69×10^{-6}
Bias Current (A)	0.06-0.075	0.10	0.06-0.075
Additional Geometric properties:			
Area of each leg (m^2)	0.0002	8×10^{-5}	0.000334
Number of turns	800	1200	540
DC Resistance (ohms)	10.6	30	2.6
Bearing Material	-----	2V Permendur	-----

Note the addition of the subscript "dc" in the inductance term. As mentioned earlier, the bearing (actuator) behavior is frequency dependent. The relationships derived above are valid for the frequency range where frequency dependent losses (eddy currents and hysteresis) are small. ("Small" implies that these material losses are small in comparison to the coil resistance, or, there is no phase difference between current in the coil and force developed in the armature). Thus, all the mmf developed by the coils is used to produce magnetic fields that cover the entire surface area and are not "crowded" by eddy currents. The Ldc term is used to denote the low-frequency force relationships of the bearings. An analysis/characterization of the high frequency behavior is given in Section 6.3.2. Also, the above analysis ignores any nonlinear current to flux properties of the magnetic material.

(2) Effective Mass

For practical manufacturing considerations, the magnetic bearing actuators within each type of shaft (piston, counterbalance, displacer) are the same, resulting in three different bearing designs. The geometric properties are summarized in the previous section.

The magnetic bearings must support these shafts (displacer, piston, counterbalance) as they are accelerated by the linear motors and maintain a safe clearance between the shaft and housing during launch accelerations. Because the shafts are long (in comparison to their diameter) the effective mass should, in theory, include some rotational terms, as well. That is, in addition to the mass of the shaft, the moment of inertia, J, must somehow be included in the analysis. However, because the bearings for each shaft type are the same, a simple and direct analysis is presented for determining the effective mass at each bearing for the purpose of bearing design.

The simplest case to consider is one in which the center of gravity is at the nominal mid-span between the bearings. This is true for the piston and counterbalance shafts. For such cases it has been shown that the eigen-frequencies are:

$$\frac{2J}{L^2},$$

and,

$$\frac{M}{2}.$$

Note that M, above, is the total mass of the shaft. For the case of a round shaft, the moment of inertia, J, about the center of gravity, is

$$\frac{1}{12}\ ML^2$$

Thus, the first eigenvalue reduces to $\frac{M}{6}$.

The larger of the two, one-half the total mass, is used to correctly size the bearings and electronics. The electronics and actuators must have sufficient power/size to accelerate the shaft to follow the housing during launch conditions and not saturate.

For the case of very unevenly distributed masses, as is only the case in the displacer, (where because of the cantilevered support of the regenerator and displacer cap, the center of gravity is closer to the cold end bearing) a simple and conservative estimate would be to use the total mass at the "cold end" bearing. Table 6-4 summarizes the effective masses used in the bearing analysis.

TABLE 6-4. Effective Bearing Mass.

Displacer	1 kg (M)
Piston	2.5 kg ($\sim\frac{M}{2}$)
Counterbalance	3 kg ($\sim\frac{M}{2}$)

The eigen value relationship provided in the earlier report [7] for a nonsymmetric shaft is incorrect, and will not be given here in corrected form because it adds little to the system analysis, understanding, or design of the bearings. The system dynamics within the frequency range of interest are dominated by damping forces (see next section) and not inertial effects. The effective mass is of concern because the load specifications are written in terms of acceleration specifications of the cooler housing. As the housing accelerates, the shaft should follow and the bearing system is to maintain the required gap to eliminate any chance of damage. The bearings apply a force sufficient to accelerate the shaft and follow the motion of the housing. These housing accelerations are greatest at the natural frequency of the isolation mount, about 7 Hz.

The analysis relating the shaft motion, x_s, to housing displacement, x_i, is exactly analogous to the analysis of a seismograph and can be written as:

$$\frac{x_s}{x_h} = \frac{ms^2}{SDK},$$

where,

SDK = shaft dynamics = $ms^2 + bs + K_e$ and, K_e = effective magnetic spring constant.

In the frequency range of interest (7 Hz), the inertial term (ms^2) and damping term (Bs) are negligible in comparison to K_e, and the above can be simplified to,

$$\frac{x_s}{x_h} = \frac{Ms^2}{K_e} ,$$

where, M = mass of suspended shaft.

As K_e gets very large, x_s/x_h is unity and the shaft exactly follows the housing. Well below the natural frequency of the magnetic bearing/shaft, the shaft motion follows the housing motion through the effective magnetic spring stiffness. Thus, what remains is to determine K_e of the bearing system. In order to the this, not only the actuator dynamics but also the total bearing system dynamics must also be modeled. The following sections deal with the dynamic modeling of each component in the magnetic bearings and finally the total system modeling.

(3) Damping-Squeeze Film and Magnetic Bearing

As the shaft moves in the radial direction, additional non-conservative forces act on the shaft. These forces are modeled classically as "damping" forces and can be related to the relative velocity between the shaft and the housing. The damping forces come from two sources, gas dynamics and eddy currents. It will be shown that gas damping is far greater than eddy-current damping in the frequency range of interest.

Gas Damping

The gas force "or squeeze film damping" on a radially oscillating, infinitely long shaft/bore is well known. The analysis is given in Cameron [8], and only the result is given below,

$$B = 12\ \pi\ L\ \mu\ (\frac{R}{c})^3$$

where,

$$B \equiv \frac{F}{\omega x} ,$$ with,

F = force on shaft.
μ = gas viscosity (dynamic, or absolute)
R = radius of shaft.
c = gas film clearance or radial gap between shaft and bore.
ω = oscillation frequency.
x = shaft displacement.

This analysis assumes that the eccentricity is small or,

$$(1+\frac{x}{g})^{1.5} \sim 1.0$$

The bearings, however, are not infinitely long and using the above relationship yield non-conservative results. A more accurate representation of the gas damping forces for the case of finite

bearings has been developed by Hays [9], and summarized in Cameron [8]. It is possible to modify the infinite bearing relationship above to account for the finite length of the squeeze film bearing. The Cameron/Hays data has been extracted and rearranged for the case of very small eccentricity.

The results of such simplifications yield the damping curve shown in Figure 6-5, where γ is a function of the specific L/D ratio of the bearing. The damping factor, B, is then given by:

$$B = 2\gamma L \mu \left(\frac{R}{c}\right)^3.$$

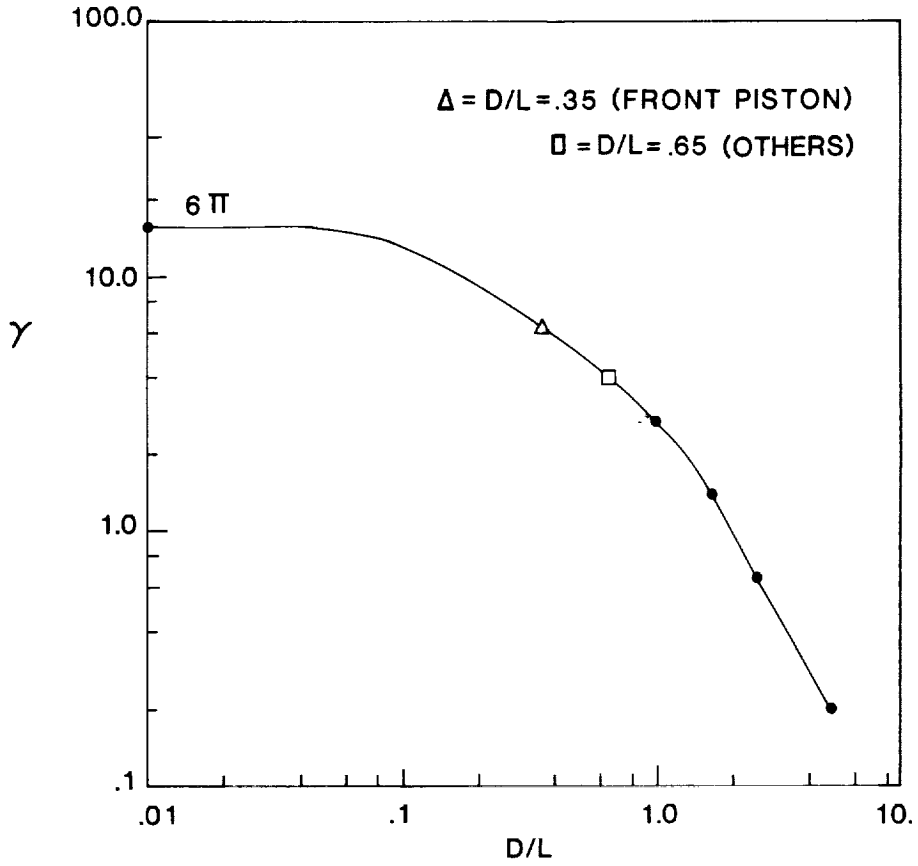

Figure 6-5. Squeeze-film damping factor correction, γ, for journal bearings of finite length.

The above relationship needs some explanation. The original Hays data was derived for the case of one-half of a journal bearing. Hays stated that if the change in pressure above the shaft can be ignored, then his results are valid for the full journal case. We take exception to that and use the factor-of-two to yield equivalent results for the infinitely long bearing case.

Table 6-5 below summarizes the γ factor and "B", used in the bearing analysis based on the above relationship.

TABLE 6-5. Damping Factors.

	D/L	2γ	B	B/M
	--	--	(N-s/M)	(rad , (kHz)
Displacer	0.65	8.0	4000.	4000, (.64)
Piston (back)	0.65	8.0	32000.	12800, (2)
Piston (front)	0.35	12.0	90000.	36000, (5.7)
Counterbalance	0.65	8.0	84000.	28000, (4.5)

where,
$c = 18.8 \times 10^{-6}$ m
$\mu = 18 \times 10^{-6}$ (for both N_2 and He in the pressure range of interest)

There is, however, still quite a bit of uncertainty in making predictions using these values. The damping coefficients are highly nonlinear; furthermore, a superposition of motions resulting from harmonics in force (in the radial direction) is NOT valid. Thus, the resulting motions predicted for a case involving large spectrum of displacements (or velocities) is only approximate.

Also, the above analysis does not incorporate the effect of reciprocation of the shaft on the gas damping forces. Thus, the boundary conditions used in Hays analyses are different from that actually found in the cooler, and the predictions based on these relationships should only be considered approximate. Nevertheless, it is important to note the sensitivity of system behavior to these gas damping values. A comparison of system response for different gas damping values is given in Section 6.3.3.

The column labeled "B/M" in Table 6-4 represents the frequency in which the inertial forces equal the gas damping forces, or,

$$m s^2 = B s$$

or,

$$s = \frac{B}{M}$$

Thus, for frequencies below B/M, gas damping dominates displacement and for frequencies above, the inertial terms are greater. An ANSYS simulation of the motion of the piston and displacer shaft subjected to a sinusoidal force is given in Figures 6-6. At the damping values of interest, the shaft response is overdamped, and there is the characteristic 20 dB/decade (1/s) rolloff. For lightly damped shafts, the rolloff is 40 dB/decade as would be expected for a purely inertial system ($1/s^2$). The phase curves are also presented. The location of the large changes in magnitude and phase correspond to resonances/antiresonances in the shaft/housing system. This is discussed in more detail in Section 6.3.2.

Eddy Current Damping

The magnetic damping forces are much smaller than the gas damping forces. An estimate of the magnetic damping magnitude is given below. An "order of magnitude" analysis that maximizes the effect of damping produces the following relationship for damping factor, C_d,

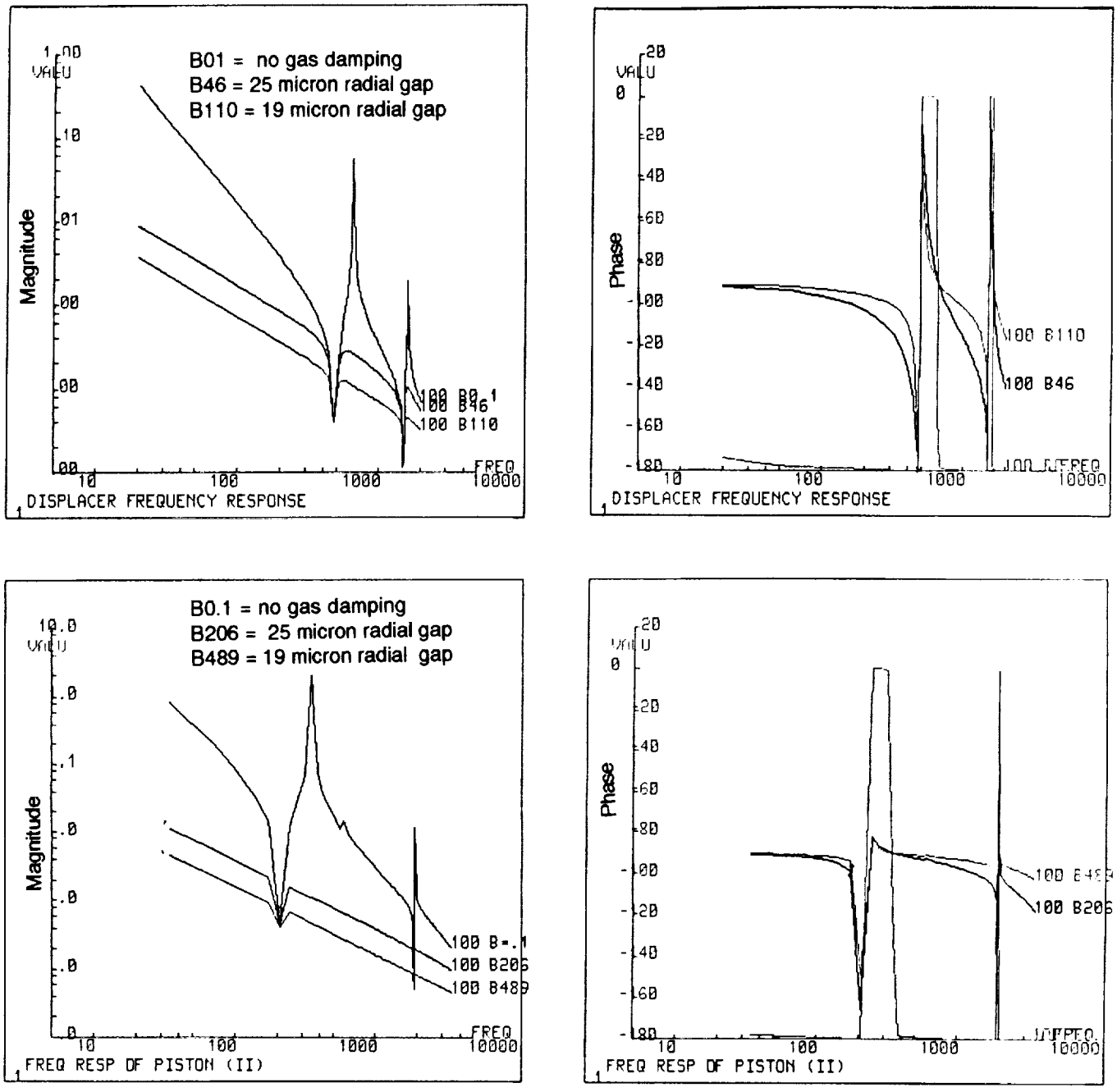

Figure 6-6. ANSYS simulation of piston and displacer shaft radial displacement as a function of frequency for different damping factors.

$$C_d = \frac{t(\pi \hat{B} D)^2}{\rho}$$

t = armature thickness
D = bearing surface diameter (shaft or armature diameter).

$\hat{B}$ = flux density
ρ = armature resistivity (40 μ-ohm-cm, typical).

Using values representative of the the displacer,

$$C_d = \frac{.004(\pi \, x \, .03)^2}{40 \, x \, 10^{-8}} \sim 10 \, N - s/m,$$

which is far lower than the gas damping coefficient, and thus magnetic damping can be ignored in comparison to gas damping forces.

6.3.2 System Dynamics

(1) Mechanical Behavior of Bearing System.

It can be shown that the the equivalent stiffness of the electromagnetic bearing including gas damping can be described as:

$$K_e = Mag(K_s G_c K_{ic} K_a + SD),$$

where, K_e , the effective stiffness, relates the motion of the shaft to external disturbance forces. For systems with high gain, the first group of terms ($K_s K_u K_i K_a G$) are much greater than the second term resulting in the following approximation:

$$K_e \sim Mag(K_s G_c K_{ic} K_a),$$

where,

K_s = transfer function of position sensor (V/m)
K_{ic} = " " " bearing force to current (N/A)
K_a = " " " current amplifier (A/V)
G_c = " " " compensator (V/V)
$SD = (ms^2 + bs - K_u) \sim K_u$ at DC.

In this specific case, G_c is a classical "lag-lead" circuit. This type of compensator increases stiffness at low (dc to launch) frequencies and improves phase margins at the gain crossover point (see next section). The compensator time constants are fine-adjusted to provide as large a sub-20 Hz stiffness as possible while maintaining classical servosystem stability requirements.

The following sections describe the dynamic behavior, i.e, the transfer function relationships, for the components in the magnetic bearing system. The component with the most influential dynamics is the bearing actuator because it has, by far, the most narrow bandwidth.

(2) Magnetic-Bearing Actuator Dynamics

The magnetic field within the bearings is a highly complex and non-linear function of winding current. In fact, due to magnetic material hysteresis, it is not a single-valued function but is, to a small degree, history dependent. Nevertheless, given the earlier engineering assumptions, it is possible to approximate the frequency-dependent nature of the magnetic bearings.

We know that eddy currents lie well within the desired bandwidth by considering the magnetic field skin depth for an "open" magnetic circuit and comparing it to the dimensions of the pole pieces. To the first order, the depth of penetration is given by

$$d = \frac{1}{(\pi f \sigma \mu)^{1/2}}$$

where,

σ = conductivity = 1/resistivity = (ohm-m)$^{-1}$
f = frequency (Hz)
μ = absolute permeability (H/m)
H = volt-second/Ampere.

One can rearrange the above to determine the "limiting frequency", or the frequency at which eddy currents reduce the flux in the core of a given geometry by 3 dB:

$$\phi_{limit} = \frac{\rho}{\pi \mu d^2}$$

For system with air gaps, one should use the "effective" or "sheared permeability" [10],

$$\mu = \mu_o \left(\frac{l}{\mu r} + \frac{l_{gap}}{l_{iron}} \right)$$

Substituting representative values for the widest bandwidth actuator (displacer):

ρ= 40 x 10^{-8} (ohm-m)
d = armature thickness = 0.005 m
μr = relative permeability = 10,000
μ_o = absolute permeability of air = 1.25 x 10^{-6} H/m
l_{gap}/l_{iron} = 0.01
$\mu \sim \mu_o \, l_{iron} \sim$ 1.25 x 10^{-4}, *resulting in*
$f_{limit} \sim$ 40 Hz,

indicating that the eddy currents are well within the bandwidth of the control loop.

One way of viewing this is that the effective area, A, given in the earlier force constant relationships is getting smaller as the frequency increases. It is conventional to consider reduction in flux as frequency dependent, proportional somewhere between the first and one-half power of frequency (in terms of control theory, a 1/s and $1/\sqrt{s}$ dependency).

It was shown above that the force constant is directly proportional to the inductance. Thus by knowing (or measuring) the frequency dependence of inductance, one should obtain an accurate measure of the frequency dependency of the motor force constant to facilitate control loop analysis.

Experiments were carried out using flat versions of the piston pole piece to measure the frequency dependency of the force constant. A very stiff piezo-force transducer and measurement system was used. Thus there was no relative motion between the pole piece, and the target and gas damping normally found in the bearing system was not present. Also, the inductance vs. frequency was measured for the the same piston bearing. Figure 6-7 summarizes the results. By knowing the frequency characteristics of inductance, one can obtain precise measure of dynamic behavior of the force constant.

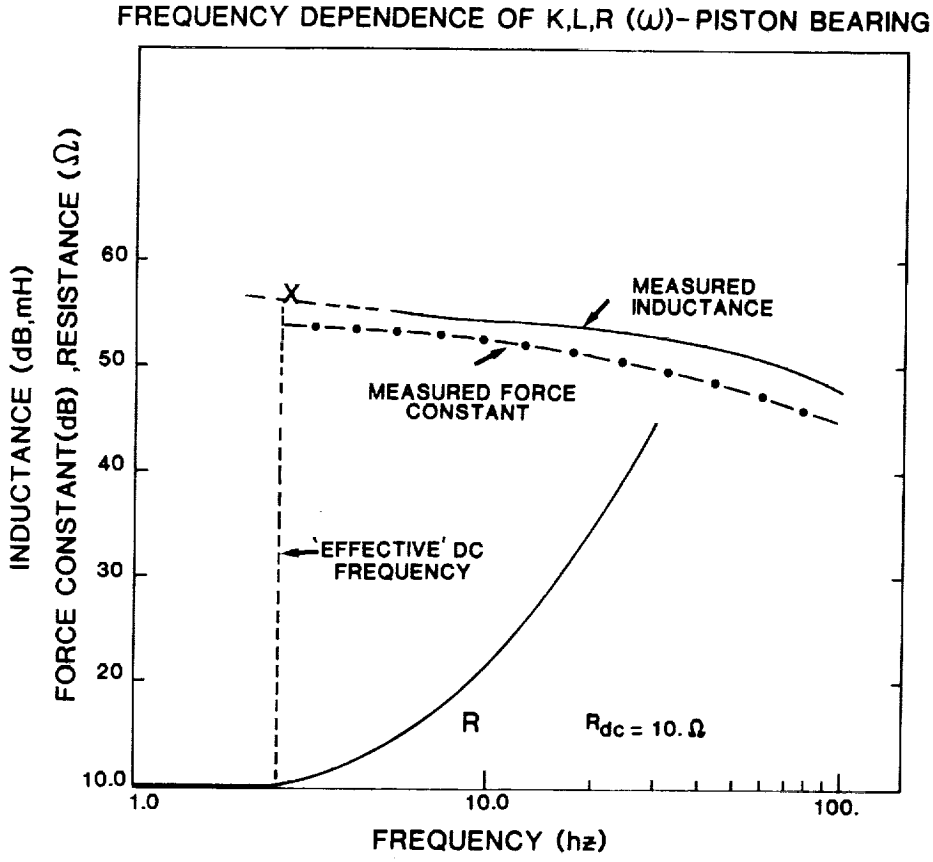

Figure 6-7. Frequency dependence of K,L,R of piston bearing.

Based on these inductance measurements, the effective dynamic properties of the magnetic bearings can be modelled by the following relationship:

$$F_b = \frac{F_b}{(1 + \tau s)^{1/2}}$$

where,

τ = effective time constant for each bearing type. The effective time constants, τ, are summarized in Table 6-6.

At a frequency corresponding to one-half the time constant, the magnitude has dropped off by 3 db.

TABLE 6-6. Effective Time Constants for Each Bearing Type.

Bearing Type	Time Constant (s)	-3dB Frequency (Hz)
Displacer	0.0035	90
Piston	0.011	30
Counterbalance	0.063	5

These "break frequencies" or time constants are again approximate. The magnitude and phase behavior are well represented by this "half-pole" model in the frequency range from dc to twice the break frequency. A more complete "transformer" model of the bearing would produce more precise results in particular at the higher frequencies; nevertheless, this is adequate for overall bearing system analysis and design. This frequency-dependent behavior of the bearings was particularly bothersome in the current loop compensation.

(3) Optical Radial Position Sensor Dynamics

The optical position sensor is described in detail in Section 6.4. The sensor has a "flat response" and introduces no significant phase within the frequency range of interest (0-200 Hz). There is only a single pole filter in the optical position sensor output at about 500 Hz, and thus the response of the optical sensor system can be adequately represented by a simple constant term, K_s, where subscript s denotes "sensor". The electronics are adjusted such that peak-to-peak displacements within the bore produce a 10 V output. Thus, the optical position sensor transfer function element is

$$K_s = 0.26 \times 10^6 \text{ V/m.}$$

This extremely large signal sensitivity is due to the small gap and that the sensor surface is flush within the housing bore -- the sensor does not have to transmit through a window which would have caused a large dc offset and decreased the signal-to-noise as in the case of the organic-based eddy current sensors used in the Engineering Model cooler.

(4) Shaft Dynamics

A classical control system model was used in the early design phases to ensure that all system components would meet the desired levels of performance. The shafts though rigid, nevertheless have a finite radial stiffness and stability. At sufficiently high frequencies, it is possible to excite the shafts/housings to their mechanical resonances. The shaft/housing must be analyzed in unison in order to get a correct picture of these resonances.

Rather than the resonances displayed in the earlier report, the displacer housing actually limits the displacer bandwidth and not the shaft as originally thought! An ANSYS simulation was performed on the displacer and piston shaft/housing systems. Unlike the displacer housing, the piston has an anti-resonance followed by a resonance. The gas damping results in an overdamped system. The anti-resonance must be avoided in our classic control loop methodology because of the very large change in phase (90°) at that point - this would lead to system instability. Thus, knowing the "pinning" frequency that we must avoid, a rough estimate of system stiffness can be made. The predicted antiresonances/resonances were quite close to that actually measured in the cooler. Table 6-7 summarizes the predicted antiresonance/resonance points of the piston, displacer, and displacer housing.

TABLE 6-7. System Resonances and Bounds on the OLTF.

	Antiresonance	Resonance	7 Hz Pinning OLTF
Piston	400	740	35 dB
Piston Housing	None	2100	N/A
Displacer	1000	1600	N/A
Displacer Housing	None	300	32 dB

Based on a 20 dB/decade rolloff, one can estimate the available gain (and thus the stiffness) at 7 Hz, the launch frequency. Given these assumptions, the available gain (in dB) is :

$$20_{log}(f_{pin}/f_{mount}).$$

where,

f_{pin} = pinning or limit frequency
f_{mount} = mount isolation frequency.

From the design relationships above, it is possible to deduce the effective magnetic bearing stiffness from the open-loop transfer function (OLTF):

$$K_e = SD\,(1 + OLTF)$$

where, SD = shaft dynamics, and we make use of the approximation for high-gain systems,

$1 + OLTF \sim OLTF$, thus

$K_e \sim SD\ OLTF$. (which is the open-loop gain with unity plant transfer function, or as shown earlier, $Mag(K_s G_c K_{ic} K_a)$)

Results for the displacer and piston are given in Table 6-6. (Note that in this simplified analysis, the high frequency characteristics of the bearing actuator, driver and sensor are ignored). Some compensation (lag) is added to increase the lower frequency stiffness, and some lead is added near the crossover frequency to increase phase margin.

6.3.3 System Predictions and Measurements

The measured open-loop response of the magnetic bearings is discussed in this section. Figures 6-8a through 6-8c are the measured OLTF for each type of bearing in the cooler. The magnitude of the OLTF at 7 Hz is noted, and the corresponding stiffness is determined through the relationships presented earlier. (The low frequency (dc) 5 Hz data is not valid for the counterbalance).

Table 6-8 summarizes the measured open-loop transfer functions at dc, 7 Hz and 20 Hz (displacer only). The high stiffness at low frequencies is derived from the integral function of the control system (lag component of the compensator).

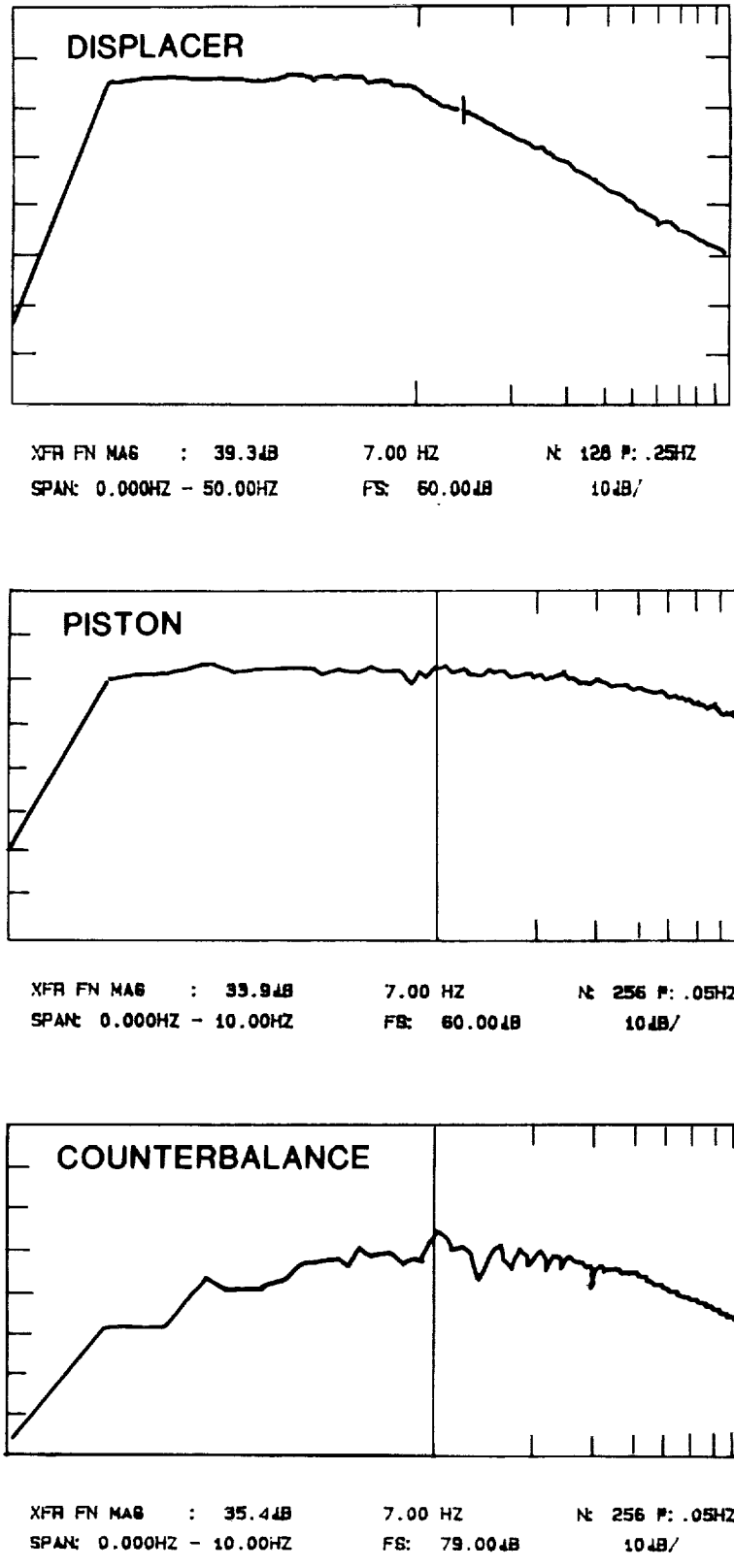

Figure 6-8. Open-loop transfer function (OLTF) measurements of the displacer, piston, and counterbalance bearings.

As noted earlier, the gas damping has a profound effect on system dynamics and hence the available bearing stiffness. The bearing stiffness at higher frequencies (typically greater than 10 Hz) is a strong function of gas damping values. To bound the analysis, two values of gas damping coefficients were used in system predictions for the displacer. Results of the analysis are presented in Figure 6-9. The "B/2" curve would be the value predicted based on the 1/2 journal bearing given by Hays. The "B" curve is the result for the nominal damping value given by equation in Section 6.3.1(3) for a finite bearing.

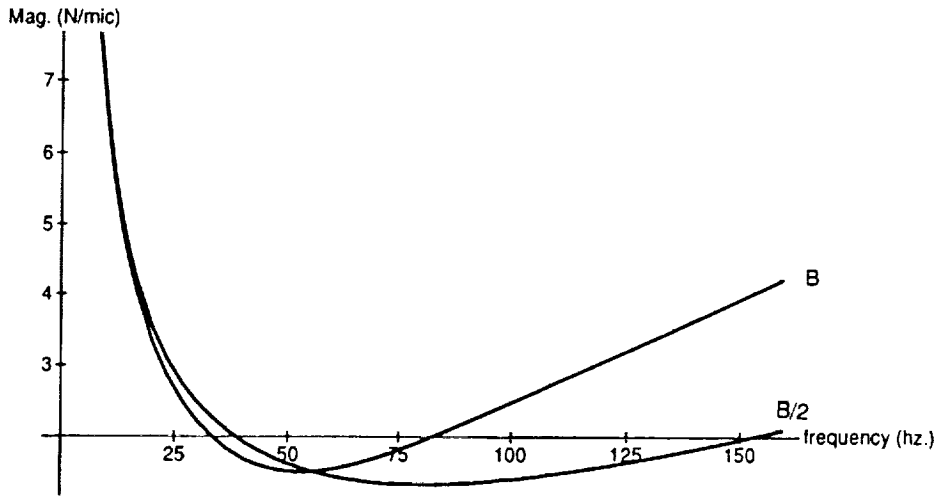

Figure 6-9. Effective displacer bearing stiffness as a function of frequency for two values of damping coefficient, B.

Though the stiffness of the piston and displacer bearings at 7 Hz is not strongly affected by the value of B, the phase response is. Figure 6-10 compares the open-loop transfer response without any additional phase compensation (G_c=K) of the piston for two cases of gas damping. Both the low and high frequency phase angles are very sensitive to gas damping. In fact, this phase response limits the size of the lag/integration at low frequencies and the bandwidth at high frequencies.

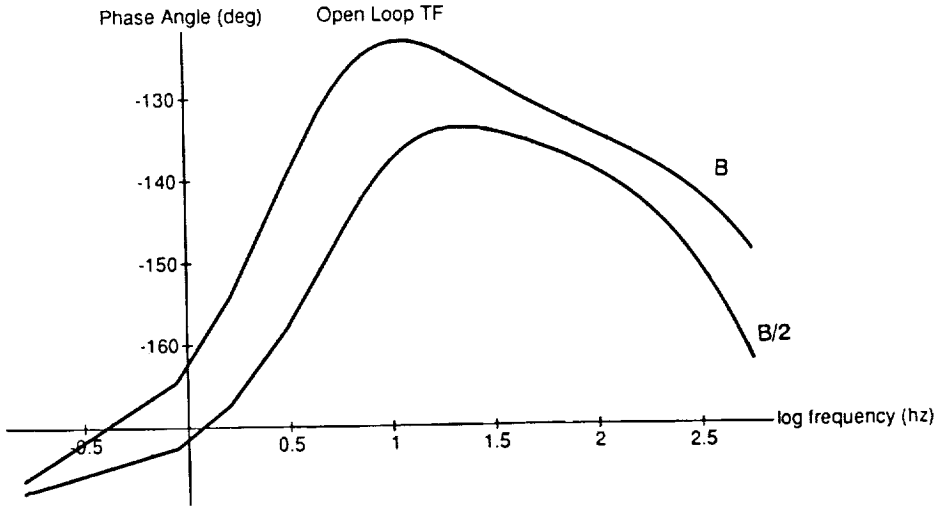

Figure 6-10. Comparison of phase of open-loop transfer function (OLTF) of piston bearing without compensation for two values of damping coefficient, B.

TABLE 6-8: Measured Open-Loop Transfer Function at Specific Frequencies and Calculated Bearing Stiffness.

	Measured dc		Measured 7Hz		Required	Measured 20 Hz	
	OLTF (dB)	Ke (N/u)	OLTF (dB)	Ke (N/u)	Kreq (N/u)*	OLTF (dB)	Ke(N/u)
Displacer (Rear)	47	20	39	9	8	24	3
Piston (Rear)	50	110	34	60	20		
Counterbalance			37	25-50	24		

(* Based on a 50% radial displacement and a 8 G load applied at 7 Hz).

The large range for stiffness presented in the counterbalance data above is a result of the uncertainty of the gas damping value to within a factor of two. Because of the very large B/M ratio, the gas forces play a larger role at an earlier frequency than in the displacer and piston. At 7 Hz, the effective stiffness is hardly different for a factor of two change in gas damping for the displacer and piston. This is not the case in the counterbalance. In any case, even taking the conservative (low) value for stiffness, all bearings do meet launch requirements.

Figure 6-11 compares the measured OLTF for a displacer in the cooler and the predicted OLTF for two different damping values.

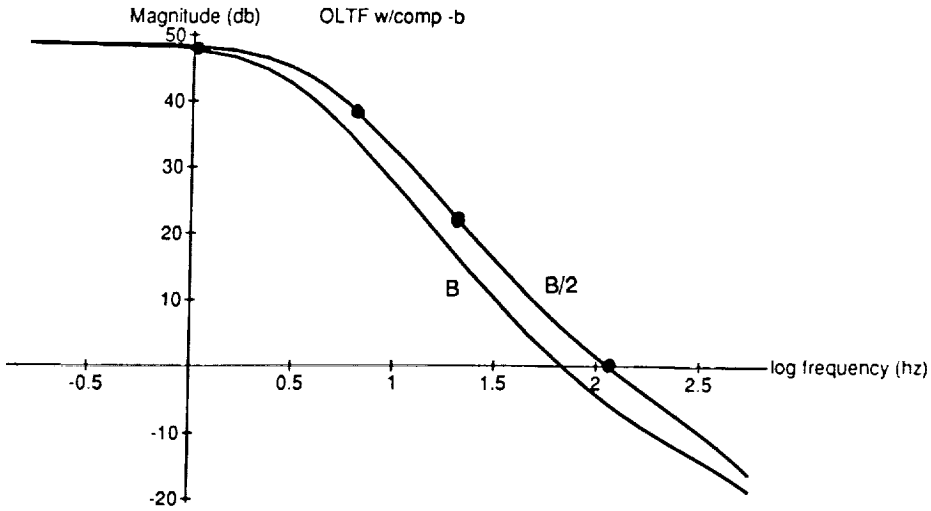

Figure 6-11. Measured and predicted behavior of the open-loop transfer function (OLTF) of displacer bearing in the cooler for two different values of the gas damping factor, B.

The test model described in Section 6.5.2 was used to verify this analysis. Even though the test displacer was operated in air, the gas damping is nearly exactly the same as in the cooler. The shaft dynamics, however, were different. Also, the optical sensors had better signal-to-noise in the test displacer. Thus, the high frequency behavior of the test shaft was not identical to that of the cooler. As such, a somewhat different compensation circuit was used that could not be used in the cooler - primarily because of very low gain and phase margins. Nevertheless, the system on the test bench was stable and produced a very high stiffness bearing. The pure lag compensator employed in the test fixture, while providing superb low frequency stiffness, added no phase lead at high frequencies. This resulted in only a marginally stable system, and thus could not be used in the cooler.

Figure 6-12 compares the predicted total effective stiffness and the measured stiffness data. As can be seen, the agreement is quite good. Note in particular the poor "high frequency" stiffness of the loop. This is because the compensator, Gc, is "rolling off" along with the mass dynamics. Thus, high frequency (40 Hz) disturbances are not really rejected by the bearing control loop and nearly all the stiffness at these high frequencies comes from the gas damping and inertial terms.

6.4 Optical Radial Position Sensors

6.4.1 Introduction

This section describes the theory and design underlying a position sensor constructed with optical fibers. The sensor was built for measuring the gap between the piston and housing of a Stirling cycle cryogenic refrigerator. In the sensor, light is transmitted through a bundle of fibers onto the

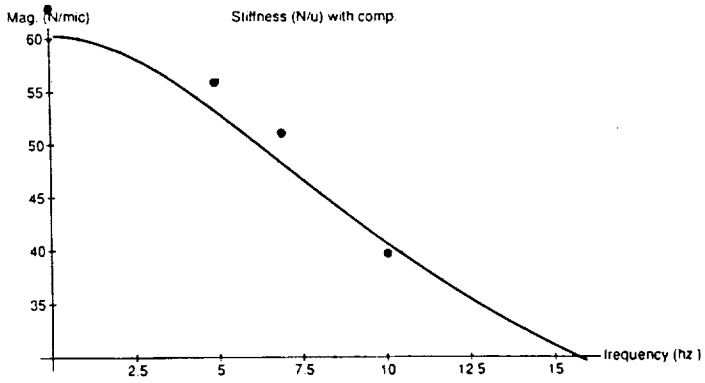

Figure 6-12a. Detail of low frequency behavior on linear frequency scale.

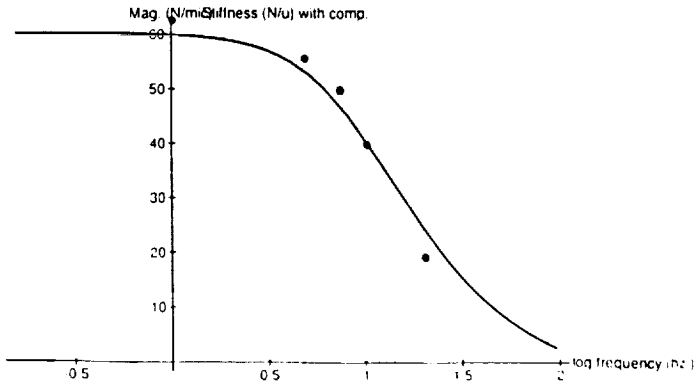

Figure 6-12b. Dynamic behavior of the stiffness of displacer test bearing over a wider frequency range (log frequency scale)

Figure 6-12. Comparison between measured and predicted behavior of displacer stiffness in bearing test fixture. (Gas damping value B = 4000 Ns/m).

shaft. The reflected light is received by another set of fibers and is finally measured by a photo transistor. The principle of operation of intensity modulated, fiber-optic displacement sensors is well documented, and the original patent is attributed to Kissinger [11]. Cook and Hamm [12] described a mathematical model used to calculate received light power versus target displacement, and calculated parameters such as the displacement detection limit. Hoogenboom and others [13] developed an empirical model of received intensity for a pair of fibers, and used it to calculate fiber bundle response. Johnson [14] reviews the types of fiber sensors used in practice. There are several trade-journal reviews, such as [15], of available sensors, the commercial sensors being typically used in on/off type applications such as object detection.

Sensor requirements for the cryogenic refrigerator magnetic bearings are related to signal characteristics and mechanics. The sensor needs a range of at least 50μm, resolution better than 1 μm, high linearity, high bandwidth, and low temperature coefficient. As the 19μm gap between the piston and housing served as a gas seal for the refrigerator pistons, the front end of the sensor has

to be integrated flush with the bore of the piston housing. It also has to be hermetic and present no organic materials such as epoxies into the helium workspace of the refrigerator. Long-life, maintenance-free operation of 5 years was desired for the refrigerator.

Section 6.4.2 outlines the principle of operation of intensity-based, fiber-optic, displacement sensors. In Section 6.4.3, a model is described for calculating the fiber pair response for an arbitrary inter-fiber distance. Responses for several bundle geometries are calculated and compared to experiment. Section 6.4.4 describes the sensor developed for magnetic bearing control and its performance. One limitation of intensity-based sensing schemes is that they are sensitive to changes in target reflectivity.

6.4.2. Principle of Operation

Consider the fiber and specular target arrangement shown in Figure 6-13. The distance between the illuminator fiber and receiver fiber 1 is d_{f1}. Light from an infrared LED is conveyed by the illuminator fiber on to the target, forming a circular pool of light on it. A portion of the reflected

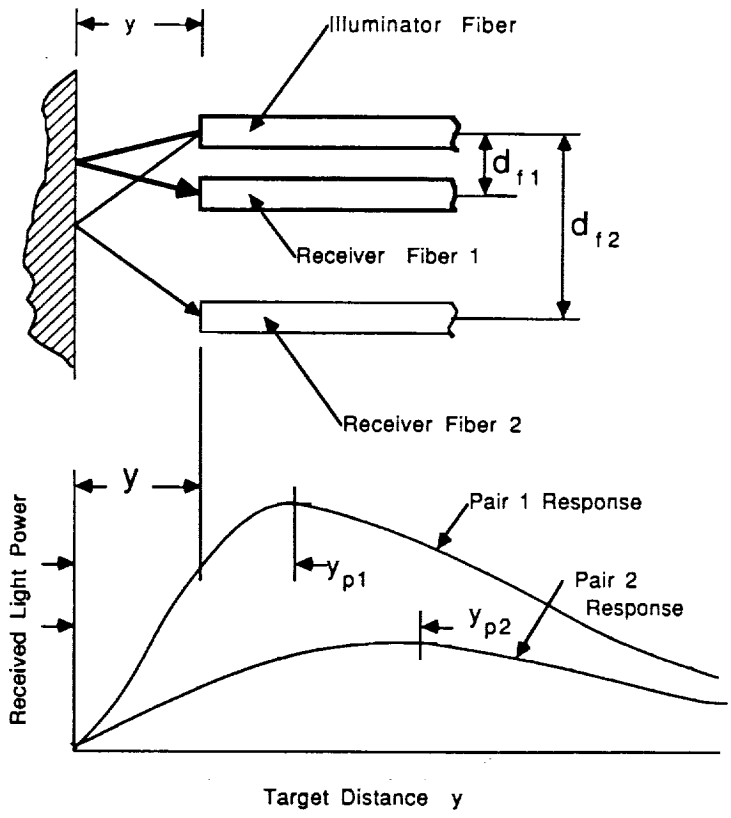

Figure 6-13. Fiber pair response.

light couples into the receiver fiber, and is measured by a silicon phototransistor at the other end of the fiber. If the target distance y is zero, all the light is reflected back into the illuminator fiber and the received signal would be zero. As y increases, more light is coupled into the receiver fiber, up to a distance y_{p1} where the intensity reaches a peak. Beyond this, the inverse square law takes effect

and the received signal falls off as shown in the figure. If the inter-fiber distance is increased to d_{f2}, the magnitude of the peak would be smaller, and the peak distance y_{p2} would be larger than y_{p1}, as shown in the figure.

Illuminator and receiver fibers can be arranged into bundle geometries, such as shown in Figure 6-14. Each illuminator couples into all receivers, the distinct pair response being determined by the particular inter-fiber distance d_{fi}. With N_i illuminators and N_r receivers, there are N_i x N_r individual responses. A bundle can consist from two to thousands of fibers. The sensor response at a particular y would be the sum of all the individual pair responses, as the light energy is scalar. Three bundle types are shown: randomized, semi-circular, and dual, together with typical responses for 1mm bundles of 25 μm fibers. Sensor design consists of determining appropriate fiber numerical apertures, fiber diameters, and bundle geometries to obtain the desired response.

6.4.3 Model of Optical Sensor Response

(1) Fiber Pair Response

An optical fiber consists of a core of glass with refractive index n_1 surrounded by a cladding of smaller refractive index n_2. The *numerical aperture* of the fiber, which indicates its light transmitting capability, is given by $NA = \sin\theta_M = \sqrt{n_1^2 - n_2^2}$. Light which enters the fiber within a semi-cone angle of θ_M is conveyed to the other end of the fiber by total internal reflection, with negligible losses. Light entering outside of this cone is lost; also, if a ray enters at an angle θ_i, it exits the fiber at the same angle, considering in the first order a meridional (in any plane containing the fiber axis) ray entering a straight fiber.

A gallium aluminum arsenide infrared light-emitting-diode (e.g., TRW OP260SL, wavelength 875nm) is a typical light source for fiber optic sensors. The output radiant flux density $I_{\theta\,i}$ (W/m^2) of this LED versus axis angle theta is shown in Figure 6-15. The output from an optical fiber (when illuminated by the LED) would have a similar characteristic intensity vs. axis angle, provided the numerical aperture of the fiber was greater than that of the diode. The output of the fiber in any case can be measured by scanning a phototransistor at several angles with respect to the fiber. This output characteristic is important and determines fiber pair response.

An assumption is made here that radiation pattern over fiber output surface is uniform. Thus, a small element dS located at any position on the fiber surface has a similar radiation pattern $I_{\theta i}$ as the overall fiber itself.

Consider the fiber pair offset a height y from the target (Figure 6-16). The target is considered to be a specular reflector, and in order to simplify the ray optics, we construct a virtual image of the receiver fiber at an equal height below the target surface. This virtual image can be used to calculate the power coupled from the illuminator fiber into the receiver fiber. The radiant flux density at the receiver fiber plane, due to a small element d S_i on the illuminator fiber, is circularly symmetric about the normal through d S_i and is given (see Figure 6-16) by the law of radiative interchange:

$$I_i(r) = \frac{kI\theta_i dS_i \cos\theta}{(2y)^2 + (r)^2} \qquad (2)$$

where k is a constant depending upon target reflectivity.

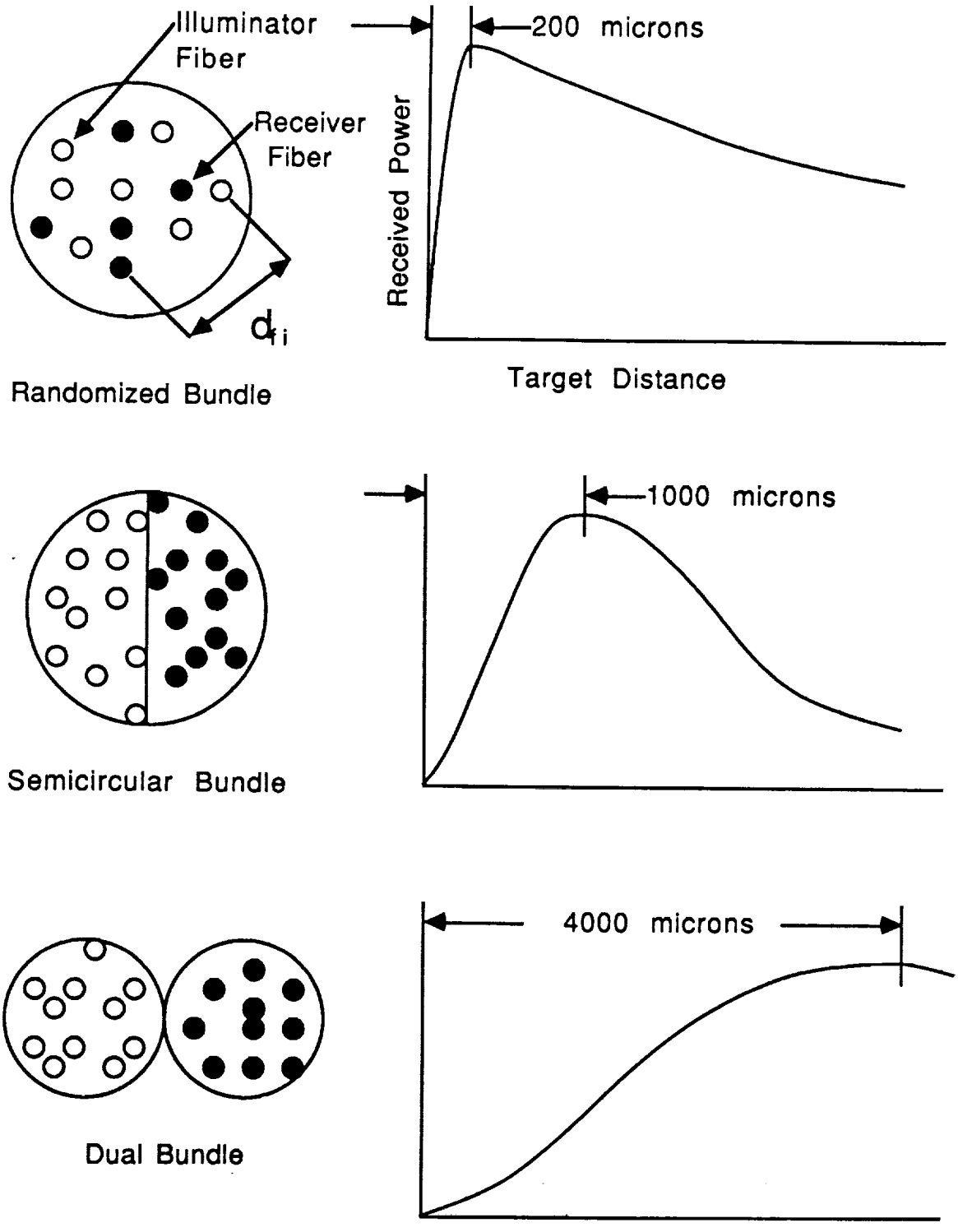

Figure 6-14. Some fiber bundles and their responses.

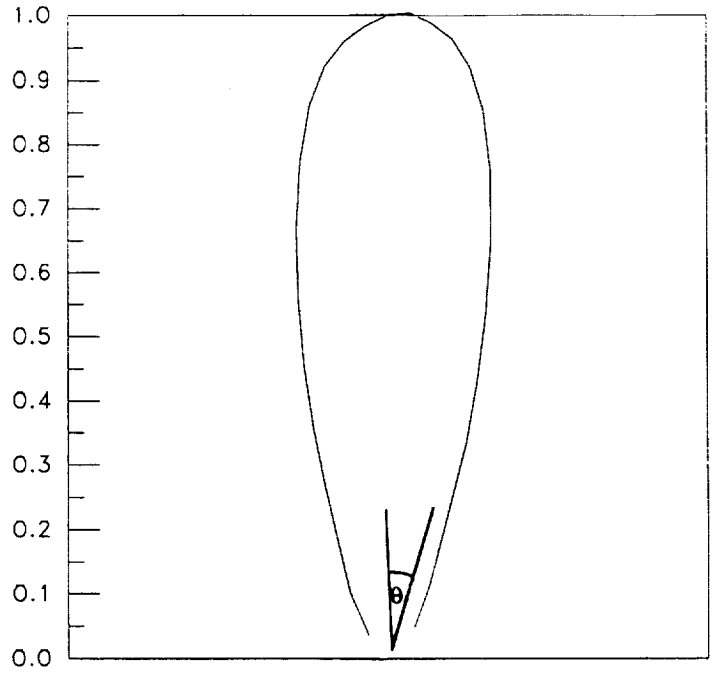

Figure 6-15. Relative radiant flux density of OP260 IR LED.

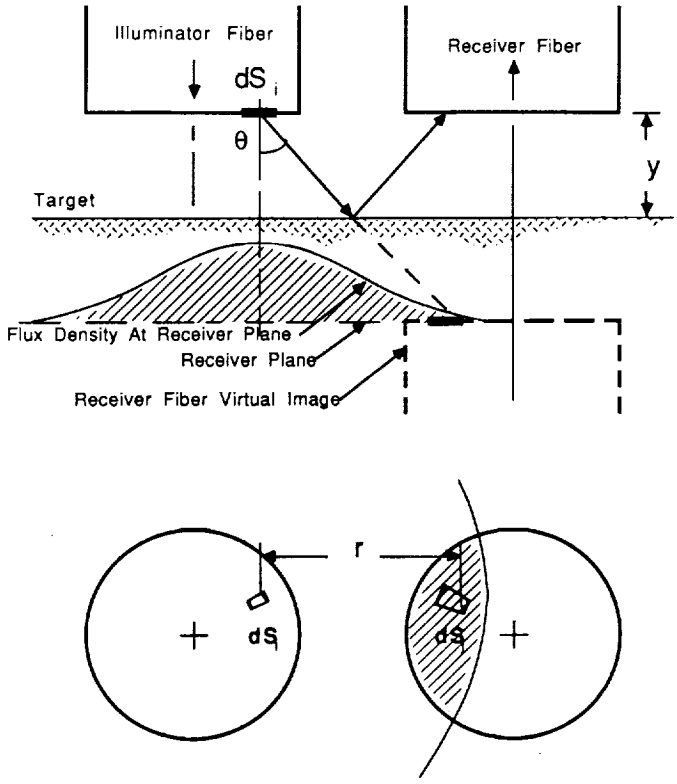

Figure 6-16. Calculation of fiber pair response.

The flux entering an element d S_j on the receiver causes a photodetector signal of

$$dP_{ij} = I_i(r)dS_j I_{\theta r} \tag{2}$$

where the distance r is the projection on the receiver plane of the line joining the two elements dS_i and d S_j, and $I_q r$ is the sensitivity of the photodetector vs. angle.

The total photodetector signal is given by

$$P = \sum_{ij} dP \tag{3}$$

Note that not all elements on the receiver fiber "see" the illuminating fiber. In Figure 6-16 only elements within the shaded area surrounding element d S_j receive light energy from d S_i. Also, no attempt is made to calculate the absolute power received by the phototransistor, and proportional factors such as the reflection coefficient of the target, reflection losses at fiber-air interfaces, absolute power output of the LED are all canceled by eventually scaling the peak sensor response to a unit value.

The above method can be used to calculate the response $P(d_{fi,m}, y_n)$ of a fiber pair with an inter-fiber distance of $d_{fi,m}$ at a target distance of y_n. Figure 6-17 consists of fiber pair responses of 25μm fibers at several inter-fiber distances.

(2) Sensor Response

Due to the number of nested summations, the above calculation (Eq. 3) of fiber pair response is time consuming. However, given a specific IR source and fiber combination, this need be done only once to obtain data for a range of fiber separations. In the present study, both fiber separations and target distances are increased in a geometric ratio to obtain an efficient database.

A sensor design geometry, e.g., of a coaxial sensor, consists of coordinates of the individual illuminator and receiver fibers. The inter-fiber distance is calculated for every fiber pair, and pair response determined by interpolation from the above database. The sum of pair responses at a particular y_n is the sensor response.

(3) Comparison With Experiment

Figure 6-18 compares sensor responses obtained using the above model and experimental measurements. Figure 6-18(a) shows the output of a 1mm randomized bundle consisting of 25 μm fibers. The measured values are shifted about 10μm to the right of the model, and this shift occurs at zero displacement. Backlash from the micrometer table is a likely cause of this shift. Figure 6-18(b) is the response of a 'dual' sensor, the individual bundles being 1mm in diameter and spaced 1.5mm apart, again constructed with 25μm fibers. Note that backlash would not show in this figure as the scale is much larger. In both cases we see that the model tracks measured values reasonably. A prediction of the general trend is thus possible, but the sensor has to be calibrated after construction in order to obtain the absolute value of the peak response and the slope of the linear regions.

6.4.4. Magnetic Bearing Sensor Design

Optical fibers by their nature offer the facility of fabricating sensors using various interesting topologies. The sensor developed for magnetic bearing position measurement is shown in Figure 6-19.

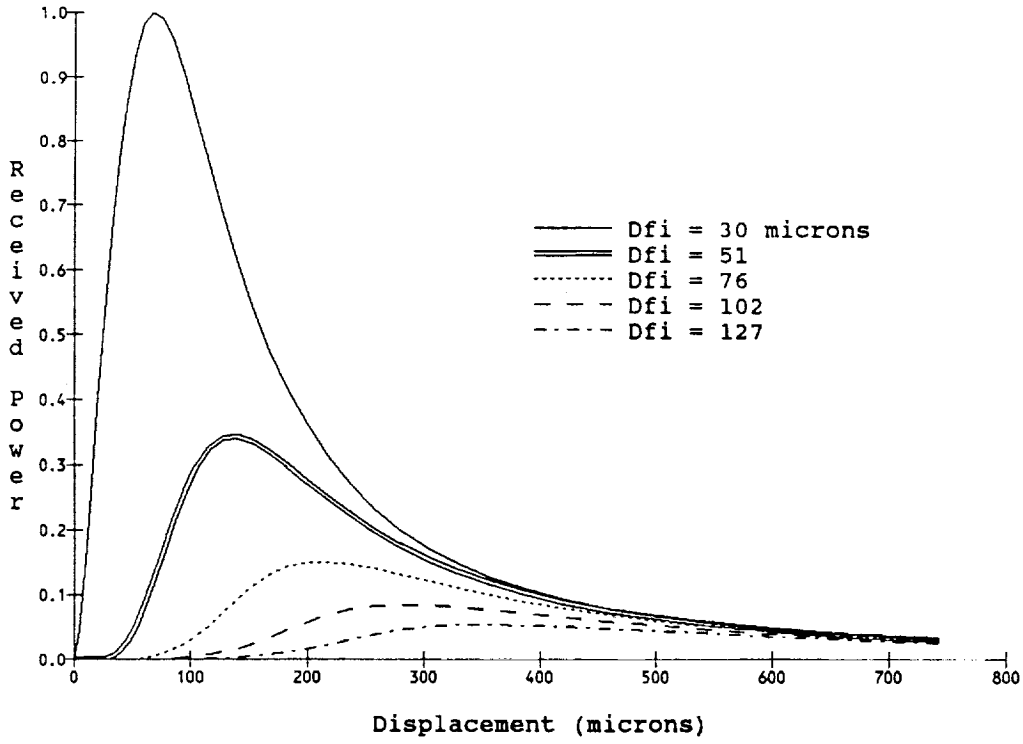

Figure 6-17. Fiber pair responses for several inter-fiber distances.

Light is conveyed into the pressurized housing by means of the *tips*. A tip consists of a bundle of fused glass fibers -- fibers which have been squeezed at a high temperature and pressure so that they are fused together into a solid leak-tight rod -- metallized by sputtering and soldered inside a cupronickel sleeve. The tip is then soldered into the housing using a lower temperature solder.

An IR-LED (peak output at 875nm) is the common light source for a pair of opposing tips. A flexible fiber bundle from the LED is bifurcated into two channels for this purpose. Intermixed randomly with each channel are return fibers conveying reflected light from the shaft back up to the respective silicon phototransistor (peak sensitivity at 900nm). This flexible bundle terminates at the tip by means of a threaded connector. This allows for easy disconnection of the optics during machining, brazing, and soldering operations performed on the housing.

The randomized fibers are not aligned with the tip's fused fibers at the connector. This raises the possibility that a pair of illuminator and receiver fibers in the flexible bundle might overlap a single fused fiber, providing a common return path for the light, and resulting in a large reflection signal at zero target displacement (undesirable). This problem is overcome by using very small diameter fibers within the fused bundle, so that the area of the common return path is minimized. 1mm bundles were used, and the bundle response is similar to that shown in Figure 6-18a. The working region is from 0 to 19 microns, and thus well within the positive going linear part of the response curve.

A pair of tips sense gaps at diametrically opposite sides of the shaft. When the gap on side A increases (sensed light also increases), the gap on opposing side B decreases (sensed light decreases). Since

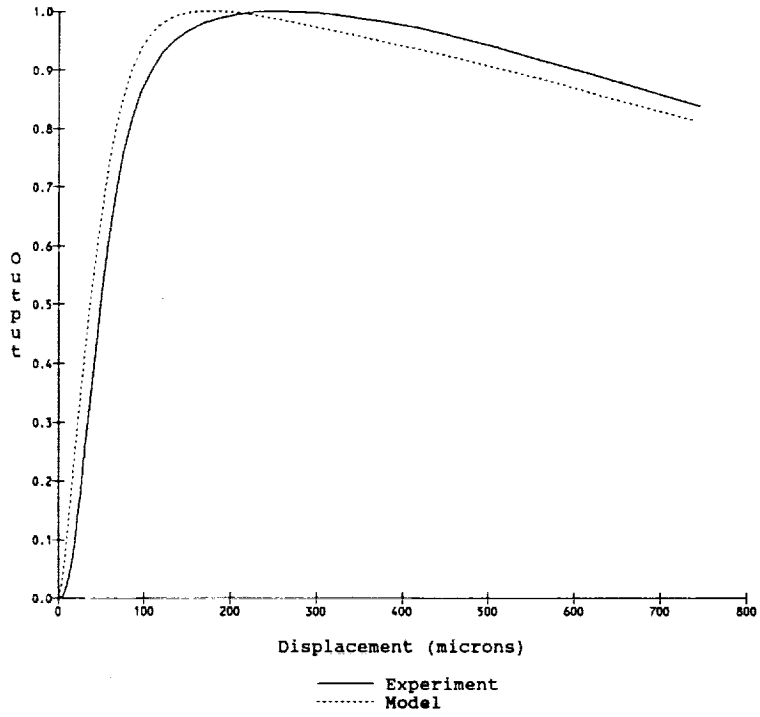

(a) Randomized bundle.

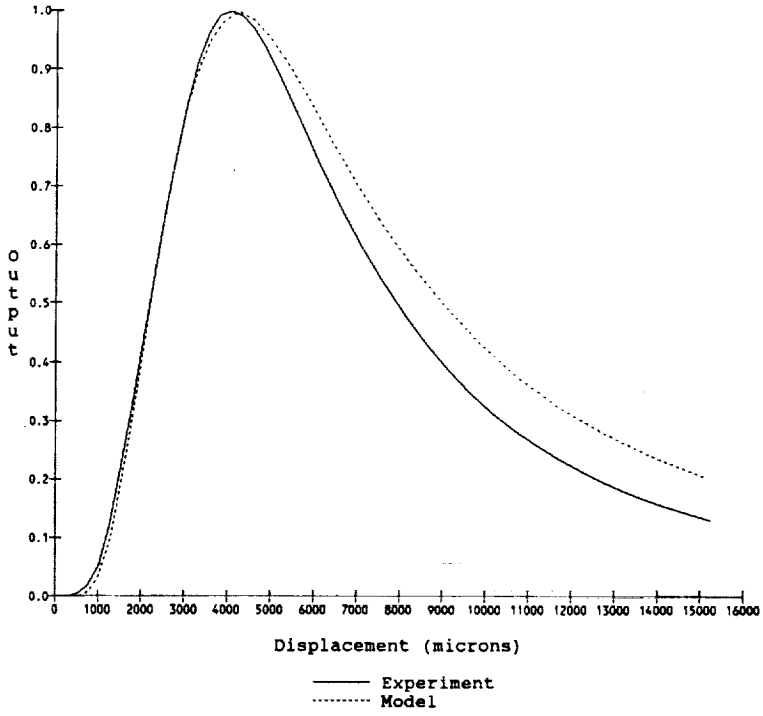

(b) Dual bundle.

Figure 6-18. Comparison of model and experiment.

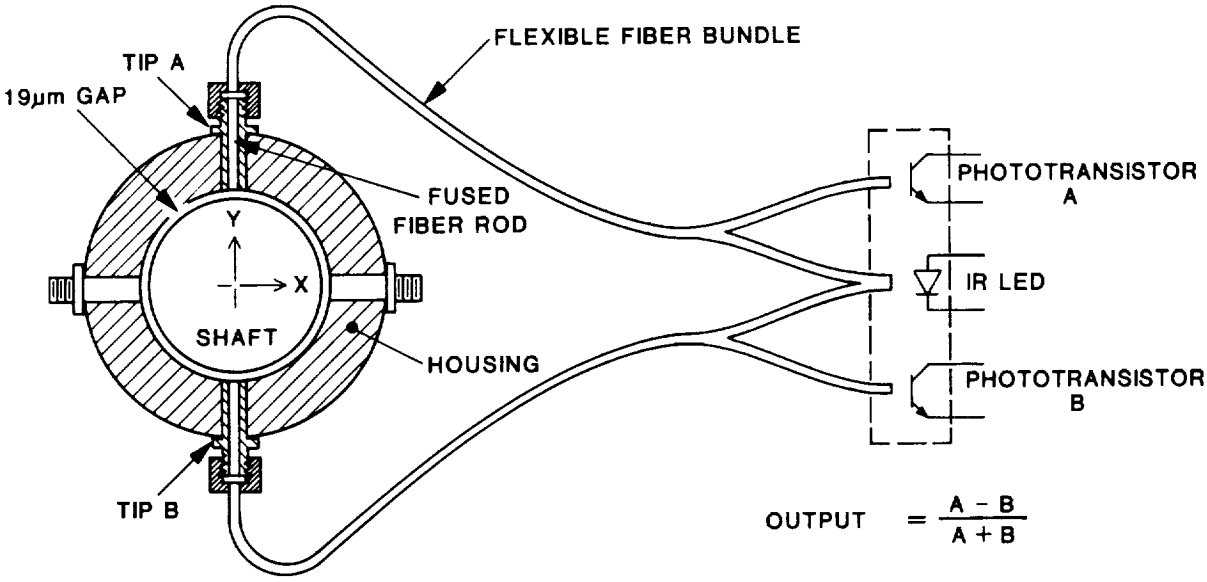

Figure 6-19. Fiber optic sensor for magnetic bearings.

the two signals are linear, the difference (A-B) would provide a signal with twice the slope. In practice, an analog dividing circuit is used to provide an output indicating shaft position (Fig. 6-20.) according to:

$$y = 10 \quad \frac{(A-B)}{(A+B)} \tag{4}$$

The above ratio provides a measure of shaft position which is independent of diode aging, ambient temperature or variations in mean reflectivity of the shaft. Diode aging causes a slow reduction in light output over time, while an increase in temperature causes increased light output. If the signals A and B were both reduced by 50% of their original value, this factor would cancel in Equation 4 and output would remain unaffected. Similarly, increases in phototransistor gain due to temperature are also compensated for as the common aluminum package ensures that the transistors follow the same temperature.

Another sensor located orthogonally to the one above provides measurement of shaft X position. The X and Y signals are used to actuate electromagnets which center the shaft within the housing. A similar set of sensors and actuators located further on the Z axis effectively controls a total of 4 degrees of freedom of the shaft. The shaft is free to rotate about its axis; a linear motor oscillates it along the Z axis for compression and expansion of the helium working gas.

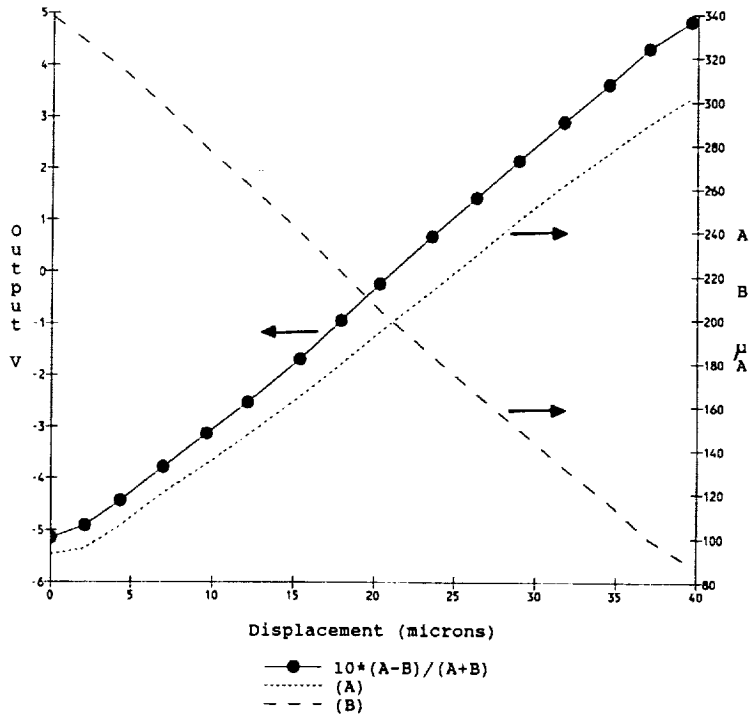

Figure 6-20. Output of magnetic bearing sensor and phototransistors A & B.

Some performance measurements of the sensor are given below: Linearity was measured to be within 3% of full scale output. Resolution is limited by noise of 14 $\mu V/\sqrt{Hz}$, which corresponds to a displacement of 4nm at a 10kHz bandwidth. The sensitivity is good with change in each phototransistor signal of about 3% of mid-position output, per micron of target motion. The temperature coefficient referred to displacement is quite low at 0.04 μ/°C. It was measured by cycling the sensor between 20 and 50°C with a fixed target gap. A spring-loaded fixture was used so that temperature expansions would not cause gap variation during the heating and cooling cycles.

6.5 Radial Control System

6.5.1 Bearing Current Driver

(1) General

The inductance of the coils of the actuator pole pieces of the magnetic bearing produces a phase shift between the voltage applied to the actuator and the resulting current. This inductance is a complex function of frequency due to the effects of eddy currents in the pole pieces. Since the magnetic bearings are position servomechanisms, i.e., the position is sensed and then controlled through the application of an electromagnetic force, an inherent 180° phase shift already exists in the controlled dynamics (ignoring any damping). Thus, any additional phase shift between the transduced position and the current which generates the force, such as that produced by the coil self inductance, can result in instability of the overall control system. This explanation is somewhat simplistic as the force is not a linear function of the pole piece current but is in fact dictated by the pole-flux which is a decreasing function of current with increasing frequency due to the effect of eddy currents in the pole pieces.

To minimize the phase shift from inductance of the coil, current feedback is used in the driver for the actuator. In previous designs linear amplifiers were used to drive the coils, the current in the coil was measured with a sampling resistor, and the applied voltage to the coil was regulated to keep the current in phase with the reference voltage.

As with most feedback loops, the advantages of the current driver are increased frequency response, reduced phase shift, and insensitivity to changes in the internal components of the loop. The disadvantages of current feedback are the possibility for instability in the current loop itself, which is now a minor loop in the overall position control system, and the need for a voltage overhead in the applied voltage to the coils. The voltage overhead is needed since the magnitude of the current produced by a given applied voltage decreases as a function of frequency. Thus, at higher and higher frequencies, more voltage must be applied to keep the current at the same levels. The overhead results in an inefficient use of the amplifier and coil magnetics. Therefore, as in most uses of feedback, the primary disadvantages are the increased possibility of instability and the use of additional power.

To address the issue of increased dissipation, a switching amplifier was used in this design, resulting in a significantly different system. The core of the switching amplifier design is the Unitrode L292 full-bridge current control switchmode driver chip. The principle difference between the linear and the switching amplifiers is that the switching amplifier applies a pulse-width-modulated voltage waveform to the pole piece coil. The duty cycle of this driver is adjusted to control the level of the current. While the switching amplifier has the advantage of being relatively efficient, it introduces additional complications. Specifically, switching noise can have an deleterious effect on the sensitive analog circuitry of both the current and servo loops, and while current mode control with switching amplifiers is a very high-speed technique, it is also known to have inherent stability problems.

(2) Current Loop Compensation

To insure stability of the current driver, the dynamics of the feedback loop were analyzed and compensation was provided. The compensator consists of a low frequency zero and a lag-lead pole-zero pair. Further, the current amplifier filter introduces additional dynamics. A lag-lead network reduces the high frequency gain sufficiently to avoid instability, but its very close proximity to the zero allows it to achieve this without compromising the phase roll-off out to 1 kHz or so.

6.5.2 Bearing Test Fixture

(1) General

The bearing test fixture (Fig. 6-21) was designed to simulate the displacer section of the refrigerator. The magnetic bearings consist of orthogonally placed coils near the ends of the test fixture housing. Opposing coils are driven via bearing electronics to maintain the shaft within the center of the housing. The optical reflective position sensors connected, via the fiberoptic cables, to the optical feedthroughs sense the position of the shaft to the housing.

The advantage of a test fixture is that radial force imparted to the shaft can be transduced. The bearing is shown on its test stand in Figure 6-22. A commercial shaker is connected to the suspended shaft via a piezoelectric force transducer. The displacement between the shaft and the housing is measured with the optical reflection position sensors, which are also used for feedback. Thus, the stiffness of the bearing, i.e., force/displacement, is measured directly.

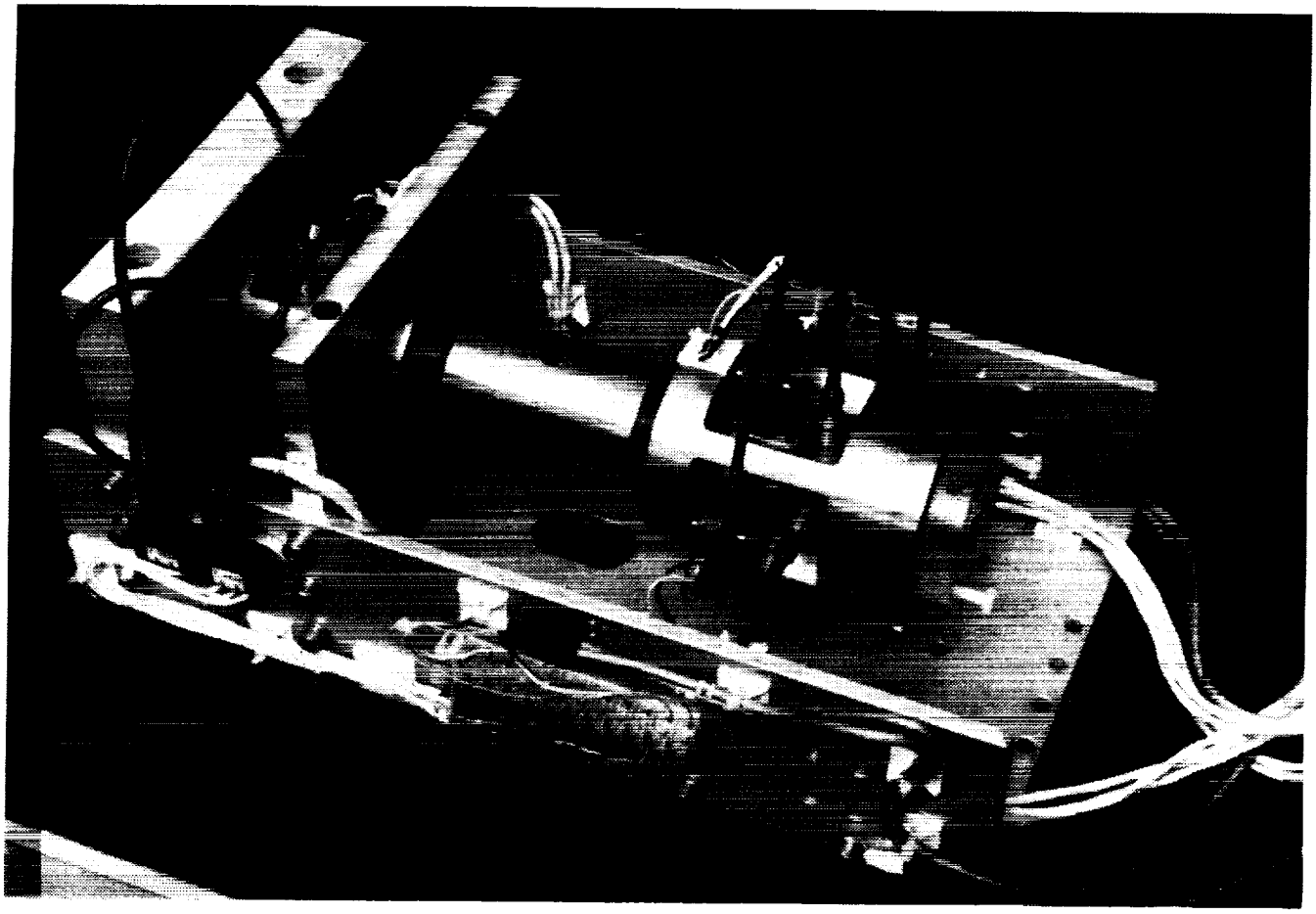

Figure 6-21. Displacer bearing test fixture.

The parts were machined to the same tight tolerances as in the actual cooler - 19 micron radial gap. The pole pieces and optical sensor feedthroughs were joined using the same techniques as in the cooler, thus testing the procedure to braze the magnetic materials and maintain their optimized magnetic properties.

(2) Measurement Techniques

Transfer function measurement is accomplished in two ways, using either a single-frequency sinusoid or a white-noise signal. When a single-frequency sinusoid is used, a lock-in amplifier extracts the desired frequency components of the measured signal from the background noise. For a white-noise signal, a two-channel Fast Fourier Transform (FFT) spectrum analyzer is used to directly measure the transfer function between two points. In this case, the instrument measures the power spectral densities of the two inputs, and the cross-spectral density, and computes the transfer function magnitude and phase by digital processing techniques.

The measurement of open-loop frequency response for the bearing requires some explanation. The control system model requires the shaft to be positioned at its nominal center. The open-loop frequency response can only be measured if the loop is closed and stable. Otherwise, the highly nonlinear nature of the system would mask any readings. To make an open-loop frequency response measurement from a closed-loop system, the technique in Figure 6-23 was used. The test signal

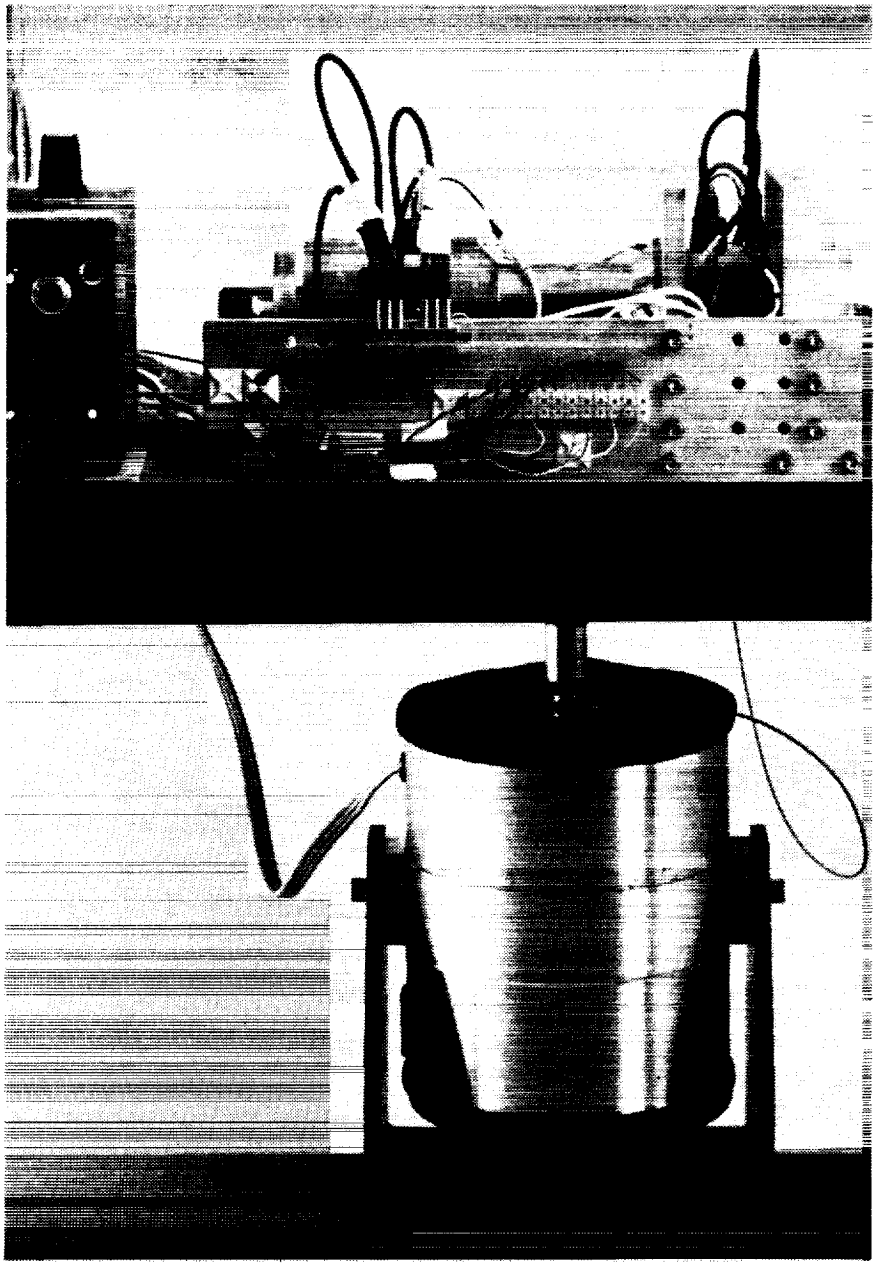

Figure 6-22. Fixture in test stand.

(V_{inj}) is injected into the loop, and signals V_1 and V_2 are measured. The desired response is V_2/V_1 and is realized by the following:

$$V_1 = V_2 + V_{inj}$$
$$V_2 = G_1HG_2 V_1$$
$$= G_1HG_2 (V_2 + V_{inj})$$

Therefore, $V_2/V_1 = G_1HG_2$ which is the open-loop response. For this analysis to be accurate, the signal V_{inj} must not load the loop. Thus, the impedance looking forward should be high and the impedance looking back should be low. The loop is broken and a non-inverting operational amplifier is inserted in the bearing electronics for this purpose. It should be noted from the figure that this technique works for arbitrary injected signals and does not depend on the dynamics included in the transfer function blocks.

(3) Results

Results of a static load test are given in Figure 6-24. Various known masses were hung from the shaft midway between the bearings, and the average displacement of the shaft was recorded. The figure shows the displacement of the shaft from center as a function of the load per bearing. The bearing driver electronics current limiting circuitry prevented extension of the graph for very large loads. For displacements over 1 micron, the stiffness is relatively constant at about 80 N/micron.

The plot of bearing stiffness vs frequency is shown in Figure 6-25. For this test, the excitation frequency for the shaker was varied, and the force and displacement were measured. Single frequency sinusoids were used corresponding to the points on the curve. This test was conducted primarily to determine the stiffness of the bearings subjected to loading at 7 Hz, the frequency of maximum loading during the launch phase. The load on each bearing was held constant for each frequency at 80 N, which corresponds to 7g at 7 Hz, the design goal for the refrigerator. The dynamic stiffness at 7 Hz of the bearing is about 50 N/micron. Figure 6-26 is a bearing stiffness vs. frequency plot with the load on each bearing held constant at 25 N corresponding to 2g at 7 Hz. The figure indicates the trend in predicted values of stiffness discussed in Section 6.3 of the magnetic circuit design at higher frequencies.

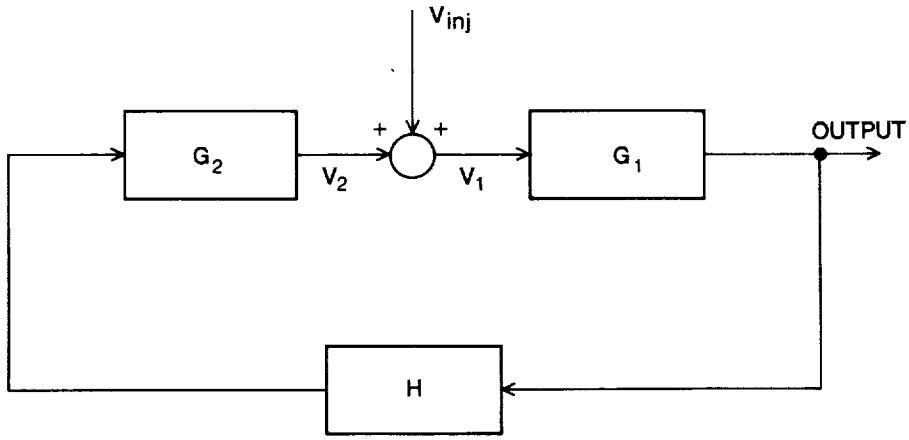

Figure 6-23. Technique for measuring open-loop frequency response.

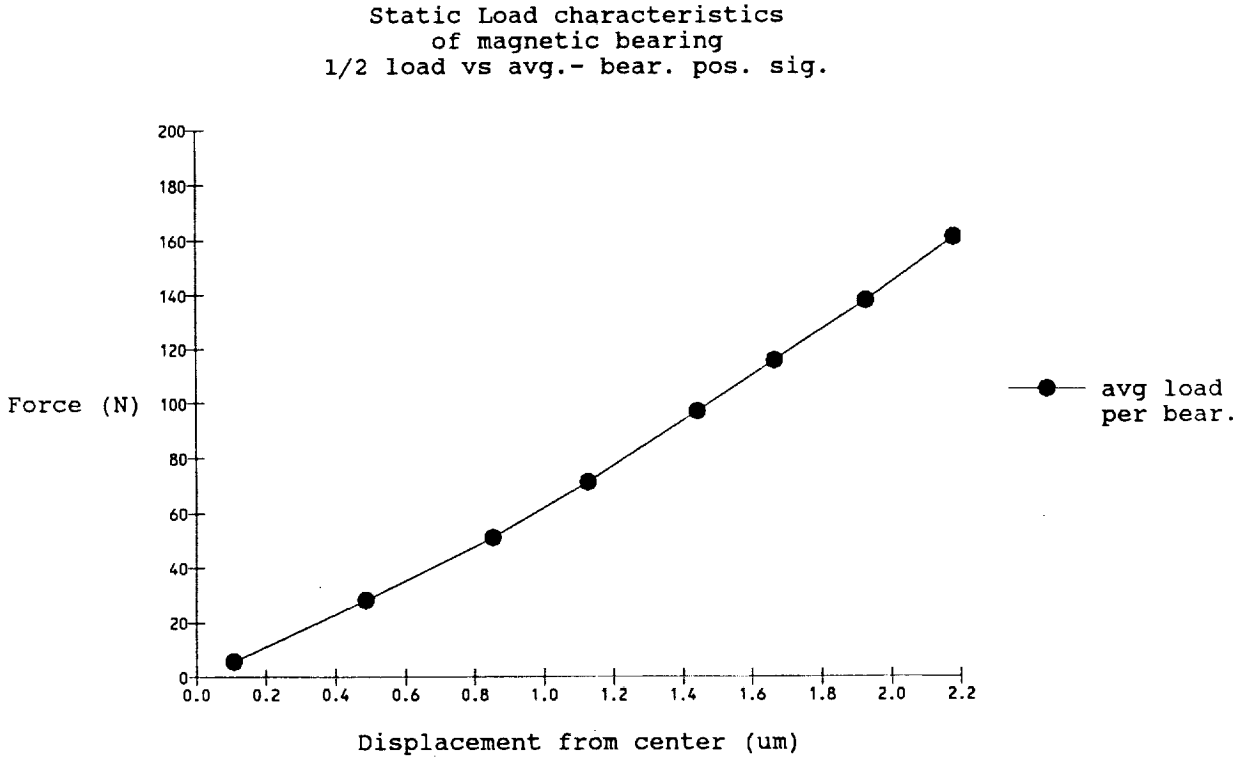

Figure 6-24. Static load characteristics. Bearing load vs. radial displacement.

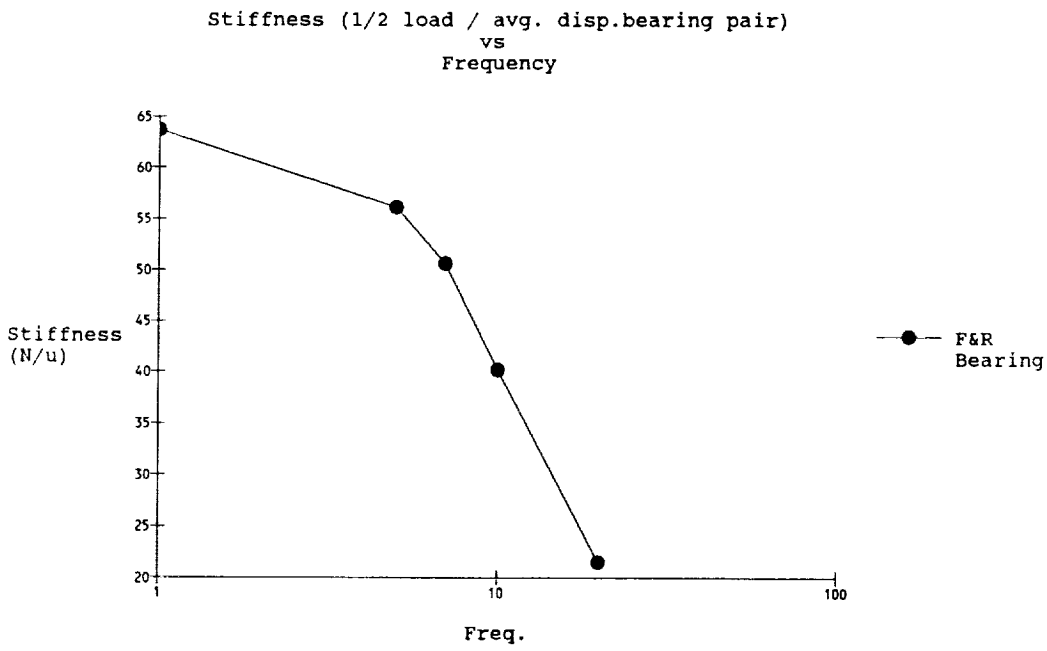

Figure 6-25. Bearing stiffness vs. frequency - 7g acceleration.

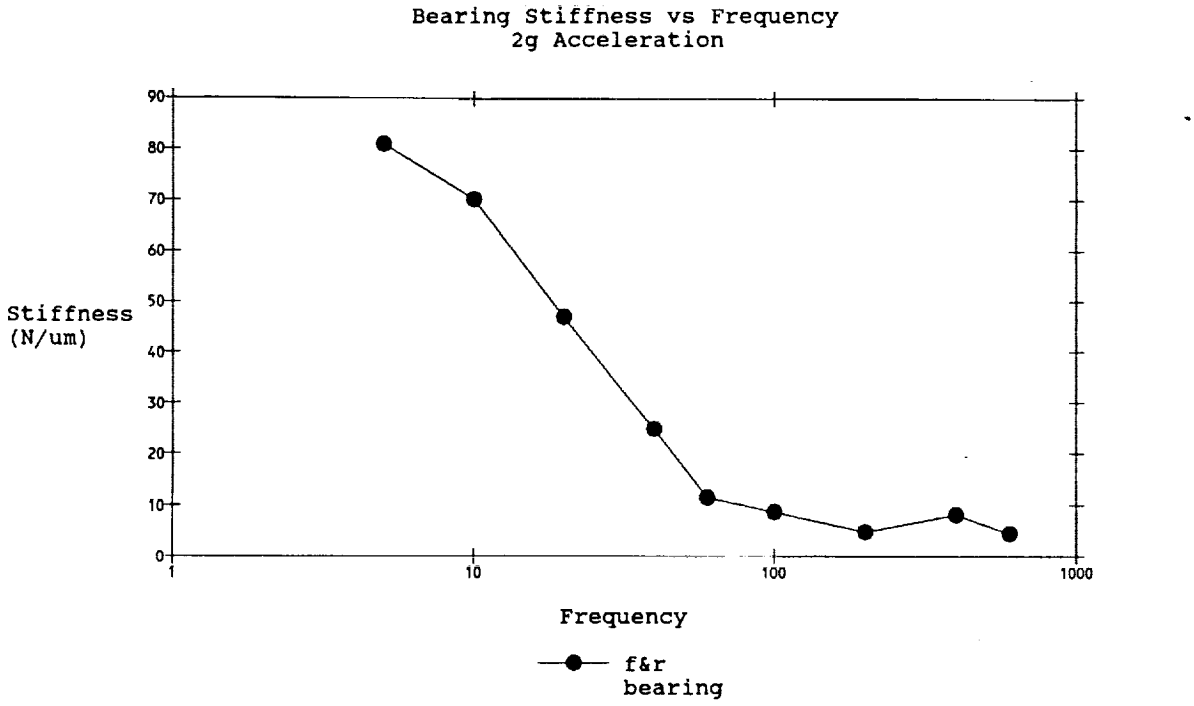

Figure 6-26. Bearing stiffness vs. frequency - 2g acceleration.

6.6 References

1. Magnetic Bearings Inc., 501 First Street, Radford VA 24141. Product Literature.

2. E.M.H. Kamerbeek, "Magnetic Bearings", Philips Tech. Rev. 41, pp. 348-361, No. 11/12, (1983/84).

3. L. Knox, P. Patt, R. Maresca, "Design of a Flight Qualified Long-Life Cryocooler", Proc. of the Third Cryocooler Conference, NBS, Boulder, CO, NBS Special Publication 698, pp. 99-118, (September 17-18, 1984).

4. F. Stolfi et. al., "Design of a Long-Life Stirling Cycle Cooler for Space Applications - Phases I and II - Engineering Model", Philips Laboratories, Final Report, Contract NAS5-26688, NASA Goddard Space Flight Center, p. 51, (March 1983).

5. Ibid.

6. Ibid.

7. Ibid.

8. A. Cameron, "Basic Lubrication Theory", Ellis Horwood Limited, Div. of John Wiley and Sons, 9, (1981).

9. D.F. Hays, "Squeeze Films: A Finite Journal Bearing with a Fluctuating Load", Journal of Basic Engineering, Transactions of the ASME, pp. 579-588, 83D, (December 1961).

10. Richard Boll, Editor, "Soft Magnetic Materials: Fundamentals, Alloys, Properties, Products, Applications", The Vacuumschmelze Handbook, Siemens Aktiengesellschaft, Heyden ans Son Ltd., p. 61, (1979).

11. C. Kissinger, "Fiber Optic Proximity Probe", US Patent No. 3,327,584, (1963).

12. R.O. Cook and C.W. Hamm, "Fiber Optic Lever Displacement Transducer", Applied Optics, 18, No. 19 (1 October 1979).

13. L. Hoogenboom et. al., "Theoretical and Experimental Analysis of a Fiber Optics Proximity Probe", SPIE, 478, Fiber Optic and Laser Sensors II, (1984).

14. M. Johnson, "Fiber Displacement Sensors for Metrology and Control", Optical Engineering, 24, No. 6, (Nov/Dec 1985).

15. R.P. Main, "Fiber Optic Sensors - Future Light", Sensor Review, (July 1985).

7. AXIAL POSITION CONTROL SYSTEMS

7.1 General

The axial motions of the three cooler shafts are regulated by independent, closed-loop position-control subsystems. Each closed-loop system consists of the linear motor and shaft dynamics (described in Sect. 4), a feedback position sensor, and a motor driver. The sinusoidal commands for the piston and displacer motions are digitally generated to provide frequency, amplitude and relative phase control. These parameters are programmable via the System Controller. The counterbalance command signal is derived from the position outputs of the piston and displacer and tuned to minimize the net vibration of the cooler housing. Each motion control subsystem has a local interlock scheme to protect the cooler from mechanical damage. The interlock status is monitored by the System Controller which can take appropriate action in the event of a fault. A block diagram of the axial control system is shown in Figure 7-1.

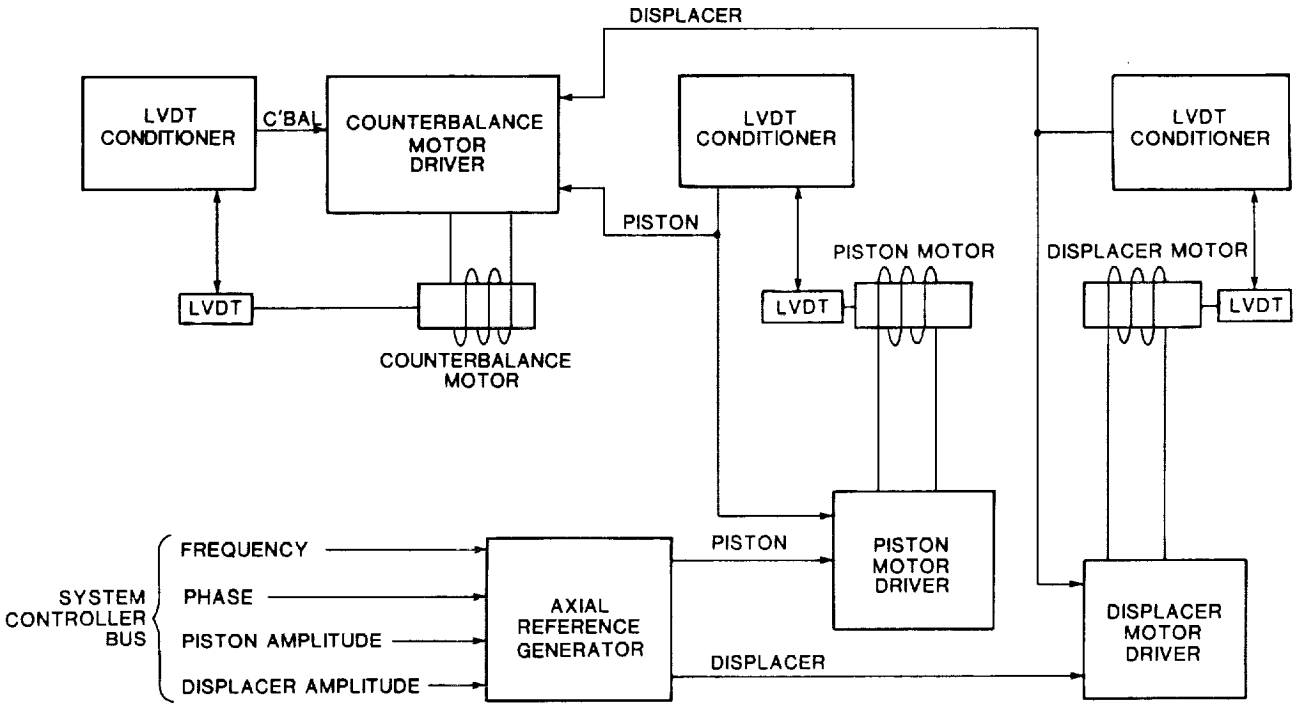

Figure 7-1. Block diagram of axial control system.

7.2 Motor Drivers

The three motor drivers are constructed in separate chassis to simplify the initial testing and calibration. They are nearly identical in design, so the description which follows applies to all three drivers (see Fig. 7-2).

The command input is compared to the measured position output of the LVDT sensor to produce an error signal. The measured position signal is tested by a window comparator to provide overstroke detection. A similar circuit monitors the magnitude of the error signal to detect a general fault in the closed loop (i.e., loss of motor power or friction of the shaft).

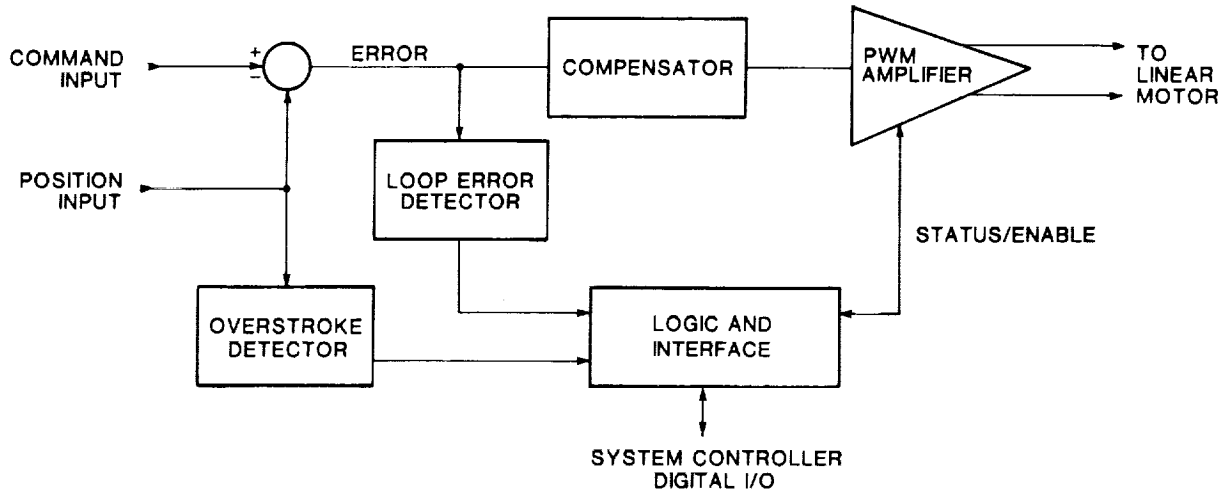

Figure 7-2. Block diagram of motor driver.

The error signal is then passed through a phase compensation/gain amplifier tailored to provide stability and bandwidth for effective control of each position control loop.

The output of the compensator circuit is applied to the command input of the motor amplifier. The motor amplifier is an efficient high frequency PWM type with local current feedback and internal fault detection (over temperature, short circuit protection). Each amplifier is sized according to the energy requirements of the particular subsystem.

Logic circuitry interfaces the motor driver with the System Controller. This allows each motor driver to be individually accessed to enable or disable the subsystem and to read status information.

The overstroke and loop errors are latched and interlocked with the driver enable/disable signal to provide protection at the subsystem level. They can be overridden by the System Controller for the purpose of initializing the system.

Motor amplifier faults will disable the motor amplifier and must be reset by a sequence from the System Controller. They will not clear if the fault persists.

7.2.1 Position Loop Optimization

Control loop optimization was performed by measuring the open-loop response of the closed loop system (see description of this technique in Sect. 6.5). The resulting magnitude and phase plots describe the gain and stability of the system's small signal response.

Figure 7-3a shows the uncompensated open loop transfer function (OLTF) for the piston driver system. The second-order mechanical system response is evident with the resonant peak near 20 Hz. It is necessary to have gain at dc in order to maintain the desired center position, because the piston is influenced by non-symmetric gas forces during normal operation. High gain at resonance is required to minimize position errors.

(a) Uncompensated.

(b) Compensated.

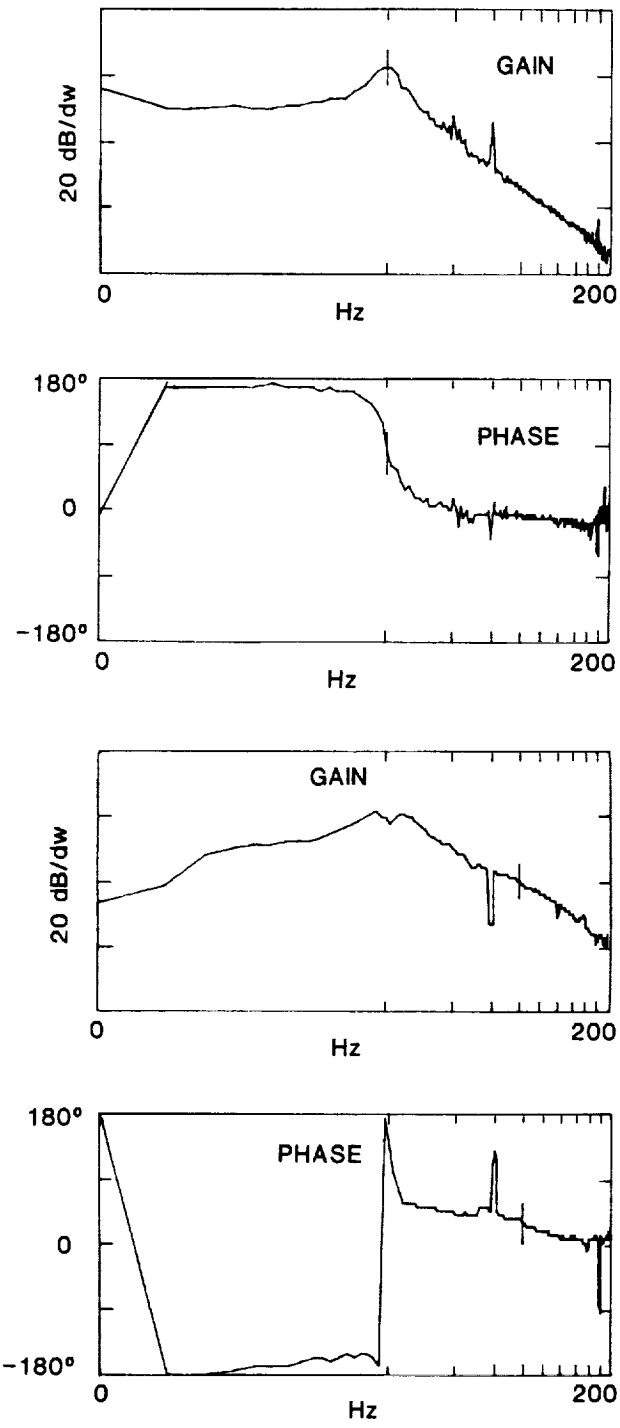

Figure 7-3. Piston open-loop transfer function.

The maximum gain can be improved by extending the bandwidth while maintaining stability. This is accomplished by adding a phase lead network to provide additional phase margin, then increasing the gain to provide satisfactory phase and gain margins (nominally 30 degrees and -10 dB). A high frequency pole (~1 kHz) is added, which does not affect the loop response, but eliminates useless (and audible) noise from the system. The compensated OLTF is shown in Figure 7-3b. Figures 7-4 and 7-5 describe the compensated OLTF data for the displacer and counterbalance, respectively.

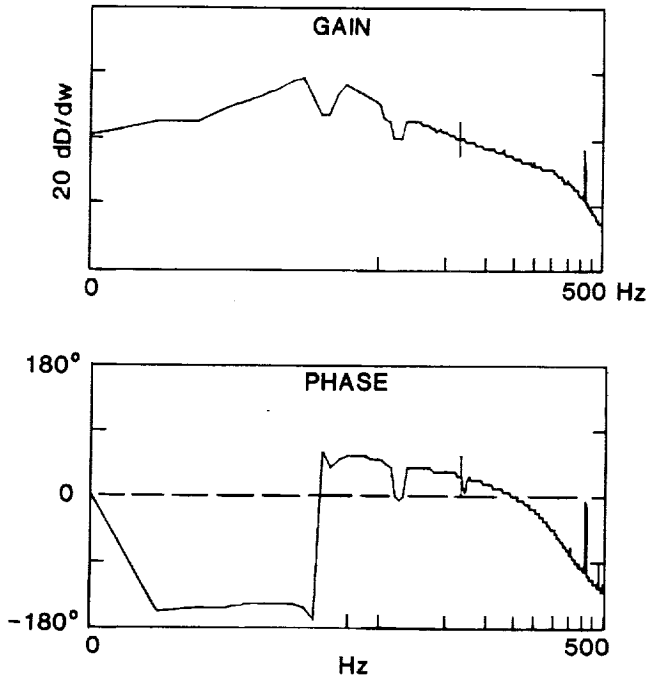

Figure 7-4. Compensated displacer OLTF.

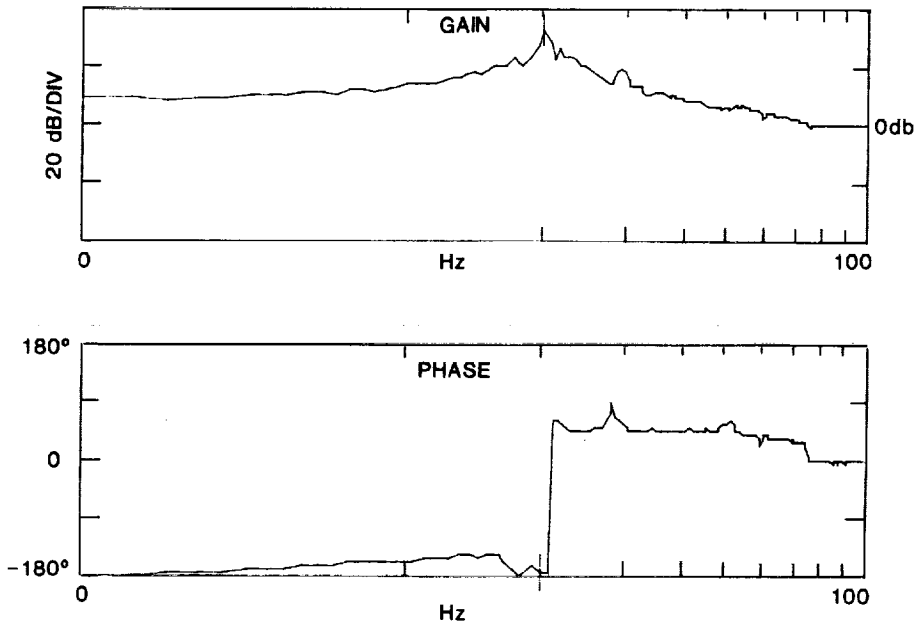

Figure 7-5. Compensated counterbalance OLTF.

Ultimately, the maximum gain is limited by the large signal response of the motor amplifier circuit, which is a function of motor impedance and available supply voltage. This introduces a pole, with its characteristic phase lag, at lower and lower frequencies as the current magnitude is increased.

The displacer operates at resonance and does very little real work, and hence requires small currents. The piston also operates at resonance, but real power is required for thermodynamic input. In both cases, the electrical time constants of the motors are sufficiently low to avoid large signal instabilities.

The counterbalance, however, has a time constant of a greater order of magnitude, and must provide forces at the higher harmonic frequencies. These conditions and requirements are at odds, so that tuning the loop for adequate small signal bandwidth (i.e., able to cancel third harmonic vibrations) would result in an unstable large signal response. This instability was observed during bench tests as the system was initially turned on with the shaft at one end and the command for 'center', providing a large signal 'step' response test.

Such conditions are possible (and probable) during normal startup, so instability must be avoided to protect the cooler from mechanical damage. Rather than sacrifice position loop bandwidth, the current limiting feature of the motor amplifier was employed to effectively roll off the large signal loop gain. The active circuitry of the current limiter does this without introducing any phase lag, which would compromise closed loop stability. The end result is to provide a stable counterbalance position control loop with bandwidth sufficient to effectively suppress fundamental and third harmonic vibrations.

7.3 Axial Position Sensors

7.3.1 Basic Operation of LVDT

An LVDT (Linear Variable Differential Transformer) is a device for measuring linear position. In its most basic form it consists of a transformer having two secondaries symmetrically wound adjacent to (or over) opposite ends of a single primary winding and includes a moveable ferromagnetic core. If the primary winding is excited by an ac source, then the position of this internal core will determine the relative degree of signal coupling between the primary and either of the two secondaries. The core (or armature) is attached to the item whose position is to be determined. Figure 7-6 shows the general construction of an LVDT. The primary consists of a cylindrical solenoid with (in the case of this illustration) the two secondaries wound at opposite ends of the primary. The entire coil assembly is contained within a ferromagnetic shield, and an internal non-magnetic cylindrical bore-liner tube completes the enclosure of the coils.

The cylindrical core is displaced axially within the liner, thereby affecting the relative levels of flux coupling the primary and each of the two secondaries. When the core is displaced (as shown) towards one of the secondaries, the mutual inductance between the primary and that particular secondary is increased. The output from this secondary will correspondingly show both an increased amplitude and an increased phase shift. Likewise, the other secondary will produce an output with a reduced amplitude and decreased phase shift. Electronic circuitry converts the differences in amplitude and phase between the two secondary ac signals to a dc voltage. The electronics are covered in more detail in Section 7.3.4.

(1) Modelling the LVDT

Figure 7-7 is a simplified broad band model of a transformer; it represents the LVDT with only one of the secondaries shown. Particularly at the higher frequencies, many of the parameters are

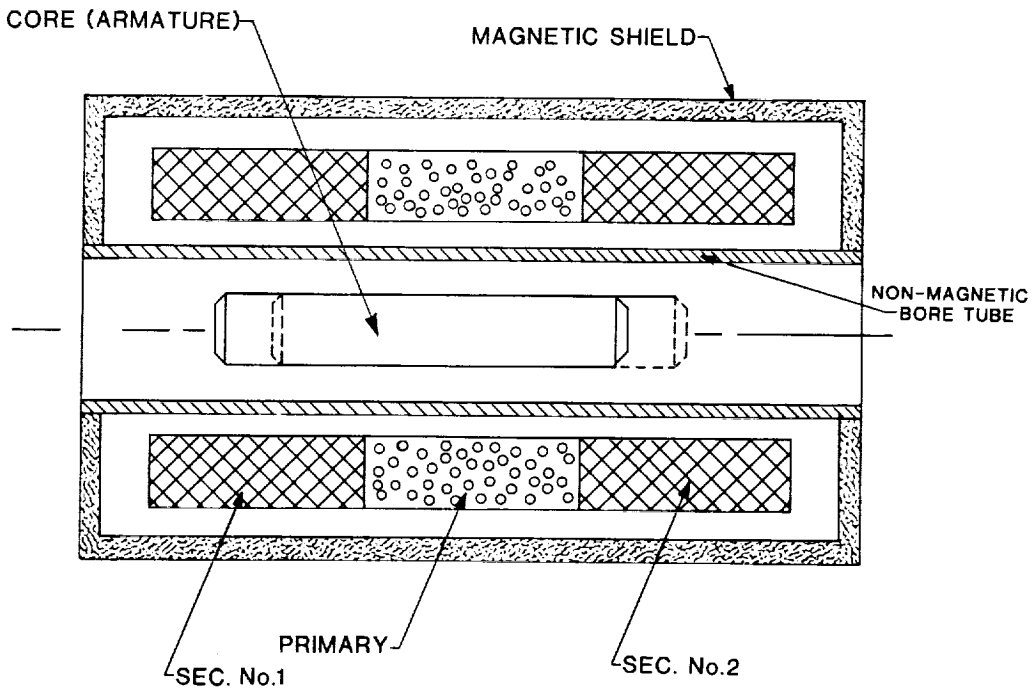

Figure 7-6. Sectional-view of a three-coil LVDT.

difficult to determine analytically and must be empirically measured. For example, C_{ps} is not only determined by the winding style used, but also by the spacing between the primary and secondary coils, and is affected both by the axial position and the material composition of the core. Likewise, the interwinding capacitances, C_p and C_s, are interactive with the core materials. R_s is a resistance representing "core" losses, but it must also include losses that are present in the shielding materials.

The simplified model assumes lumped parameters and linear differential equations. In practice, the LVDT windings actually appear more like a transmission line with distributed capacitances and resistances. Also, any fully useful model must include the mutual coupling between the secondary windings and the electrostatic effects (capacitance vs. voltage) of each secondary referenced to the primary.

(2) Empirical Methods

The straight-forward, high-frequency transformer model is not accurate enough to apply directly to the design of the coils and bobbin. However, if the model diagram is reconfigured to approach more closely the transmission line appearances of the true LVDT, this modified circuit can be used as a tool for predicting the qualitative effects of design modifications. That is, by testing an actual bobbin and then using these measured values in the model, it is possible to analyze trends associated with small design changes about this empirical operating point. Figure 7-8 shows an expanded circuit model of an LVDT transformer; the values were derived from data on an actual test bobbin. If this model is simulated with an ac analysis program, the predicted response is as shown in (b). Precisely

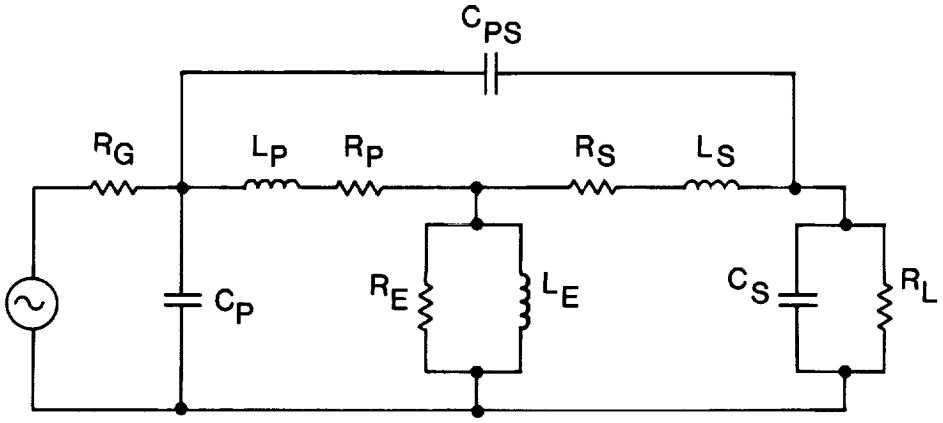

Figure 7-7. Simplified model of a broadband transformer. For correct comparison with an actual LVDT, an additional secondary winding would have to be included as would a value for the inter-secondary capacitance. Since this model assumes lumped discrete parameters, it is generally unsatisfactory for precise analysis.

R_g : source (generator) resistance
C_p : primary winding capacitance
L_p : primary leakage inductance
R_p : primary winding resistance
R_e : core (titanium, etc.) losses
L_e : primary magnetizing inductance
R_s : secondary winding resistance
L_s : secondary leakage inductance
C_s : secondary winding capacitance
C_{ps} : primary to secondary capacitance
R_l : equivalent load resistance

how the circuit is broken down into individual elements will have a considerable effect on the output from the model.

Figure 7-9 shows the final winding style used in the LVDTs. The primary is wound evenly section-by-section along the bobbin. The winding with a sectioned bobbin as shown here provides reduced inter-winding capacitances and allows the numbers of turns to be carefully controlled. The two secondaries are then wound at either end over the primary. The number of turns per section in the secondaries is graduated to provide a precisely linear output from the LVDT when the core is displaced. The actual displacer bobbin has twelve sections, and the piston (and countermass) LVDTs have seventeen sections.

7.3.2 Use in Refrigerator

Three LVDTs are included in the cryogenic refrigerator design (Fig. 7-9). One LVDT, with a range of nominally 10 mm, measures the axial position of the displacer armature. Two other units, similar

(a)

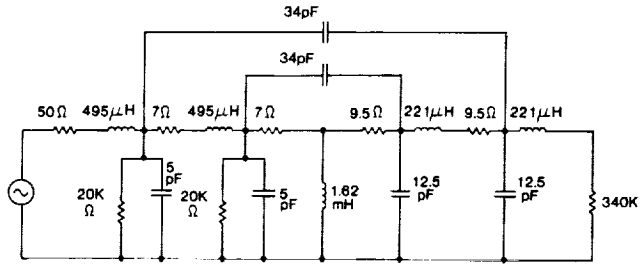

(b)

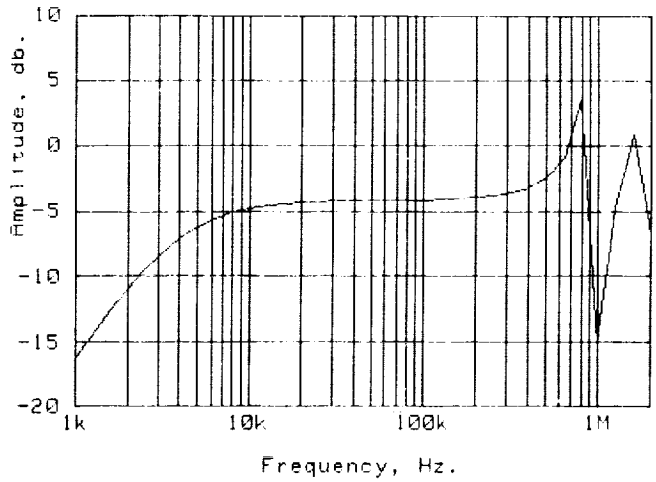

Figure 7-8. Broadband model expanded (a) to represent more closely transmission line characteristics of actual transformer. Values shown were obtained from a test bobbin with segmented construction. See Figure 7-7 for a description of parameters. Predicted response is shown in (b).

to the first LVDT except for length (a linear range of 20 mm), are used for axial position measurement of the piston and countermass armatures. In addition to providing positional information for their respective local control loops, the piston and displacer LVDTs provide information to the control loop electronics for the countermass driver system. The LVDT system outputs, therefore, not only have to provide positional information at the fundamental operating frequency (nominally 20 Hz) of the machine, but also must have a bandwidth sufficient to provide information on the harmonic content to the countermass control logic.

The specifications for the LVDT accuracy, linearity, and frequency response were dictated mainly by the control requirements of the countermass drive system. With the higher frequency response characteristics imposed on the LVDTs, the bandwidth of the LVDT position sensing system had to be essentially "flat" (0 dB gain attenuation, minimal phase shift) to 100 Hz. For this reason, the final filter poles in the electronics (see Sect. 7.3.4.) were placed at 10 kHz. The operating frequency was then chosen as 100 kHz in order to reduce the output ripple to an acceptable level.

7.3.3 Special Considerations

Skin depth is defined as that depth at which the alternating current in a conductor has decreased to 1/e of its surface value. This depth is a function of frequency and of both the resistivity and permeability of the conductor material. For example, in the design of the LVDTs, the wall thickness

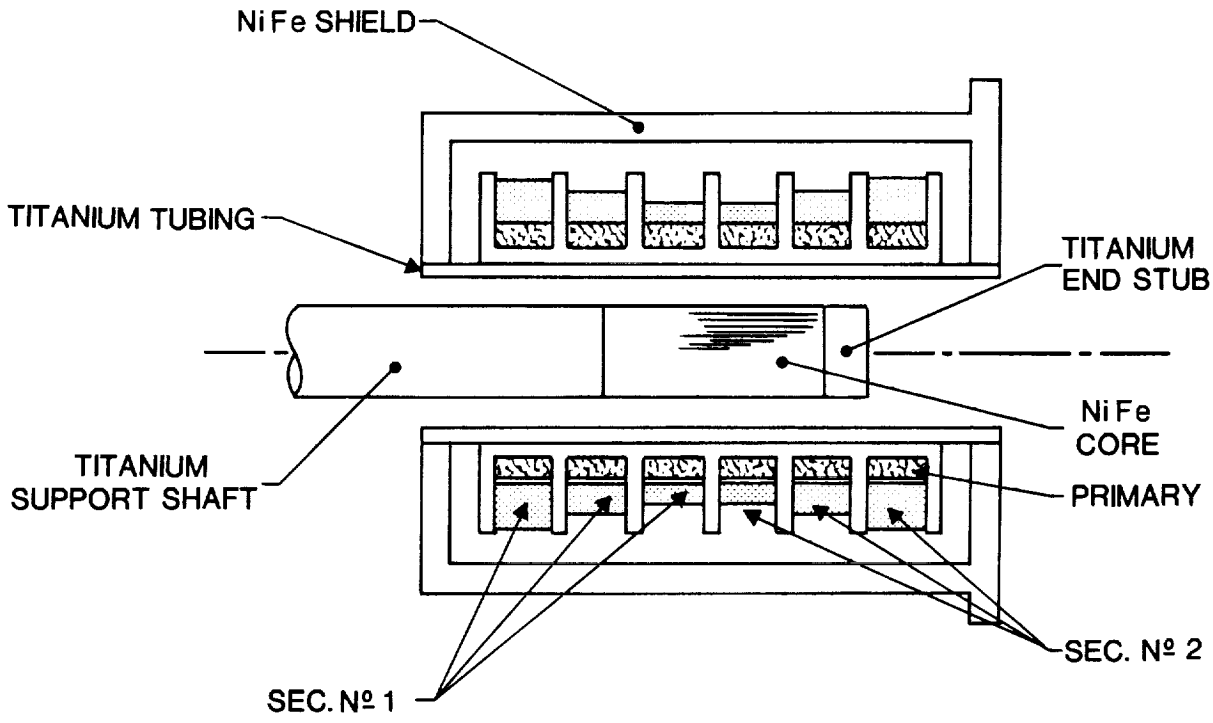

Figure 7-9. Multi-section multi-winding LVDT as used in final design. For clarity, only six sections are shown.

of the titanium bore liner tube is nominally 0.5 mm. At the 100 kHz operating frequency, the titanium tube has a skin depth of about 1.1 mm and therefore would be a partial magnetic shield. By reducing the primary flux reaching the core, the titanium tube significantly reduces the voltage output from the secondaries and (due to induced eddy currents) effects the overall phase shift seen in the secondary outputs. Because of joining and hermetic seal requirements, however, titanium was chosen as a compromise material for the bore liner.

The moving ferromagnetic core is supported on a nonmagnetic shaft that is, in turn, attached to one of the refrigerator motor armatures. If the core itself is a cylinder with "square" ends, local saturation may occur at these end edges. The higher levels of flux entering the end faces of the core rod will reduce the linear range available from a given LVDT. In the case of operation at 100 kHz, the titanium supporting rod effectively becomes a partial magnetic shield (due to eddy currents and the associated skin effects) to the one end of the nickel-iron core. In addition to reducing the flux entering the end of the core, the eddy currents induced in the titanium itself add phase shift to the secondary output signals. To maintain as much as practical this eddy current and shielding symmetry, a short titanium stub was included at the opposite end of the supporting shaft.

Heat treatment and mechanical finish are now important for optimal LVDT performance. The skin depth of nickel-iron at the 100 kHz operating frequency is shallow (.01 mm) and perturbations in

the surface finish could result in degraded performance; at 100 kHz much of the permeability (cross section) of the core may be lost. Additionally, if this permeability (in the "skin" of the core) is some non-linear function of the local field strength, the core itself may generate harmonics of the primary frequency.

The overall differential voltage output of the LVDT secondaries is not determined solely from the numbers of turns, but is a complex function of the various LVDT impedances. At higher frequencies, the phase shifts associated with interwinding capacitances and eddy currents must be considered.

7.3.4 Electronics Signal Conditioning Circuit

Commercial LVDT signal conditioning electronics generally operate at frequencies below 50 kHz. It was necessary, therefore, to develop circuits to allow operation at 100 kHz. The circuit was assembled from readily available components consistent with the stability and frequency response requirements. A description of the electronics used in the test and development phases of the LVDT design follows. Figure 7-10 is a block diagram of the circuit. The LVDT primary and secondaries are shown schematically on the left of the diagram. The remainder of the diagram outlines the electronics used to convert the ac outputs of the LVDT secondaries to a dc voltage level representing the position of the core.

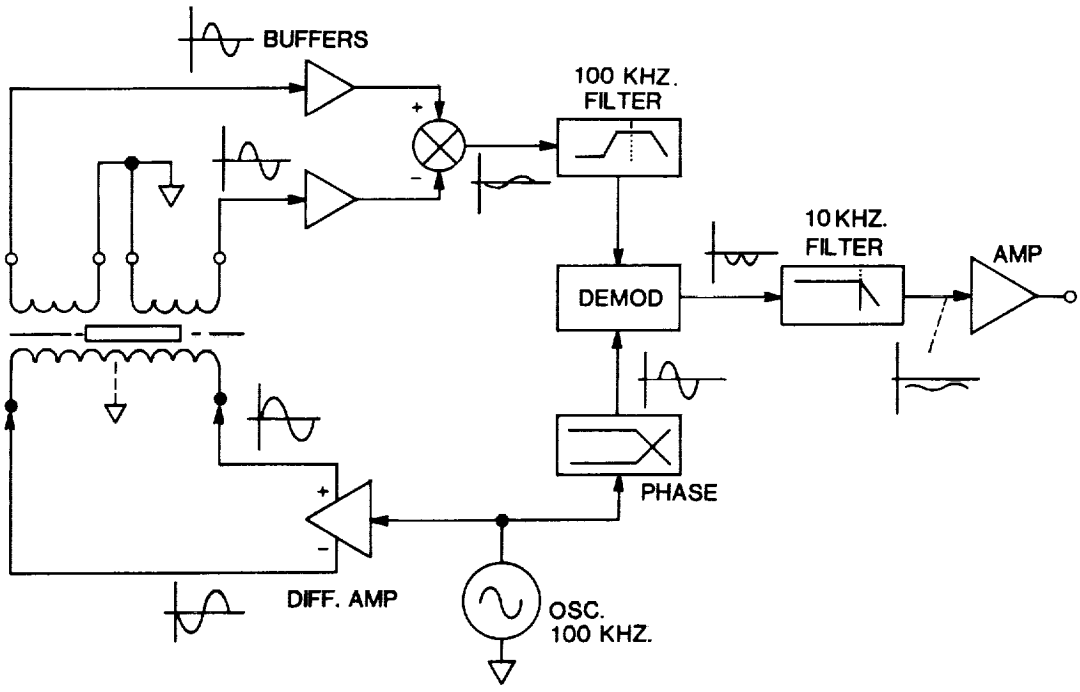

Figure 7-10. Block diagram showing LVDT and associated signal-conditioning electronics. Core is shown slightly off-center and resulting waveforms are illustrated for various points in circuit.

(1) Oscillator-Driver

The oscillator is a commercially available CMOS crystal-controlled, square wave generator. This is followed by a seven-pole passive filter yielding a stable output sinewave at 100 kHz with harmonic

attenuation measured at -55 dB or better. Because of the filter sections used in the circuit and the generation of harmonics within the LVDT itself, good frequency stability is required to prevent the signal amplitude change that would result from a drift in operating frequency. Harmonic attenuation is necessary as conditions for the balance (null output) of the LVDT may not be the same for the harmonics as it is for the fundamental. Rather than using feedback methods, low amplitude drift is achieved by powering the entire circuit with precision voltage regulators. Amplitude stability is then principally a function of component thermal drift with temperature. Low-drift passive components are used throughout the circuit.

The sinusoidal signal thus generated was then applied to the single input of an amplifier with a differential output. The LVDT primary is connected across the two outputs of this amplifier. This differential drive method is used here because the conditions for precise balance (that is, symmetry in the output of secondaries) preclude the need for a voltage and flux balance across the secondaries. From Figure 7-10 it can be seen that a balanced differential voltage input to the primary will result in an essentially zero voltage node at the center of the primary coil. The two secondaries now see identical magnetic fields (magnetically coupled, due to the flux from the primary) and identical electrostatic fields (capacitively coupled, due to the voltage gradients in the primary). With the proper gain and offset adjustments made, a nearly zero output voltage can be obtained from the LVDT with its core in the mechanical center position.

(2) Phase Shifter

A second output from the oscillator is fed into a unity-gain phase shifting circuit. This phase shifter and its associated buffer provide the "carrier" (i.e., reference) drive for the synchronous demodulator. The phase shift is required in order to match (synchronize with) the phase shift resulting from the mutual inductance between the LVDT primary and secondaries. Due to the low coupling factor, a minimal change in total (i.e., combined secondary) phase shift is seen with an axial change in the LVDT core position. Once the phase adjustment has been set, it is adequate for all core positions within the linear range of the LVDT. A switch within this section permits the choice of either a lead or a lag in phase, allowing the polarity of the dc output of the electronics to be changed.

(3) Secondary Inputs

The outputs from each of the LVDT secondaries are separately brought (through miniature coaxial cables) to identical high-impedance input buffers. Both secondary voltages are routed to the electronics so as to be able to adjust individually the output from each of these windings. These adjustments are used to achieve both gain and phase balance between the two secondary outputs when the core is at center position.

The outputs of the two buffers feed a subtractor whose output is now the difference between the two inputs (i.e., the LVDT secondaries). In addition to the capacitive trimmers at each buffer input, an adjustment is included in this section of the circuit to allow matching of the gains of the two secondary winding/buffer input paths. From here, the signal is sent through a bandpass filter centered at 100 kHz. The filter attenuates both the higher frequency harmonics of the 100 kHz carrier (that may have been generated within the LVDT) and the low frequency components (e.g., 60 Hz) that could result from the environment or background. The filter bandwidth (skirt) frequencies are set at approximately 80 kHz and 120 kHz, respectively. This bandpass width is adequate to allow passage, without significant amplitude attenuation or phase shift, of the position information contained in the modulation components present on the 100 kHz carrier.

(4) Synchronous Demodulator and DC Output

The synchronous demodulator is useful to several hundred kilohertz; the unity gain bandwidth is specified as 2 MHz. The circuit functions essentially as a multiplier, the output being the product of the carrier reference signal (from the oscillator) and the difference signal (from the LVDT secondaries). The output of the demodulator is, therefore, the absolute value of the measured input (i.e., the difference between the secondaries) with the output sign (or polarity) determined by the phase of the combined secondary input signals. This output is filtered by a third order, low-pass active network with poles at approximately 10 kHz. A final amplifier stage includes the necessary adjustments to trim both the gain and offset of the dc output signal.

7.4 Reference Waveform Generator

A digital-analog waveform generator provides axial command sinusoids for the displacer and piston motion control subsystems. Through this, the System Controller can program the system operating frequency, piston and displacer stroke amplitudes and relative phase (piston lags displacer). A block diagram of the reference generator is shown in Figure 7-11. Performance specifications for the circuit are listed in Table 7-1.

TABLE 7-1. Axial Reference Generator Performance.

Parameter	Range	Resolution
Frequency	15 - 30 Hz	< 0.2 Hz
Relative Phase	0 - 90°	0.3°
Piston Stroke	0 - 100% Full Scale	< 0.5% FS
Displacer Stroke	0 - 100% Full Scale	< 0.5% FS

A crystal timebase output is passed through a programmable divider circuit to provide scaling for the operating frequency. The scaled clock signal drives a binary counter, the output of which is used to address the sinewave data memories (PROM).

Each identical PROM contains 1024 8-bit values which comprise amplitude data for one complete sinusoidal cycle. As the address values are sequentially selected at the input, the output amplitude data is presented to a digital-to-analog converter. A low-distortion analog sinusoid appears at the output of each converter.

Address values for one of the PROMS are offset via a full adder circuit to provide a relative phase shift in the two sinusoidal outputs. The amount of offset (phase) can be programmed by the System Controller.

Each analog sinusoid is passed through a multiplying digital-to-analog converter to provide amplitude scaling. By scaling the 8 bit resolution sinusoids in an analog (rather than digital) fashion, distortion due to quantization error is avoided.

A four-pole, low-pass filter (f_c = 100 Hz) follows the amplitude scaling stage to remove any discontinuities in the sinusoidal reference waveform which arise from the digital processing. (The worst case transients appear when changing the amplitude scaling - they could also be minimized

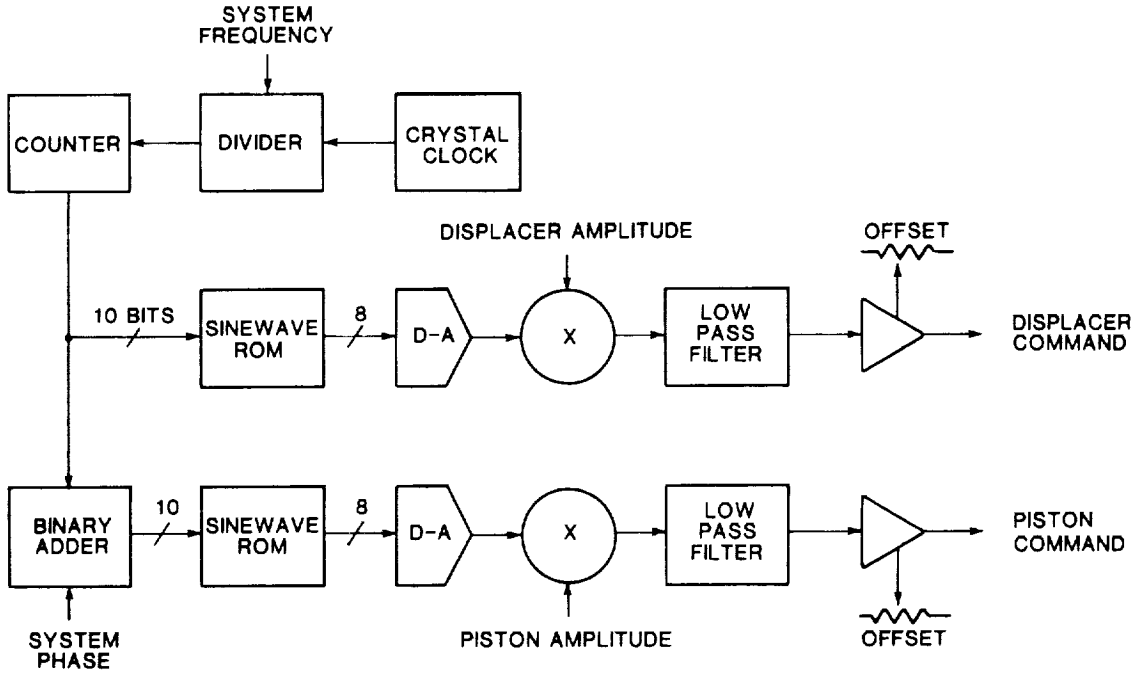

Figure 7-11. Block diagram of Axial Reference Generator.

by changing as the value of the input waveform is at a minimum, but this is a more complex solution.) Because the two filters are identical, phase shift (10 ° at 20 Hz) applied to each channel is the same, and the relative phase of the output waveforms remains as programmed.

Full scale gain and dc offset adjustments are included in the output stages for each waveform circuit. These are set during initial calibration.

7.5 Counterbalancing

Axial cooler vibrations are minimized by driving the counterbalance mass in opposition to the inertial forces produced by the piston and displacer shafts. Mechanical adjustment of the counterbalance housing, relative to the piston/displacer housing allows the two motion systems to be aligned co-linearly to minimize any introduction of radial vibrations.

A simple circuit (Fig. 7-12), located within the counterbalance driver, scales the piston and displacer position outputs (according to their masses relative to the counterbalance mass) and sums the two to create a command signal for the counterbalance. Trimpots on the circuit card permit the scaling to be adjusted while the system is running. Provisions for phase shifting each of the input signals accommodate feed-forward to compensate for closed-loop phase response errors in the counterbalance position control loop, once the residual frequency components of vibration have been identified.

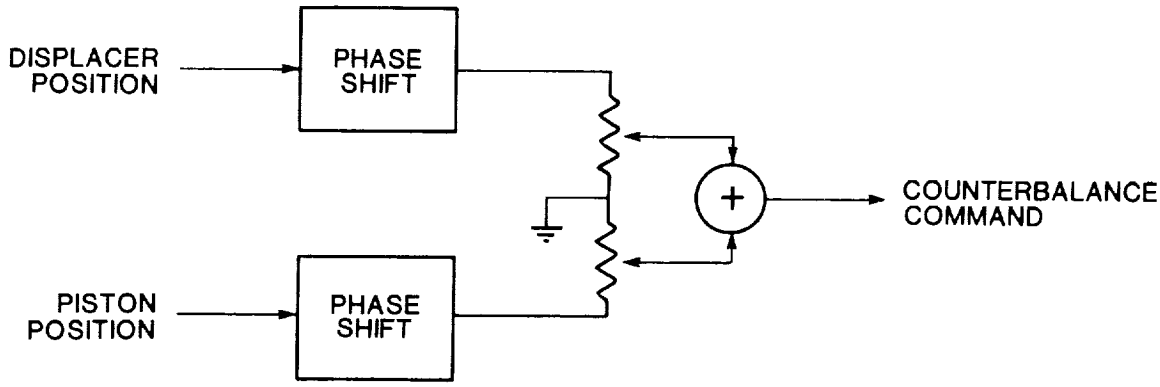

Figure 7-12. Block diagram of counterbalance command circuit.

The calibration of the LVDT signals, in particular their polarity with respect to actual motion, is critical for the function of the system. Both the piston and displacer LVDT outputs are positive-going as the shafts move toward the cold end of the cooler. The counterbalance LVDT output is positive going as the shaft moves away from the cold end.

The cooler is equipped with an axial accelerometer, located at the counterbalance end, to provide quantitative measurement during test. The output of the accelerometer was observed on an oscilloscope. The accelerations induced by the piston motor dominate the net vibration spectrum, so it was first necessary to operate the displacer motor alone (piston amplitude set to zero, displacer to design stroke), then slowly increase the weighting of the displacer command to the counterbalance (via the trimpot) while observing the accelerometer output. The trimpot is tuned to minimize peak excursions viewed on the scope.

The system was then operated with the piston operating at 20% full stroke (displacer at design stroke), and similar tuning of the piston weighting was completed. The piston stroke was increased to design stroke, and the system was permitted to cool and stabilize its operating conditions before making final adjustments of the weighting values. It is interesting to note that the minimum accelerometer output can be attained by tuning the system while placing one hand on the cooler. The tactile sense is more sensitive than the instrumentation.

8. SYSTEM CONTROL AND INSTRUMENTATION

The electronic systems required support the cooler operation are shown in the block diagram of Figure 8-1. The cooler electronics are housed in a separate enclosure and interconnected to the cooler cradle assembly (not shown) through detachable umbilical cables. AC power from the utility line is backed up by an uninterruptible power system, then converted to dc power required for system operation. Axial and radial subsystems and cooler instrumentation are coordinated by the System Controller which acts as an intelligent interface for the operation of the cooler. The following section describes the support systems which are not covered by the sections which detail essential motion control.

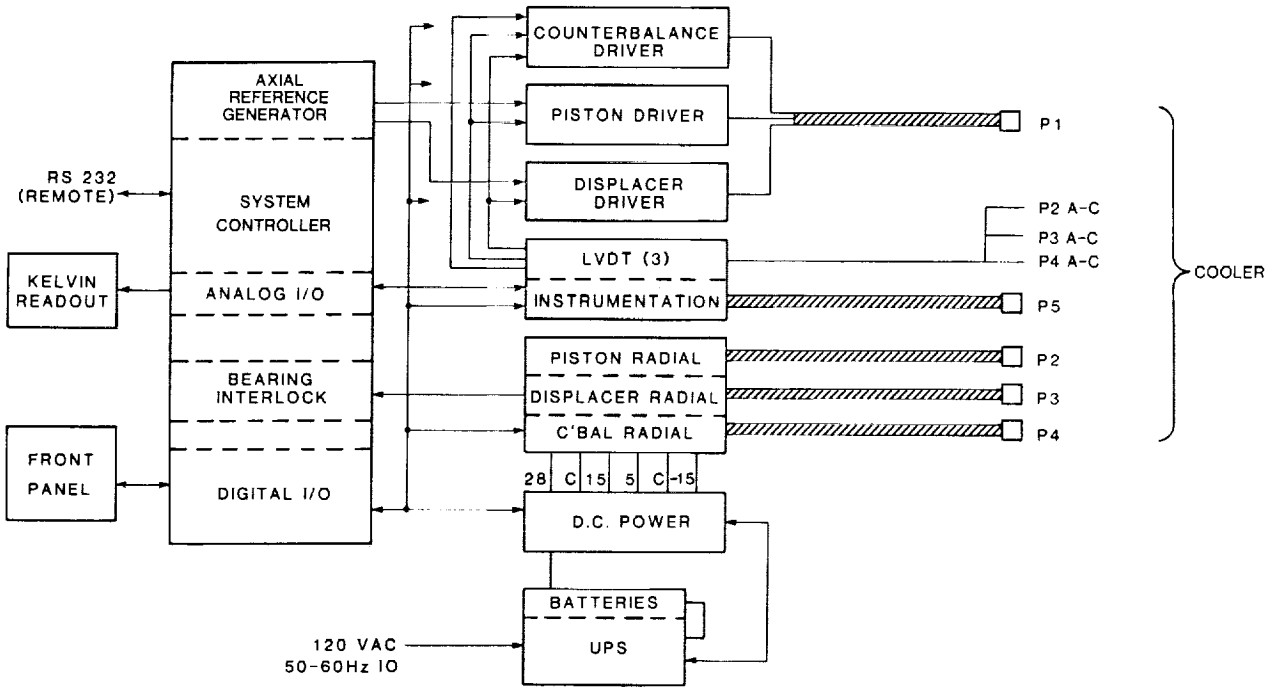

Figure 8-1. Block diagram of cooler electronic system.

8.1 System Controller

The System Controller is a microprocessor-based system which provides an orderly sequence of operation on both start-up and shutdown, monitors interlocks, responds to faults, and provides an interface through which the user can command or monitor operation (see Fig. 8-2). The interface operates on two levels: a local mode which provides simplistic control of the essential cooler function; and a remote mode in which a desktop computer (and software) provides an extended command set and displays detailed status information.

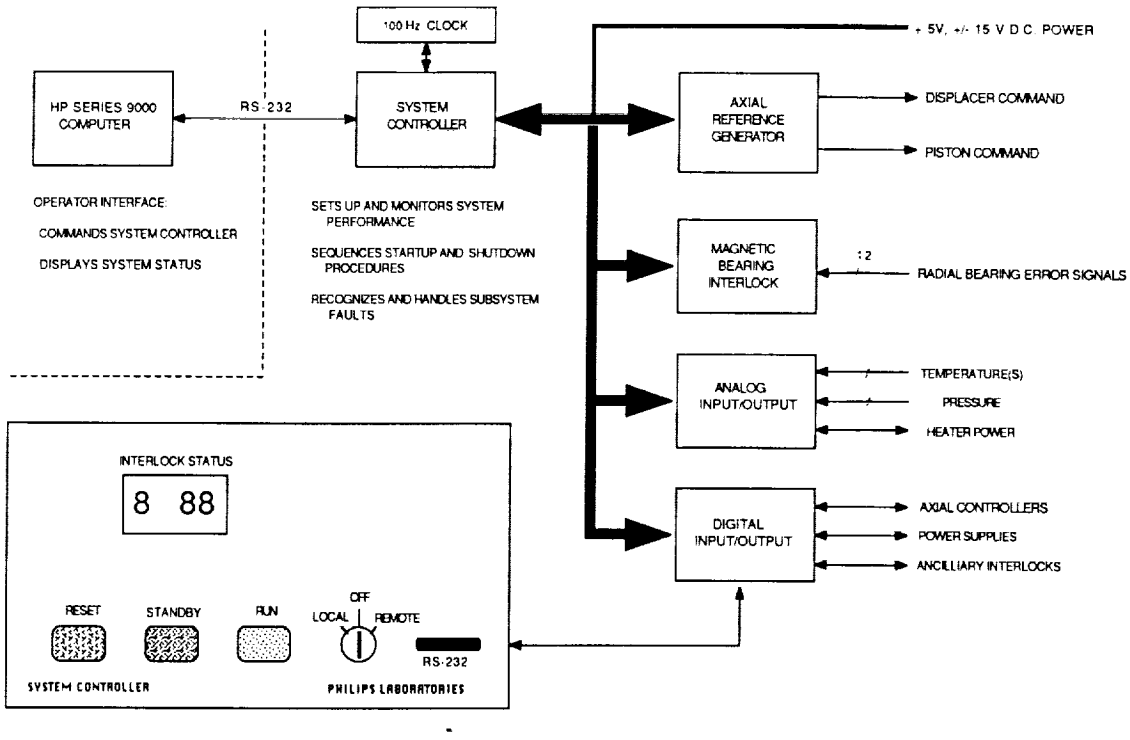

Figure 8-2. Block diagram cooler system controller.

8.1.1 Hardware Description

The System Controller uses the popular STD Bus and a mixture of commercial and custom circuit boards to implement the functions of the cooler system. A Motorola 6809 based microcomputer board contains the system processor, the associated hardware reset switch, the ROM based executable code, and the serial communications port. The STD Bus interface ties it into a commercial digital input/output board, a commercial analog input/output board, the axial command reference generator (described in Sect. 7.4), and the bearing interlock (described in Sect. 8.5).

The digital I/O circuit contains four 16-bit ports which operate in a mixed mode (each port has 8 input bits and 8 output bits) mapped as memory. The current status of the output bits in each port can be read back by the processor. The I/O ports support the front panel interface, power supply control and status, motor driver control and status, and bearing control and external interlock status.

The analog I/O board contains a multiplexed analog-to-digital converter (presently using 8 of 16 single-ended input channels) with 10 bit resolution, which monitor various run time parameters. Two 8-bit digital-to-analog converters support heater power control and the front-panel temperature readout.

Included on the bearing interlock circuit card is a 100 Hz clock circuit which activates the processor Non-Maskable-Interrupt. This is used as both a general purpose timing source and a 'watchdog timer' capable of forcing a system recovery in the event of a software execution fault.

8.1.2 Software Description

The software description is presented in a top down approach, with high level functioning described first, followed by the local and remote command function subroutines, and finally brief descriptions of the specific task subroutines.

(1) Main Program

Figure 8-3 is a simplified flow chart of the fundamental software execution.

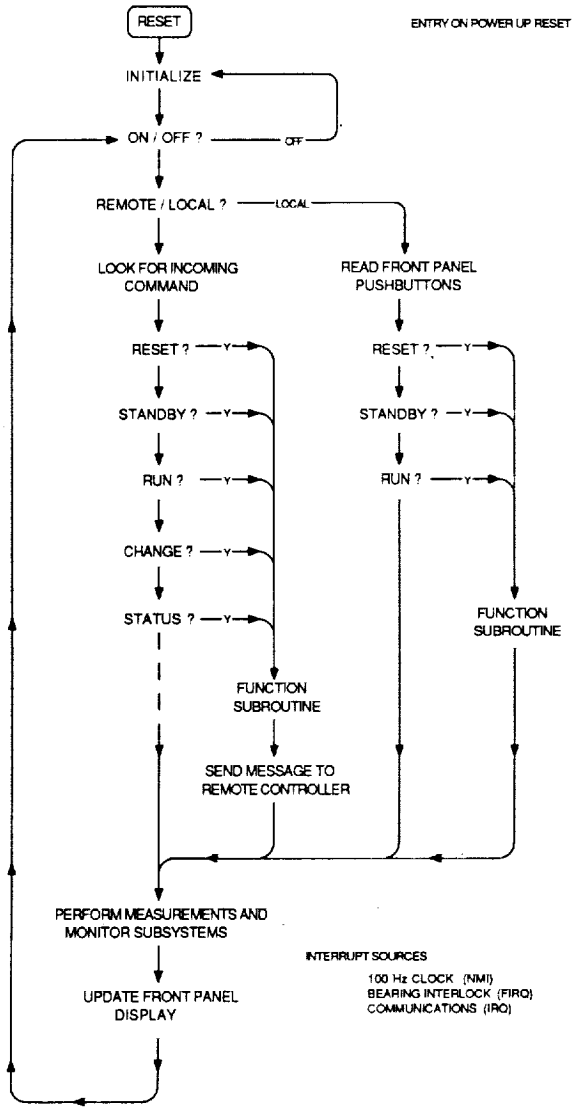

Figure 8-3. Flowchart of fundamental software execution.

An initialization routine checks the status of critical subsystems and will prevent startup if faults are detected. Error codes are presented on the front panel INTERLOCK STATUS display.

The key switch is tested. If it is OFF, then the system simply loops and rechecks status. If the key switch is in LOCAL or REMOTE and system is ready, the front panel RESET button will light, indicating that dc power is on and that the magnetic bearing systems are active.

If the LOCAL mode has been selected, then the front panel pushbutton status is tested, and the appropriate command routine is entered, if selected. From RESET, one may only proceed to the STANDBY (launch) mode, in which the axial drives are activated and commanded to maintain 'center' position. (The sequence interlocking is omitted from the flowchart for clarity.)

Cooling is initiated by proceeding to the RUN mode. The axial frequency and phase angle are established, and then the piston and displacer amplitudes are gradually increased to the final operating point (65°K 5W). Operation will continue unless the system is commanded to return to the STANDBY or RESET mode, or if it is forced to the RESET mode by the interlock system.

In the REMOTE mode, commands are received via the RS-232 serial communications port. In addition to activating the three basic operating modes, the remote command set includes functions which can modify the axial operating conditions or report on the cooler system status. This permits more sophisticated control of the cooler system, via the remote control software, as may be required to attain various operating points for parametric testing or in the target application. Each REMOTE command generates a reply at the serial communications port, to acknowledge the command or return requested status information.

Once a particular operating mode has been entered, and no further commands are encountered, the program simply loops and performs the following tasks:

- Watchdog timer is reset to prevent a forced return to the RESET mode.
- Power supplies are checked for faults. (PWRFLT)
- Axial drivers are checked for faults. (AXCHK)
- Analog instrumentation readings are checked and stored in a memory buffer area .(ANALOG)
- Ancilliary interlocks are checked. (ANCLRY)
- Front panel displays (including the INTERLOCK STATUS) are updated. (DSPLAY)
- System checks for new commands from the LOCAL or REMOTE source.

Interrupt sources

Under certain conditions, the main program will be interrupted to attend to more urgent tasks. Operation generally returns to the main loop once the interrupting task has been completed.

The Non-Maskable-Interrupt (NMI) is generated by the hardware derived 100 Hz clock. This routine first tests the status of the front panel RESET pushbutton, providing the local operator capability to override any task in progress (whether LOCAL or REMOTE), with minimal delay. The routine then decrements a general purpose variable, used to generate timing delays throughout the program. When the watchdog timer is active (always, except during initialization and in the event of a forced system shutdown), the watchdog timer parameter is decremented and tested for zero value. If it reaches zero, the system is forced to the RESET mode and the INTERLOCK STATUS display indicates the system timeout fault code (700).

The bearing interlock hardware can activate the Fast Interrupt Request (FIRQ), which calls the interrupt service routine (BERINT). This routine determines the severity of a bearing fault and, if warranted, will take action to remove the fault source. A more detailed description of the bearing interlock is given in Section 8.5.

The serial communications device, when enabled, will generate an Interrupt Request (IRQ) whenever the transmitter register has completed a byte transmission or whenever the receiver register has been filled. The communications service routine (COMINT) determines which event has occurred and steers software execution to the appropriate handler subroutine (WRTOUT or READIN).

(2) Command Functions

The command function routines are briefly described in text and flowchart forms (see Figs. 8-4 through 8-10). Each REMOTE command elicits a reply from the System Controller. Some commands require parameter information to be included with the command transmission, while others obtain status information with the reply. Program execution returns to the main control loop after completion of the command task.

The RESET routine disables the axial drivers, disables the cold finger heat load and clears the front panel interlock status display.

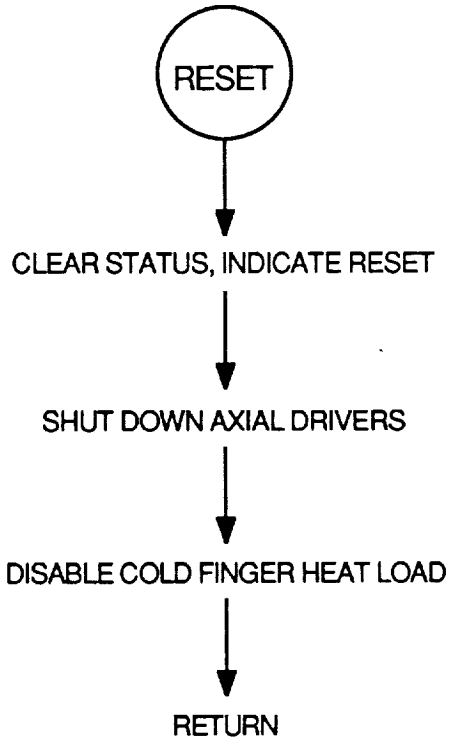

Figure 8-4. RESET flowchart.

The STANDBY routine activates the axial driver subsystems and brings the axial commands to zero (or 'center') position. If the system was running, the amplitudes are incrementally decreased to zero. During this transition time, both the RUN and STANDBY pushbuttons will be illuminated. (The RESET and STANDBY will be illuminated during that transition also, but it is generally too brief to be visually detected.)

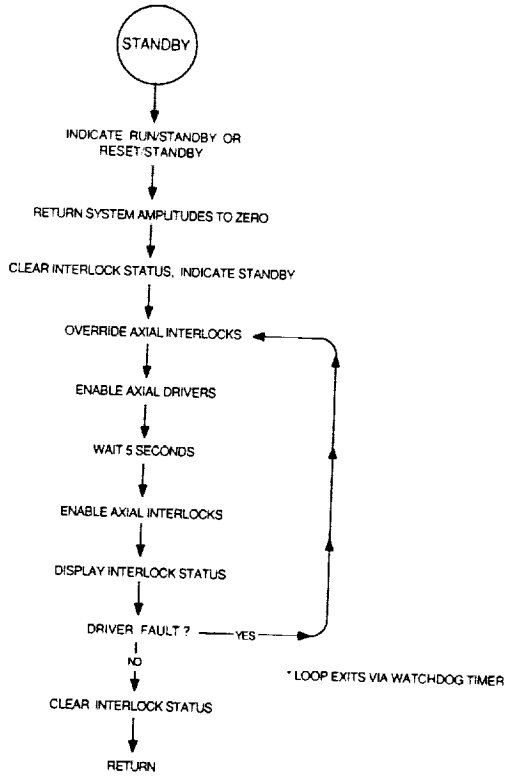

Figure 8-5. STANDBY flowchart.

The INTERLOCK STATUS will be cleared and the axial driver interlocks overridden for 5 seconds. This should provide sufficient time for the axial shaft positions to come to center if they were not previously there (i.e., on initial startup). If the drives do not reach center, then the interlocks will detect and report the offending axial system upon their reactivation. The standby routine will loop back and try again to center the shafts. This process continue until the shafts attain center (and the routine exits normally) or the watchdog timer forces the system back to the RESET mode. (If this happens, one can manually attempt to re-enter the STANDBY mode.)

The RUN routine first illuminates the RUN pushbutton, indicating that the system is going toward or has attained the final operating position. The routine then copies the default axial parameters (frequency, phase, amplitude) from the program ROM to a RAM buffer area. The proscribed operating point is attained incrementally by the CHGFRQ, CHGPHZ and CHGAMP routines. The order of these routines ensures that the axial motions will always provide cooling (rather than heating) at the cold finger.

The routine exits when the final operating point has been reached.

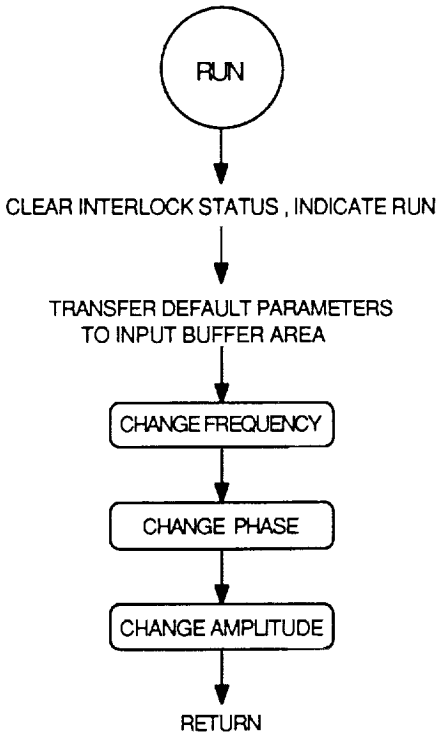

Figure 8-6. RUN flowchart.

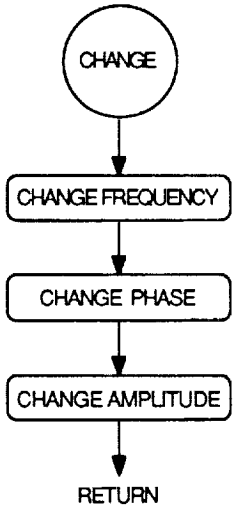

Figure 8-7. CHANGE flowchart.

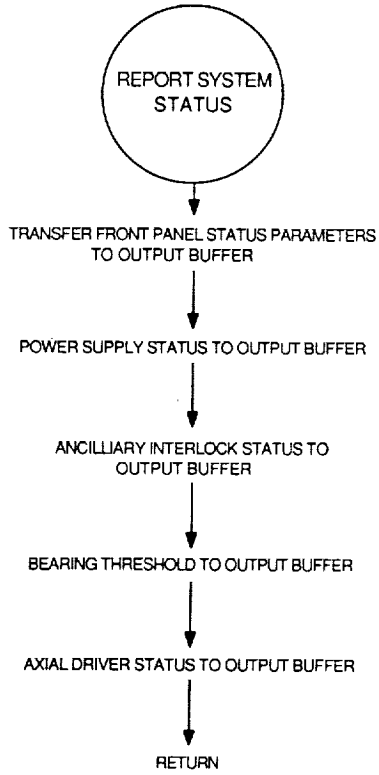

Figure 8-8. REPORT SYSTEM STATUS flowchart.

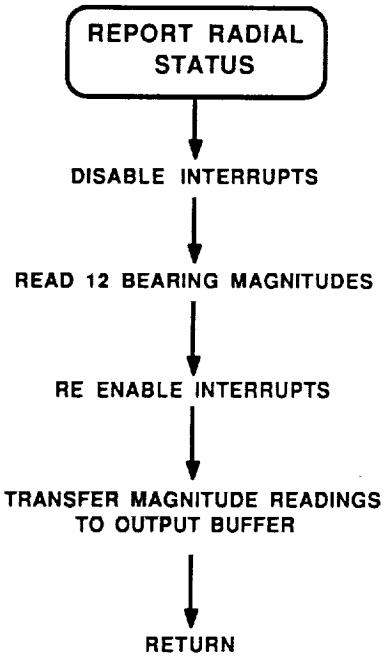

Figure 8-9. REPORT RADIAL STATUS flowchart.

The CHANGE routine is a REMOTE command which utilizes the CHGFRQ, CHGPHZ and CHGAMP subroutines to attain a new axial operating based on parameters included with the command transmission. In practical operation, only the piston amplitude will be varied, as this proportionally regulates the cold production.

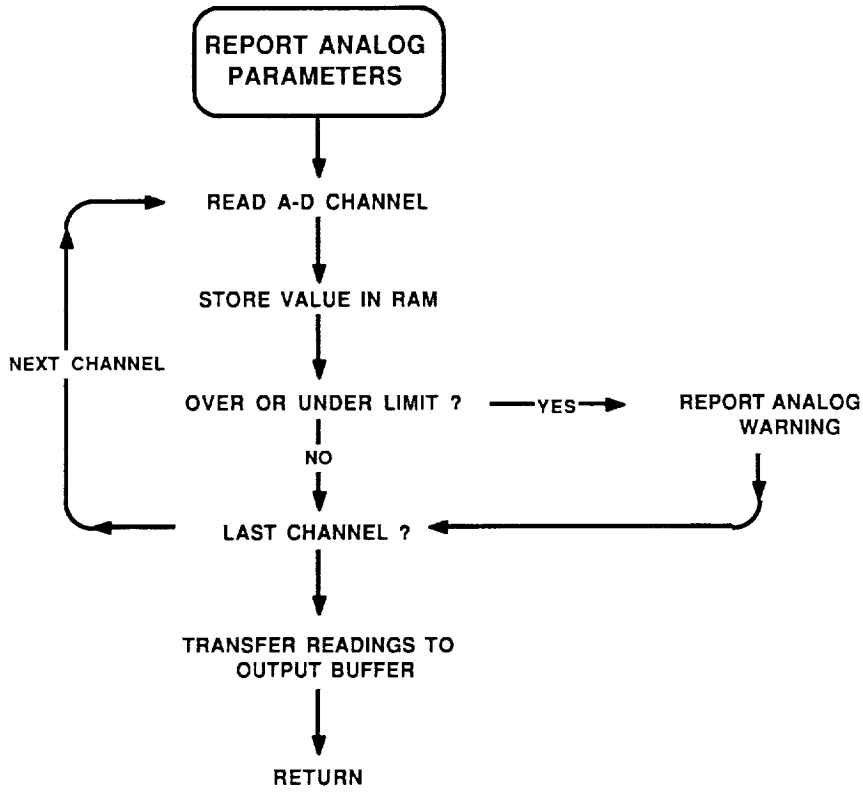

Figure 8-10. REPORT ANALOG PARAMETERS flowchart.

REPORT SYSTEM STATUS transfers current run time status information to the RAM output buffer for subsequent transmission to the remote control computer.

REPORT RADIAL STATUS reads and stores current (instantaneous) radial bearing magnitudes (12 readings) to the output buffer area for subsequent transmission to the remote control computer.

REPORT ANALOG PARAMETERS reads and stores current (instantaneous) analog scanner (14 readings) to the output buffer area for subsequent transmission to the remote control computer.

SET HEATER CONTROLLER programs the cold finger heat load power (in WATTS) based on a parameter included with the command transmission. If the programmed value is zero, then the heater output is physically disabled (see Sect. 8.4).

(3) Task Subroutines

The individual task subroutines used by the main program and command routines are described here briefly. The specifics of their implementation are highly dependent on the hardware configuration and may be determined from the annotated software listing in conjunction with the electrical schematics.

INIT	initialize System Controller
AXRSET	reset axial drivers
CHKAX	read axial driver status
CHGFRQ	change axial reference frequency
CHGPHZ	change axial reference phase
CHGAMP	change axial reference amplitude(s)
PWRFLT	determine power supply fault
BRGINI	initiate bearing interlock
BERINT	interpret bearing interlock fault (FIRQ)
BRSTAT	measure bearing error magnitudes
DSPLAY	update front panel displays
PNLTST	lamp test
ANALOG	read instrumentation parameters, update temperature readout
ANCLRY	read ancilliary interlock status
DLA500	5 second software delay
DLA100	100 millisecond software delay
INCOMM	initialize communications hardware
READIN	read incoming command message
WRTOUT	write outgoing reply message
COMINT	interpret communications request (IRQ)
NMI	Non-Maskable Interrupt service
SWI	SoftWare Interrupt (used to return from fault conditions)

8.2 Power Supplies

The power conditioning system is designed for maximum reliability to maintain the operation of the magnetic bearing system and protect the cooler from mechanical damage. An uninterruptible power system (UPS) provides conditioned 120 Vac, 60 Hz, single phase power to the cooler power supply system. The UPS uses normal 120 Vac facility power. In the event of a facility power failure, the UPS will continue to supply ac power to the cooler system, without interruption or degradation, drawing energy from a battery reserve. The System Controller monitors the status of the UPS and will shut down cooler operation, in a controlled fashion, prior to the loss of battery reserve, in the event of a prolonged power outage.

The cooler electronics and axial and radial drive systems are sustained by the dc power supplies, which are integrated into a single chassis. The required dc voltages are derived using commercial switchmode power supplies, for maximum conversion efficiency. Each voltage is supplied from parallel, redundant subsystems so that voltage is maintained with an individual failure. The System Controller monitors power supply status, and takes appropriate action to protect the cooler mechanism in the event of a power subsystem failure. A block diagram of the power supply system is shown in Figure 8-11.

8.2.1 DC Supplies

28 Vdc power is used to operate the axial and radial position control systems, with the majority of the power required for driving the piston. A system of three 28 V power supplies, which operate from the 120 V source, are paralleled via power rectifiers to a common capacitor bank. The regulated voltage outputs of each supply are carefully adjusted to promote current sharing while all three are in operation. The diode coupling will isolate a failed power supply and prevent it pulling down the rest of the system. The capacitor bank provides some output filtering for improved

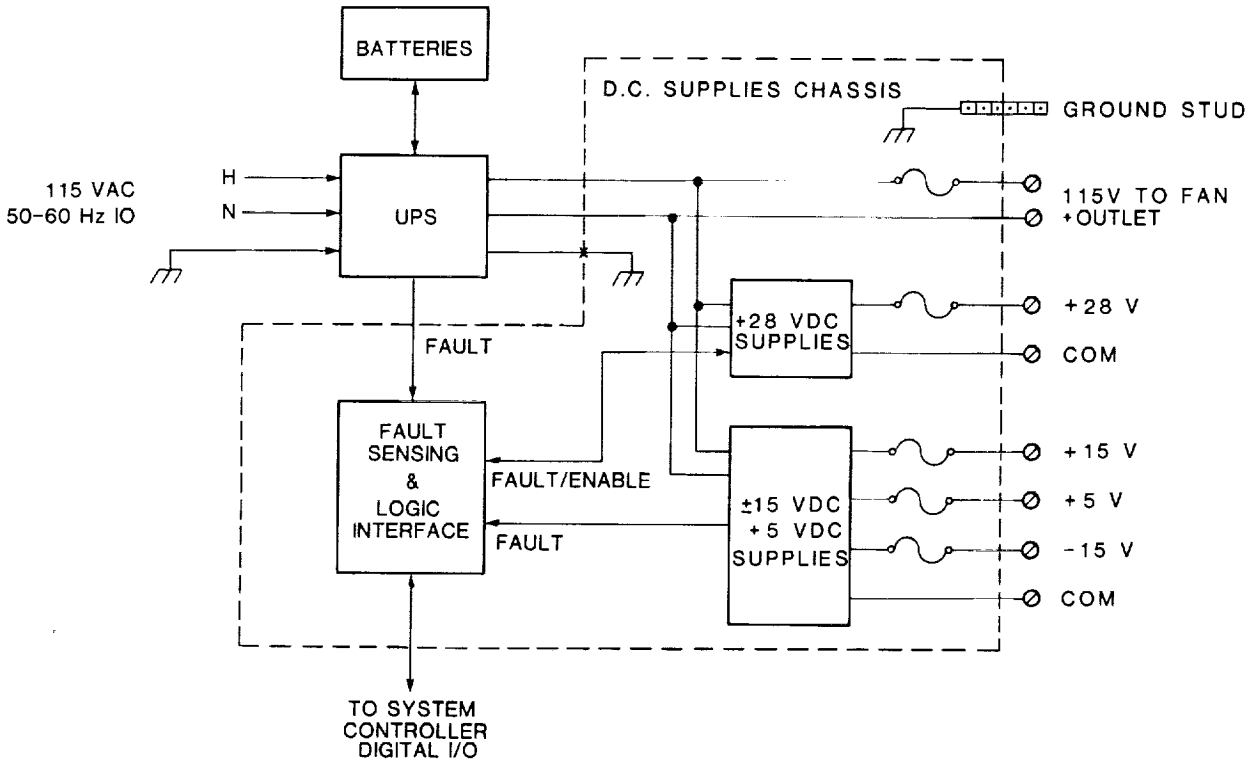

Figure 8-11. Block diagram of power supply system.

transient response, and has enough capacity to prevent an overvoltage condition which could arise from regenerative power produced in the axial motion systems.

Positive and negative 15 Vdc power is used by the signal conditioning circuitry of the axial and radial control systems, as well as for cooler system instrumentation. 5 Vdc is required by the System Controller and associated logic interface circuitry. These dc sources are provided by two multiple output power converters, which are designed for redundant mode operation. Key features include diode isolation and interactive voltage regulation to ensure current sharing.

The combined dc power supply outputs are fused at the rear of the power supply chassis. This is especially important with a power system which is designed NOT to fail, to prevent a fire in the event of a catastrophic circuit failure (i.e., short circuit due to human error). Specifications for the power supply system are listed in Table 8-1.

TABLE 8-1. Power Supply Specifications.

- Uninterruptible Power System (UPS):

Input	Output	Comment
96 - 132 Vac 57 - 63 Hz 6 kVA	120 Vac ± 2% 60 Hz 3 kVA	Single phase

- Battery:

72 V	3.6 kVA 120 Vac	Lead acid type, 5 minutes duration

- DC Power Supplies:

(3) 28 Vdc ± 0.3%, 13.7 A (3) 15 Vdc ± 0.5%, 3 A (3) -15 Vdc ± 0.5%, 3 A (2) 5 Vdc ± 0.5%, 30 A	Similar voltage outputs are paralleled using diode isolation. Active current sharing on all but the 28 volt supplies. Output currents rated at 50°C ambient.

8.2.2 Logic Interface

An isolated logic interface permits the System Controller to monitor the status of the power supply system and to enable or disable the 28 Vdc supply output.

The UPS has a relay isolated 'summary output' which will indicate any condition that impedes continued operation of the system (loss of input power, battery over/undervoltage or UPS circuit failure).

The 28 Vdc supplies are optically isolated from logic circuitry which can report a warning (loss of single supply) or failure (loss of two or more outputs) to the System Controller. An optically isolated enable circuit permits the System Controller to hold the power off during system initialization and to shut down in the event of a severe subsystem failure.

The two 5 V supplies have optically isolated fault outputs which are presented separately at the interface.

Summary fault signals are presented at the interface for both the positive and negative 15 V, each of which is comprised of three paralleled supplies. Optically isolated, open collector fault outputs are wire OR'ed together to indicate a fault if any one of the three should fail.

The System Controller response to power supply faults is discussed in Section 8.5.

8.3 Instrumentation

Temperature and pressure measurements obtained from instrumentation attached to the cooler are read into the System Controller where they are used for interlocking or available for performance testing. This section describes the instrumentation and related signal conditioner(s).

8.3.1 Cold Finger Temperature

The cold finger temperature is monitored by two (for redundancy) calibrated silicon diode sensors installed into opposite sides of the cold plate and secured with thermal epoxy. A four-wire measurement system excites the diode with a precision 10 microampere dc forward current, while accurately reading the diode forward voltage drop (which increases with decreasing temperature). The forward voltage reading is amplified and passed on to the System Controller analog-to-digital converter for subsequent interpretation and display.

The diode exhibits an approximately linear V_f vs. temperature over the range of 300 to 40°K. Precise measurement must be interpreted via a calibration table supplied by the diode manufacturer.

The System Controller uses one of the diode readings to index a ROM look-up table (based on linear interpolation between points given in the manufacturer's data sheet) which provides corrected numeric data for output to the front panel COLD TEMPERATURE display. This display is accurate to 1°K over the 300 to 20°K range. The amplified outputs of the signal conditioner are also available to the remote control computer with improved resolution, and can be reliably interpreted to within 0.5°K.

8.3.2 Housing Temperature

The cooler is outfitted with platinum-resistance temperature detectors (RTD) at key locations on the motor housing. The System Controller monitors three housing temperatures of particular interest: the displacer motor/heat exchanger area (where heat of compression is removed); the piston motor winding area (maximum electrical input power); and the counterbalance motor winding area.

The signal conditioning circuits for the RTD uses a 4 wire measurement technique with a 1 mA dc excitation. Voltage drop is measured and amplified (scaled) to provide good resolution in the range of 0 to 100°C. The amplified reading is passed on to the System Controller analog-to-digital converter. The information is used as part of the interlock system and is also available via the remote control computer.

8.3.3 Housing Pressure

The cooler internal pressure is monitored at three locations: the compression side of the piston (working volume), the buffer side of the piston, and in the counterbalance housing. The pressure transducers use a strain-gage element as part of a bridge circuit (with temperature compensation) to provide a basically self-contained measurement device. The 15 Vdc supply powers the bridge circuit, and the output is scaled by the differential amplifier of the signal conditioning circuitry to provide good resolution through the System Controller analog-to-digital converter. The readings obtained by the analog-to-digital converter are instantaneous values, while the actual gas pressures are dynamic. The digitally obtained data may be used to determine extreme or average values (as required for interlocking). The continuous analog outputs of the pressure transducer amplifiers are available at the front edge of the signal conditioner circuit card to accommodate parametric testing.

8.4 Heat Load

A resistive heater element is attached to the cold plate surface to provide a test load for evaluating cooler performance. A closed-loop control system maintains a constant programmed power dissipation in the heater element, even as the resistance varies with cold finger temperature (see Fig. 8-12).

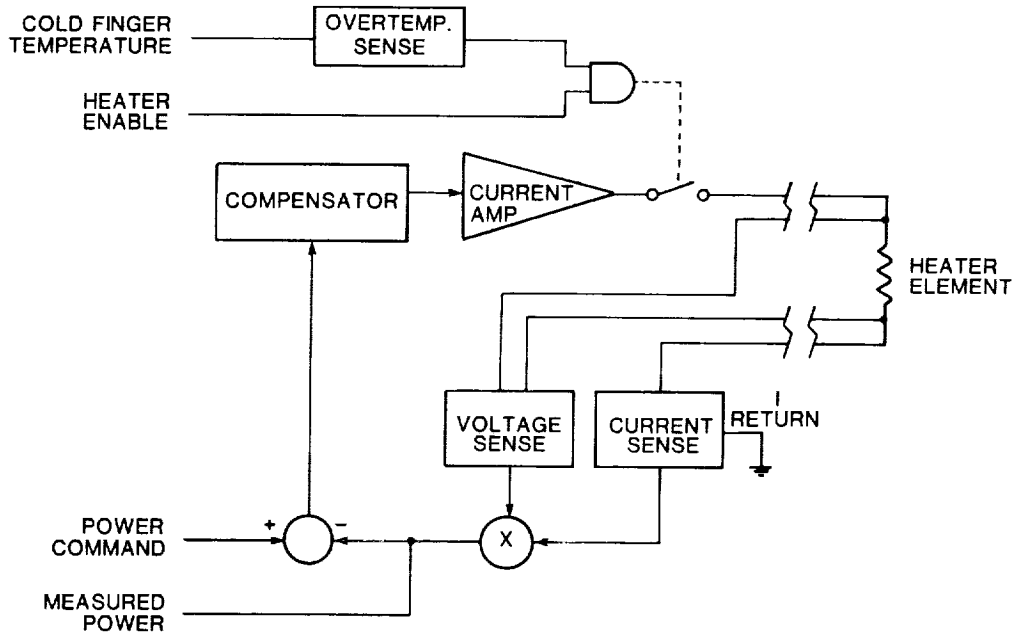

Figure 8-12. Block diagram of heater controller.

A four-wire system supplies regulated current to the heater element and accurately measures the voltage drop across the element terminals. The controller circuitry multiplies the regulated current and measured voltage to determine the instantaneous power. The measured power is compared to the command input to establish an error. The error is amplified and compensated to regulate the output current in a stable fashion to maintain constant heater power.

A relay placed between the current source and the heater element can ensure zero power into the heater element. Closure of this relay to enable the heater requires two conditions. The System Controller must set the heater controller enable input and the cold finger temperature must be below a preset level. The first condition is met anytime the System Controller demands a power output

of more than zero watts. The second condition is provided by a comparison circuit on the heater controller board. An adjustment trimpot is preset to prevent heater operation above 150°K.

Note that the heater can only be enabled through the remote control interface, which provides both programming of the power level and readback of the measured power. The heater is automatically disabled whenever the system enters the RESET mode of operation.

8.5 Interlocks

The interlock system consists of both hardware and software devices for protecting the cooler mechanism. The interlock system recognizes two types of faults. Warnings are issued for faults which should eventually be attended to. Failures arise from faults which can damage the cooler mechanism and thus warrant some protective response from the System Controller. Table 8-2 lists valid INTERLOCK STATUS codes and their meaning. Codes beginning with an even number indicate a warning, while codes beginning with an odd number indicate a failure. The remainder of this section describes the interlock fault conditions and the System Controller response with respect to the individual subsystems.

8.5.1 Power Supplies

Power supply status is tested twice during the initialization procedures following a hard (processor) reset. At the first pass, all supplies, except the 28 Vdc should be active. The second pass rechecks status after the 28 Vdc has been activated. If any faults are detected, the INTERLOCK STATUS display will register the appropriate warning or failure code and the system will not enter the RESET mode.

Loss of any of one of the redundant dc supply components will be reported as a warning to the INTERLOCK DISPLAY. The system will continue to operate normally, assuming that the backup supplies are operating. The error should be attended to as soon as it is practically possible. A loss of two of the three 28 Vdc supplies will force a system shutdown. The 28 Vdc fail code will appear at the INTERLOCK DISPLAY.

A UPS fault should only be generated in the event of a facility power failure, assuming that the UPS itself is functioning correctly. Upon detecting a UPS fault, a warning is issued to the INTERLOCK STATUS display and a timer is initiated to begin a delayed system shutdown, based on power drain for full output operation and battery capacity. If power is restored prior to shutdown, the countdown will be aborted and normal operation will continue. If not, the system will shut down and the UPS fail code will be displayed.

Recovery from a system shutdown due to a power supply failure requires a hardware reset. The system will not re-initialize unless the offending circuit has been corrected.

8.5.2 Axial Drivers

Each of the three motor drivers has three interlock devices, any of which can disable that amplifier (see Sect. 7.2). During normal operation, the status of the amplifier command is tested during each pass of the main program loop. If the system is in the STANDBY or RUN mode, the amplifiers

TABLE 8-2. Valid Interlock Status Codes.

Fault Code	Identifier	Fault	Identifier
0 01	UPS warning	1 01	UPS failure
0 02	28 V p.s. warning	1 02	28 V p.s. failure
0 03	5 V p.s. warning		
0 04	15 V p.s. warning		
0 05	-15 V p.s. warning		
2 00	Piston X-front bearing warning	3 00	Bearing failure
2 01	Piston Y-front bearing warning	3 01	Bearing failure
2 02	Piston X-rear bearing warning	3 02	Bearing failure
2 03	Piston Y-rear bearing warning	3 03	Bearing failure
2 04	Displacer X-front bearing warning	3 04	Bearing failure
2 04	Displacer Y-front bearing warning	3 05	Bearing failure
2 06	Displacer X-rear bearing warning	3 06	Bearing failure
2 07	Displacer Y-rear bearing warning	3 07	Bearing failure
2 08	C'balance X-front bearing warning	3 08	Bearing failure
2 09	C'balance Y-front bearing warning	3 09	Bearing failure
2 10	C'balance X-front bearing warning	3 10	Bearing failure
2 11	C'balance Y-rear bearing warning	3 11	Bearing failure
5 1X	Displacer axial fault		X is a binary weighted value:
5 2X	Piston axial fault		1 = amplifier disabled
5 3X	C'balance axial fault		2 = servo loop error
			4 = overstroke error
7 00	Watchdog timeout (system forced to RESET mode)		
8 00	Cryo temperature 1 parameter over or under limits		
8 01	Cryo temperature 2 set in program ROM		
8 02	Displacer housing temperature		
8 03	Piston housing temperature		
8 04	Spare temperature		
8 05	C'balance housing temperature		channels 9-15 are available
8 06	Piston housing pressure (He)		for expansion
8 07	C'balance pressure (N)		
8 08	Heater power		
9 00	Reserved radial bearing LED current fault		
9 01	Reserved LVDT oscillator fault		
9 02	not used		
9 03	External interlock		cabinet over-temperature
9 04	External interlock		coolant flow loss
9 05	External interlock		spare
9 06	External interlock		spare
9 07	External interlock		spare

Note: Odd-valued FAULT CODES will result in RESET or shutdown.

will be enabled. A serial poll of each of the amplifiers tests the status of all three fault flags. Any fault will force the system to the RESET mode, disabling all of the axial drivers. The exception to this is during the transition from RESET to STANDBY mode, when the axial interlocks are overridden (Sect. 8.1.2-2).

The INTERLOCK STATUS display will show an axial driver failure code, indicating the source and specific nature of the fault. Note that it is possible for the code to reflect multiple faults.

8.5.3 Watchdog Timer

The watchdog timer, activated during system initialization, will force the system to the RESET mode if the software execution does not include a watchdog timer parameter reset. The timer parameter is decremented during the NMI service routine, which must occur so long as the processor and timer circuits are working.

Most of the executable code includes provisions for maintaining the timer parameter, so the error should never occur in normal program flow. The exception to this is during the transition from RESET to STANDBY mode, where the watchdog is utilized provide an exit if the process takes longer than expected.

The watchdog timer is disabled if another fault forces the system shutdown, so that the interlock display will reflect the cause of the system shutdown rather than a timeout indication.

8.5.4 Analog Parameters

During a read of the analog scanner, which takes place upon each pass of the main program loop, each scanner parameter is compared to a predetermined high and low limit, stored in the program ROM. A warning code is issued if any of the parameters is outside of the limits. The code identifies the offending channel.

The warning may or may not be trivial, depending upon environmental conditions. Therefore, the system does not necessarily take any corrective action to alleviate the symptom. It is recommended that the operator be aware of any analog parameter warning and decide what action to take or that the remote control system possess the ability to make such a decision.

8.5.5 Bearing Interlock

The bearing interlock is probably the most critical subsystem of the cooler, since a shaft touchdown (while the shafts are in motion) will result in damage to the clean metal surfaces. Even minor damage in the clearance seal areas can render the cooler useless and require disassembly for repair.

The bearing interlock is comprised of two parts: the bearing monitor, which is the hardware portion, and the interlock software. The software provides flexibility by screening the monitor output to discriminate between transients and genuine faults. If a detected fault magnitude is below a preset critical limit, the sensitivity of the monitor is reduced to permit continued operation.

The bearing monitor circuit is designed to operate as a free running scanner which will alert the System Controller processor via the Fast Interrupt Request (FIRQ) whenever a reading is out of tolerance. This provides continuous observation of the bearing errors and minimizes the software overhead for the System Controller processor.

(1) Circuit Description

The block diagram of Figure 8-13 shows the essential components of the monitor circuit. The signals on the left side represent the interface to the system processor. The bearing error signals enter the circuit via the multiplexer on the upper right. Error outputs from the bearing control circuits are sequentially selected by the analog multiplexer for presentation to the window comparator circuit. A presettable counter circuit scans the multiplexer at 10 microseconds per channel, viewing all 12 channels in 120 μS. An 8 bit digital-to-analog converter determines the magnitude at which the window comparator will generate a fault signal.

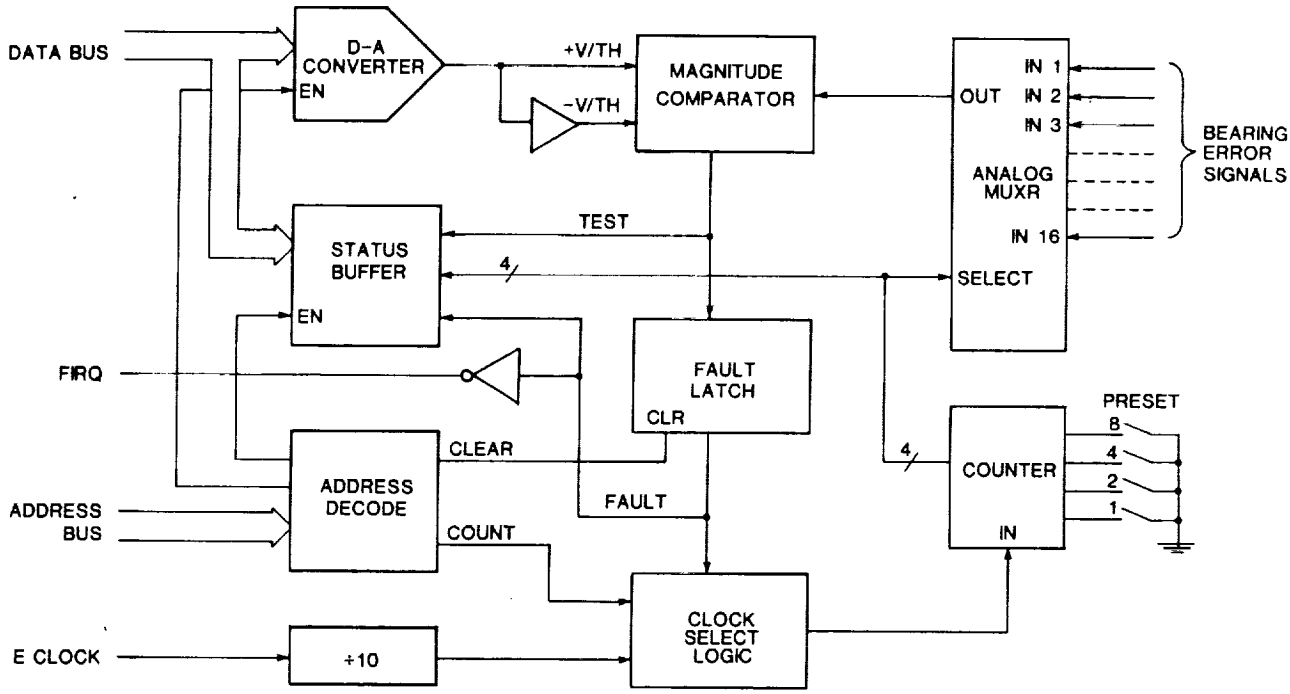

Figure 8-13. Block diagram of bearing monitor.

The occurrence of a fault will halt the scanner at the offending channel and alert the system processor via the FIRQ signal. The bearing interlock software can then determine the status of the interlock (read channel number, TEST and FAULT) and the magnitude of the fault (reprogram the D-A until TEST is clear).

The system processor can also write to the interface to produce a pulse on the COUNT and CLEAR signals. The COUNT signal can single step the channel selector whenever the FAULT signal is active. The CLEAR signal is used to reset the fault latch. This removes the FIRQ request and resets the clock logic to resume scanning.

(2) Software

During initialization following bearing activation, the bearing monitor is loaded with a minimal THRESHOLD value (stored in program and RAM memory), and the CLEAR line is pulsed to begin scanner operation. (see Fig. 8-14)

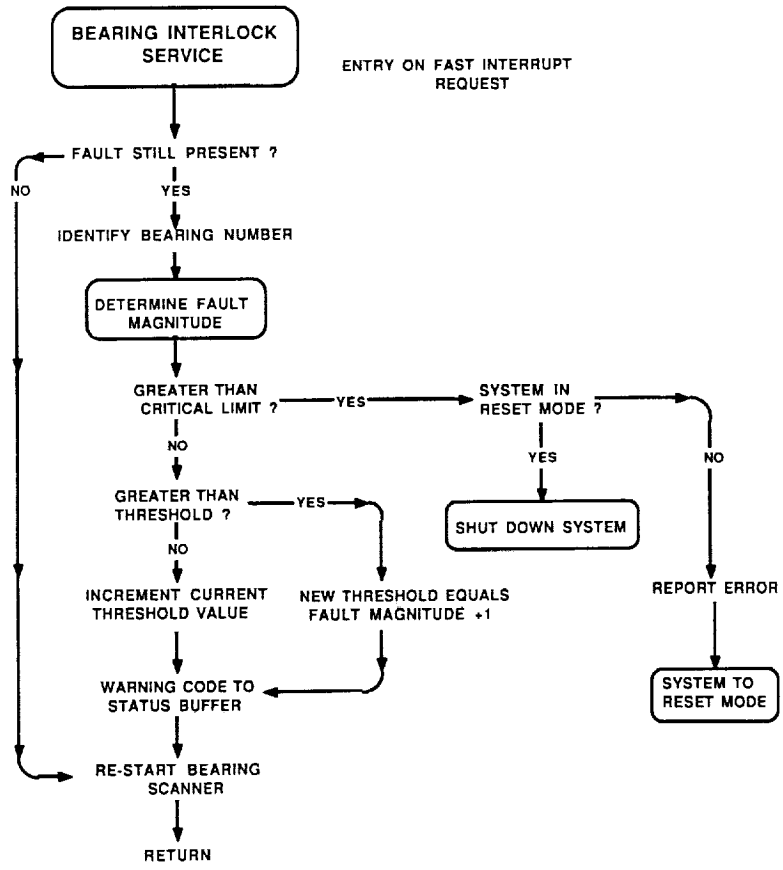

Figure 8-14. Bearing interlock service - flow chart.

Upon receiving an interrupt request, the service routine checks the monitor status and checks for the TEST signal. If this signal is clear, the FAULT was probably due to a transient condition. The CLEAR line is pulsed to clear the FIRQ request and scanning is resumed.

If the fault is still present (TEST true), the CRITICAL LIMIT value is retrieved from program memory and loaded to the D-A converter. If the TEST flag is still true, the fault is severe enough to warrant the initiation of one of two shutdown sequences:

- If the system is in the RUN or STANDBY modes, then the axial drives are disabled and the system is returned to the RESET mode. The error is reported as a fault and the scanner is re-started. The shutdown of the axial drives will generally clear the fault condition.
- If the system is in the RESET mode, then the fault is probably due to a bearing circuit failure. The 28 Vdc is shut down to prevent further damage to the bearing electronics. The fault is reported and System Controller operation is halted.

If the TEST signal is clear, then the fault is not critical. The routine seeks the magnitude of the fault by ramping down the value of the D-A converter until the TEST signal goes true. If the measured fault magnitude is greater than the present THRESHOLD value, then a new THRESHOLD is established by adding 1 count to the measured fault magnitude. If it is less than the present THRESHOLD, then the present THRESHOLD is incremented by 1. A bearing warning is issued, and program execution is re-entered in the current mode of operation.

The bearing THRESHOLD parameter is available via the remote control software and provides an indication of overall bearing performance. Additional software routines uses the bearing monitor circuit to determine the instantaneous magnitude of all the bearings (one scan of all channels), which can be reported to the remote control computer.

8.5.6 Remote Operation

The RS-232 interface provides a communications path for accessing the remote control routines embedded in the System Controller software. Commands are transmitted and replies received as 16 word (32 byte) blocks transmitted at 19.2 kilobaud, with RTS/CTS handshaking (compatible with INPUT and OUTPUT functions of Hewlett Packard Basic 2.0 or higher).

A Hewlett Packard series 9000 desktop computer served as the Remote Controller during the cooler evaluation tests. Custom software was written to sequence the fundamental operations (RESET,STANBDY and RUN) and cooler run-time data was acquired and updated once per second. Automatic data logging to a hardcopy printer is enabled during the RUN mode. Additional screens can be called up, using softkeys, to observe the radial bearing status or to control the cold finger heat load. The remote control system has a far greater potential than we were able to utilize within our development time frame. More sophisticated data logging and the addition of closed-loop control would enable parametric testing which would otherwise require intensive manual manipulation of the system over an extended period of time (e.g., find design stroke to maintain x degrees to a heat load of y watts).

8.5.7 Ancilliary Interlocks

A set of external interlocks is provided to connect with external equipment necessary for safe operation of the cooler. These are accessible on a terminal strip located inside the electronic cabinet, near the umbilical feedthrough. Each input is optically isolated from the logic circuits, and can be configured to operate by opening or closing a path to circuit common (also provided). One input is wired to a thermal switch within the cabinet to provide enclosure overtemperature protection. Another is connected to a liquid flow meter in series with the linear motor cooling jackets. Two more are available for future expansion. A fault at any of these interlocks will force the system to the RESET mode, where risk of cooler damage is minimal.

9. MECHANICAL FABRICATION

9.1 General

In designing the refrigerator parts, consideration had to be given to the fabrication sequence, the heat-treating and heat-processing schedules, and the long-term stability of the completed components and assemblies. One important design decision was the choice of materials to be used for the refrigerator. Titanium was selected as the primary material due to its excellent long-term stability, ensuring that the dimensions of the parts would not change after fabrication if suitable care was used. Additionally, titanium offers an excellent strength-to-weight ratio, making it desirable for spaceborne applications. Since tight tolerances and close clearances were involved, thermal-expansion coefficients were important. Almost all metal parts were made of titanium, with the major exceptions being magnetic materials. Where minimum size or weight was the overriding concern, as in the displacer motor armature and the moving armatures for the magnetic bearings, vanadium Permendur was chosen as the ferromagnetic alloy, because it has the highest flux-carrying capacity available. For motor stators, Corovac, a compressed powder iron, was used. It has reasonably high flux capacity and excellent electrical resistivity. Magnetic-bearing pole pieces were made of vanadium Permendur which closely matched the coefficient of thermal expansion of titanium. These pole pieces were brazed into the housings, and the heavy walls of these parts required the thermal match. The cold-cap at the end of the cold finger was fabricated of aluminium, thermal conductivity being the most important parameter. Where electrical insulation was required, ceramics were used. It should be noted that all of these materials are inorganic. The complete absence of any organics from the working space of the refrigerator ensures successful operation for long periods of time with no degradation in cold performance. All parts of the machine can be vacuum baked at 100°C to drive out any adsorbed gaseous contamination.

Many of the internal joints in the machine are braze joints in which a filler metal is used to permanently join two components at an elevated temperature. Careful planning was required to combine the brazing processes with the other heat-treating processes. Magnetic materials had to be joined and magnetically annealed at the same time, in order to achieve optimum magnetic properties as well as a strong joint. The titanium parts were generally stress-relieved during the brazing operation, and this had to be done at a point in time when the heavy machining operations were completed. In some cases, many components of widely varying wall thickness were joined simultaneously, requiring careful consideration of the heating and cooling rates to prevent permanent distortion. Before ceramic parts could be brazed, they had to be prepared with several metallization steps. Braze metals had to be identified which would not react adversely with any of the metal components. In some cases a nickel transition piece was first joined to one of the parts, to allow the joining of two incompatible metals (such as copper to titanium). Quality control required testing every joint for helium leak-tightness, using a mass-spectrometer.

Another joining technique used was miniature TIG (tungsten inert gas) welding. This was used to form the hermetic seal for the thin cans around the motor coils, to hold the ceramic window assemblies in place, to join the two sections of the displacer, and to attach the end caps on the piston. The advantage of TIG welding is its highly localized heat which can be used on high-precision, finished parts without causing distortion. Additionally, the joint itself is very small, less than a millimeter thick, so it can be used on small components or in tight locations.

9.2 Displacer and Regenerator

The displacer in the Prototype Model serves two main functions: (1) as the armatures (moving parts) of the magnetic circuits for the magnetic bearings, magnetic springs, linear motor and the linear variable differential transformer (LVDT), (2) as a displacer performing the thermodynamic

functions of shuttling gas from the compression space to the expansion space through heat exchangers and the regenerator, and (3) as the housing for the thermal regenerator.

The warm end of the displacer has two vanadium Permendur rings which carry the flux of the magnetic bearings. In between the bearing areas there is the moving armature of the linear motor with its permanent magnets and the inner rings of the magnetic springs. The cold end houses the regenerator matrix. Along the length of the regenerator, the temperature drops from about room temperature down to 65°K or lower. To minimize heat leak into the cold end imposed by its large temperature gradient, the regenerator matrix itself and its containment wall need to have poor thermal conduction along the length.

The regenerator matrix material is 200 x 200 mesh phosphor bronze wire cloth. Circular discs were punched out from the wire cloth and stacked inside the displacer to achieve a 36% volumetric fill-factor. The wire discs are oriented with the weave direction 45° offset from one layer to the next. This is to achieve minimal thermal contact between layers resulting in high axial thermal resistance. Also, to avoid excessive heat leak, the regenerator wall is 0.020" thin.

9.3 Electrical Coils

9.3.1 General

This section describes the processes to be followed and the equipment, materials and techniques to be employed for impregnation of the wound electrical coils. This includes exposed units as well as those coils which are sealed within the working space of the cooler.

Several components of the cooler require a potting or impregnation treatment to immobilize wire members and fill interstices within the chambers of the windings. Vibration and motion can cause failure of wire leads and sections unless wire movement is eliminated by potting or impregnation.

Each magnetic-bearing pole coil is wound in a fixture without the use of a bobbin and the unit is rigidized and stabilized by the impregnation process before the coil is removed from the winding fixture.

Motor coils of the several linear motors are impregnated and baked prior to being sealed within their titanium covers.

The delicate (fine wire) coils of the LVDT sensors are similarly stabilized during fabrication by an impregnation treatment prior to the final encapsulation and sealing operation.

A list of the applicable component drawings is as follows:

Dwg. No.	Item	Notes
001304	Coil, Stator Iron Assy-Outer (Piston Motor)	1
000670	Inner Stator Assembly	2
000649	Stator (Insep. Assy.), Displacer Motor	3
001370	Coil, Magnetic Bearing, Displacer	5
001368	Coil, Magnetic Bearing, Piston	5
001374	Coil, Magnetic Bearing, Counterbalance	5
000633	Coils, LVDT Bobbin	6
001335	Motor Stator, Counterbalance	4

9.3.2 Requirements

(1) Equipment

Vacuum/Pressure Impregnation Chamber. Essentially any chamber of sufficient volume to hold the component in a fully immersed and completely withdrawn position over the varnish container and which can withstand a forepump vacuum (a few microns pressure) and moderate pressurization (about 15 psig nitrogen) is satisfactory. The chamber should be valved in such a manner that repeated evacuation/pressurizations can be performed easily. A means to immerse and withdraw the component from the varnish container while within the chamber should be provided. A custom-made chamber constructed of an 18" length of 8" dia. Pyrex pipe together with "O" ring seals, end-plate flanges and a cover equipped with appropriate fittings, valves and gauges are shown in Figure 9-1.

Air Oven, Blue M: Forced convection oven, Model OV 490A-2, 1600 watt or equivalent.

B&L Zoom Stereo Microscope, 0.7-3.0 X: With 10 X wide field oculars or equivalent.

Miscellaneous Hardware: Mandrels, small tools, spatulas, soldering iron, mixing pads, etc.

Simpson Meter, Model 260 Multimeter - or Equivalent: This instrument is used for checking electrical continuity and electrical isolation.

Jigs and Fixturing: Each motor coil and LVDT require an impregnating jig or fixture which will prevent varnish from entering or collecting on surfaces that are not to be coated or areas which would be difficult to clean at a later stage. Specific fixtures are described at the appropriate level. Generally, aluminum fixtures with screwed or bolted fastening and sealed with "O" rings have proved to be most useful.

Ultrasonic Cleaner: Branson Model PSD or equivalent.

Vacuum Oven, Fisher Isotemp Model 281 or Equivalent: To remove last traces of cleaning solvents from coils and chambers.

(2) Materials

Coils for Impregnation: Each coil and its fixture or bobbin shall have been checked for electrical and physical specifications. Appropriate marks or identification features shall be present so that the each component can be positively identified after treatment.

GE 707 Solventless Varnish: A semi-rigid, solventless, high-temperature varnish for general purpose insulation suitable for VPI application.

Two Component Epoxy Cement/Adhesive: DEVCON 5-minute epoxy or equivalent.

3M Structural Adhesive, Scotch-weld Ec2214 Hitemp or Equivalent.

Isopropyl Alcohol, Acetone, Trichloroethane: Mallinckrodt Transistar grade or equivalent.

Solder, Tin/lead (60/40), Kester 44 or Equivalent.

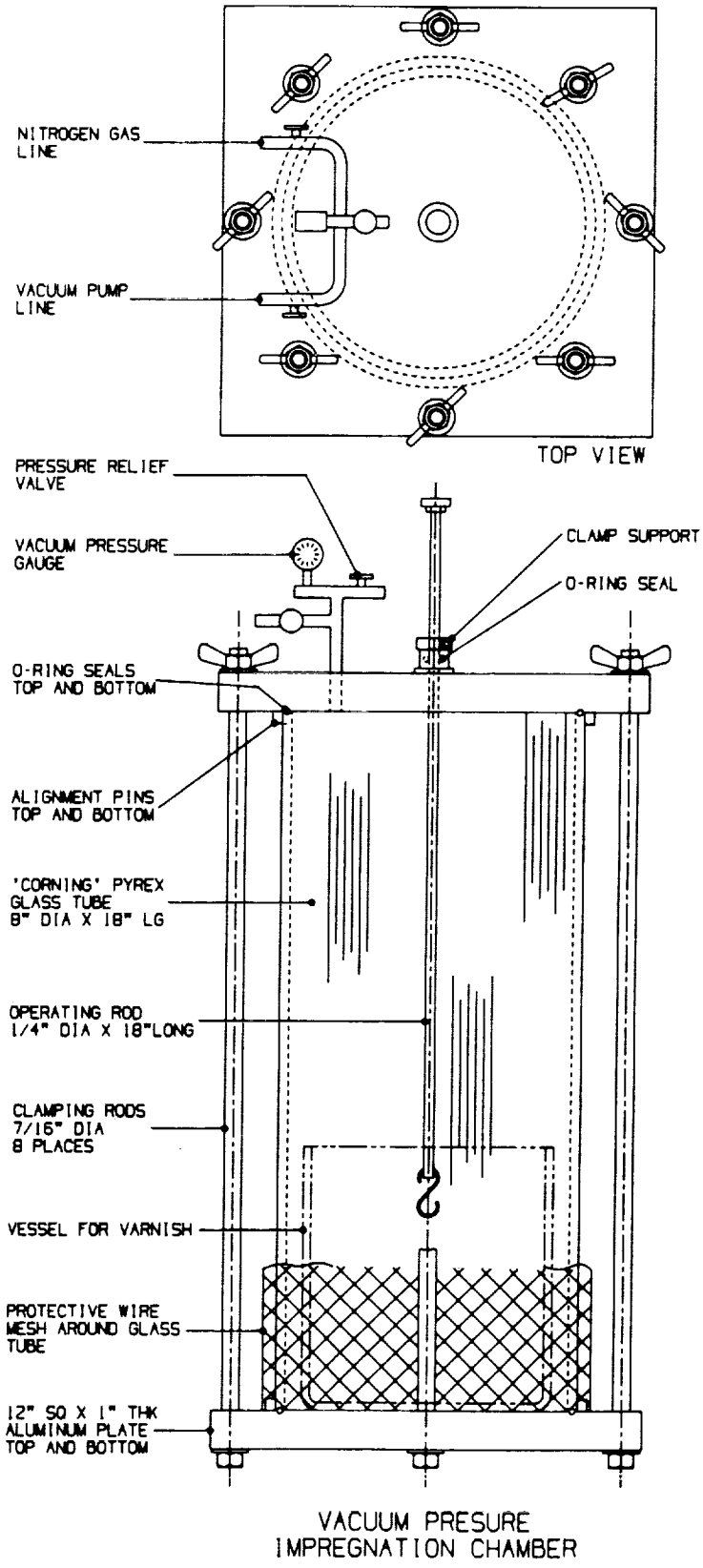

Figure 9-1. Vacuum pressure impregnation chamber.

9.3.3 Preparation of Varnish

The varnish should be filtered at periodic intervals to rid the bulk of any globs and masses which might otherwise hinder the impregnation process. Typically, the varnish is initially filtered and then again, if necessary, at four week intervals. A lintless filter cloth of the type used by painters is quite adequate.

A varnish container is chosen which fits closely within the inside dimension of the chamber, i.e., in this case a 4-liter lipless stainless steel beaker. A Pyrex glass 4-liter beaker is also appropriate for the chamber described. An appropriate amount of varnish is filtered into the beaker and the necessary quantity of catalyst is added and thoroughly mixed. The amount of varnish is determined by the liquid level in the beaker when the part is fully immersed in the chamber. This amount will vary, obviously, depending on the volume of article being impregnated. It is recommended that initially the varnish be outgassed by vacuum pumping until the violent bubbling subsides. There will be some bubbling when a part is initially immersed in evacuated chamber but it should soon abate.

A winding is best cleaned by immersion in isopropyl alcohol followed by vacuum outgassing to remove the last traces of solvent. The jigs and fixtures are also cleaned with ultrasonic cleaning in acetone and trichloroethane solvents. "O" rings are generally cleaned with alcohol and not greased, but rather held in place in captive grooves designed to provide adequate ring exposure to give a good seal.

Final assembly of components and fixtures should be done with lint-free gloves to prevent contamination (fingerprints) of critical surfaces.

9.3.4 Procedure for Impregnating Coils

Linear Motor Coils. The counterbalance and displacer sections each have a single stator coil while the piston motor is made of two wound coils, an inner and outer member. This requires that four different fixtures be prepared to expose the respective coils for impregnation and seal off the areas where no varnish is to occur.

LVDT Coils. A minimum of three units are required for the machine. All are essentially identical in size except for the overall length, and a single fixture should accommodate all units.

Bearing Coils. Each section (expander, compressor, counterbalance) uses identical coils for individual bearing sets, but the coils from section to section are different. The coils are open-wound on individual forms so that no additional fixturing is necessary. Each section requires a minimum of eight coils and, in general, a spare pair is recommended.

1. Fixtured unit is placed on hook and cover lowered into place on chamber. Chamber cover is secured with wing nuts.

2. Chamber is then evacuated to about 10 to 25 Torr pressure and pumped for about 30 minutes.

3. Unit is then lowered into varnish and pumping is continued for about one hour or until bubbling subsides.

4. Pumping is stopped and chamber pressurized to 15 psi with nitrogen for 30 min. Unit is then raised from varnish and allowed to drain for 10 min.

5. Steps 2, 3 and 4 are repeated after which chamber is opened and unit suspended within baking oven.

6. Unit is baked at 167°C in air for 2.5 hrs.

7. Unit is removed from oven, cooled and inspected. If any deep fissures or crevices appear, the process is repeated until adequate fill is obtained.

The unit is removed from its jig or fixture and checked visually for complete impregnation. Electrical checks are made to insure continuity and isolation, as necessary. Unit is then submitted to Quality Control.

9.3.5 Procedure Notes

(1) Drawing 001304, Coil/Stator Iron Assembly-Outer (Piston Motor).

The wound assembly is first fitted with the back iron segments. These consist of two hemi-cylinders of Corovac which are held in place with 3M Scotchcast structural adhesive, aluminum filled, designated 2214 High Temp.

An aluminum jig is then prepared which exposes the windings and back iron to the impregnating varnish but which seals off the inner cylinder, ends and TIG weld areas from the varnish. It is important that the jig be designed, fabricated and assembled so that no varnish leaks to the inner surfaces.

All components which will see the impregnating varnish are cleaned by immersion in isopropyl alcohol followed by degassing in a vacuum oven heated to about 100°C, 2-3 hours. The component and jig are then assembled, visually inspected for tightness and then mounted within the chamber while in the elevated or drain position. Impregnation is carried out as previously described.

When it is apparent that the part is adequately impregnated and baked the jig is removed and surfaces examined. The varnished unit is checked for electrical continuity and coil isolation.

The unit is submitted to Quality Control.

(2) Drawing No. 000670, Inner Stator Assy. (Piston Motor).

This item requires an aluminum jig which will expose only the wound coil surfaces to the varnish, as described. All other surfaces should be shielded from the impregnating varnish. This requires a jig similar to that for the previous coil but of different dimensions. The item and jig are degreased and assembled and positioned within the chamber. Impregnation is carried out as described. After the final bake, the jig is removed, the coil inspected for complete fill and electrically checked for continuity and coil isolation.

The unit is submitted to Quality Control.

(3) Drawing No. 000649, Stator, Displacer Motor.

The dimensions of this unit differ from the other motor coils so that another aluminum jig with "O" ring seals is required for the impregnation process. Again the fixture is designed to expose coil surfaces to the varnish while all other surfaces are shielded from the varnish. Procedure of cleaning, assembly, impregnation, baking and inspection is as described previously.

The varnished motor stator is submitted to Quality Control.

(4) Drawing No. 001335, Motor Stator, Counterbalance.

Counterbalance This unit is not intended to be hermetically sealed. The outer surface of the coil is covered with a thin titanium shell to confine any loose particles which may be generated over time. There are several slots and races which are not sealed. The counterbalance chamber is pressurized with a gas other than helium, and the unit contains no surfaces or components which might be affected by gaseous impurities. However, it is desirable to keep the weld areas free of varnish. A jig was designed which covered the TIG weld areas by use of "O" rings and also prevented the varnish from entering the inner bore of the coil assembly.

(5) Drawing Nos. 001368, 001370, 001374, Magnetic Bearing Coil.

For Piston, Displacer and Counterbalance. Each section requires a minimum of eight units and since all coils are similar except for wire size and outside dimensions, the impregnation process is identical for all.

As wound on its jig, a coil consists of a winding between two teflon-faced flanges with start and end leads.

- Strip of 3M polyimide insulating tape is laid down between terminal lug area and coil body. Coil ends are dressed to length, stripped of insulation, tinned and soldered (60/40, Sn/Pb solder, rosin flux) to terminal lugs.
- Strip of phenolic linen insulation with slots to accommodate lugs is laid over terminals and epoxy bonded in place.
- Strip of fiberglass mesh with slits to accommodate terminal lugs is laid over entire coil surface and epoxy-bonded in place.
- Entire unit is then soaked in isopropyl alcohol for 15 minutes followed by a vacuum oven pumping for 30 minutes. At this point coil is ready for impregnation.

Two impregnations and bakes are performed on each coil. After baking the flange restraints, the side flanges and the core section are removed. Each coil is inspected for complete fill (impregnation). No voids or fissures should appear. The unit is checked for electrical continuity and then submitted to Quality Control.

(6) Drawing No. 000633, Coil, LVDT Bobbin.

Each LVDT unit is impregnated with the inner shield in place using a fixture which provides for complete filling the spaces in and around each bobbin coil. It is important that the cavities be completely filled while keeping the regions where subsequent TIG welds are to be performed free of varnish. The jig should allow the varnish to enter the bobbin chamber and also prevent it from contacting the weld regions. A sketch of these features is shown in Figure 9-2.

The parts are cleaned with isopropyl alcohol dried in the vacuum oven and assembled. Each unit is impregnated in the manner described taking care to immerse the part only to the depth of the vent holes. Impregnation and baking is performed twice.

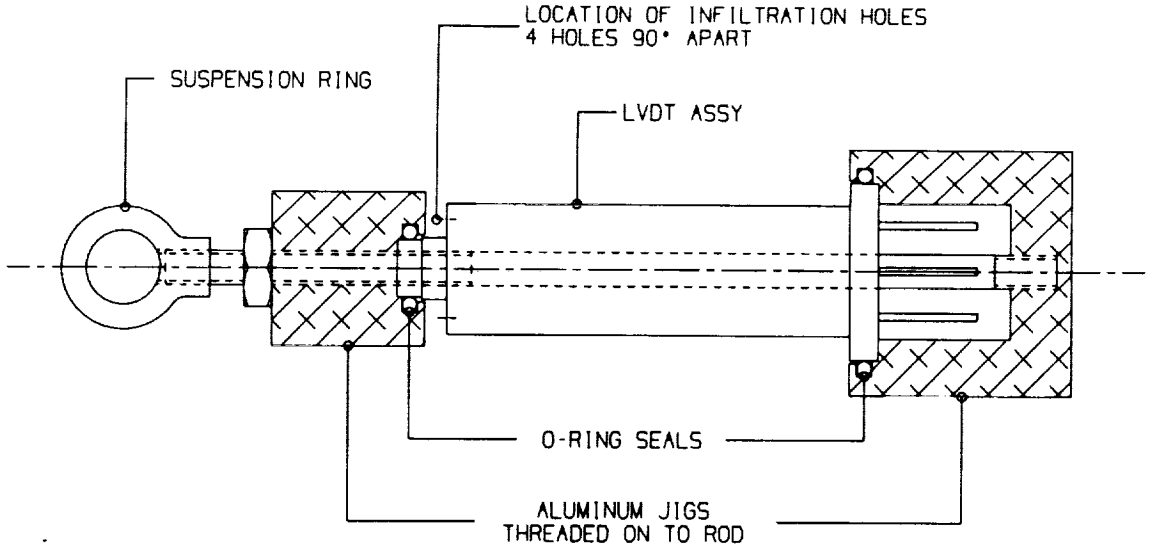

Figure 9-2. LVDT Impregnation fixture.

The fixture is carefully removed from the unit. Electrical continuity is checked, serial number identified and then submitted to Quality Control.

9.4 Heat Exchangers

9.4.1 General

There are two heat exchangers of interest in the refrigerator, both of which are located in the cooler portion of the machine. The lowest temperature is developed at the cold end which consists of an aluminum-titanium, brazed assembly, machined to provide the proper exchange surface, and a second exchanger located around the displacer motor area where the heats of compression and extraction are conducted through a brazed titanium-titanium assembly to an externally mounted cooling jacket. The fabrication of these two heat exchangers is described next.

9.4.2 Aluminum-Titanium Heat Exchanger

The following drawings are referenced to aid in identifying the various components and stages of fabrication.

Item	Dwg. No.	Description
1.	002644	CORE, Aluminum 1100
2.	002641	CAP, (Casting Vessel)
3.	002642	Cover, (bottom, Casting Vessel)
4.	001251	Cold Finger Cap, (cast Assembly)
5.	002676	Cold Finger Cap, (component For Machining)
6.	001252	Cold Finger Cap, (machined Exchanger)
7.	000736	Cold Finger Cold End, (Final Assembly)

The cold side exchanger consists of an aluminum-titanium assembly in which commercially pure aluminum is vacuum cast in a clean titanium vessel so that a strong hermetic joint between the two components, aluminum and titanium is formed.(1) The dimensions of the vessel are chosen such that the final exchanger component is easily machined from selected portions of the aluminum casting and its titanium vessel.

A titanium cylinder is machined as shown, Item 2, and to one end a bottom, Item 3, is miniature TIG (Tungsten Inert Gas) welded, Item 4. The vessel is cleaned and leak checked. A charge of Aluminum 1100 is machined to size, Item 1, cleaned and loaded within the vessel and the assembly placed within a vacuum furnace equipped with a quench tube (2) and with suitably located thermocouples. The furnace is pumped and heated to give a melt of aluminum at which point the temperature is lowered at a controlled rate so that the aluminum begins to solidify first at the base of the vessel, above the quench tube and the solidification front progresses upward toward the mouth of the titanium vessel. The final shrinkage cavity which generally occurs during solidification is produced in the upper region of the cast and is discarded, as excess, during the work-up of the heat exchanger, Item 5. The raw cast is Hot Isostatically Pressed (HIPPED) at 520°C for 4 hours, at 15,000 psig argon atmosphere, to consolidate the cast and remove any residual voids which might remain in the aluminum material.

The cold finger cold-end cap is machined from the processed assembly. The wall of the casting vessel becomes the titanium shell with its mounting lugs and miniature TIG weld joint while the aluminum cast is developed into the expansion space, Item 6. The internal cylindrical surface of the expansion space is slotted to achieve a larger surface area for the heat exchanger. In this instance, forty slots are generated by means of electrochemical discharge machining (EDM). This process produces a cast surface as is characteristic of an electric discharge which involves a limited melting of the basis metal. For this reason it is extremely important that all loose and friable metal particles be removed totally from in and around the slots. (This exchanger is but a short distance away from the displacer shaft clearance seal and any debris which might break free from the exchanger surfaces in this region could seriously damage the seal and the entire machine.)

The cold side heat exchanger is joined to the thin wall cold side cylinder by means of a miniature TIG weld as shown in Item 7. All components are mass spectrometer helium leak checked for hermeticity at every stage of the fabrication/assembly process.(3)

Comment Notes:

(1) Much investigative work went into this technique of casting pure aluminum into a titanium vessel with subsequent controlled cooling to obtain a sound, reliable and reproducible joint between the titanium and the aluminum. Metallographic specimens demonstrate conclusively that the interface bond is sound and reliable with no brittle intermetallic compounds formed. Repeated cycles of cooling to liquid nitrogen temperature followed by warming to room temperature, in the

order of thousands of times, while the unit was internally pressurized to 400 psig helium produced no indication of a leak. No indication of failure at the joint area has been detected. The differences in linear coefficient of thermal expansion of the two materials appears to be accommodated by the soft ductile properties of the pure aluminum. Tensile test specimens demonstrate that, when prepared as described, the Al-Ti joint is stronger than the strength of the cast aluminum member.

(2) A quench tube is simply a gas supply connection through the wall of the vacuum furnace which provides a means of initiating the solidification process at the bottom of the titanium vessel and thereby having the solidification front advance upward through the melt. The vacuum level is allowed to degrade during the solidification process. The quench tube together with a reasonable temperature control of the furnace insures a good directional cast.

(3) Several specimens were prepared and welded as miniature TIG welds as would be done in the final assembly. These units were pressurized, liquid-nitrogen-quenched and cycled repeatedly. Pressure levels of 400 psig were used. Rupture tests were run, and the rupture pressure was found to be about 2500 psig helium.

9.4.3 Titanium-Titanium Heat Exchanger

The following drawings are referenced as shown:

Item	Dwg. No.	Description
1.	002661	Exchanger, Heat, Displacer Motor Housing
2.	000621	Exchanger, Heat (Machining Details)
3.	000606	Displacer Motor Housing (Brazing Assembly)
4.	000607	Displacer Motor Housing (Machining)
5.	000600	Displacer Housing Assembly (Solder Assembly)
6.	000608	Displacer Motor Housing (Machining Detail)

The displacer motor heat exchanger consists of a brazement involving a multiplicity of gas passages machined into the surface of a liner brazed to the inner surfaces of the motor housing. The surfaces are final machined after optimization of the magnet pole pieces and following the installation of the fiber-optic radial sensors.

The exchanger is developed from rough-machined stock of commercial grade titanium which is given a stress relief heat treatment in a vacuum furnace, Item 1. The unit is then machined to provide the gas passages, plenums and grooves for the pre-placement of braze metal as shown in drawing of Item 2. The braze metal is entirely captive within the contact surfaces and is of an amount which will provide adequate material for the faying surfaces with no excessive corner fillets or runouts. Simultaneously with this brazing operation, the radial sensor inserts, pole piece subassembly, and feed through inserts are also installed in the displacer motor housing at this time, Item 3.

At this stage the gas passages are susceptible to contamination by chips and debris from machining operations. For that reason the passages are intentionally filled with a material which is easily introduced and removed and which withstands the solvent action of grinding and machining fluids. The chemical, potassium sodium tartrate, $KNaC_4H_4O_6.4H_2O$, works well for this purpose with a melting point of 70/80°C. It can be easily melted and poured into slots and cavities. In this manner with the passages and ports filled it can be assured that no small particle will become temporarily lodged within the gas passages only to become dislodged later when its presence in the clearance seal would likely ruin performance. The chemical is easily removed from the slots by warming the

assembly to allow the bulk of the material to flow out and then followed by copious washing with warm water. A flame test for the alkali metals is run on the final rinses to assure that all of the chemical has been removed from the passageways.

The sensors and electrical feed-throughs are installed, Item 5. after which the passages are again filled for the final machining operations as shown in the drawings for Item 6.

9.5 Fiber-Optic Radial Position Sensors

9.5.1 General

The position of each cylindrical component within its housing must be known at all times so that the proper clearance can be established and maintained for the reciprocating members, displacer rod, piston shaft and counterbalance. A fiber optic sensor is used to establish and maintain the necessary radial clearances. The terminus of each sensor is a bulkhead fitting which is mounted into the wall of the refrigerator and acts as a emitter/receiver of a position signal for each magnetic bearing pole as well as providing a hermetic seal for the pressure vessel. There are four poles to each bearing and two bearings for each shaft resulting in twenty four optic sensors for the entire refrigerator. Essentially a single sensor is described although it is obvious that the remaining twenty three units are identical.

9.5.2 Procedure: Fiber Optic Sensor, Bulkhead Fitting

The following list of drawings is for reference in identifying various components and stages of the fabrication.

Item	Dwg. No.	Description
1.	002743	Optical Sensor Rod (bundle)
2.	002742	Optical Sensor Housing
3.	001386	Optical Sensor Assembly (bulkhead fitting)
4.	001202	
5.	000600	Housing Mounts Displacer
6.	000611	
7.	000693	Housing Mount Piston (Compressor)
8.	000695	
9.	001388	Housing Mount Counterbalance

The fiber optic element is available in many different fiber sizes and bundle dimensions. The element selected for the bulkhead fitting consists of about 50,000 fibers fused into bundle and sized into a cylinder so that the interstices of the fibers are complete hermetic, Item 1. The surface of the fibers was metallized by sputter coating with thin films of titanium, platinum and gold. These films are easily tinned and wetted by a tin-silver solder alloy consisting 96.5% Sn and 3.5% Ag. The bulkhead Housing was prepared from 70/30 cupronickel alloy as described in Item 2. The bore of the housing was also tinned with the Sn/Ag alloy. The bulkhead assembly was prepared by re-flow soldering the components in a hot oil bath to obtain the fitting desired, Item 3. The fitting was inspected for complete flow of solder in the joint and also leak checked for hermeticity.

The final installation of the sensor into the pressure vessel wall is noted in Items 4 and 5 for the cold side, Items 6 and 7 for the compressor, and Items 8 and 9 for the counterbalance.

9.6 LVDT

The LVDT consists of a plastic bobbin wound with three coils, one primary and two secondaries. The coil wires are brought to six gold pins which extend from one end of the bobbin. The entire bobbin/coil assembly is enclosed within three nickel-iron cannister shaped shields. The bobbin (with the completed coils) is potted before insertion into the shields. The assembly is then hermetically sealed by welding the first shield closed and soldering the pins to a ceramic insulator.

9.6.1 Bobbin Description and Assembly

The bobbin is machined from Vespel (DuPont, Inc.). This thermosetting plastic provides both the mechanical stability required and also can safely withstand the temperatures seen during the soldering and potting operations. Six gold pins are press fit into a flange at one end of the bobbin, and they serve as terminations for the coil wires. The sectioned (or segmented) bobbin is machined from a single cylindrical piece of Vespel. A longitudinal groove through each of the section walls allows for routing the wires from one section to the next. The displacer bobbin has twelve sections and the piston (and counterbalance) bobbin has seventeen. Use of this style of bobbin yields two benefits. First, the sectioned style of winding results in overall lower interwinding capacitances; and, second, the sections allow the number of turns to be adjusted for each portion of the coil.

The primary is wound first. For both the displacer and piston bobbins this consisted of three layers per section for the entire length of the bobbin. A two part wire tacking adhesive is used to hold the ends of each winding in place. A layer of tape is then placed over each section of the primary. The secondaries are started at the center of the bobbin and then wound section-by-section towards either end. For the smaller displacer bobbin this results in there being six sections occupied by either of the two secondaries. In the case of the larger piston bobbins, the center section is not used for the secondaries, and there are now eight sections allocated to each secondary. This center-to-end sequence of winding the secondaries ensures that there is an electrical symmetry between each secondary and the primary. Figure 9-3 is a pictorial of the LVDT windings. While the number of turns per section is constant for the primaries, the secondaries are wound with an increasing number of turns as one approaches either end of the bobbin. The effect is to linearize the LVDT voltage output as the core is brought through its total range of travel. A step motor driven coilwinder was used to wind the fine wire incorporated in the bobbins. The two motors (spindle and feed) were step synchronized so as to be able to precisely control the winding pitch and the number of turns.

The secondary windings were tacked and attached to the termination pins in the same manner as had been the primaries. A final layer of Mylar tape completed the procedure. Figure 9-4 shows a completed displacer bobbin. A final calibration test was conducted and then the bobbin assemblies were made available for installation in the nickel-iron shields.

9.7 Mechanical Fabrication - Manufacture of Clearance Seals

9.7.1 General

Specifications for the expander and compressor called for clearance seals with values of 0.00065 to 0.00095 in. radial spacing and 0.0007 to 0.0010 in. radial spacing for the counterbalance section. Such values imply that the sum of the tolerances of the three components could not exceed 0.0006 in. on diameter. Ranked in order of increasing difficulty, the tasks are as follows:

- Roundness and straightness of shafts (see Step 3, grinding of shafts).

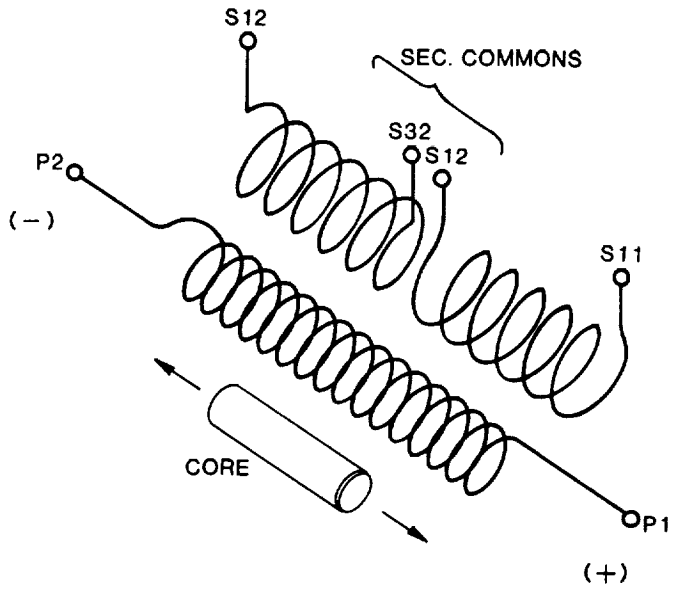

Figure 9-3. Pictorial illustrating direction of wind for each coil. Note that common of the two secondaries is at the center of bobbin. Numbers refer to pin connections external to LVDT.

ORIGINAL PAGE
BLACK AND WHITE PHOTOGRAPH

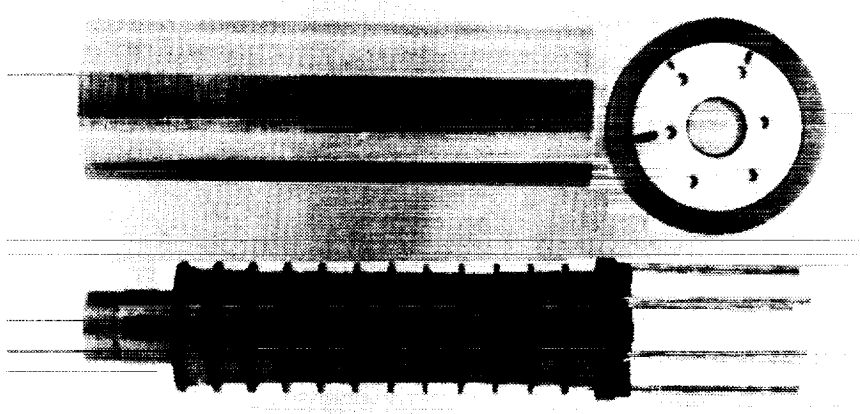

Figure 9-4. Displacer LVDT bobbin shown prior to installation within first shield. Shield is the cylindrical tube at upper left. Disk to right is end cap with ceramic insert. Titanium bore liner tube protrudes from left end of bobbin.

- Roundness of each housing, bearing bore, in each pair of housings (see Step 1, grinding bores).
- Alignment of bearing bores to each other in any pair of housings (see Step 2, aligning of bores and pinning).

It was determined that the finish grinding of the bearing diameters on the pistons would involve the least risk; therefore, that operation would be the last step.

9.7.2 Procedure

(1) Step 1: Grinding of Bores (reference following drawings).

Item	Dwg. No.	Description
1.	000604	Coldfinger Housing
2.	000608	Displacer Motor Housing
3.	00614	Piston Motor Housing
4.	000709	Piston Motor Rear Housing
5.	000712	Counterbalance Front Housing
6	000697	Counterbalance Rear Housing

The bores were ground with each housing clamped in a vertical position on a Moore(1) Spintable. The spintable has a trueness of rotation within 0.000005 in. and a maximum axial deviation (including camming, flatness and parallelism) of 0.00002 in.

The banking or mounting surfaces on each housing were lapped flat to 0.00003 in. in order to minimize the effect of distortion caused by the clamping forces.

The bores of each housing were ground perpendicular to within 0.0001 in. to the "C" seal surfaces which are common to a housing set. In the case of the components 000604, 000608 and 000709 the bore and "C" seal surface were ground in the same setup. For the other three housings, 000614, 000712, 000697, the unit was clamped on the "C" seal surface and for reference purposes the opposite end face was ground with the bore in the same setup.

Each bore was ground to ± 0.0001 in. The exact size of each bore is not very important as long as roundness and straightness fall within the ± 0.0001 in. The bores were inspected with an air gage and several roundness graphs were recorded with a Bendix PORTA-RON unit at different locations along the bores. It is important that the optical fiber glass bundles do not protrude into the bores. Preferably the ends of the bundles should be recessed 0.0001 to 0.0002 in.

(2) Step 2. - Aligning of Bores and Pinning (reference following drawings):

Item	Dwg. No.	Description
1.	000609	Cold Finger and Displacer Motor Housings
2.	000713	Piston Motor Housings
3.	000737	Counterbalance Housings

One piece of a housing pair is mounted vertically on a rotary or Spintable. The rotary may have a maximum runout of 0.00003 in. and should be motorized. The bore is trued in position to the rotary

table to about 0.00005 in. The housing is clamped to the table securely and runout rechecked. (Spintable by Moore, Bridgeport, Conn.).

The second member of the housing pair is positioned atop the first and the tramming procedure is repeated. There should be no "C" seal between the two housings at this point.

The alignment is inspected on a Surface Plate, with the housings in the horizontal position in a large "V" block on top of a leveling plate (i.e., Federal, Model TE 20). The CENTERLINE of the far ends of each bore are leveled with respect to each other using an electronic indicator. This means that if one bore is say, 0.0002 in., on diameter, larger than the other then that bore has to be 0.0001 in. lower in order to have the centerlines level to each other. Each bore is then checked all the way through its length to be straight to each other within 0.0001 in. If, using the 0.00005 in./div. scale on the indicator, the bores should have some taper as checked and recorded in Step 1, allowances will be made.

The housings are rotated 90° and the inspection process is repeated. After the assembly passes inspection the four dowel pin holes, 0.2500 +0.0001, -0.0000 in. are bored in line through both flanges.

The assembly is then taken apart, the pin holes are deburred and inspected and the stepped dowelpins (Part No. 002897) are pressed with the large diameter end into the flange with the through hole. The housings are then cleaned and the housing with the "C" seal groove is positioned on a surface plate and the dowel pin and threaded screw holes are lightly lubricated with moly grease.

An appropriate "C" seal is positioned in the groove and the top housing, fitted with three jackscrews is lowered into position. Parallelism of the two flanges is maintained by frequent checks with a height gage and by turning the jackscrews in unison. (This process is described in Section 10 Assembly Procedures). When the housing touches the "C" seal the jackscrews are removed and the sockethead cap screws and washers are inserted and drawn up to the flange. The "C" seal is evenly compressed by maintaining parallelism on the flange and by torquing the screws in numerical sequence. Great care must be used during this procedure to assure repeatability of the alignment of the bores to within 0.0001 in. and this is verified by rechecking on the surface plate using the leveling plate and "V" block as described previously.

Disassembly must be done with the same care using the surface plate, jackscrews and indicator as before. This is necessary in order to minimize the wear and distortion of the dowel pin system.

(3) Step 3: Grinding Shafts (reference following drawings):

Item	Dwg. No.	Description
1.	001303	Displacer Rod
2.	000666	Piston Rod
3.	000705	Counterbalance Piston and Armature.

The final clearance seal value was determined by taking the smallest region of each bore diameter then subtract the minimum clearance on diameter to give a number which represents the maximum shaft diameter, +0.0000 -0.0004 in. The following table represents values actually taken for the components developed.

	Expander Housing	Displacer Mtr.Hsng.	Piston Mtr.Hsng.	Piston Mtr.Hsng.	Count'bal. Front Hsng.	Count'bal. Rear Hsng.
Smallest bore Diam. (inch)	1.2492	1.2491	1.75015	1.7509	2.7232	2.72405
(-)Min. diametr'l clearance (inch)	0.0013	0.0013	0.0013	0.0013	0.0014	0.0014
Shaft Diameter +0.0000 -0.0004 (inch)	1.2479	1.2478	1.74885	1.7496	2.7218	2.72265

9.8 Magnetic Bearing Pole Pieces

9.8.1 General

The material chosen for use as the magnet pole members is 2-Vanadium Permendur, a soft magnetic material consisting of 2% Vanadium, 49% cobalt and the balance iron. Its physical properties indicate that this should be good pole piece material. The coefficient of thermal expansion is close to that of titanium into which it must be hermetically sealed and it is well wetted by those braze materials which are compatible with titanium. The metal machines well and has heat treatment (optimization) values which can be adapted to the brazing/heat treatment schedules required during fabrication.

For 2V Permendur to attain its maximum soft magnet properties it is necessary that only the lightest of machining stress be imparted during the final dimensioning operations. Standard, single-point machining operations results in too high a stress level. Low friction grinding has proven to be quite satisfactory as a final operation and still maintain acceptable magnetic properties. For these reasons, the components are machined to near final dimension by regular techniques and then given a heat treatment for optimization of magnetic properties followed by final grinding to finish dimensions. These precautions are maintained in the following fabrication procedure.

9.8.2 Procedure

The following drawings identify the various components with the operations to be performed.

Item	Drawing No.			Description
	Cold Side	**Piston Sect.**	**C'Bal. Sect.**	
1.	002620,	002703,	002717	Pole Piece (machining)
2.	002619,	002704,	002716	Pole Piece Block (machining)
3.	001244,	001349,	001371	Braze Pole Piece Block (assembly)
4.	001222,	001350,	001372	Pole Piece Radius Grind (raw dimension)
5.	001369,		001373	Machine Braze Gap (final sizing)
6.	000602,	000613,	000688	Braze Block into housing (assembly) 6
	000606,	000708,	000716	
7.	000603,	000720,	000711	Grind Pole Piece to Bore(raw dimension)
	000607,	001408,	000696	
8.	Same as (7) above.			Re-optimize pole pieces (heat treat)
9.	001202,		000695	Solder sensors (assembly)
	000600,		001388	
10.	000604,	000614,	000712	Finish Machining (final dimensioning)
	000608,	000709,	000697	

In the following operations the complete detail of the brazing and heat treat schedules are not repeated at each instance. Suffice as to mention at this point a large vacuum furnace is used which is capable of maintaining a good vacuum at temperature and in which the atmosphere and temperature can be changed in a controlled manner. Brazing titanium requires an inert atmosphere and the use of Gapasil-9 (braze alloy of palladium, silver and gallium by Wesgo, Calif.) as a braze alloy is best done not under a hard vacuum because of the volatility of the silver content of the alloy. The vacuum furnace was scheduled in the following manner.

The cleaned, jigged parts were placed in the furnace with thermocouples appropriately placed all within a sheet titanium tent. The furnace was closed and pumped to a diffusion pump vacuum, about 10 to -5 Torr and the temperature then brought to 250°C and held for 15 min., then the temperature was raised to 650°C. and held for 15 min., then the atmosphere was let up to 1000 microns with argon and heating then continued at 20 degree/min. to 940°C. The parts were held at temperature for 15 min. and then ramped at 15 degrees/min. to 840°C or to 300°C (depending on whether a optimization step was necessary) after which the power was removed and load allowed to cool to room temperature.

The pole pieces, Item 1, are machined to dimension and heat treated as a group to establish the optimum magnetic properties in the 2V Permendur. The treatment involves heating to 840°C. for four hours and controlled cooling to 300°C followed by furnace cool to room temperature. Heating is performed in a controlled atmosphere furnace, in this case a vacuum furnace. Immediately following the vacuum firing the pole end surfaces which are the faying surfaces of the subsequent braze joints are sputter coated with 2 to 3 micron thickness of pure nickel. It was established that a sound nickel coating on the permendur surface produced a reliable and repeatable hermetic joint when the it is brazed to titanium with Gapasil-9 braze alloy.

The pole pieces, Item 1, and titanium blocks, Item 2, are cleaned, jigged and fitted with braze sheet and preforms to make up the subassembly, Item 3. The units are brazed in a vacuum furnace at a temperature of 940°C for 15 minutes, at temperature. Upon cooling, the brazed assemblies are inspected for full braze flow and checked for hermeticity with a helium mass spectrometer leak detector (MS).

The pole piece surfaces are rough ground, Item 4., to establish the basic bore curvature. The radius size is 0.065 in. less than that of the finished bore, for example the piston motor housing has a final diameter of 1.750 in. or a radius of 0.875 in. so the the pole piece block will have a 0.810 in. radius. Following this operation the subassembly is machined, Item 5, to fit the housing ports into which the subassemblies are to be brazed, Item 6. The pole piece blocks protrude into the bore by 0.055 in. (This protrusion is made in case it becomes necessary to add additional braze material to achieve full braze penetration.) The brazing of the bearing subassemblies into the housings is a titanium-titanium joint and is made with Gapasil-9 in a vacuum atmosphere furnace at a temperature of 920°C following which a soak at 840°C for 1 hour is used to re-optimize the magnetic properties of the permendur components. Attention must be given to fixturing and jigging the several components which are simultaneously brazed during this operation. The nickel inserts, the fiber optic sensors, and electrical feedthroughs are brazed also at this time. The inserts are brazed into the housings also with Gapasil-9 alloy. The brazed housings are inspected for full flow and penetration of the braze alloy into the faying surfaces. The entire housing is MS leak checked.

The protrusions of the pole piece blocks and the nickel inserts are then machined flush to the bore which is at this point about 0.011 to 0.012 in., undersize, from the finish diameter, Item 7. The bores of the nickel inserts for the optical sensor bulkheads and feedthroughs are finished machined at this level.

The housings, as an assembly, are re-optimized for magnetic properties by heating to 840°C in vacuum for one hour and ramp cooled to 300°C, Item 8. The units are again inspected and MS leak checked for hermeticity.

The optical sensors are then soldered into place, Item 9. The housings are cleaned and again MS checked for hermeticity. The sensor bulkhead and excess solder are machined away and finally the protrusions are ground flush with the bore, Item 10. The final grinding of the bore is performed as described in the section on fabrication of Clearance Seals.

10. ASSEMBLY PROCEDURES

10.1 General

The following procedures were used to assemble the components of the three main sections of the Stirling refrigerator. The critical tolerances involved and the demonstrated value of performing an assembly under the cleanest of conditions mandated that the assembly be performed in a Class 100 Clean Room. Such a facility is available at Philips Laboratories, and an area of about 150 square feet was made available. All usual precautions and procedures respecting Clean Room garb, tooling, and components were maintained throughout the assembly.

A practice assembly of each section was made prior to the final Clean Room operation. This proved to be extremely valuable in establishing a confidence level, demonstrating the best procedural sequences to be followed, and providing final procedural improvements and corrections. It was also of value in proofing the various jigs and fixtures required for assembly.

After the practice run each component was thoroughly cleaned, inspected and bagged. Hardware was grouped, bagged and labeled to provide rapid and easy identification during the final assembly within the Clean Room. The cleaning equipment consisted of an ultrasonic vapor degreasing unit fitted with a spray wand, a gas-filtered air line, a stereo microscope and appropriate illumination for final inspection of components. Each component and designated hardware was heat-sealed within a clean polyethylene bag which was sealed within a second bag.

The basic units of the cooler are the Counterbalance, Piston (compressor), and Cold Side (expander).

The **Counterbalance** is possibly the least work-intensive of all the components, and, therefore was selected as the forerunner of the assemblies. This unit is a complete pressure vessel and is mechanically joined to the compressor/expander assembly.

The **Compressor** was assembled, covered and set aside in a vertical position within the Clean Room to be mated later with the third Expander. There is a common flange surface for these two units so that when joined they become a single pressure vessel.

The **Expander** was assembled and joined to the Compressor at which point they were both mounted on a large aluminum plate for stability and then transported, in the vertical position, from the Clean Room area to the Test Lab where the **Counterbalance** was attached. During transport the internal shafts were immobilized by powering one axial set of magnetic bearing poles with a portable battery pack. All necessary external hardware and electronics were also installed in the Test Lab.

10.2. Counterbalance Assembly

The following is the procedure followed for the Clean Room assembly of the Counterbalance. Numbers within the parenthesis designate the hardware package, i.e., screws, bolts, washers, spacers, etc.

1. The front housing of the Counterbalance is positioned on the Assembly Fixture and held with two cap screws, 5/16-18 x 1 1/2 in. (16). The motor stator is positioned within the housing and fastened with eight cap screws and washers, 8-32 x 1/2 in. and torqued to 24-26 in-lb (12).

2. The two coil wire leads are soldered to the feedthrough terminals. Each joint is tested, cleaned and checked to be free of debris.

3. Three jack screws are engaged within the rear housing so as to protrude 3-3/4 in. beyond the interface. Dowel pin ends are lubricated with a minimum amount of grease. The screw threads should be pre-lubed and bagged in such condition.

4. The LVDT core (armature) is positioned within the motor armature and secured with the four screws and washers, 4-40 x 1/2 in. and torqued to 7-8 in-lb (10).

5. The front end of the motor armature is located on the Delrin tip of the assembly fixture. The armature is lowered into the front housing by rotating the lead screw until the armature bottoms on the front housing.

6. Remove the assembly from the fixture and locate the housing on the surface plate. Position a "C" seal in its groove in the front housing.

7. Position the rear housing by engaging the jack screws and aligning the fiducial marks on the two flanges. Lower the rear housing to the "C" seal by means of rotating the jack screws in unison. Maintain the flange level by use of the height gauge/surface plate.

8. Insert twelve cap screws and washers, 1/4-28 x 3/4 in. and torque to 125-135 in-lb in the sequence 1-11-8-5-2-12-9-6-3-10-7-4(14).

9. Remove each screw, one-by-one, and replace with a new screw and washer, torqued to 95-100 in-lb(15). Assembly to remain on surface plate.

Note: Steps 10 through 13 inclusive are best done as a subassembly outside the Clean Room, inspected, tested, cleaned and bagged, and installed as required as a complete component.

10. Prepare the LVDT/Closure Flange of the Counterbalance by placing the inner locating spacer on LVDT transformer, Ser. No. 3, and placing both within the LVDT outer shield (note position of aligning arrow and the marked pin lead). Insert the outer positioning spacer.

11. Mount the outer shield to the Macor disk/Holder by feeding the leads through the disk and maintaining position of "X" marks on housing and transformer. Install three cap screws, 8-32 x 3/4 in. and torque to 24-26 in-lb (7).

12. Solder the lead wires into the circuit troughs and dress the ends through the solder pad openings. Mount the end cap to the assembly while matching "X" marks, using three cap screws and washers, 8-32 x 1/2 in. torque to 24-26 in-lb (8).

13. Solder ends of LVDT leads to feedthrough terminals of end cap. Check and clear of debris. Place a "C" seal in the groove.

14. Thread the three guide rods, 1/4-28 x 4 in. into the Rear Housing Flange (17). Engage the three jack screws into the rear closure flange with a protrusion of 3-1/4 in. Locate the jack screws onto the rear counterbalance flange and lower the rear closure. Maintain the flange parallel by use of the height gauge on the surface plate. Remove the guide rods when the flanges are about 5/8 in. apart.

15. As the flange contacts the "C" seal, remove jack screws and install twelve cap screws and washers, 1/4-28 x 3/4 in. and torque to 95-100 in-lb. (9) in the sequence 1-11-8-5-2-12-9-6-3-10-7-4.

16. Position the entire assembly on the piston-raise fixture and using a 5-1/2 in. long Delrin plunger raise the piston to its limit and lock the plunger in position. There will be considerable resistance to movement due to the gas spring effect. The entire assembly is now inverted. Remove the fixture and Delrin rod.

17. Position a "C" seal in its groove. Attach the 14" long installation handle to the bumper plate and lower it into the front counterbalance flange. With twelve cap screws and washers, 8-32 x 1/2 in., torque the closure to 24-26 in-lb (13), in the sequence 1-11-8-5-2-12-9-6-3-10-7-4. Install a Schraeder valve core (Part No. 9914A) and torque to 1.5 to 3 in-lb.

18. Mount a single, magnet-bearing coil assembly in the same quadrant at each bearing site with a 0.010" pole piece shim between each leg and the pole piece top (17), torqued to 7-8 in-lb. (use only eight of the 4-40 x 3/4 in. cap screws). With a portable power supply, energize each of the bearing coils and transport the Counterbalance to the Test Laboratory while in the vertical position.

Counterbalance Parts List

The following parts are cleaned, inspected and then double-bagged for subsequent assembly in the Clean Room Facility:

	Item		Drawing No.
1.	LVDT Subassembly	LVDT Calibrated Assembly	000739
2.	Inner Locating Spacer	Shim, inner-LVDT	002638
3.	LVDT Transformer	LVDT Assembly, Piston	000633
4.	LVDT Outer Shield	LVDT Holder Assembly	002706
5.	Macor/Disc Holder	LVDT Conductor Plate	001398
6.	End Cap	End Cap Assembly	001397
7.	Counterbalance Front Housing	Piston Housing Assembly	000712
8.	Motor Stator	Stator Assembly	001341
9.	Counter Balance Piston Assembly		001336
10.	LVDT Core	LVDT Rod Assembly	001348
11.	Piston/Armature	Piston Assembly	000705
12.	"C" Seal	Seal, Metallic "C"	001221-4
13.	Counterbalance Rear Housing	Housing, Piston LVDT	000697
14.	Two "C" Seals	Seal, Metallic "C"	001221-1
15.	Piston Housing Bumper Plate		001383
16.	Two Magnetic Bearing Coils	Magnetic Bearing Assembly	001413-1
17.	Shims, Pole Piece	Placed in Hardware Package 17	002896-3

Note: The LVDT transformer (3) and Items (2), (4), (5), (6) are assembled, inspected, tested and cleaned outside the Clean Room and are to be final cleaned and bagged, as a subassembly, to be taken into the Clean Room.

Counterbalance Assembly Hardware

Hardware Pack No.	Item	Qty.	Soc. Head Cap Screw Size	Torque value (in-lb)	Washer 002737 #
7	LVDT outer shield to Macor Disc	3	8-32x3/4	24/26	-1
8	LVDT Assembly to End Plate	3	8-32x1/2	24/26	-1
16	Front Housing to Assembly Fixture	2	5/16-18x1-1/2		
12	Stator to Front Housing	8	8-32x1/2	24/26	-1
10	LVDT Core to Armature	4	4-40x1/2	7/8	-3
14	Housings, pull down	12	1/4-28x3/4	125/135	-5
15	Housings, final	12	"	95/100	"
9	Endcap to Rear Housing	12	"	"	"
13	Bumper Plate	12	8-32x1/2	24/26	-1
17	Pole Piece, Coil Assembly	8	4-40x3/4	7/8	-3
17	Pole Piece, Coil Assembly	4	Shims		
18	Schrader Valve No. 9914A				

Counterbalance Assembly Tooling

1. Delrin Tip ring for lead screw.
2. Thrust Bearing
3. Three pieces, jack screws, 5/16-24x9 in. long.
4. Piston raising fixture with 5 1/2 in. long Delrin plunger.
5. Three pieces LVDT Assembly guide rods, 1/4-28x 4 in. long.
6. Bumper plate installation handle.
7. Battery Pack, 4-volt.

10.3 Compressor Assembly

(Parenthetical numbers refer to Hardware Packages.)

Note: The LVDT is prepared as a subassembly outside the Clean Room and after the unit is checked it is cleaned and double bagged for use in the Clean Room The subassembly of the unit is described in Steps 20 through 23, inclusive.

Note: The cooling jacket for the Piston Motor Housing with its "O" rings is installed outside the Clean Room after which the unit is cleaned and inspected and re-bagged for introduction into the Clean Room A lubricant is necessary since one "O" ring will be drawn over the entire surface of the motor housing.

1. Mount the armature (magnet assembly) on the Assembly fixture, using the armature base, brass ring, yoke and threaded rods (40).

2. Elevate the lead screw fully, upward, insert the Delrin tube to guide the piston, insert the piston rod and hold in place by hand while lowering the lead screw fully, downward. Install screws (20) and torque the six 8-32 x 3/4 in. cap screws and washers to 24/26 in-lbs.

3. Mount the LVDT armature core in the Piston Rod (21). Four 4-40 x 3/8 in. cap screws and washers. Torque to 7/8 in-lb.

4. Remove the yoke and threaded rods. Place the piston alignment fixture over the piston and secure with Delrin clamp. Remove the entire assembly from the assembly fixture and set aside for Step No. 9.

5. Mount the piston motor Housing to the assembly fixture using six 1/4-28 x 1 in. cap screws (41).

6. Install the eight captive screws with threaded washers into the Piston Motor Stator Mounting plate (30).

7. Attach **Inner Stator Coil** to Stator Plate, aligning identification marks and using twelve 8-32 x 3/8 in. cap screws (29). Torque to 24/26 in-lb. in the sequence 24-13-17-21-15-19-23-14-18-22-16-20 (see Fig. 10-1).

Place the Inner Stator and Plate on the **Outer Stator Coil** which is fitted with its lead-protecting ring, again aligning marks on leads with plate openings. Install twelve cap screws and torque to 24/26 in-lb. in the sequence 1-9-5-11-3-7-2-10-6-12-4-8. (see Fig. 10-1).

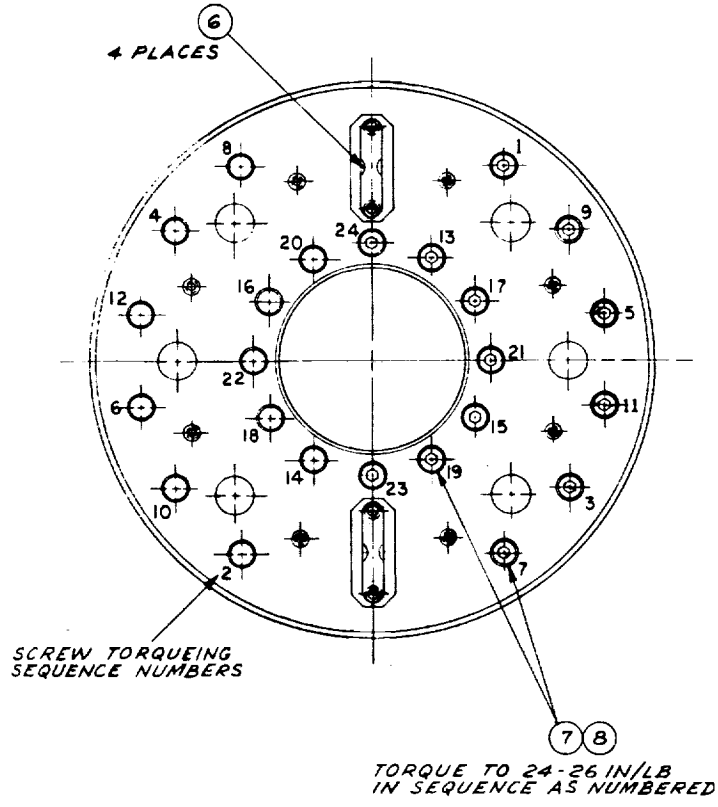

Figure 10-1. Compressor motor stator assembly plate.

Install the copper bus bars and complete the solder connections. Use only Sn/Ag (96.5/3.5) solder (Eutectic Alloys No. 157). Test for continuity, isolation and resistance. Check area for debris and contamination. Clean as necessary.

8. Install crosshandle on aluminum lead-protection ring using four 10-32 x 5/8 in screws (43). Insert the **Stator Assembly** in the piston housing being careful to align motor leads into Housing Feedthrough Terminals.

   Engage the captive screws with the threaded bosses in the PM housing. Torque to 24-26 in-lb.

   Complete the solder joints, the coil leads to the feedthrough terminals, two places. Check area for debris and contamination, clean as necessary.

   Install 0.5 micron Filter Assembly (Part No. 002907) and torque to 100 in-lb.

9. Engage lead-screw of the assembly fixture fully upward. Mount the **Armature** assembly and alignment fixture from Step No. 4 to the Piston motor housing using four 5/16-24 x 1" cap screws (41). Install the thrust bearing and the 1.800" dia. by 0.75" long Delrin ring.

10. Advance the lead screw to just touch the Piston assembly.

11. Remove the Delrin clamp.

12. Lower the Piston/Armature Assembly into the Motor Housing. To prevent the piston from rotating, insert the Delrin guide plug before the piston enters the alignment fixture. Remove the guide plug and the alignment fixture from the Piston Motor Housing.

13. Place the entire assembly on the surface plate.

14. Install the "C" seal and center in groove. Lubricate the 5/16-24 tapped holes with grease as well as the dowel pin sockets. An absolute minimum of lube is to be used.

15. Install the three jack screws into the rear housing.

16. Place the Piston rear housing to the Piston front housing while maintaining the alignment marks.

17. Lower the rear housing into place using the height gauge and and dial indicator to maintain the flanges parallel.

18. When the rear housing contacts the "C" seal surface remove the jack screw and install twenty 5/16-24 x 1 in. cap screws with washers (28). Continue checking for parallelism with height gauge as the seal is compressed. Torque screws to 16.5-16.8 ft/lbs. (200 in-lb.) using the sequence 1-4-7-10-13-16-19-2-5-8-11-14-17-20-3-6-9-12-15-18.

19. Mount the guide ring to the Macor plate frame of the LVDT Subassembly with two 12-24 round head screws (35). Install the three 3/16" x 6" studs with 8-32 threads into the piston rear housing (35). Align and locate the LVDT Subassembly onto the studs and lower the unit into place in the rear housing. As this is being done, insert the two disc clamps in the cutouts in the outer shield (25).

Note: The following four steps are to be done outside the Clean Room, with the subassembly then being inspected, cleaned, bagged and returned to the Clean Room.

20. Install the INNER LVDT SPACER in the outer shield and insert the transformer (Ser. No. 1) into the shield. Align the pin marked with the arrow on the o.d. to the "x" marking on the outside of the housing near the feedthrough.

21. Install the outer spacer atop the LVDT.

22. Install the **Clamp Ring** to the **Macor Disc** with two cap screws, 4-40 x 5/16 in. and torque to 7/8 in-lb (22).

23. Align the "X" mark on the Macor Disc Holder with the index pin (marked pin) on the LVDT. Guide the Macor Disc over the **Feedthrough** wires and the LVDT pins. All parts should locate easily, no forcing should be required. Attach the LVDT clamp ring to the outer shield with two 8-32 x 1/2" cap screws, torque to 24/26 in-lb (23).

24. Fasten the Macor Disc to the Rear Housing using three low profile head cap screws, 8-32 x 3/8 in., torque to 17/18 in-lb (24). Secure the two disc clamps with the 4-40 x 5/16 in. cap screws and torque to 7/8 in-lb (25).

25. Dress the six leads to lay in tinned grooves. Cut to length, being careful to remove all debris. Solder leads and immobilize same in grooves using Sn/Ag, (96.5:3.5), solder. Do not use tin/lead solder. The lead in conventional solders will strip the metallization and render soldering impossible. Inspect joints for height, debris, clean as necessary.

26. Install the "C" seal and center it in its groove.

27. Attach the 14" long installation handle to the end plate and lower the endplate into the rear housing. Install the **End Plate** with twelve 1/4-28 x 3/4 in cap screws and torque to 95-100 in-lb(26). The torquing sequence shall be 1-11-8-5-2-12-9-6-3-10-7-4. (Reference depth from housing end face to plate is 0.125" when "C" seal is compressed.

28. Set aside until the cold side (Expander) is completely assembled; then proceed as follows:

29. Place Piston Housing, as in step 28 above, upon the piston raising fixture fitted with the 2 1/8 in. long Delrin plunger using four 1/4-28 x 1-1/4 in. cap screws (42).

30. Carefully raise the piston by advancing the plunger by hand until the piston rod is at its upward limit. Tighten the plunger at that point.

31. Mount the 11 1/2" Dia. x 5/8" thick aluminum base plate on top of the assembly; use eight 1/4-28 x 3/4" (45).

32. Invert the entire **Piston Housing Assembly**. Remove the plunger and raising fixture. Inspect the internal surfaces for absence of trash and debris. Clean as necessary.

33. Locate "C" seal and center in groove.

34. Mount the **Cold Side (Expander)** to the **Piston Housing Assembly** with the reference markings of both assemblies aligned. Bring together with twelve 1/4-28 x 7/8 in. cap screws and torque to 95-100 in-lb, in the sequence: 1-11-8-5-2-12-9-6-3-10-7-4 (19).

Note: If the "C" seal does not fully compress at these torque values increase to 135 in-lbs and when fully compressed re-torque the screws to 95-100 in-lb.

35. Mount one magnetic bearing coil assembly on each housing, preferably all along one axis and not adjacent to the reference mark. Use shims and 4-40 x 3/4" cap screws and torque to 7/8 in-lb. (51). Power the bearings whenever the unit is to be transported. Install a Schrader valve core (Part No. 9914A) and torque to 1.5 to 3 in-lb.

36. Transport the assembled unit to the Cryo Lab in the vertical position with the bearings powered.

Compressor Parts List for Pre-Clean Room Assembly

Item	Drawing No.
HOUSING-PISTON Motor	000614
COOLING JACKET	000727
Two "O" rings, Parker No. 2-370	
Cooling Jacket Ring (Ring, Pressure)	000728
LVDT Assembly (LVDT calibrated assembly, Piston)	000654
LVDT Outer Shield (Shield and base assembly)	000659
LVDT Inner Spacer (Shim, inner-LVDT)	002638
LVDT Transformer (LVDT assembly, Piston)	000633
LVDT Outer Spacer (Shim, outer-LVDT)	002639
LVDT Clamp Ring (Ring, Clamp-LVDT)	001255
LVDT Macor Disc Holder (Disc, Insulator and holder assembly)	000700

Compressor Parts List for Clean Room Assembly

Piston Motor Armature (Armature Assembly)	001250
Piston (Piston Assembly)	000667
LVDT Rod and Core Assembly	000626
Piston Motor Stator Mounting Plate (End Cap)	000676
Inner Stator Coil (Inner Coil Assembly)	001277
Outer Stator Coil (Outer Stator Assembly	001306
Two Copper Bus Bars for Feedthroughs	002678
"C" Seal (Seal, Metallic "C")	001221-4
Housing, Rear	000709
Two Disc Clamps (Disc retainer-LVDT) (In Hdwre Pkg.25)	002741
"C" Seal (to end plate)	001221-3
End Plate (Plate, end cap)	001384
"C" Seal (Cold Side Interface with Compressor)	001221-2
Two Magnetic Bearing Assemblies	001413-2
Pole Piece Shims (Shims, Pole Piece Magnetic Bearing. Pkg 51)	002896-2
Adapter and 0.5 micron Filter Assembly	002907
Schrader Valve Core No. 9914A	

Compressor Assembly Hardware

Hardware Pack No.	Item	Quantity	Soc. Head Cap Screw Size	Torque Value (in-lb.)	Washer 002773 #
19.	Cold Side Expander-Piston	12	1/4-28 x 7/8	95/100	-5
20.	Armature to Piston Rod	6	8-32 x 3/4	24/26	-1
21.	LVDT Core/Piston Rod	4	4-40 x 3/8	7/8	-3
22.	Macor Disc-clamp Ring	2	4-40 x 5/16	7/8	-3
23.	LVDT Clamp Ring-Outer Shield	2	8-32 x 1/2	24/26	-1
24.	Macor Disc To Rear Housing	3	8-32 x 3/8LP	17/18	-1
25.	Two Disc Clamps-rear Housing	2	4-40 x 5/16	7/8	-3
26.	End Plate	12	1/4-28 x 3/4	95/100	-5
28.	Front-Rear Housings	20	5/16-24 x 1	200	-4
29.	Stators to Yoke Plate	24	8-32 x 3/8	24/26	-1
30.	Stator Assembly-Housing-Housing	8	8-32 x 3/4	24/26	-Spec.
			CAPTIVE THREADED.		
31.	Cooling Jacket	12	10-32 x 1/2	Hex Heads	
51.	Pole Piece	8	4-40 x 3/4	7/8	-3
51.	Pole Piece Shims	4			

FIXTURING HARDWARE

35.	Guide Ring to LVDT Assembly	2	12-24 x 2	Round Head
35.	Guide Ring Studs	3	8-32 x 3/16	Dia.6" Long.
45.	Base Plate to Rear Housing	8	1/4-28 x 3/4	
40.	Armature-piston Rod Assembly	3	1/4-20 x 6	Threaded Rod
	"	3	1/4-20	Nuts
	"	2	5/16-24 x 1 1/4	
41.	Piston Alignment Fixture	4	5/16-24 x 1	
	"	6	1/4-28 x 1	
42.	Piston Raising Fixture	4	1/4-28 x 1 1/4	
43.	Guard Ring With Bar to Insert Stator	4	10-32 x 1 1/2	
44.	Piston Housing to Assembly Fixture	6	1/4-28 x 1	

Compressor Assembly Tooling

1. Protective Ring for feedthroughs on Outer Stator.
2. Brass Ring (locator) for assembly fixture armature base.
3. Armature Base.
4. Armature Yoke.
5. Delrin Tube (to fit on end of lead screw).
6. Thrustbearing.
7. Piston alignment fixture.
8. Delrin clamp for Piston Rod.
9. Cross handle for Stator Assembly (for Item No.1).
10. Delrin Ring, 1 3/16" Dia. x 3/4" long.
11. Delrin Guide Plug.

12. Three jack screws, 3/8-24 x 6" long.
13. LVDT Assembly Guide Ring.
14. End plate installation Handle.
15. Piston Raising Fixture with 2 1/8" long Delrin plunger.
16. Base Plate, 11 1/2" dia.

10.4 Expander Assembly

NOTE: The numbers in parenthesis refer to hardware packages. The preferred assembly technique involves a subassembly of the LVDT unit outside the Clean Room followed by inspection, testing, cleaning and bagging of the unit prior to introduction into the Clean Room.

10.4.1 Subassembly LVDT Unit

Place the inner LVDT positioning spacer within the LVDT outer shield. Install the transformer and align reference marks. Add the outer spacer and the clamp ring with its four 2-56 screws and torque to 3.1/3.4 in-lb. (1). Add the framed Macor Plate with proper alignment and secure in place with two 4-40 x 3/8" screws torqued to 7/8 in-lb. (2). Dress the LVDT leads within the tinned grooves of the Macor plate and solder with the tin-silver alloy. Clean the area of residue and inspect to insure the absence of trash, powder and debris. Mount the guide ring to the Macor plate frame with two 12-24 round head screws (35). This subassembly should now be inspected, tested for continuity and isolation, cleaned and bagged for entry into the Clean Room area.

10.4.2 Subassembly of Dewar Housing

Install the "O"ring in the Dewar flange of the cold finger housing. Mount the Housing and the two piece clamp using eight 8-32 x 1/2" Hex Head cap screws. This assembly is to be done before the unit enters the clean room area as a protection for the cold finger and its instrumentation.

10.4.3 Assembly of Cold Side (Expander) Section

1. Insert Displacer Motor Stator within Displacer Motor Housing and fasten with six cap screws, 8-32 x 5/16 in., and washers. Torque to 24-26 in-lb. (5).

2. Locate and position the motor leads into the feedthrough terminals. Apply a light crimp on each terminal to secure the lead in place. Reflow the solder in the lead/terminal joint, add more solder if necessary. Inspect and test the connection and adjoining area. Remove and clean the area, check for electrical continuity and isolation.

3. Place brass ring on assembly fixture. Position the displacer motor housing (stator side up) on the fixture while threading the LVDT feedthrough wires into the holes provided in the fixture. Secure the Housing to the Assembly fixture with three 1/4-28 x 3/4 in. cap screws and washers (32).

4. Elevate leadscrew to its uppermost point. Install thrust bearing and Delrin guide plug and thence the displacer rod (Armature). Lower leadscrew while applying strong pressure on the upper end of the ROD to insure that the ROD follows the leadscrew as the magnetic spring magnets in the Rod and Stator interact during the engagement. Note, that at some point there will be a strong repulsion during the introduction of the shaft. The springs will tend to center the shaft when the end of the regenerator extends about 6.250 in. from the stator surface.

5. Mount displacer rod clamp fixture on the stator end of the housing with the use of four 1/4-28 x 7/8 in. screws(33). Place the delrin ring over the displacer rod and clamp it securely. Place two aluminum rings on two opposite legs of the fixture and tighten them.

6. Remove the three screws holding the displacer housing, ROD and clamp fixture to the assembly fixture. Remove the assembly and invert the unit.

7. Mount the LVDT armature in the displacer rod body using four cap screws and washers, 4-40 x 3/8 in. (11). Insert a 1/4 in. dia. pin into the Delrin clamp ring and buttress it against a leg of the fixture to prevent the displacer rod from turning while torquing the screws to 7-8 in-lb.

8. Install the three 3/16 x 6" studs with 8-32 threads into the Displacer Motor Housing.(35) Align and locate the LVDT subassembly onto the studs and lower the unit into place in the Displacer Housing. Secure with three 8-32 x 3/8 low profile screws, torque to 17/18 in-lb (3).

9. Mount the manifold plate using eight low profile screws, 8-32 x 5/8 in (4) and torque to 17/18 in-lb. Torque the inner set of four and then the outer four screws. This surface is now the interface to the compressor front end. Inspect for cleanliness.

10. Invert the entire assembly and place it upon the surface plate. Remove the aluminum fixturing and Delrin clamp rings and fixtures.

11. Remove Dewar from cold finger housing.

12. Install the three long jack-screws into the cold finger housing so that the screws extend 7 1/2 in. beyond the flange surface. Locate and center the "C" seal in its groove in the displacer housing. Lubricate the dowel pin holes. Locate the cold finger housing atop the displacer motor housing with the reference marks aligned. Level the dewar flange surface with the height gauge and lower the cold side housing by rotating the three jack screws in unison. Check the level often with the height gauge. When the cold side flange contacts the "C" seal surface remove the jack screws and install twelve cap screws and washers, 1/4-28 x 7/8 in (6) and torque to 95/100 in-lb. following the sequence, 1-11-8-5-2-12-9-6-3-10-7-4.

13. Re-install the "O" ring in Dewar flange and mount cover and split clamp ring with eight, 8-32 x 1/2 in., hex head bolts (36).

This Assembly Now Becomes a Part of the Piston (Compressor).
Proceed to Step 29 of the piston assembly, page 10-7.

Cold Side---Pre-Clean Room Assembly Parts List

LVDT Subassembly

Item	Drawing No.
LVDT Calibrated Assembly, Displacer	000655
LVDT Transformer (LVDT Assembly, Displacer)	000625
LVDT Inner Spacer (Shim, inner, LVDT)	002638
LVDT Outer Shield (LVDT shield, manifold)	001258
LVDT Outer Spacer (Shim, outer, LVDT)	002639
LVDT Clamp Ring (Ring, LVDT Clamp)	002652
LVDT Macor Disc/Holder (Disc, Insulator and Holder Assembly)	000700
Cold Finger Housing	000736
"O" Ring, Parker No.2-150	
Dewar Assembly	000657
Two Dewar Clamps	001253

Cold Side (Expander) Clean Room Parts List

Displacer Motor Housing	000735
Stator Assembly	001247
Displacer Rod Assembly	000686
LVDT Armature (LVDT Rod and Core Assembly)	001239
Manifold Plate	000660
"C" Seal	001221-1
Four Pole Piece Shims (Hardware Pkg. 52)	002896-3
Two Magnetic Bearing Assemblies	001413-3

Cold Side Assembly Tooling

Brass Ring
Thrust Bearing
Delrin Guide Plug
Displacer Rod Clamp fixture with Delrin Clamp Ring and 1/4" dia x 3-3/16" pin
LVDT Guide Ring
Three Jack Screws, 5/16-24 x 9" long

Cold Side (Expander) Assembly Hardware

Hardware No.	Item	Qty.	Soc.Head Cap Screw Size	Torque Value (in-lb.)	Washer 002773
5	Stator-to-housing	6	8-32 x 5/16	24/26	9
11	LVDT Core	4	4-40 x 3/8	7/8	2
1	LVDT Clampring	4	2-56 x 3/8	3.1/3.4	6
2	Macor Disc-to-outer Shield	2	4-40 x 3/8	7/8	3
3	Macor Disc-to-displr. Housng	3	8-32 x 3/8LO	PRO17/18	1
4	Manifold	8	8-32 x 5/8LO	PRO17/18	5
6	Housings	12	1/4-28 x 7/8	95/100	5
36	Dewar	8	8-32 x 1/2	hex head	1
52	Pole Piece	8	4-40 x 1/2		3
		4	Shims		

Fixturing Hardware

32	Displr Housng To Assmbly Fix	3	1/4-28 x 3/4	
33	Displr Clamp Fixture	4	1/4-28 x 7/8	1/4 dia. Pin
34	Guide LVDT Outer Shield	2	4-40 x 3/4	
35	Guide Ring, For LVDT Assembly	2	12-24 x 2	Rnd.head
35	Guide Ring Studs	3	3/16 x 6	(8-32 thread)

10.5 Purge and Fill Procedure

10.5.1 General

This section describes an acceptable and proven method for purging and filling the working volumes of the Prototype Cooler with the appropriate gases. High purity helium is used in the Stirling cooler portion while pure, dry nitrogen is used in the active counterbalance chamber. It is necessary to establish and maintain a clean, dry, working gas at all times to insure a long-lived, stable, refrigeration machine.

The basic closure is achieved by means of a small core valve similar to that used in an automobile tire and of an aircraft manufacture quality. The valve is inserted into and removed from its position in the housing by use of a Core Removal Tool (CRT) similar to that used in the refrigeration industry. The tool was modified to provide simple and direct mounting to the pressure chambers. Both chambers are serviced with the same tool whereby the chambers can be pressurized, bled down, pumped and re-pressurized, repeatedly, to achieve a clean working volume. Once pressurized, the fill system is further sealed by a small "C" seal which is installed and torqued by use of a special spanner tool.

A sketch of the modified CRT is shown in Figure 10-2. A list of applicable drawings is as follows:

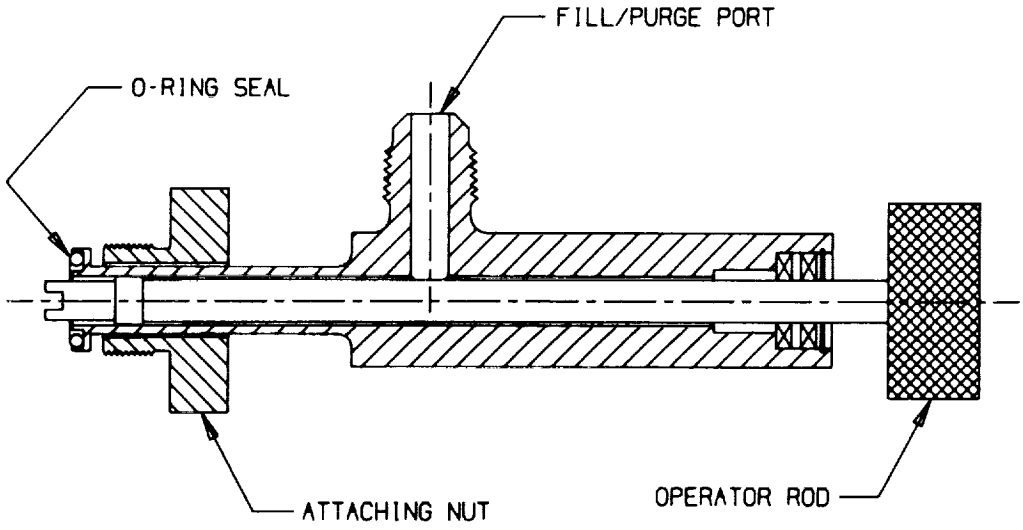

Figure 10-2. Core removal tool.

Dwg No.

001415	Seal Cap, Fill Valve
001221-5	"C" Seal, Lead Coated
002903	Disc, Slip Washer, Fill Valve
001414	Cap-Nut, Fill Valve
9914A	Valve Core, Schraeder P/N 9914A (*)
	Spanner, Trammel Installation Tool.

(*) Available from Schraeder Automotive Inc., P.O.Box 675, Nashville, TN 37202.

10.5.2 Requirements

All chambers are assembled within the Clean Room and should have a core valve installed to close off the working space from possible contamination by the Test Laboratory atmosphere. A core valve tool is used to purge and fill each chamber with its appropriate gas. An appropriate filling system is used which provides filtered dry gas to be introduced and evacuated from the chamber by means of a programmed valved switching setup. A liquid nitrogen trap is used to dry the gases during the operation. A block diagram of a typical setup is given in Figure 10-3.

10.5.3 Procedure

Any protective fixture or cap is removed from the area of the fill valve, and the CRT is installed into the pressure chamber. The appropriate filter (0.2 micron size), LN_2 trap, switching valve array and gas bottle is assembled and joined to the CRT connection. The tool operator rod is used engage the core valve and to unscrew and back the valve body away from its seat. The valve is held in this retracted or withdrawn position until the purging and pressurization operation is complete. It is important that all components and connections be kept as clean as possible throughout the

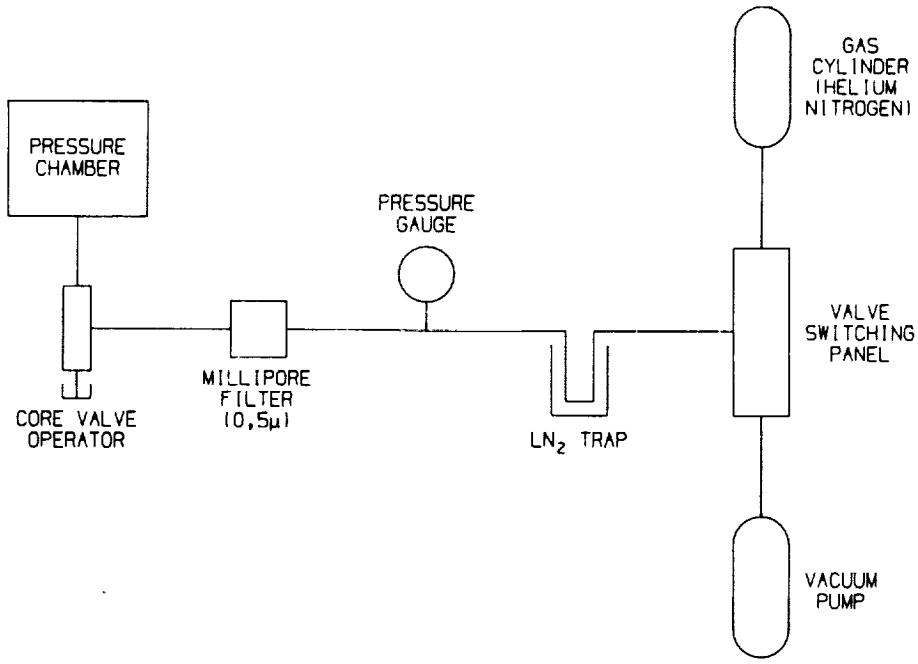

Figure 10-3. Fill-purge setup.

purging/fill operations. Although the compressor portion of the cooler is fitted with a 0.5 micron filter to retain any possible contaminants from entering the working space, it is still good practice to maintain conditions as clean as possible.

The sequence of the programmed purge/fill operation is as follows:

1. Fill chamber to 250 psig, helium. Three minute holding time.
2. Evacuate to few microns Hg pressure. Three minute hold.
3. Cease pumping and hold system for three minutes.
4. Fill and repeat from (1.) above. (*)

(*) Other purge/fill cycles could be chosen. The three minute interval happened to be the programmed switching interval which was readily available and proved to be quite adequate.

The purging operation is repeated for thirty-five (35) cycles, after which the procedure is stopped at a chamber pressure of 250 psig helium.

The operator rod of the CRT is then advanced, and the core valve threaded into its seat. The operator rod will exhibit a distinct back pressure during the insertion and seating of the valve core due to the helium pressure within the line. The valve is torqued to 1.5 to 3 in-lb. The CRT assembly is then removed from the housing. A "C" seal is positioned in place, and the components consisting of the Seal Cap, the Slip Washer and Cap-Nut are assembled over the seal. The Seal Cap is held stationary by an Allen wrench while the Cap-Nut is torqued to value. A spanner is used to torque the seal to 35-40 in-lb.

11. REFRIGERATOR PERFORMANCE TESTS

The section describes the measurement techniques and accuracy of the measured data. Performance test data is presented, and the instrumentation used is listed in Section 11.6.

11.1 Performance Measurements

Cryogenic Temperature:

Cold finger temperature was monitored with the diode instrumentation described in Section 8.3. A digital multimeter was used to monitor the diode forward voltage which was then used to calibrate the signal conditioning circuitry so that the front panel readout was in agreement with the manufacturer's calibration data sheet. Independent confirmation of the cold temperature measurement was verified with the TRI precision calibrated diode and the cryo-controller unit. The front panel temperature readout and the TRI readout agreed within plus or minus 0.5°K during an initial cooldown from room temperature (295°K) to 40°K.

Heat Load:

Calibration of the cold finger heat load and its controller was performed on the bench prior to installation in the system. The heater element was immersed in a liquid nitrogen bath (77°K) and the current through and voltage across the heater element were monitored using digital multimeters. This calibration data was then used to confirm the performance of the heater controller when integrated into the cooler control system. The errors between command and measured power values (as determined via the D-A/A-D system circuits and remote computer) were in close agreement with the benchtop calibration data (Table 11-1). Heater command values were adjusted to provide accurate power loading at the cold finger for performance testing.

TABLE 11-1. Heater Controller Performance.

Programmed Power	Measured Output Power (W)	
(Control Voltage)	Benchtop VI	Computer Readout
1.0	1.11	1.13
2.0	2.10	2.07
3.0	3.07	3.07
4.0	4.04	4.02
5.0	5.02	5.00
6.0	5.96	5.97

Axial Motion:

Axial motion of the reciprocating shafts was measured at the output of the LVDT circuits. The LVDT outputs are all scaled so that plus or minus 5 volts corresponds to the mechanical limits of free travel for each shaft (± 9 mm for the piston and counterbalance; ± 3.38 mm for the displacer). Figures 11-1 and 11-2 shows the position and motor current of the piston and displacer.

(a) Piston position and piston current.

x - 3.6 mm/div.

I - 10 A/div.

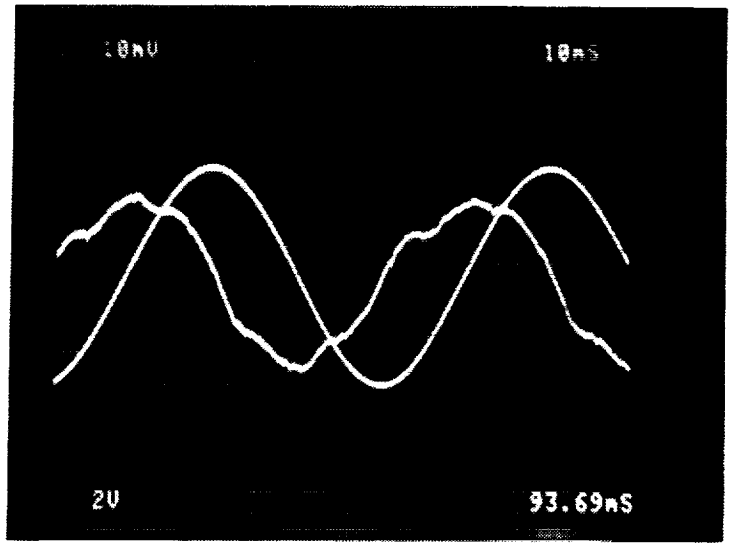

(b) Piston motion spectrum.

3.6 mm/V

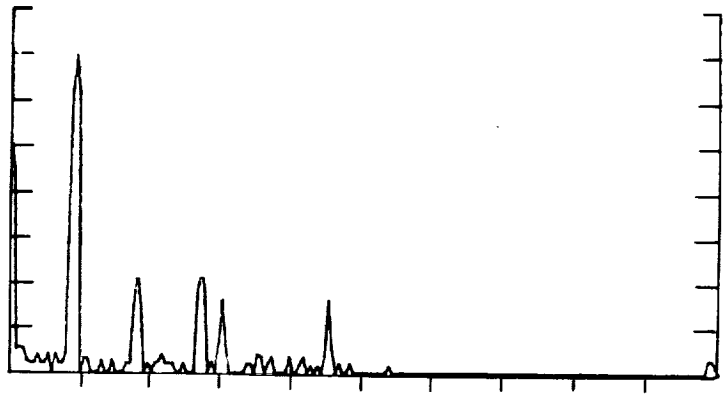

(c) Piston current spectrum.

10 A/10 mV

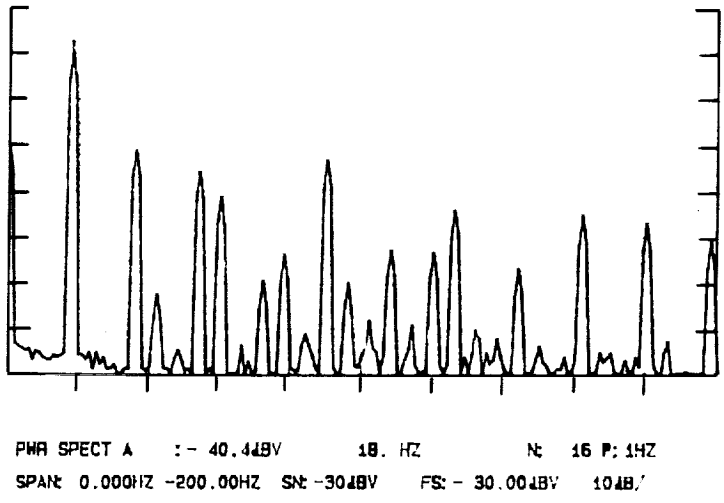

Figure 11-1. Spectral behavior of piston.

(a) Displacer position and current.

x - 1.34 mm/div.

I - 1 A/div.

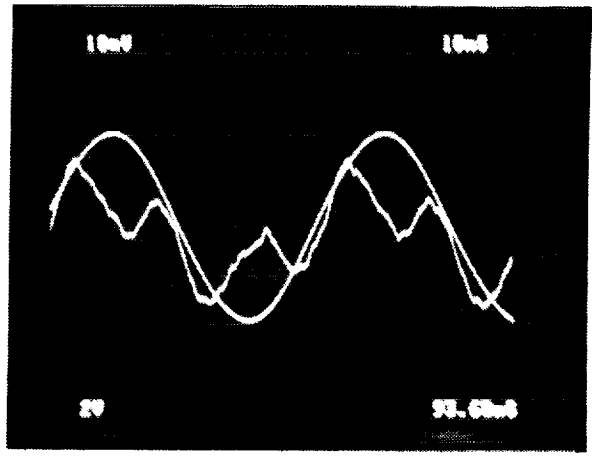

(b) Displacer motion spectrum.

0.667 mm/V

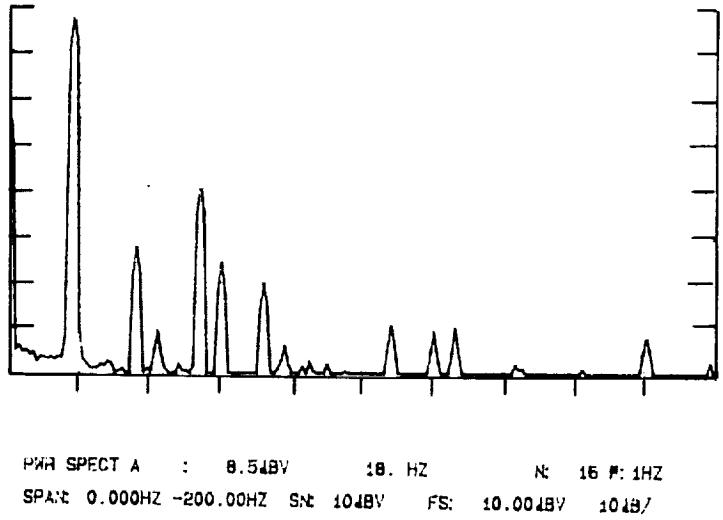

(c) Displacer current spectrum.

1 A/10 mV

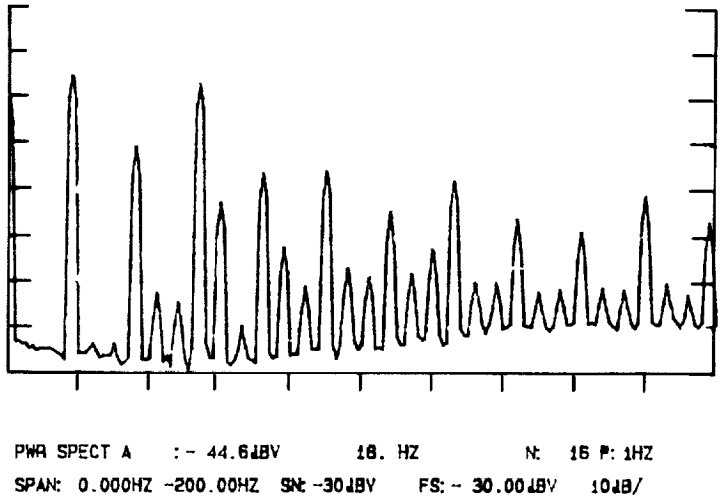

Figure 11-2. Spectral behavior of displacer.

Amplitude and frequency measurements were made using the waveform calculator of the digital oscilloscope. Because the position control operates in an open loop fashion, servo errors (which drive the motors) are not corrected. Therefore, the actual motion will be somewhat less than the command parameter, especially in the case of the piston subsystem which provides thermodynamic input power. The maximum error of the piston subsystem is about 5% when the load is greatest (minimum cold temperature). Overall amplitude stability (cycle to cycle) of all the axial control systems was good, with a measured average deviation of less than 0.5%. The stroke amplitudes presented in the performance test data reflect the measured values.

The operating frequency of the system is digitally derived and is therefore very stable. The digital resolution of the reference generator is about 0.1 Hz, the same as the frequency resolution of the oscilloscope. A test of the frequency control demonstrated repeatable control to within ± 0.05 Hz.

Phase resolution of the reference generator is about 0.3°. The phase delay is digitally derived and is accurate and stable. Servo loop errors, however, add a worst case offset of 3 to 4° (piston lag), which is not corrected by the System Controller. This phase error is constant at a fixed operating point. The phase presented in the performance test data reflects the actual value as measured by the Dranetz instrument.

Radial Motion:

Radial displacements of the shafts can be monitored at the buffered outputs of each of the bearing circuits. The radial bearing circuits are calibrated for a ± 5 volt deviation corresponding to the mechanical limits of travel (in all cases: ± 19 micron clearance seal annular gap), yielding an approximate resolution of 4 microns per volt. The remote control software is equipped with a peak detecting/peak holding display which provides an accurate assessment of bearing performance while the machine is running. Because this routine interferes with the operation of the bearing interlock, it should not be used continuously.

Scope photographs of all 12 bearing displacements at the design operating point are included in Figure 11-3. It is interesting to note that the peak bearing excursions vary during cooldown, as the changes in gas temperature and thermodynamic loading affect the harmonic current content of the motor drive currents. Once the system has attained resonance at the operating point, the radial errors are reduced and stable.

Electrical Power:

The electrical power input requirements of the cooler in both the STANDBY and RUN modes of operation were assessed; the power requirements of the support electronics were measured as well.

Axial motor power was determined by simultaneously acquiring (in one acquisition) the real-time voltage and current waveforms with the digital scope. A software routine scaled and multiplied the stored waveform data (VI). The mean value (over 1 cycle) of the resulting power waveform was then summed into a cumulative average power reading.

Radial bearing power figures are based on both measured and estimated figures. The sensor electronics, as configured, require considerable power for the illumination sources (12 sources, 60 mA each). The sensor amplifiers require a small additional current (24, 2 mA each). The STANDBY power for the bearing pole piece actuators (in a 1g environment) was estimated using a nominal bias current of 100 mA per coil, with dissipation for each coil based on resistance losses. The RUN power estimate for the pole piece actuators was based on the difference of the measured

(a) Piston bearing displacements.

3.8 microns/div.

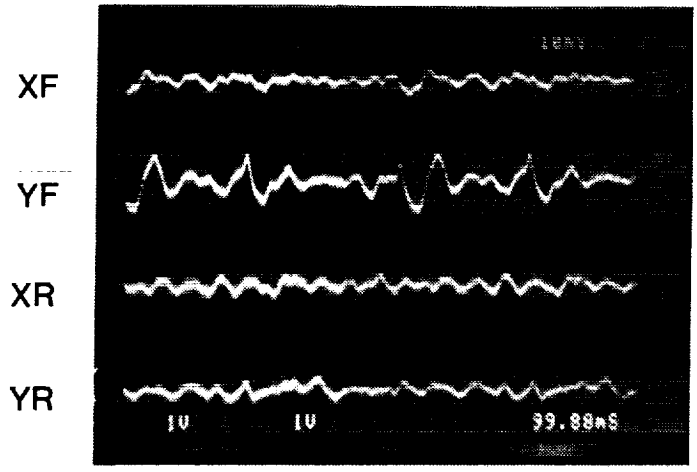

(b) Displacer bearing displacements.

3.8 microns/div.

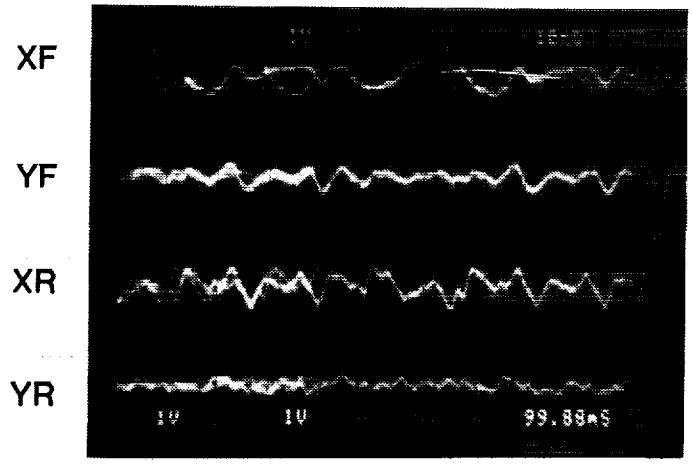

(c) C'balance bearing displacements.

3.8 microns/div.

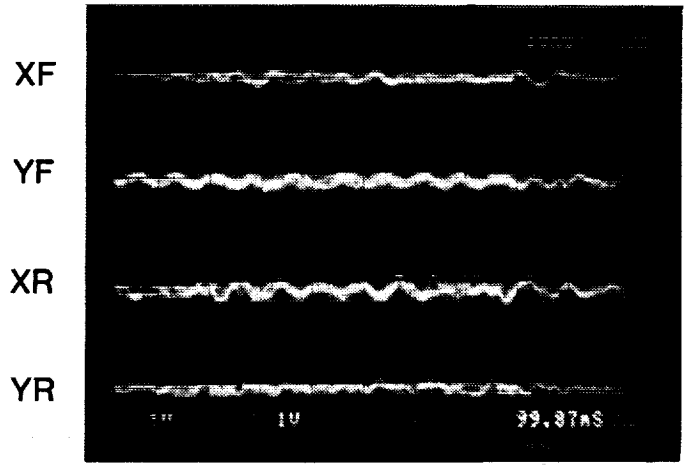

Figure 11-3. Bearing displacement errors.

28V power input to the bearing driver circuits when the system was running. This assumes that the current drivers are 100% efficient and hence is a conservative estimate. Cooler instrumentation requires an insignificant amount of power.

The voltage and current input requirements of each of the electronic subsystems were measured in both the STANDBY and RUN modes. They are presented in Tables 11-2 and 11-3. No attempt was made to minimize the electronic power requirements.

TABLE 11-2. Electrical Power - System in STANDBY Mode.

- Breakdown of dc Current Requirements (Amperes):

DC Subsystem	+5V (A)	+15V (A)	-15V (A)	+28V (A)	Power (W)
Bearing Rack	0	1.02	0.28	0.99	47.2
LVDT & Instrumentation	0	0.25	0.30	0.17	13.0
Computer Rack	2.04	0.11	0.11	0	13.5
Axial Drivers (3)	0.12	0.01	0.02	-	1.05
Piston Driver	-	-	-	0.08	2.2
Displacer Driver	-	-	-	0.09	2.5
C'balance Driver	-	-	-	0.28	7.8
Ampere (A)	2.16	1.39	0.71	1.61	
Volts (V)	5V	15V	15V	28V	
Power (W)	10.8	20.9	10.7	45.1	87.5 W

- Power Delivered to Cooler:

Radial Sensors	(12 x 0.06A + 24 x .002A) x 15V	=	11.5
Displacer Radial	8 x $0.1A^2$ x 31 ohms	=	2.5
Piston Radial	8 x $0.1A^2$ x 10.5 ohms	=	0.84
C'balance Radial	8 x $0.1A^2$ x 2.6 ohms	=	0.21
Displacer Axial	$0.4A^2$ x 2.2 ohms	=	0.35
Piston Axial	$0.25A^2$ x 0.34 ohms	=	0.02
C'balance Axial	$0.2A^2$ x 2.6 ohms	=	0.1
			0.1
	Total Power Delivered		15.5 W

115 Vac input power to dc supplies VI = 267 W (17A pk for 2ms)

AC input power to the dc power supplies was measured to determine the electrical demand for operation. Because the power supplies are of a switched-mode power conversion type, they typically draw high peak currents at a low power factor. The peak current measurements are given along with the average power data.

TABLE 11-3. Electrical Power - System in RUN Mode (65°K 5W).

- Breakdown of dc Current Requirements (Amperes):

DC Subsystem	+5V (A)	+15V (A)	-15V (A)	+28V (A)	Power (W)
Bearing Rack	0	1.20	0.32	1.25	57.8
LVDT & Instrumentation	0	0.56	0.33	0.30	21.75
Computer Rack	2.81	0.23	0.12	0	19.3
Axial Drivers (3)	0.15	0.02	0.02	-	1.35
Piston Driver	-	-	-	5.40	151.2
Displacer Driver	-	-	-	0.14	3.92
C'balance Driver	-	-	-	0.89	24.9
Amperes (A)	2.96	2.01	0.79	7.98	
Volts (V)	5V	15V	15V	28V	
Power (W)	14.8	30.2	11.9	223.4	280.3 W

- Power Delivered to Cooler:

Radial Sensors	(12 x 0.06A + 24 x.002A) x 15V	=	11.5
Displacer Radial	8 x 0.1A^2 x 31 ohms	=	2.5
Piston Radial	8 x 0.1A^2 x 10.5 ohms	=	0.84
C'balance Radial	8 x 0.1A^2 x 2.6 ohms	=	0.21
Bearing Rack Input	(1.25 - 0.99) x 28 V	=	7.28
Displacer Axial	(0.8A^2 x 2.2 ohms = 1.4 W); VI	=	1.6
Piston Axial	(9.9A^2 x 0.34 ohms = 33.3W); VI	=	125
C'balance Axial	(0.7A^2 x 2.6 ohms = 1.28 W); VI	=	11.5
	Total Power Delivered		160.4 W

115 Vac input power to dc supplies VI = 461 W (25A pk for 2ms)

Environment:

The ambient temperature maintained by the laboratory air conditioning system was 22°C. The recirculating bath which provided coolant to the three housing cooling jackets was maintained at 21°C.

A vacuum system maintained a pressure of less than 10^{-6} Torr within the insulating dewar. The long term integrity of the insulating vacuum was found to be inadequate and will need to be monitored during operation.

11.2 Search for Optimal Operating Conditions

The refrigerator was optimized for minimum total input power. In the design phase of the program, analyses were performed to obtain the optimal design and operating parameters for minimum input power. Upon completion of the refrigerator, experimentation was carried out to verify the optimal operating conditions and to make adjustments due to fabrication tolerances and some higher order effects which were not accounted for in the design study.

The total input power is the sum of the thermodynamic input power to the Stirling cycle and the electromechanical inefficiency of the motors. Based on thermodynamic analyses, confirmed by measurement on refrigerators fabricated in the past, a small adjustment of the optimized operating parameters does not significantly affect the Stirling efficiency, but would seriously compromise the motor efficiency. The refrigerator consists of three damped oscillatory spring-mass systems actuated by linear motors. The conditions for minimum power input operation of these systems are a first-order function of the refrigerator operating parameters such as cycle speed, spring stiffness, and mean pressure (Sect. 3.2 and 5.2). Of these three systems, the piston input power is about 80% of the total input power; thus, it is important that the piston be operated under minimum power conditions.

After the Prototype Model was assembled, one could optimize the Stirling performance by hunting for the minimum thermodynamic input power by perturbing the operating parameters while maintaining 65°K and a 5 watt load. The operating conditions were optimized to achieve the minimum power operation of the piston; this resulted in better than predicted efficiency.

Minimum power operation of the piston was accomplished by first setting the refrigerator to run under the design parameters until it reached 65°K. Then, the phase between the first harmonics of the piston motor current and the piston position waveform was measured. Adjustments to the cycle speed and mean pressure were made to obtain a 90° phase. This ensured the piston was operating under the minimum power condition. The piston and displacer strokes were subsequently adjusted to obtain 5 watts of cooling. The total power was further reduced by installing a radiation shield around the cold end section. The shield was made from multilayers of insulated mylar sheets with highly reflective metallization coatings.

Table 11-4 shows the design operating parameters and final optimized values. The close agreement between the two sets of values validates the accuracy of the engineering analyses in this program.

TABLE 11-4. Refrigerator Design and Optimized Operating Parameters.

		Design (predicted)	Optimized (measured)
Cold End Temperature	K	65	65
Heat Sink Temperature	K	293	293
Cooling Capacity	W	5	5
Speed	Hz	18.3	18.0
Mean Pressure	psia	263	290
Displacer Amplitude	mm	2.3	2.6
Piston Amplitude	mm	7.3	6.67
Phase (displ./piston)	degrees	60	63.5
Motor Input, Piston	W	136	125
Motor Input, Displacer	W	3	1.6
Motor Input, Counterbalance	W	10	11.5

11.3 Cooldown Characteristics

The remote control computer was used to log the cold end temperature at one minute intervals during cooldown from room temperature. Two tests were performed, using the design stroke and an increased stroke (Fig. 11-4). No heat load was applied at the cold finger. Note that the values recorded by the remote computer rely on the linearized temperature estimate. These cooldown curves may be utilized as a benchmark to gauge any deterioration in cooler performance.

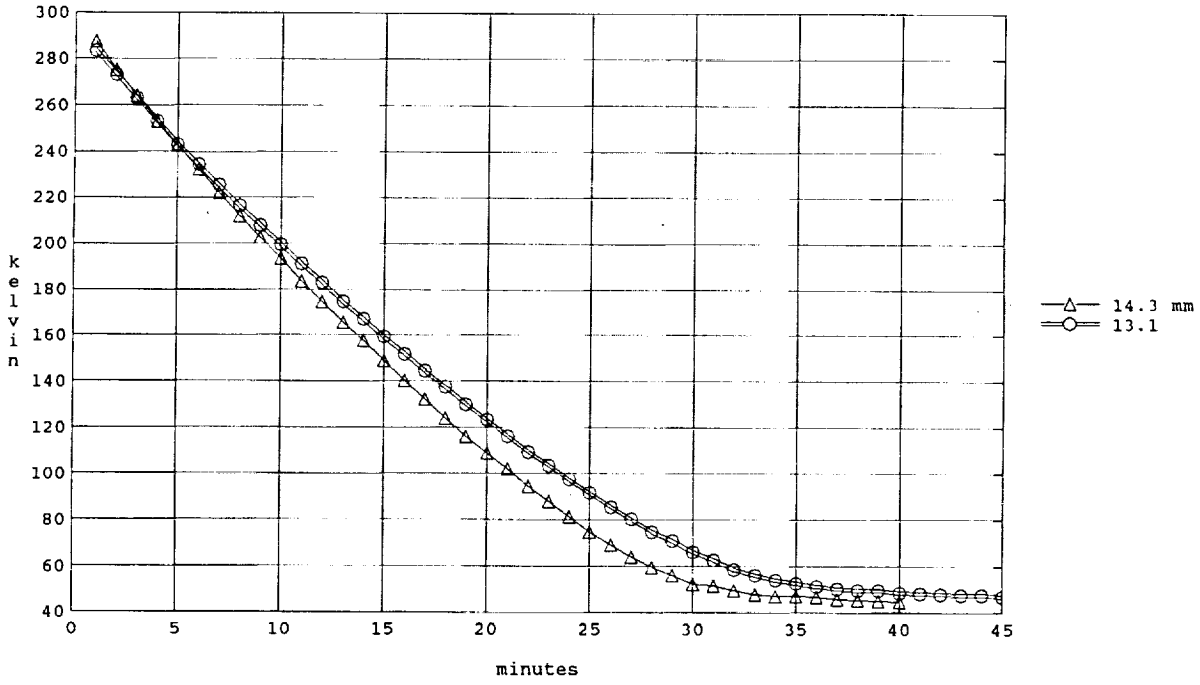

1) 18 Hz, 63° phase, piston stroke = 14.3 mm, displacer stroke = 5 mm.
2) 18 Hz, 63° phase, piston stroke = 13.1 mm, displacer stroke = 5 mm.

Figure 11-4. Cooldown curve - no heat load.

11.4 Vibration Measurements

Axial accelerations of the cooler housing were measured at the ends of the housing, and radial accelerations were measured at three points along the length of the housing with the accelerometer. Power spectra of this data are shown in Figures 11-5 to 11-7.

Axial and radial displacement measurements were made at the extreme edges of the cold finger insulating dewar, where we would expect to find worst-case excursions. To minimize extraneous

vibrations, the instrument was securely anchored to the same rigid surface as was the mounting cradle of the cooler. Photographs of the displacement waveforms appear in the performance data. A power spectrum of the axial displacement is included for correlation with the axial acceleration data. The results are shown in Figures 11-5 to 11-7.

11.5 Parametric Testing

A remote control computer offers wide flexibility in the performance of parametric testing. Dynamic parameters such as frequency, phase, and amplitude of the piston and displacer motions can be changed while the cooler is running. Feedback of the cooler performance parameters (i.e., cold temperature, heat load) provides a means through which parametric testing and data logging can be automated via programming of the remote computer. The parametric testing for the cooler was not automated.

Two parametric tests were performed. In the first, the cooler was run at the design point (sufficient to provide 5 watts at 65°K), and heater power was varied. Final temperature and cooler input power were measured once stable operation was established (Fig. 11-8). This test was performed prior to the addition of radiation shielding in the insulating Dewar and reflects performance with the added radiation heat load.

In the second test, the piston stroke amplitude was varied to maintain a constant temperature (65°K) into a heat load of 5 watts and 2 watts. These points establish a performance curve for comparison to predicted performance based on computer modelling (Fig. 11-9).

a) Cold end axial displacement.

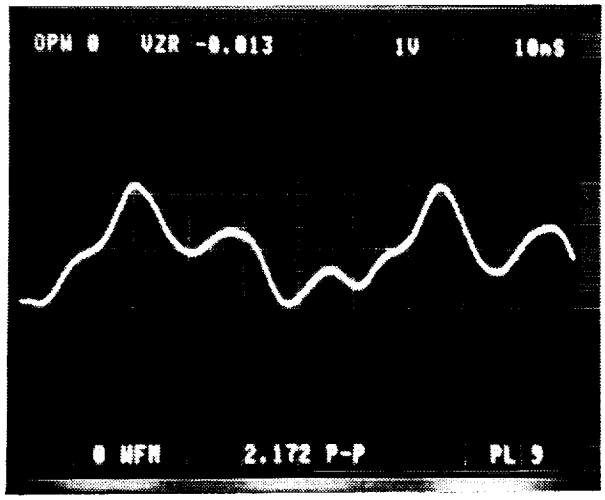

600 micro inches/Div.

b) Axial acceleration spectrum.

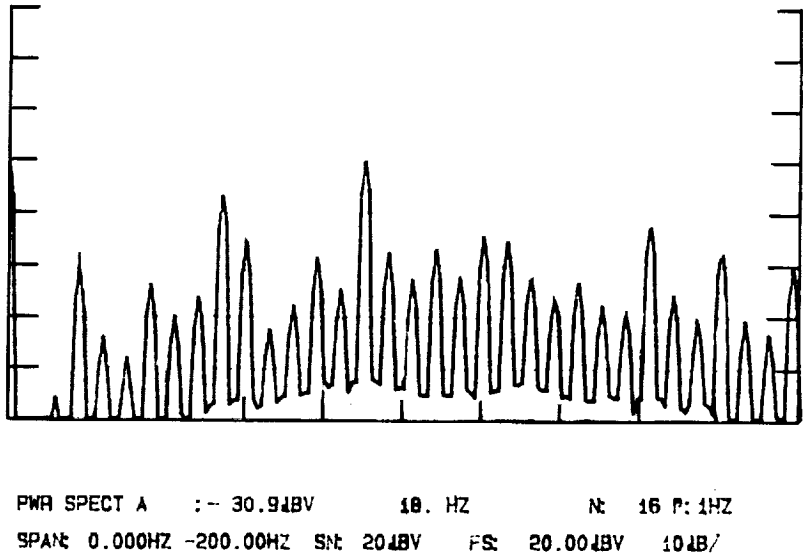

1 m/s^2/volt

Figure 11-5. Displacement and acceleration at cold end. (Cont'd.)

c) Cold end radial displacement.

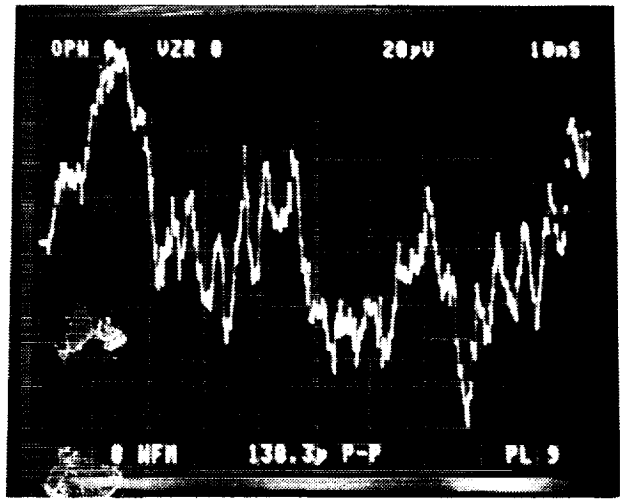

20 micro inches/Div.

d) Radial acceleration spectrum.
(at cold end)

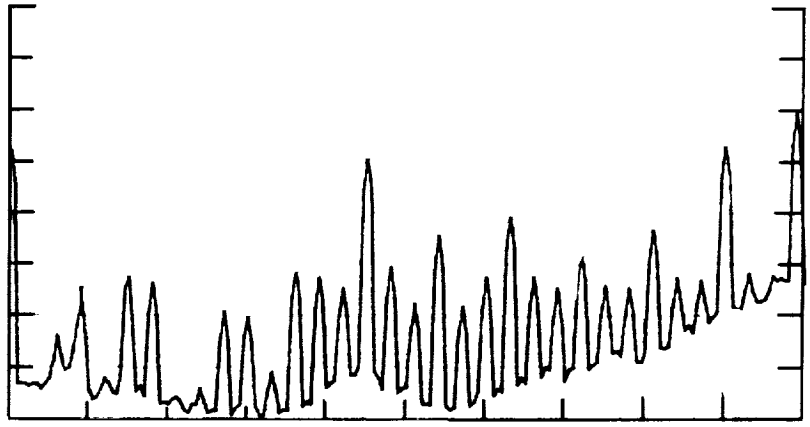

1 m/s^2/ volt

Figure 11-5. Displacement and acceleration at cold end.

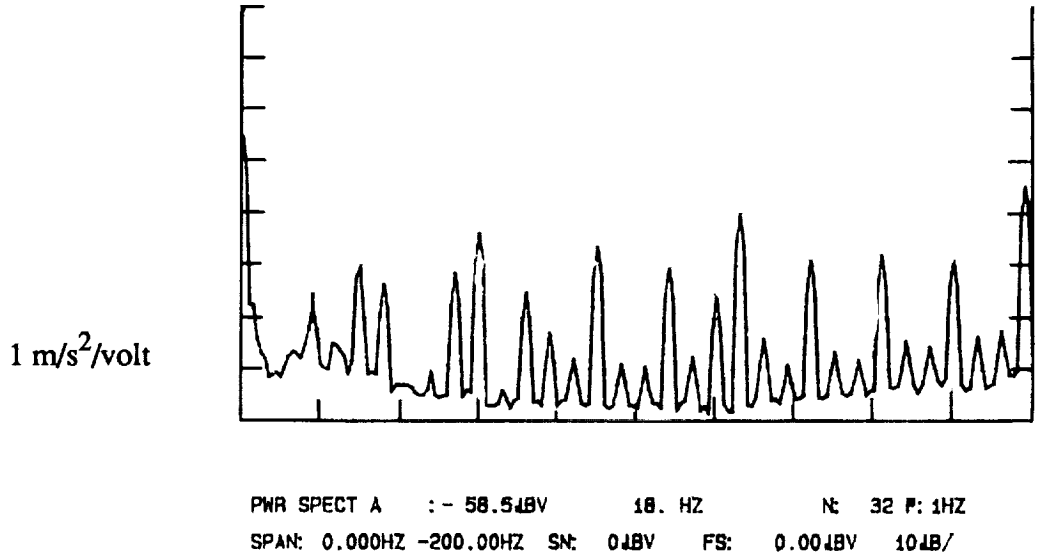

Figure 11-6. Radial acceleration spectrum at piston housing.

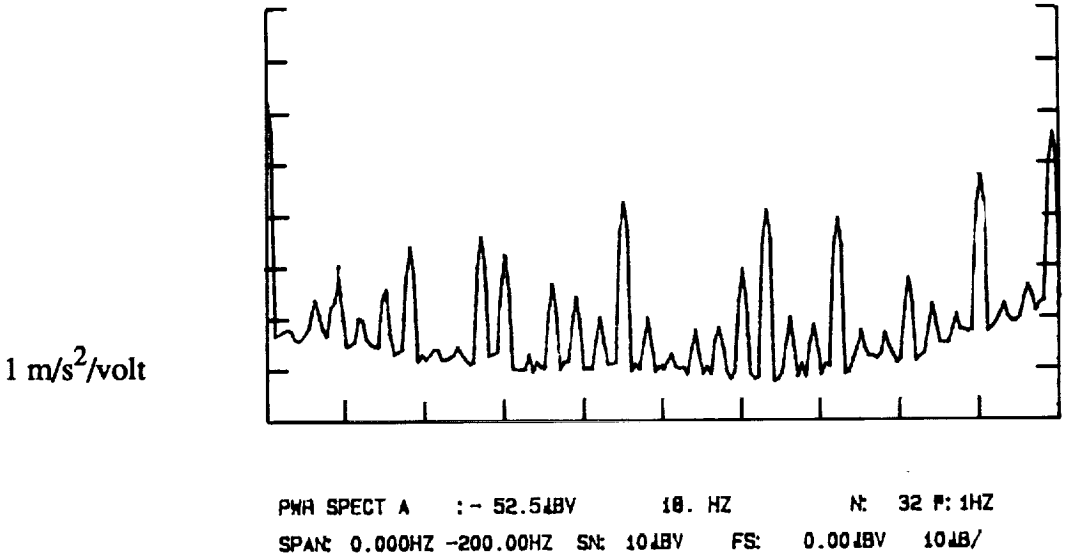

Figure 11-7. Radial acceleration spectrum at counterbalance end.

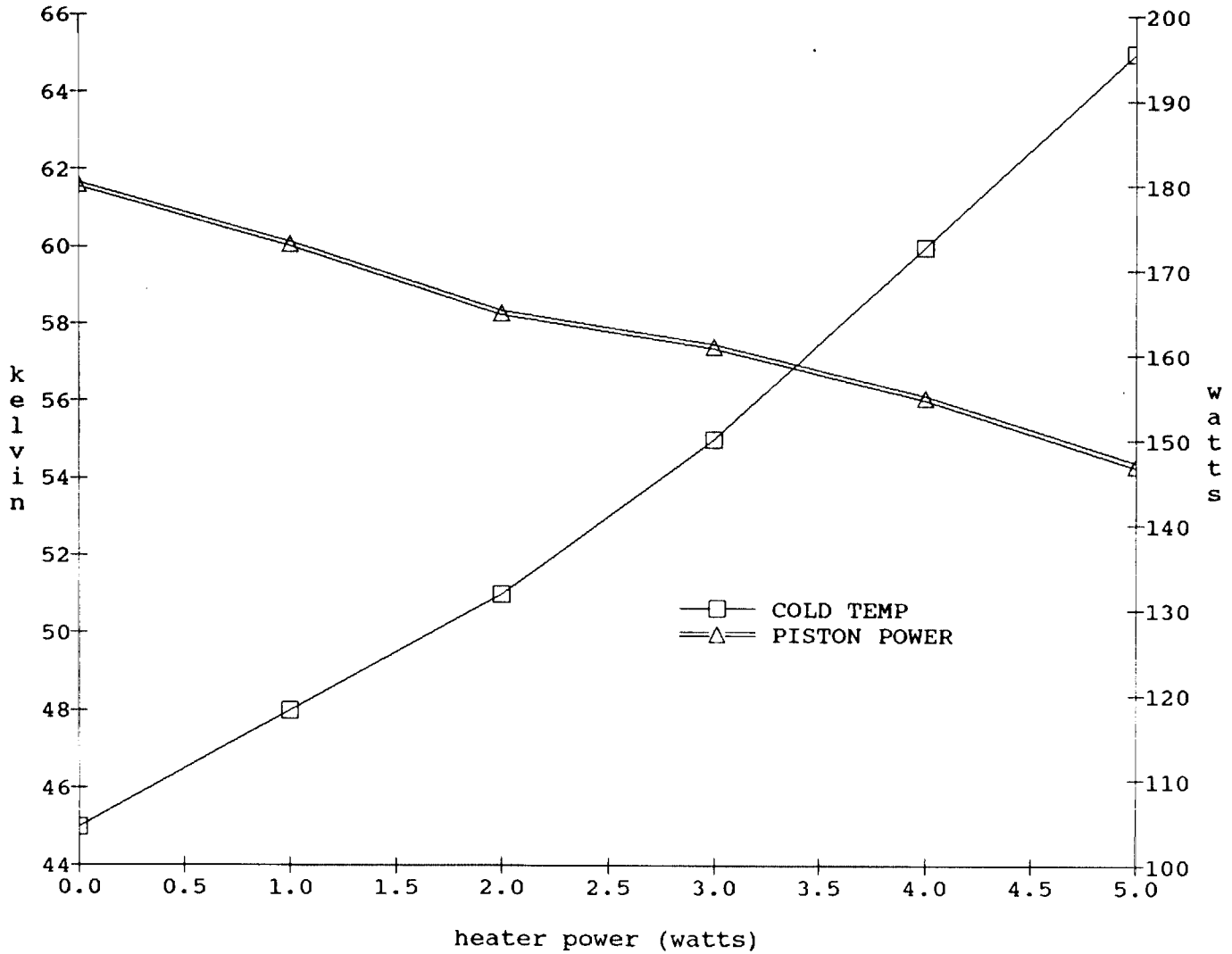

18 Hz, 63°, p = 14.8 mm stroke, d = 5.2 mm stroke

Figure 11-8. Cooler performance for varied heat load (constant motion parameters).

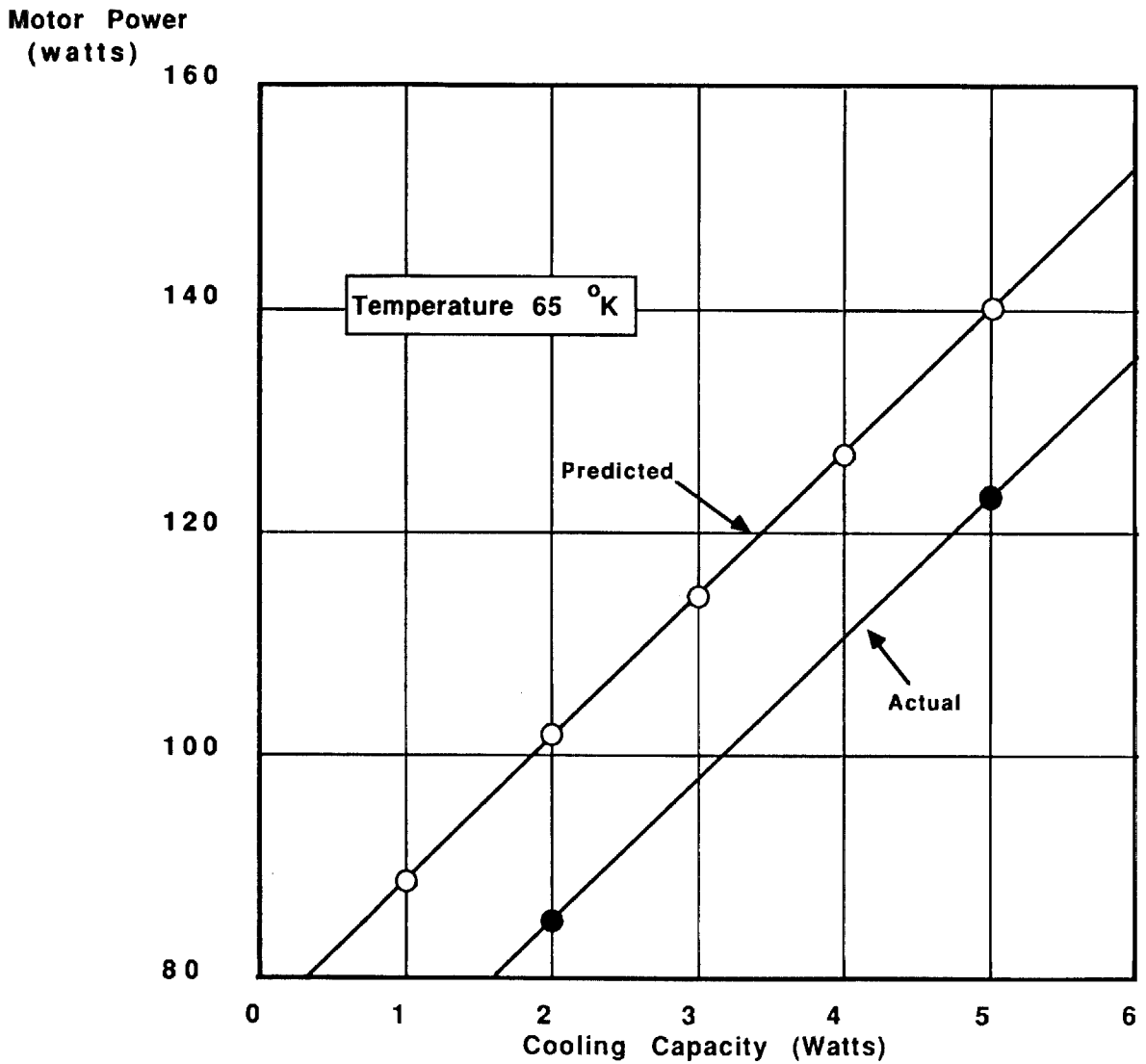

Figure 11-9. Piston motor power required to produce cooling at 65°K.

11.6 Instrumentation for Performance Tests

The following instruments were used for evaluating the cooler performance:

❖ Waveform Measurements

- Tektronix 7854 Digital Oscilloscope With Waveform Calculator.
- Tektronix 7B87 Timebase.
- Tektronix 7A26 Dual Trace Amplifier.
- Tektronix 7A22 Differential Amplifier.
- Tektronix 6063B 1x/10x Probe(s).
- Tektronix TM504 Powered Module Rack.
- Tektronix AM503 Current Amplifier.
- Tektronix A6303 Current Probe.

These were used for voltage (i.e., stroke amplitude, voltage, current, dynamic pressure) measurement with nominal vertical resolution of 0.2% of reading, assuming 5 divisions deflection. Horizontal resolution was 2% of selected time/division (typical frequency resolution to within 0.1 Hz at 20 Hz).

The waveform calculator was used to extract waveform parameters and compute RMS current and (VI) power. The calculator was also programmed to perform iterative averaging of dynamic measurements. Waveform calculator measurement parameters and arithmetic functions are accurate to four significant digits.

❖ Temperature Measurements

- TRI Research Model T-2000 Cryo-controller.
- TRI Research Model CD301-SO-PB-SC3 Cryo Diode.

These were used for temperature measurements. Diode/controller combination is rated accurate to ± 0.1°K over the range of 25 to 300°K

❖ Phase Measurements

- Dranetz Model 305 Phase Angle Meter.

Assuming an undistorted sinewave input, specified resolution is ± 0.01°. Practical readings indicate an accuracy of ± 0.2 °.

❖ Vibration Measurements

- Bruel & Kjaer Model 4368 Accelerometer.
- Kistler 504E Charge Amplifier.
- MTI 1000 Fotonic Sensor.

The accelerometer/signal conditioner used for vibration measurement was calibrated for an output of 1 meter per second squared per volt output. Frequency response is flat to beyond 1 kHz.

A non-contacting (optical reflectance) displacement transducer used for vibration measurement. The unit was calibrated prior to each measurement, using a micrometer mount, to a sensitivity of 0.0006 inch per volt output.

❖ Other Measurements

- Wavetek 5820 Cross Channel Spectrum Analyzer.
- Hewlett/Packard 3466 Digital Multimeter(s).

This analyzer was used primarily during optimization of the axial and radial control systems and spectral analysis of vibration measurements. It was also useful to confirm relative phase angle measurements, particularly where the fundamental frequency was of interest.

General purpose volt-ohm-ammeter with 4-1/2 digit resolution used to monitor the forward voltage drop of the temperature sensing diode(s) and for calibration of the axial and radial position sensors.